Crack Formation and Growth During Thermal-Shock and Mechanical Cycles in Refractories

Maria João Margarido Rodrigues

Master Dissertation

Supervisor in FEUP: Prof. Jorge Lino Alves

Supervisor in Tata Steel: Kirill Andreev

U.PORTO
FEUP FACULDADE DE ENGENHARIA
UNIVERSIDADE DO PORTO

Integrated Master in Mechanical Engineering

July 2019

Para os meus pais

Abstract

The present dissertation aimed at studying crack formation and growth in silica refractories under cyclic thermal-mechanical loading, which is one of the main causes of failure in service conditions. Two methodologies of tests were carried out: mechanical and thermal-shock cyclic tests. The application of Digital image correlation (DIC) for both approaches was also studied.

The thermal shock tests were carried out between 200 °C and room temperature for samples of different sizes. The damage was assessed by ultra-sound measurements. The crack development was visually registered after each cycle and the Hausdorff parameter was calculated for the fracture surfaces. A theoretical approach was also used and confirmed the results obtained

The mechanical test selected was the wedge splitting test. The compliance and irreversible displacements were calculated to evaluate damage development throughout the test. The fracture surfaces were analysed using a wide area 3D measurement system and different roughness parameters (including the Hausdorff parameter) were calculated.

It was possible to observe that in thermal shock tests the strain is determined by the size of the sample. Three patterns of damage development were observed: exponential, sigmoidal and saturation for large, intermediate and small samples respectively. It was observed that the standard size for thermal-shock testing might not represent the service conditions. In mechanical tests, both exponential and sigmoidal behaviours were observed depending on the amplitude tested (higher amplitude - higher tendency for exponential behaviour).

For thermal shock tests, the roughness increased with the number of cycles until a peak was reached, after which the roughness decreased and stabilized for a high number of cycles. In mechanical tests, due to the lack of relevant data, the presence of this peak could not be confirmed. The roughness in the thermal shock surfaces tended to be higher than in the mechanical tests.

DIC was used to measure crack opening during the tests. It also enabled to identify cracks before they were visually detected and to predict their path. The crack opening measurements were in agreement with the experimental results obtained and the theoretical approach used.

While mechanical and thermal shock tests are inherently different, similar behaviours in the damage and crack development were possible to observe.

Formação e Desenvolvimento de Fendas em Refratários Durante Ciclos de Choque Térmico e Mecânicos

A presente dissertação focou-se no estudo da formação e crescimento de fendas em tijolos de sílica submetidos a cargas termomecânicas, as quais são uma das principais causas de falha nas condições de serviço. Foram utilizadas duas metodologias de teste distintas: testes cíclicos mecânicos e de choque térmico. A aplicação de correlação digital de imagem, para ambos os testes, foi também estudada.

Os testes de choque térmico foram efetuados entre 200 °C e a temperatura ambiente para amostras de diversos tamanhos. A degradação das amostras foi estudada através da medição da velocidade do som durante os ciclos. O desenvolvimento das fendas foi visualmente registado em cada ciclo e a constante de *Hausdorff* foi calculada para cada superfície de fratura. Foi também utilizada uma abordagem teórica que confirmou os resultados experimentais obtidos

O teste mecânico escolhido foi o *wedge splitting test*. A flexibilidade e os deslocamentos irreversíveis foram calculados de modo a avaliar a desenvolvimento do dano durante o teste. As superfícies de fratura foram analisadas usando um sistema de medição de área 3D e foram calculados diversos parâmetros de rugosidade.

Foi possível observar que nos testes de choque térmico a carga/deformação é determinada pelo tamanho das amostras. Foram observados três comportamentos de desenvolvimento de dano distintos: exponencial, sigmoidal e saturação, para amostras de grandes, intermédias e pequenas dimensões respetivamente. Foi observado que o tamanho normalizado para testes de choque térmico pode não ser representativo das condições de serviço. Nos testes mecânicos, tanto o desenvolvimento de dano exponencial como sigmoidal foram observados, dependendo da amplitude de teste utilizada (quanto maior a amplitude mais provável é observar-se o comportamento exponencial).

Para os testes de choque térmico a rugosidade aumentou com um número de ciclos até ser atingido um pico, após o qual a rugosidade decresceu e estabilizou para um elevado número de ciclos. Nos testes mecânicos a presença deste pico não pode ser confirmada devido à falta de dados relevantes. A rugosidade encontrada nos testes de choque térmico tendeu a ser superior à dos testes mecânicos.

A técnica de correlação digital foi utilizada para a medição da abertura da fenda durante os testes. Esta técnica permitiu ainda detetar fendas que não eram visíveis e prever a sua trajetória. As medidas de abertura de fenda obtidas em ambos os testes estiveram de acordo com os resultados experimentais obtidos e com o algoritmo utilizado

Embora os testes térmicos e mecânicos sejam inerentemente distintos foi possível observar um comportamento similar para ambos, tanto no desenvolvimento do dano como na formação e crescimento das fendas.

Acknowledgements

Firstly, I would like to thank Sido Sinnema for the possibility of participating in this project.

I would also like to thank my supervisor at Tata Steel, Kirill Andreev for the help and guidance throughout the project.

Additionally, I would like to thank Paul Tamis for the help in the simulation and Donald Mittertreiner, Frank Van der Does and Mustafa Keskin for all the support during the experimental procedures.

Moreover, I would like to thank all the employees at the Ceramic Research Centre which were very welcoming and created a friendly work environment.

I would also like to thank the University of Porto and specially my supervisor at FEUP, Fernando Jorge Lino Alves which, was always available for my questions and doubts throughout the project.

I would like to thank my family for all the support they gave me throughout this project.

Finally, I would like to thank both Tata steel IJmuiden and the Erasmus programme for the financial support.

Contents

List of Symbols

A - Area

A total - Total area created if crack fractured.

A_P - Area of the projection of the fracture surface

An - Percentual increase in the area in the respective n cycle.

b - Height

Bi - Biot number

C - Compliance

D - Hausdorff dimension

D_b - Displacement correspondent to the minimal force reached in a given cycle

dh - Distance grown in the normal direction

D_t - Displacement correspondent to the maximal force reached in a given cycle

D_{irr} - Irreversible displacement for a N cycle

dw - Distance grown in the transversal direction

E - Young's modulus

E_0 - Young's modulus before the experiment

E_d - Young's modulus after the experiment

Fb - Minimal force reached in a given cycle

F_H - Splitting force (horizontal component of the force in the wedge splitting test)

FV - Vertical force of the test machine in the wedge splitting test

F_{Hmax} - Maximum load

F_t - Maximum force reached in a given cycle

H - Hurst exponent

H - Coefficient of heat transfer

K - Thermal conductivity

KI - Stress intensity factor

KIC - Fracture toughness

K_m - Maximum stress intensity factor

K^* - Normalized maximum stress intensity factor

L - Length

Lc - Characteristic length

$Leff$ - Effective characteristic length

Lth - Theoretical characteristic length

N - Number of the cycle

n - Euclidian dimension

R'''' - kinetic thermal shock damage resistance

R_{st} - quasi static thermal shock resistance

Sa - Arithmetical mean height

Sq - Root mean square height

Sz - Maximum height

t_{σ}^{*} - Dimensionless time of occurrence of σ^{*}

t_{k}^{*} - Dimensionless time of occurrence of K^{*}

V - Volume

v - Velocity of sound

α - Linear coefficient of thermal expansion

β - Slop obtained from the straight-line fit performed on the Fourier power spectrum

γ_{wof} - Work-of-fracture (measured originally by Nakayama and subsequently by Tattersall and Tappin);

δ - Load point displacement

δult - Ultimate displacement

ΔT - Thermal gradient

Δx - Displacement in the x direction

Δxi - Displacement in x direction in point i

$\Delta x\ crack$ - Crack opening

ε - Real strain

ν - Poisson's ratio

P - Specific density

σ - Nominal strength

σ_{m} - Maximum stress

$\sigma_{u,}$ - Tensile strength

σ^{*} - Normalized maximum stress

Φ - Wedge angle in the wedge splitting test

List of Figures

Appendixes

List of Graphs

Appendixes

List of Tables

Appendixes

1 Introduction

1.1 Project Framing

The present dissertation was conducted at Tata Steel IJmuiden in the COE Refractories at Lab 3 of Tata Steel R&D in a partnership with the Mechanical Engineering Department of the Faculty of Engineering of the University of Porto, Portugal, as a Master Thesis Dissertation within the Production, Conception and Manufacturing option of the Integrated Master in Mechanical Engineering.

1.2 Increasing Value in Use of Refractory Linings in Tata Steel IJmuiden

Tata Steel is one of the largest and most advanced steel producers in the world. To produce steel, it operates various high temperature units (e.g. blast furnace, coke ovens) that are lined with special ceramic refractory materials (refractories). During service, refractories are exposed to cyclic thermo-mechanical loads. Over time, the loads cause cracking and degradation of the units. A part of the direct costs is allocated to restore the lining. Moreover, the unplanned failure of refractories can inflict significant losses due to unrealised production and can ultimately be a cause of serious material damage. Additionally, it can also represent a threat to the health of the personnel. Proper refractory lining is one of the key enablers of a reliable and efficient steelmaking process.

There are many alternative refractories on the market. Tata Steel IJmuiden, as the user of these materials, constantly monitors the market to select the most suitable. In-house Ceramics Research Centre has the duty to provide, in cooperation with other technical and financial departments, the best value in use concepts of the refractory linings. Those should combine high reliability and be cost effective. On annual basis, the savings of several millions of Euros are achieved. The duties of the Centre include testing of refractories, modelling of the linings and related process, data analysis (including Advanced Analytics), in-field measurements of the linings. The testing is done for Quality Control and to assess the specific properties of refractories. The latter is seen as a critical enabler for all other activities of the Ceramics Research Centre.

1.3 Project Goals

The project aims at contributing to the development of advanced test procedures to assess the refractories resistance to cyclic failure. Traditionally, the selection of the materials is based on the ranking of properties measured for the alternative materials. Modern trends of prolonged campaign lives and increased demand for reliability of the performance warrant algorithms predicting the response of materials in given process conditions. In this way, the material properties are to be compared with the loads inflicted by the process. The project goal is to contribute to the activity to develop effective methods to predict and monitor cyclic fatigue degradation due to thermal and mechanical cyclic loads. Damage development due to different loading schemes will be assessed by non-destructive techniques and by fractography. For the latter, alternative techniques will be tried. The correlation of the test piece geometry and the

damage progress will be studied. The diagrams relating the progress of damage and load intensity will be created.

1.4 Project Methodology

The organization of the work was based on Table 1. The first weeks were used for literature survey and preparation of samples. When samples were prepared the experiments were carried out. Weekly meetings were conducted throughout the project for updates on the results of the experimental procedure and decision making in relation with the direction of the project. A mid-term presentation was also carried out to show the progress development. The experimental procedures were not completely delimited from the beginning since they depended on the results of the first tests. Therefore, the approach used was an iterative one, which allowed to define new tests based on the results and questions which would arise from the first results. To enable this type of organization the analysis and interpretation of the results were done in parallel with the experimental procedure. The dissertation was developed throughout the project. The final weeks were left for the finalization of the dissertation.

Project plan:

Activity 1: Literature survey

Activity 2: Preparation of samples

Activity 3: Conduction of the experiments, post-processing of the results

Activity 4: Analysis of the experimental results

Activity 5: Final report: Reporting of experimental findings and analysis.

Xx* - mid-term presentation

Tabel 1 – Weakly Project planing

	Weeks (Start at : 06/02/2019)									
	1-2	**3-4**	**5-6**	**7-8**	**9-10**	**11-12**	**13-14**	**15-16**	**17-18**	**19-20**
Activity 1	xx	xx	xx	xx	xx	xx	xx	xx		
Activity 2	xx			xx		xx				
Activity 3		xx	xx	xx	xx	xx	xx	xx		
Activity 4				xx	xx	xx	xx	xx	xx	
Activity 5						**Xx***	**xx**	**xx**	**xx**	**xx**

1.5 Structure

The structure of this dissertation was defined to enable an easier understanding of the problems at hand. Firstly, a bibliographic review of refractories is presented. In this section, the different types of refractories as well as their application and main properties are studied. The failure of these materials and the crack formation is also explored as well as the influence of their microstructure in the failure mechanisms. This brief overview of these materials is followed by the study of different methodologies used in literature to access thermal shock resistance in refractories. Three different approaches are explored as well as their advantages and limitations: analytical, mechanical and thermal approaches. The last section in the bibliographic review is dedicated to several techniques used during the project which required some background information and, therefore, a brief presentation of them was considered pertinent.

Secondly, the materials and methodology used during the work are presented. The project can be divided into two different branches: the mechanical and the thermal tests. Despite the materials study in both being the same, the methodologies used are different, and therefore these branches are presented independently. In both approaches the main focus is to study how damage and cracks develop.

The following section is the results and discussion. Since a high number of different tests and analysis were carried out for the different branches, it was considered that presenting both the results and the analysis simultaneously would enable a better understanding of the discussion. To validate the results, an analytical approach already developed by Lu and Fleck (1998)[1] is also considered. In both branches, the application of digital image correlation was also studied. In the last section of this chapter, a comparison of the different methodologies used (mechanical and thermal) is also presented.

Finally, the conclusions of the work developed are presented as well as some consideration for future work.

To avoid an unnecessary descriptive and dense dissertation, several methodologies carried out are presented with more detail in the Appendixes. In this section, images representative of crack development during the thermal cycles are also presented for all the samples sizes.

2 Bibliographic Review

2.1 Refractories

Refractories are materials capable of withstanding high temperatures. These materials are normally ceramics with high melting point that are able to maintain their properties at elevated temperatures. ASTM C71 defines them as non-metallic materials having chemical and physical properties that make them applicable for structures or components of systems that are exposed to environments above 538°C [2]. The main consumer of this type of materials is the iron and steel industry, which consumes about 65% of production [3]. Other industries such as the glass melting, cement and ceramic industries are also significant consumers of refractories, using 8 % of production [3]. Globally, the total refractory production is about 38.6 million tons. Graph 1 shows the percentual production of the primary refractory manufacturing countries [2].

The main application of these materials is for furnace linings, kilns, boilers, incinerators or applications where resistance to high temperature is necessary ([4], [3]).

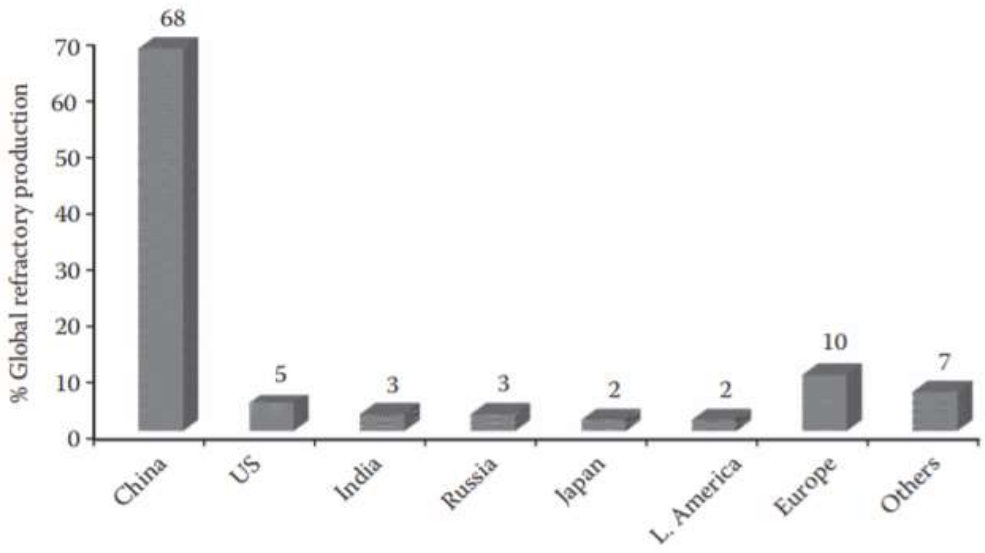

Graph 1 - Production (%) of the major refractory producing countries [2].

There are several ways to classify refractories. They can be divided by their chemical nature: basic, neutral or acid. They can also be distinguished by a physical classification, based on the shape of the products: shaped (bricks or cast shaped), unshaped (monolithic) and fibrous materials [5].

Acidic refractories are those that are resistant to any acidic conditions like slag, fume, and gases at high temperatures. But they are readily attacked by any basic slag or basic environments. Examples of acid refractories are Silica or Zirconia. On the contrary, basic refractories are attacked by acidic components but stable against alkaline slags, dust, fumes, and environments, for example refractories such as Magnesia or Doloma (calcined dolomite). Neutral refractories

are chemically stable to both acidic and alkaline environments. However, some of these materials behave with some chemical affinity at high temperatures and therefore their use for high aggressive environments at high temperature is rare. Examples of these refractories are Carbon or Graphite and Alumina [2].

In Table 2 the most common refractories are represented as well as their main advantages/limitations and applications.

Table 2 – General features and application of several refractories. Adapted from [4].

Families		General Features	Application
SiO_2	Silica	• High strength at high temperatures • Residual expansion • Low specific gravity • **High expansion coefficient at low temperatures** • Low expansion coefficient at high temperatures	• Coke ovens • Electric arc furnace roof
	Fused Silica	• Low thermal expansion coefficient • Hight thermal shock resistance • Low thermal conductivity • Low specific gravity • Low specific heat	• Coke oven door • Ladle shroud
Al_2O_3	Alumina	• High refractoriness • High mechanical strength • High slag resistance • High specific gravity	• Hot stove • Stopper head
	High Alumina		• Aluminium melting furnace • Incinerator
MgO	Magnesia	• High refractoriness • Relatively low strength at high temperatures • High basic slag resistance • Low thermal shock resistance • Low durability at high humidity - Hygroscopic	• Hot-metal mixer • Electric arc furnace wall
ZrO_2	Zircon	• High thermal shock resistance • High slag resistance • High specific gravity	• Ladle • Nozzle
	Zirconia	• High melting point • Low wettability against molten metal • Low thermal conductivity • High specific gravity	• Nozzle for continuous casting • Crucible
	Alumina zirconia silica	• High slag resistance • High corrosion resistance against molten glass	• Incinerator • Ladle
C	Carbon	• High refractoriness • High slag resistance • Low oxidation resistance	• Blast furnace hearth • Electric arc furnace
SiC	Silicon carbide	• High refractoriness • High strength at high temperature • Hight thermal conductivity • High thermal shock resistance • Reduced oxidation resistance at high temperature	• Blast furnace • Incinerator

Refractories in industrial installations are usually subjected to thermo-mechanical cyclic loads, which are the major cause leading to their premature failure. This happens due to temperature fluctuations during batch production cycles, for example, when molten metal is introduced into a relatively cold ladle or when an operating furnace is suddenly opened, exposing the refractory to cold air [6]. These loads are mainly strain-controlled since they result from the thermal expansion of the materials [7].

Refractory materials will work in high temperature conditions and under thermomechanical loads. Therefore, they must be chemically and physically stable at high temperatures. Depending on the operating environment, they need to be resistant to thermal shock, to be chemically inert, and/or to have specific ranges of thermal conductivity and of the coefficient of thermal expansion [2].

In terms of physical properties, the porosity is one of the most important properties since it influences not only the mechanical properties and thermal properties but also the reaction between the refractory material and gas or liquids during service at high temperatures [4].This interaction is mostly affected by open pores. The closed pores are the ones that are not connected to the surface. The apparent porosity is the ratio of the volume of the open (surface) pores, into which a liquid can penetrate, to that of the total volume of the sample, expressed as a percentage [2]. The porosity of these materials can range from relatively dense (up to 10% porosity) bricks to low density (90% porosity) fibrous thermal insulation [8].

The chemical properties should also be taken into consideration since refractories are in contact with different chemical environments and with chemically active solids, liquids, or gases at high temperatures. Hence, for refractories, resistance to these chemicals is necessary to ensure structural integrity, performance, and life of refractory and furnace structure. The corrosion behaviour depends not only on the chemical affinity but also on the porosity, impurities (amount and types) and strength [2]. The evaluation of the chemical composition of a refractory is important to understand and predict how will the combination of phases given by the equilibrium diagram vary with temperature [4].

Thermo-mechanical properties are also of extreme importance since the refractory will be subjected to mechanical loadings with varying degrees of intensity. The behaviour of a material is greatly dependent on the temperature. The main important thermal properties are the thermal expansion, the thermal conductivity and heat capacity [2]. In service, refractories face compression, bending, shear, and sometimes partial tension and twisting. Moreover, all these different loadings are generally active simultaneously. The principal mechanical properties used to describe the mechanical behaviour of refractories are the cold crushing strength and the modulus of rupture (MOR). To characterize the fracture behaviour, the wedge splitting test can be used [2].

Since the service temperature of refractory materials is high, it is important to evaluate the mechanical properties at the same range of temperatures of the service conditions. Refractories must have enough strength to withstand the load of the furnace and the mechanical action of the charge and process materials at the processing conditions [2].

Refractories are made from natural materials so, the presence of impurities, even in a small amount, is very common. A minor quantity of impurities is enough to form a low melting phase in the refractory which can cause the degradation of strength at elevated temperatures. Since refractories are subjected to high temperatures and loads during long periods of time, they are also susceptible to creep. Under heat and load, the material tends to deform through a viscous flow, which is not elastic. The presence of liquid phase in the material at high temperatures under load cause grain sliding and deformation. A refractory material has better creep resistance if the liquid phase at high temperatures has a higher viscosity [2].

There are two common techniques for measuring strength at high temperatures: the hot modulus of rupture (which is measured in three-point bending test inside a furnace at a desired temperature) and compressive creep which measures the deformation against time under a specific load and temperature conditions.

2.2 Microstructure and Failure

The microstructure of refractory materials can be explained by their manufacturing process. Shaped (brick) manufacture is most often done from powder mixtures which commonly combine grains of several mineral types, graphite flakes and polymer resins to form the final product. These powders have a broad particle size distribution (PSD) which enables small (sub-μm) particles to pack in the gaps between large (up to several mm) particles so that most of the densification occurs during the shape forming operation. This is unlike most engineering ceramics where most densification occurs in the sintering step. Unfired, powder processed, refractories are often 85% dense. Processing from large PSD powders leads to a complicated microstructure composed of large, discrete aggregate (filler) refractory grain particles held together by a continuous bonding matrix often containing extensive porosity, grain and bond microstructure, which can be seen in Figure 1- (a). This microstructure is similar to that of civil engineering concrete. Refractory blocks can also be made from molten liquids produced in electric arc furnaces (EAF) that are poured into graphite moulds and cooled slowly over several days. This process is normally called fused cast. The microstructure obtained with this type of process is much like a cast metal, Figure 1– (b). In this process, crystallization from the melt, and subsequent grain growth, leads to interlocked grains that may be up to several mm long, which results in low levels of porosity and little glassy phase. Because of this, fused blocks are interesting for applications where extreme chemical resistance is required, since liquid ingress is limited by such a microstructure [8].

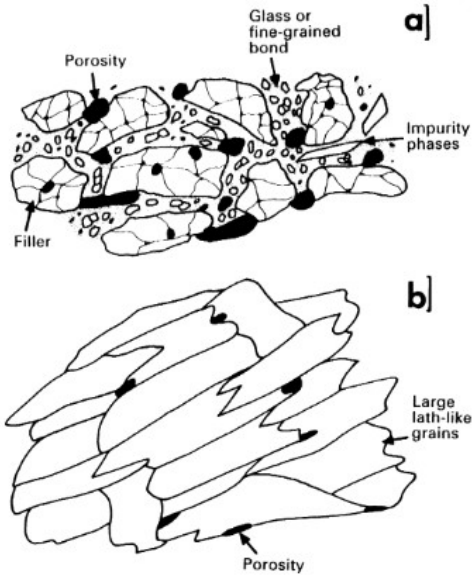

Figure 1 - Schematic microstructures of refractories made from (a) large aggregate and finer matrix powders and (b) cast, electrofused ceramic [3].

The microstructure of a typical refractory obtained from powder processing consists of grain and bond phases. The grain materials can be made by fusion (alumina, mullite, MgO) and sintering (MgO, Mg aluminate spinel). Fusion is an expensive process due to the high temperature. However, it might promotes the volatilization of impurities which improves the purity of the grains. On the other hand, although sintering is a cheaper process and often achieves lower density grains, these grains have impurities in their boundaries which reduce

the high temperature properties. Fused and sintered grains can easily be distinguishable since fused grains contain a lower proportion of second phase at grain boundaries (Figure 2). Grains can also be obtained from raw materials such as quartz, dolomite, graphite, bauxite, materials that have normally simple pre-processing [8].

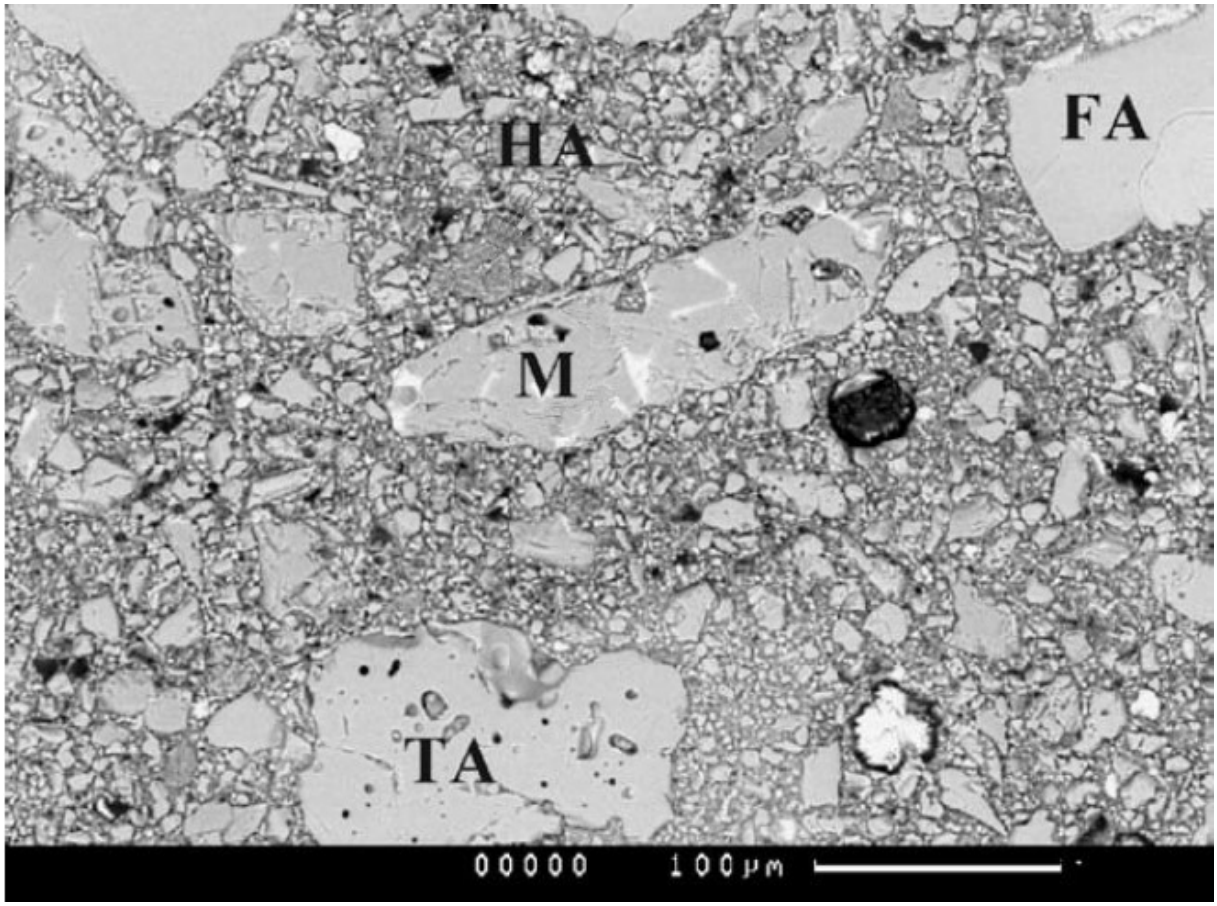

Figure 2 - SEM image of a low cement castable containing a range of aggregate phases including tubular Alumina (TA), white fused alumina (FA, lack of second phases) and sintered magnesia (M, with light contrast calcium and magnesium silicate second phases). HA is a hydratable alumina in the matrix. Adapted from [8].

The resistance of refractories to initiation of fracture and crack propagation is regulated by different mechanisms and can be explained by the analysis of refractories with different microstructures [9].

In refractories, material flaws are one of the principal sources of fracture. These flaws can be introduced during the manufacturing process, exposure to aggressive environments or surface preparation. The critical flaws act as stress concentrators and initiate crack propagation, which will lead instantaneously to failure, unless crack arrest mechanisms are developed. These mechanisms are found in some quasi-brittle materials where flaws initiate crack-induced damage [10].

Refractory materials are quasi-brittle material and, therefore, exhibit a non-linear portion of the load-displacement curve (Graph 2). This non-linearity can be explained by the inelastic phenomena occurring near the crack. Two different regions where this phenomena occurs can be defined: the following wake region and the frontal process zone, both regions are illustrated in Figure 3. [5]. In the frontal process zone, microcracking and multiple crack branching are usually observed. In the wake process zone, grain bridging and friction of the crack faces consume energy [9].

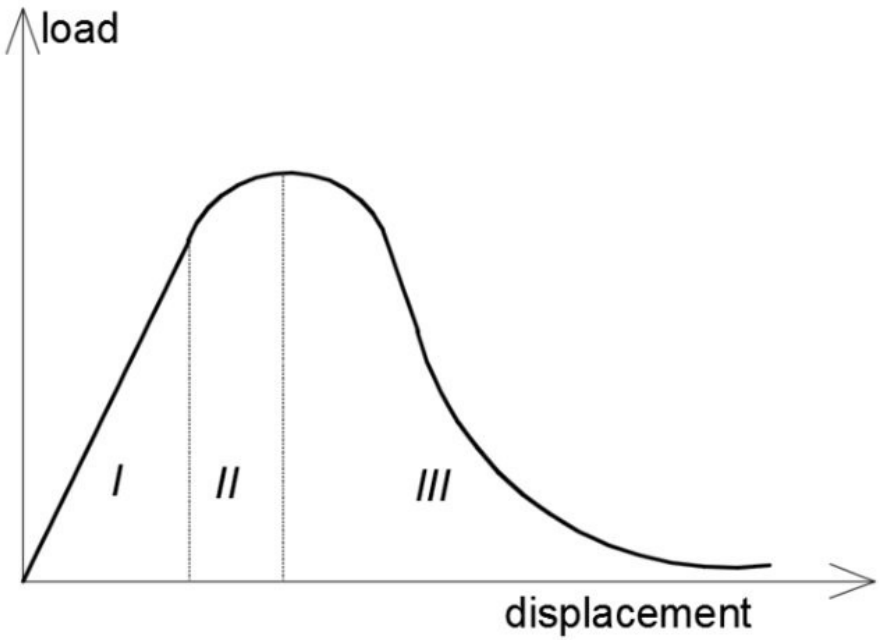

Graph 2 – Typical load displacement curve of quasi-brittle materials in the wedge splitting test; Region I is linear, region II is non-linear and region III is post peak softening [11].

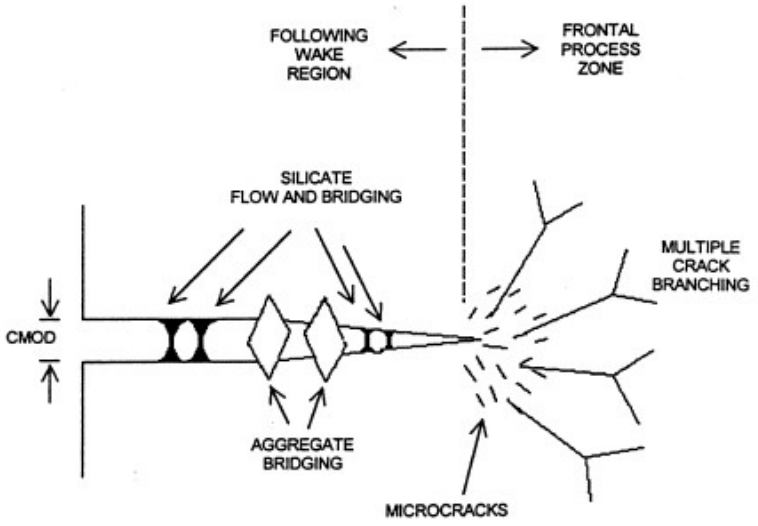

Figure 3 – Schematic of the crack process zone for refractory materials. CMOD – Crack mouth opening displacement [5].

Microcracking is typical in this type of microstructures due to the thermal expansion mismatch of the different phases, and due to the lower sintering time of the fine particles, which causes shrinkage and opens cracks between the large particles that take longer to sinter. These microcracks, if smaller than the critical flaw size, can increase the resistance to crack propagation and to thermal shock [3].

The microcrack growth and development is intrinsically connected with the characteristics of the aggregates. Microstructures with low porosity and well sintered aggregates have a higher toughness in comparison with aggregates where a high level of porosity is found. Porosity acts as stress intensity sinks during fracture, which leads to an increased fracture energy and therefore a lower fracture toughness [9].

On the other hand, the presence of microstructural features capable of crack arrest and deflection is needed for high resistance to crack propagation. Materials with homogenous composition throughout the microstructure and well bonded constituents tend to present lower toughness. When aggregates are tougher than the matrix, a more tortuous crack propagation

tends to develop (crack surrounds the aggregates) in comparison with well bonded aggregates of homogenous composition, where the crack path tends to be straight and transverse to the grains and, therefore, less resistance to crack propagation is observed in the latter [9, 12].

2.3 Analysis of Thermo-Mechanical Failure

The several alternative approaches to study the thermo-mechanical response of refractory materials found in literature can be divided in three main groups: analytical, thermal cycle tests and mechanical cycle tests. In each subsection, each group of methodologies will be addressed along with their respective limitations.

2.3.1 Analytical

The ability of a refractory to resist failure according to its thermo-mechanical response can be evaluated by analytical tools, based on material properties obtained in monotonic loading tests.

A simple fracture criterion is considering that fracture will occur when nominal stress reaches a critical value, the strength of the material;

$$\sigma=\sigma_u \tag{2.1}$$

where:

σu, is the tensile strength
σ, is the nominal strength

The stress criterion provides good results for crack-free bodies. However, for bodies containing a crack, it provides a null failure load due to considering a singular stress field in front of the crack tip [13].

On the other hand, Griffith (1921) studied the failure in brittle materials and correlated the low fracture strength observed in these materials with microscopic flaws [14]. From this concept, fracture mechanics was developed. A common used criteria is an energy-based criterion, which states that failure will happen if the crack driving force G equals the crack resistance Gf, where Gf represents the energy necessary to create the unit fracture surface (fracture energy) [10, 13]. This criterion is called the maximum energy release rate criterion.

It can be expressed equivalently in terms of stress-intensity factor K_I and fracture toughness K_{IC} (Irwin's relationship) [13]:

$$K_I = K_{IC}(x) \tag{2.2}$$

where:

K_I, is Stress intensity factor
K_{IC}, is Fracture toughness

The maximum energy release rate criterion is physically sound for bodies containing a sufficiently large crack. However, it provides an infinite failure load for a crack-free body because, in the absence of cracks, the stress-intensity factor is zero [13].

Both criteria above only work for the extreme cases. In order to overcome this drawback, several failure criteria have been proposed in the literature. These can be divided into 3 distinct groups: Stress-based, strain-based and energy-based criteria. In Table 3, a list of these different criteria is presented. Among these, the Maximum tangential stress criterion (MTS), the strain energy density criterion (SED) and the maximum energy release rate criterion (G) are classical fracture criteria and have been widely used to study brittle failure [15].

Table 3 – List of three criteria categories: stress-based criteria, strain-based criteria and energy-based criteria [15].

	Criteria
Stress-based	Maximum tangential stress criterion, MTS Generalized maximum tangential stress criterion, GMTS Modified maximum tangential stress criterion, MMTS
Strain-based	Maximum tangential strain criterion, MTSN Extended maximum tangential strain criterion, EMTSN
Energy-based	Strain energy density criterion, SED Generalized strain energy density criterion, GSED Averaged strain energy density criterion, ASED Generalized averaged strain energy density criterion, GASED Maximum energy release rate criterion, G

Each group is based in a different concept to describe the fracture mechanism and has intrinsic advantages and disadvantages. The stress-based fracture criteria are usually described with a simpler set of equations than the energy-based criteria, and the role of each stress field parameter is clearly represented in estimating the onset of fracture. On the other hand, the energy-based criteria are based on the concept of energy dissipation due to the crack extension which are based on more realistic platforms [16].

Heping Xie *et al.* (2009) pointed out the limitation of a strength criteria based on classical elasto-plastic theory to analyse the behaviour of rocks (quasi-brittle materials). These limitations are mainly due to the inhomogeneous microstructure of the rocks. The application of external forces changes the stress and strain distribution within the material, while at the same time some of the dissipated energy may produce damage. Locally, high stress and strain can cause strength deteriorations but not structural failures. The deformation and failure are irreversible processes involving energy dissipation. It is only when strain energy is released completely that failure is achieved [17].

Strength-based criteria as well as criteria based on linear elastic fracture mechanics are not representative of the behaviour of quasi-brittle materials since fracture process zone has an intermediate size (it does not cover all of the sample or is negligible) and shielding mechanisms are developed (micro cracking, bridging) [18].

The strain-based criteria are less common. However, for some geometries and materials, the fracture propagation can be predicted in a more accurate way with these methods than by applying any of the other criteria. Wu *et al.* [16] pointed out the adequacy of this criteria for predicting the fracture behaviour of concrete. A scalar-valued function of strain tensor was found to determine the onset of fracture.

Several researchers have applied these criteria and extensions thereof in a wide range of geometries materials and conditions (e.g. fatigue, notch analysis or mixed modes fracture) [13].

The extent of damage during fracture in refractory materials when subjected to thermal stresses can also be approached by an energy criterion. Hasselmen (1996) [19] considered two types of crack propagation: although usually a quasi-static crack extension is observed, a kinetic crack growth is also possible. Similar equations address both situations. In eq 2.3 and 2.4 the kinetic thermal shock damage resistance (R'''') and the quasi static thermal shock resistance (R_{st}) are shown [5, 20].

$$R'''' = E\gamma_{wof}/\sigma_u^2 \tag{2.3}$$

$$R_{st} = \left(\gamma_{wof}/E\alpha^2\right)^{1/2} \tag{2.4}$$

where:

E, is the Young's modulus;
γ_{wof}, is the work-of-fracture (measured originally by Nakayama and subsequently by Tattersall and Tappin [21]);
α , is the coefficient of thermal expansion;
$\sigma_{u,}$, is the tensile strength.

Considering that the thermoelastic stress can be expressed in simple form for total linear restraint in one dimension, eq 2.5:

$$\sigma = \alpha E \cdot f(T) \tag{2.5}$$

where:

$f(T)$, is a function of temperature;

which, when squared on both sides indicates that:

$$\sigma^2 \sim \alpha^2 E^2 \tag{2.6}$$

Combining eq 2.4 with eq 2.6, it is possible to assess the inverse proportionality of R'''' and R_{st} with the stress squared divided by the Young modulus (σ^2/E). This coefficient represents the stored elastic strain energy in an object at the stress level σ, which is the driving force for fracture or crack extension. Therefore, it is possible to conclude that the thermal stress damage resistance decreases as the strength increases and it does so as the square of the strength, which makes high-strength refractories much more susceptible to thermal shock damage [5]. However, this analysis neglects the thermal conductivity, which is a central parameter to thermal shock resistance [1].

Lu and Fleck (1998) developed an analytical algorithm to allow the comparison of the materials performance to cyclic thermal shock over the full range of Biot numbers:

$$\mathrm{Bi} \equiv \mathrm{Lc} \cdot \mathrm{h}/\mathrm{k} \tag{2.7}$$

where:

Bi, is Biot number
Lc, is characteristic length
h, is coefficient of heat transfer
k, is thermal conductivity

As can be seen from eq 2.7, the Biot number is not only dependent on the properties of the material but also on the geometry of the sample. The maximum stress in the centre and surface of a plate subjected to thermal shock is plotted against the inverse of the Biot number in Graph 3. For higher Biot numbers (higher heat exchange) higher stress is generated in thermal shock. Therefore, in order to successfully predict the fracture behaviour of a component subjected to thermal shock, the material properties, geometry and the thermal field characteristics must be coupled. The faster the heat can diffuse out of the system (smaller thickness, higher thermal conductivity), the lower the gradient temperature will be and therefore lower stress will be generated.

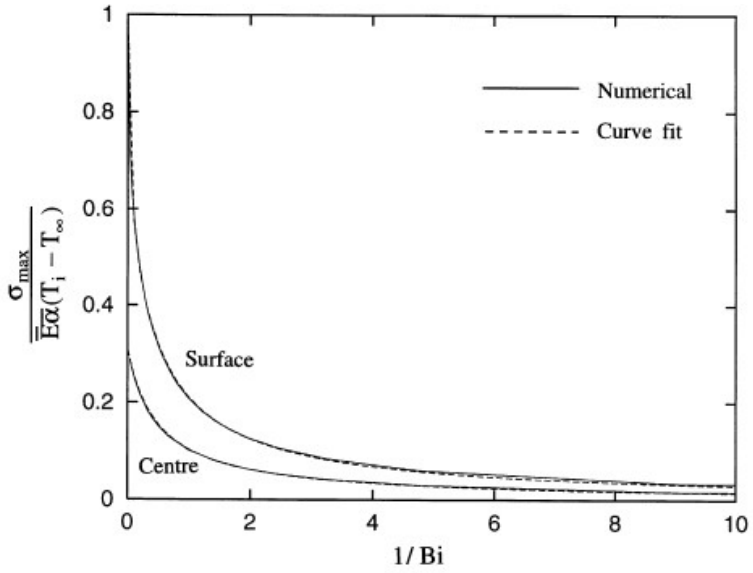

Graph 3 – Maximum surface stress (cold shock) and maximum centre stress (hot shock) as a function of 1/Biot [1].

However, the experimental failure data obtained for brittle materials is generally not reproducible and can fluctuate by an order of magnitude. This can be attributed to the random number and distribution of flaws present in brittle materials. The severity, location and dimension of the flaws is an unknown factor which disables an accurate prediction of the behaviour of a brittle material with these methods. The probability of the presence of a flaw that initiates the crack must be introduced in the analysis.

Because of this, several statistical approaches have been developed, based on functions that describe the distribution of fracture strengths. Two different types of probabilistic-statistical approaches can be distinguished: the phenomenological/macroscopic type (e.g. the Weibull model) and the fundamental type, which considers flaws as physical entities and is based on flaw strength density functions [10].

2.3.2 Thermal Cycle

Another way to study the resistance of refractories due to thermo-mechanical cyclic loads is by the simulation of thermal shock service conditions and by quantifying the damage. The material is more thermal-shock resistant during thermal cycles when no cracks are developed, and a lower loss of Young's modulus and higher residual strength occurs [22].

The damage can be assessed by measuring the longitudinal velocity of sound between the cycles. Damage causes an increase in transit time (due to micro-cracks) and thus a decrease in the velocity of sound and dynamic Young's modulus. The latter can be calculated from eq 2.8 [23] :

$$E = \rho \left[\frac{(1+\nu)(1-2.\nu)}{1-\nu}\right] \mathrm{v}^2 \qquad (2.8)$$

where:

E, is the Young's modulus
ρ, is the specific density
v, is the velocity of sound
ν, is the Poisson's ratio

Therefore, the relative change of the Young's modulus during the experiment can be used to calculate the damage, considering that the sample density and Poisson's ratio are not affected by the damage – eq 2.9 [23]:

$$Damage\ (\%) = \frac{E_d - E_0}{E_0} * 100 \quad (2.9)$$

where:

E_0, is the Young's modulus before the experiment
E_d, is the Young's modulus after the experiment

This type of tests are normally done at a fixed ΔT with N > 1 (number of cycles) [24]. The extent of the thermo-mechanical induced damage can be quantified by its effect on a physical property, for example the Young's modulus. The accumulation of damage can be a function of the increasing N [24]. Generally, since the resulting damage (elastic modulus) is a function of the number and lengths of the cracks, the decrease in the elastic modulus after a thermal shock is directly related with the nucleation and propagation of the cracks in the material [25]. However, damage may saturate (become independent of N), a behaviour that was found for several ceramic materials and is represented in Figure 4. This phenomenon is not always observed but it is associated with the microstructure (porosity, grain size, second phases or initial damage). This phenomenon develops when short crack behaviour is developed (crack whose length is comparable to the grain size of the specimen). The transition into a long crack is inhibited by the dispersed pore phase. When this happens a break-away from the damage saturation behaviour is observed and failure will develop [24, 25]. In some refractory materials this saturation behaviour can be observed either for low levels of thermal shock or severe thermal shock [26].

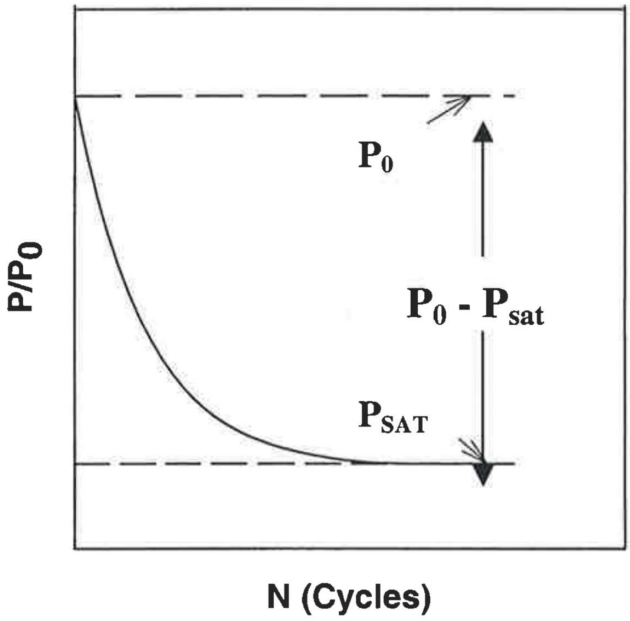

Figure 4 – Thermal fatigue damage curve for a general property P, where P decreases with increasing thermal fatigue damage. P_0 is the property before the cycles and Psat the property after N number of cycles when saturation occurs [24].

Nicolas Rendtorf (2014) observed the degradation of the Young's modulus in the first 3 to 6 cycles, followed by the saturation of damage which occurs when the energy provided by the thermal shock is not high enough to propagate the existing cracks. Before reaching saturation, despite an increase in damage is observed, the variation between two consecutive cycles is decreasing until saturation is reached [25, 27].

The advantages of the thermal shock test are that all the properties of the material relevant for the thermal shock resistance are considered. On the other hand, this test is similar to the service

conditions. The main differences are the dimensions and the thermal and mechanical boundary conditions, which difficult the interpretation of the test results, not allowing a direct translation of the number of cycles to failure. This translation may be possible by measuring the strain development throughout the cycles. Another question regards the saturation of damage, which can either happen permanently or as a secondary phase of degradation (which is reportedly seen in mechanical tests) [22].

2.3.3 Mechanical Cycle

Another methodologies to evaluate the resistance of refractories to thermo-mechanical cyclic loads is to study the behaviour of refractories to mechanical cyclic loadings [7]. A correlation between the mechanical cyclic fatigue and the thermal shock test has been pointed out for several refractory materials [7, 27-29].

The similarity of these approaches (fatigue induced by mechanical loading and fatigue induced by thermal loading), can be explained by the thermal expansion that occurs in thermal loading. The thermal expansion introduces strains which cause fatigue after several cycles, the same way as an entirely mechanical load would cause. However, there are several differences that should be considered, such as: the rate at which mechanical and thermal-stress are conducted (generally very different), the effect of the temperature variations on mechanical behaviour of the material and the combination of this effect with the strain variation (which may not occur on mechanical cycles, which are generally done at a fixed temperature) [28].

Because of all these factors, it can be challenging to predict life in thermal fatigue from life in mechanical fatigue. The life found for the thermal-stress fatigue tests tends to be considerably inferior to the life of the mechanical cyclic tests [28].

The advantage of using mechanical cycle tests is the decoupling of fatigue failure from other material properties such as conductivity. The consideration of temperature distribution and gradient are not relevant, rendering this method as attractive for analytical algorithms and computational models to predict failure [7]. It allows a direct correlation of loads and the material response in the stress-strain response curve, enabling the quantification of the degradation due to repetitive cycles [17].

The fatigue degradation can be evaluated from the stress-strain parameters, such as irreversible strains. In some cases, cyclic stress-strain measurements performed at discrete temperatures can be representative of the failure due to temperature fluctuations [22, 28, 29].

Several methods of cyclic fatigue tests can be used: either a force controlled, or displacement-controlled method. The method chosen should be the one that represents the service solicitations.

Force controlled methods are simpler to implement and allow a comparative analysis of the refractories. However, these are not representative of the service conditions which result mostly from strain loads [7].

Different displacement control methods have been used by K. Andreev et al. (2016) such as Method II (constant displacement) and Method III (constant displacement amplitude). The difference between these resides in the fact that in Method II the loading piston is allowed to decouple from the samples in contrast with Method III where the piston does not decouple from the sample and therefore the unloading stops when the zero force is reached. A scheme of the cyclic test with both methods is represented in Figure 5 [7, 30].

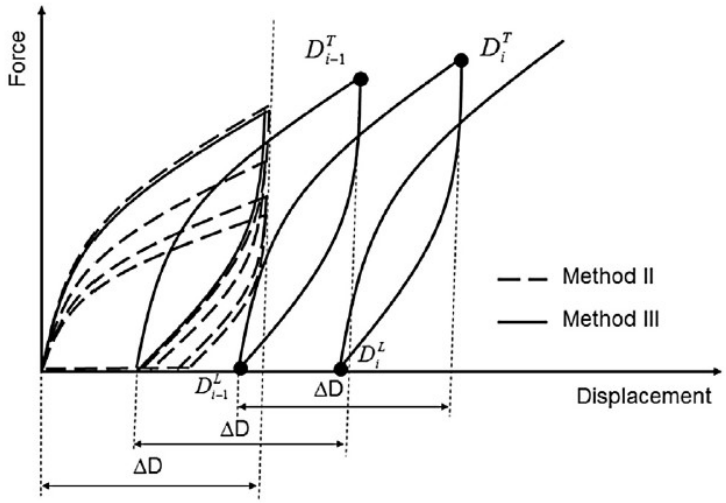

Figure 5 – Schematic representation of cyclic tests for both Method II and Method III [7].

Compressive test of Method II is the most representative of service conditions where thermal expansion is constrained. This can happen when material compaction occurs and the joints between the refractory bricks open up during unloading parts of the cycle [7].
Method III performed in bending is the most representative of service conditions where lining parts are unconstrained, which are considered to be the most dominant comportment in furnaces of silica refractories [7].

The methodologies chosen will have an impact on the damage development. In tests with fixed maximal strain (Method II) the development of irreversible strains results in the reduction of the effective loading amplitude which promotes the development of damage saturation. In tests with constant effective strain amplitude (Method III) the maximal strain grows with the damage development. Saturation is less probable and appears mainly when amplitude is small [22, 31],

The temperature is an influential factor on the failure process in cyclic fatigue. K. Andreev et al. (2017) reported a more brittle failure in cyclic fatigue tests at high temperatures for silica bricks, where post peak softening was not developed. This can be explained by the thermal expansion which promotes less damage location available for crack initiation and propagation and therefore a less tortuous crack is expected [7].

Commonly, the fatigue cyclic tests are done either in compression or bending. Bending allows a simpler analysis of the tensile failure in comparison with the compression where the shear and tensile stress are more complicated. Failure in bending test occur by the formation of a single crack which allows a more accurate estimation of the fracture mechanism parameters. However, the size of the standard bending samples is smaller in comparison with the size of the fracture process zone measured in refractories.

The fatigue degradation is controlled by the formation of damage and its subcritical loads [7]. This degradation occurs due to the gradual growth and merging of micro-cracks. These micro-cracks exist at pre-existing cavities in the matrix. In compression these micro-cracks can also appear in a larger grain. Resistance to crack propagation is expected to increase for cracks with tortuous paths. These paths can form either by two pre-cracks located on different parallel planes that grow together or by large grains without pre-cracks that deviate the crack trajectory from a straight line (most important mechanism in bending). Displaced debris are formed during the process disabling the closure of the cracks upon unloading. Locations with large amount of debris are expected to allow the formation of the major crack. De-bounding and rotation of large-grains was also identified as a critical mechanism of failure for fatigue crack growth in

refectories. This mechanism can develop when cohesion of the large grains and the matrix is not high [7].

Three different periods of damage accumulation can be usually found in refractory materials. Firstly, the rates of strain accumulation decrease. In this phase the formation and growth of micro-crack occurs due to encountering barriers, and the rate of micro-crack growth reduces. Secondly the rates of strain accumulation are constant. In this phase, the barriers are overcome by the reduction of friction and bringing effects in the crack wave. Finally, in the third phase the irreversible strain increases. It is in this phase that a major crack is formed, which causes the sample fail. Having a well-developed third phase should mean considerable resistance to major crack forming and propagation. The three different phases are schematized in Figure 6 [22, 31].

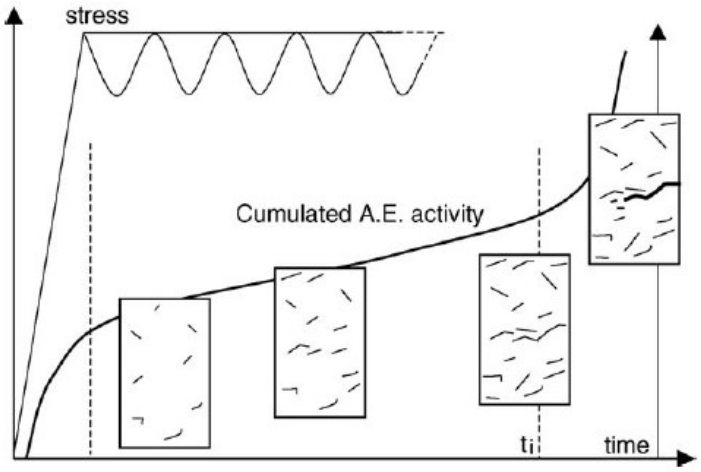

Figure 6 – Schematic drawing showing the cumulative acoustic emission signals (A.E) and the load, function of time. Representation of three different periods of damage accumulation for refractory materials in cyclic loading [31].

In cyclic tests a less brittle failure is observed, which can be resultant from a more distributed failure process (where more tortuous cracks occur) and from the more gradual nature of the cyclic test (energy is consumed by the crack propagation). When a larger crack is formed, the material is unloaded outside of the crack zone. If the load is not capable of overcoming the material resistance, the defects in a larger volume of material are loaded and grow. These defects increase the possibility of the crack to deviate from a straight line. Therefore, an increase in the number of cycles to failure is expected when a high concentration of critical defects is developed before the resistance to the crack propagation is overcome [7].

2.4 Wedge Splitting Test (WST)

The wedge splitting test is particularly interesting to study fracture since fully stable fractures are developed, which allows a reliable record of the total energy for crack propagation throughout the sample [5]. This test favours a stable crack propagation because of a relatively low ratio of specimen volume to fracture surface area and a reduction of the testing force by action of a wedge, thus decreasing the energy elastically stored in the testing machine [20].

The scheme of this test is represented in Figure 7. As it can be seen, cubically shaped samples are equipped with a groove. The groove hosts a load transmission equipment which transforms the c into a horizontal force (F_H).

The specimen size was studied by Harmuth et al. (1995) and an ideal size which enables stable crack propagation for a high range of brittle materials was determined, as it is represented in Figure 8 [32].

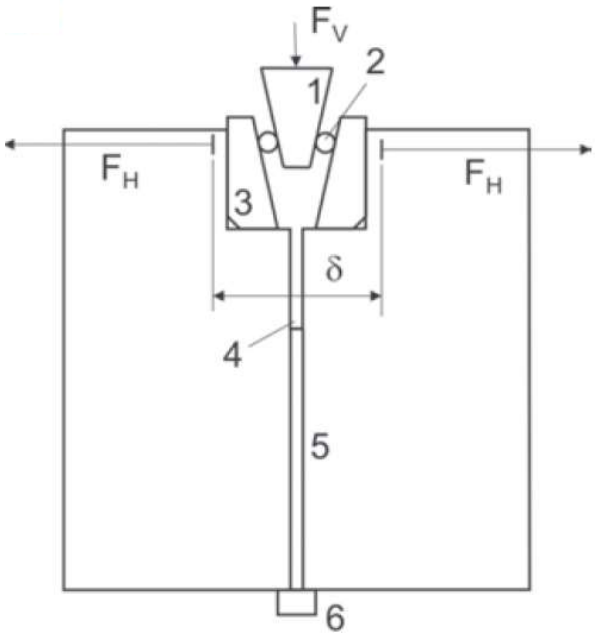

Figure 7 – Schematic representation of the wedge splitting test. F_V – vertical load, F_H – horizontal load, δ - displacement, 1 – wedge, 2 – rolls, 3 – load transmission pieces, 4 – starter notch, 5 – side groove, 6 – linear support [20].

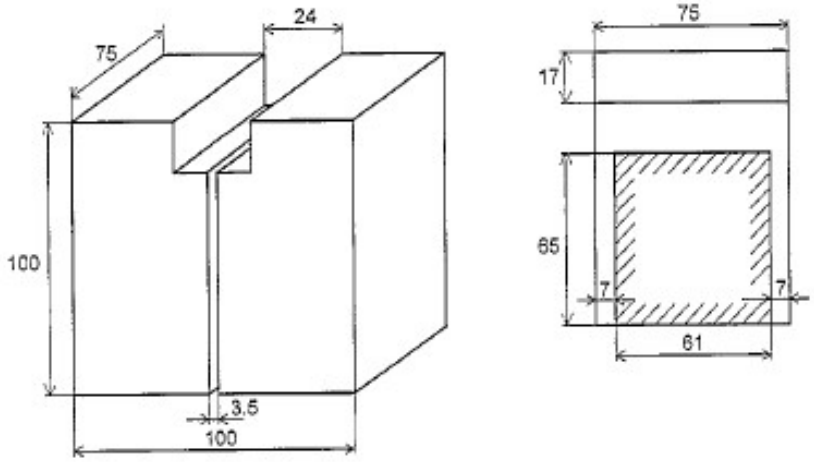

Figure 8 –Geometry of the specimen for WST to enable stable crack propagation (dimensions in mm) [32].

During the test, the applied load F_V, and the crack opening displacement (δ) are measured. The splitting force, which is the horizontal component of the force F_H acting on the rollers is calculated taking the wedge angle φ into consideration, eq 2.10 [33]:

$$F_H = F_V/(2 * \text{tg}\ \varphi) \quad (2.10)$$

The δ is measured by means of transducers or a clip gauge, which should be fixed at the level where the splitting force acts on the specimen [33].

By measuring the displacement of the loading point, a loading displacement diagram can be obtained. The specific fracture energy can be determined by equation 2.11 [20]:

$$G_F = \frac{1}{Ap} \int_0^{\delta_{ult}} F_{Hmax}\, d\delta \quad (2.11)$$

where:

δ,is the load point displacement
$\delta_{ult,}$ is the ultimate displacement
A_P, is the area of the projection of the fracture surface
$F_{Hmax,}$ is the maximum load

Figure 9 illustrates typical load-displacement curves for wedge-splitting refractory specimens. It is possible to see the development of a non-linear region in the curve which is characteristic of the quasi-brittle nature of these materials.

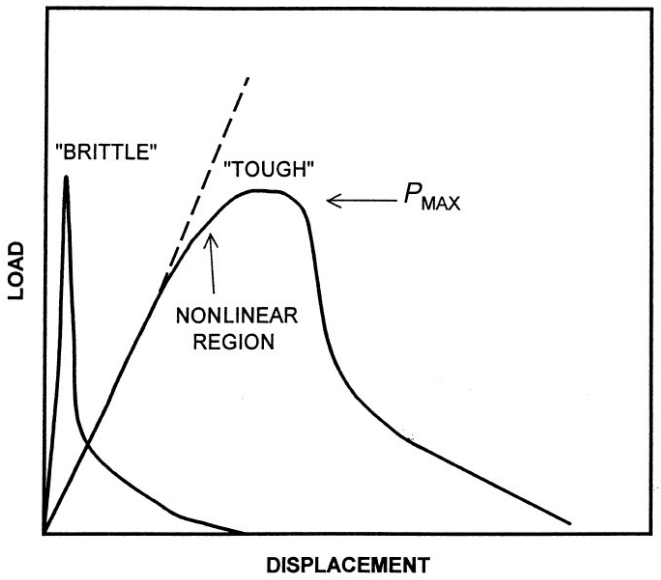

Figure 9 – Schematic load-displacement curves for refractories in the wedge splitting test [5].

2.5 Digital Image Correlation

Digital Image correlation (DIC) is a non-contact full field measurement method that was introduced in the 1980s. This method is based on assessing the displacement fields over a surface of a deforming material by comparing two different images acquired at different stages of deformation. The first image is the “reference frame” where desired measured area is manually defined and divided into small subsets (quadrilaterals). Then, the method defines a grid of analysis points over the reference frame. For each node of this grid a group of pixels called “subset” is defined. By identifying the most similar subsets in the deformed frame based on a statistical measure of correlation, it is possible to find the location of each point in the deformed frames, and therefore the local strain tensor can be determined from the spatial distribution of the displacement field for each frame [34].

However, for DIC to work effectively, the pixel blocks need to be random and unique. In many cases the natural surface of material has enough image texture for DIC to work, when the natural texture is not enough, a surface preparation is needed (which consists of creating an artificial texture) [35].

The Images used for DIC can be obtained from a wide variety of sources including conventional CCD or consumer digital cameras, high-speed video, macroscopes, and microscopes, including scanning electron and atomic force microscopes. Even with commercial digital cameras it is possible to measure surface deformation down to one part per million of the field of view [35].

DIC is now widely used in different scientific fields. Examples of its applications are the study of a diverse range of material specimens including examining the evolution and uniformity of strain in materials testing, crack tip and crack propagation studies, detecting damage

development in composites, structural deflections, high temperature strain mapping and dynamic vibrational analysis [35] .

In Figure 10, it is possible to see a concrete sample after being subjected to a load test, where is only possible to distinguish visually one big crack. By using DIC and taking a photo before and after the test, it is possible to see the full extent of crack opening. This allows crack identification in a low cost and a contactless way, Figure 11 [35].

Figure 10 – Concrete step after being subjected to load test, showing one large crack but no other visible cracks [35].

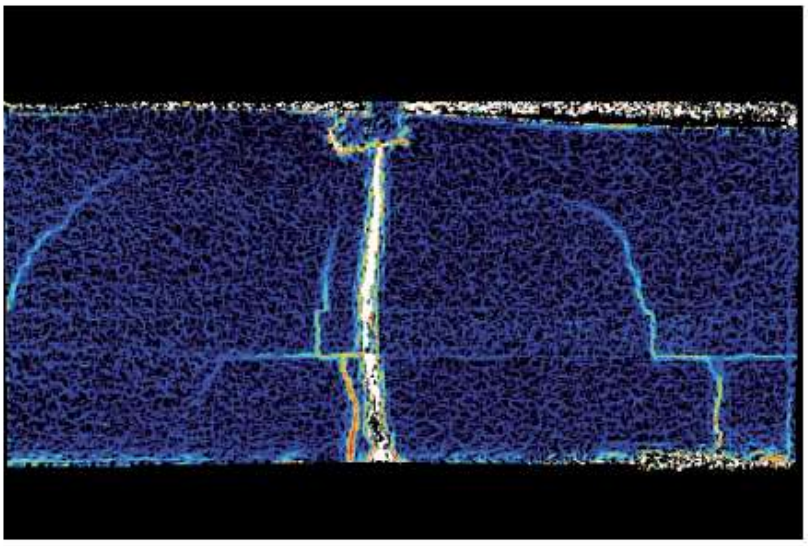

Figure 11 – Output from DIC as a map of local deformation showing cracks not visible to the human eye [35].

2.6 Fractal Analysis

Fractals are geometries which describe naturally occurring geometric features (such as clouds, mountains, coastlines) they can be described by scale invariant parameter called as Fractal Dimension which attempt to quantify a subjective feeling on how dense the fractal occupies the metric space in which it lies. There are two types of fractal dimension: The Hausdorff Fractal dimension and Hurst dimension. The Hurst constant is a characteristic parameter of long-term memory dependence or persistence in time series or spatial data [36]. It ranges from 0 to 1, where a value of 0.5 signifies no long-term memory, lower than 0.5 means anti-persistence, i.e.,

a more fluctuating profile, and higher than 0.5 means that the process is correlated. The Hausdorff constant D, quantifies the roughness or smoothness of spatial data. Higher value of D means higher roughness and waviness. The Hausdorff and Hurst constants are independent of each other since fractal dimension is a local property, and long-memory dependence is a global characteristic. Nevertheless, the two notions are closely linked in self-affine processes (local properties are reflected in the global ones).

The profile of a fracture surface z(x) is assumed to be continuous even at the small scales. This assumption is not valid at atomic scales, but for engineering studies the continuum is assumed to exist down to the limit of a zero-length scale. It is seen that under increasing scale of magnification more and more details emerge. Therefore, a tangent at any point cannot be defined. Thus, the profile has the mathematical properties of being continuous but not differentiable anywhere [37].

Majumdar and Bhushan 1990 [38] showed that the power spectra of the surface fracture profiles follow a power law. Therefore, under appropriate magnification the magnified image of the surface looks very similar to the original surface. This property of an image appearing similar to the original image under different magnifications has been mathematically defined using the properties of self-similarity and self-affinity. These seemingly qualitative properties of the image have been quantified by the use of fractal geometries, which have also been shown to have the property self-similarity and self-affinity. The fractal dimension of a fractal is an essential property which can be used as a measure of surface roughness. For a curve the Hausdorff dimension can vary between 1 (for smooth curve) and 2 (rough curve)[39].

A typical fractal analysis is the Fourier power spectrum. The Fourier transform is a mathematical approach which divides a signal into its frequency components. It is possible to transform all practical signals, and thus also any surface profile. The Fourier power spectrum (square magnitude of the Fourier transform) method is used to estimate the roughness constants. A straight-line fit is performed to the (loglog) data. With the slope (β) obtained from the fit, it is possible to estimate the following constants, Hurst and Hausdorff – eq 2.12 and 2.13 [39, 40]:

$$H = (\beta - 1)/2 \tag{2.12}$$

$$D = n + 1 - H \tag{2.13}$$

where:

H, is the Hurst exponent
D, is the Hausdorff dimension
n, is the Euclidian dimension
β, is the slope obtained from the straight-line fit performed on the Fourier power spectrum

3 Materials and Methods

The material studied in the experimental work were commercially available silica bricks (KOK). Silica is one of the most commonly available oxide on the earth's crust, which can be found in nature commonly in the crystalline form and rarely in an amorphous state. The main raw material used to manufacture silica bricks is quartzite, which is composed of quartz. The amount of impurities such as Al_2O_3, Fe_2O_3, and TiO_2 of the raw material should be minimal because they greatly reduce the liquidus temperature and restrict high-temperature applications. Silica bricks contain about >93% SiO_2, with a minor amount of other oxides such as lime (CaO), alumina (Al_2O_3), and iron oxide (Fe_2O_3). Silica refractories have an acidic nature and can be divided in two groups: Super duty cycle (impurities < 0.5) and high-duty (impurities from 0.5–2 wt%)[4].

The manufacture of silica bricks involves crushing, grinding and sieving of quartzite raw material. Sintering aid is added (lime) and binder. The resulting homogenous mixture is shaped dried and fired. Shaping is done mainly by pressing [4].

Silica bricks are very sensitive to thermal shock up to 600°C / 700 °C because of the thermal expansion of the silica phases present and the phase changes which occur below this temperature. Quartz shows a transformation at 573°C, tridymite between 117°C and 163°C, and cristobalite between 220°C and 280°C [2]. Because of this, silica bricks, when subjected to thermal shock in this range of temperatures, are prone to cracking and disintegration. Above this temperature there is significant improvement in the thermal shock resistance [4]. In Graph 4 it is possible to see the thermal expansion values of different crystallographic forms of silica.

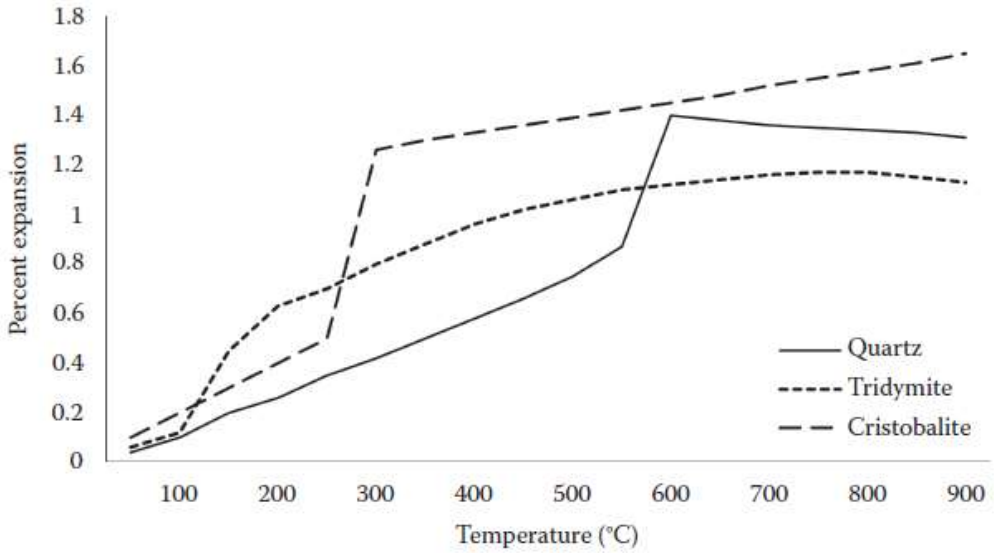

Graph 4 – Thermal expansion values of different crystallographic forms of silica [2].

Silica bricks are used in coke ovens of steel industry and in blast stoves serving blast furnaces and glass producing units. Their maximal service temperature is typically between 1100 °C and

1400 °C. The bricks studied in the present work were provided by a confidentiality protected brand, and are reported to have been produced by pressing, with calcium hydroxide acting as a binder and sintered at 1400–1500 °C. Although no further details of the material were given, the properties of these bricks were determined in Tata Steel IJmuiden as presented in Table 4.

Table 4 – Properties of silica bricks (KOK).

Temperature, °C	Conductivity, W/m/K	Heat Capacity, J/(kg·K)	Density, kg/m^3	Linear thermal expansion coefficient, K^{-1}	Dynamic Young Modulus, GPa	Strength (bending) MPa
20	1.5	800	1830	3.45E-05	10.0	9.5
200	1.6	1070	1830	3.45E-05	5.0	5.0

Different types of analysis were carried out. Cyclic thermal shock tests were used to study the damage development during cyclic thermal shock as well as crack formation and propagation. Mechanical tests (wedge splitting test) were performed and the fracture surface of the samples were analysed to allow the comparison of the different test methodologies. In Figure 12 a scheme of the experimental procedure undertaken is presented.

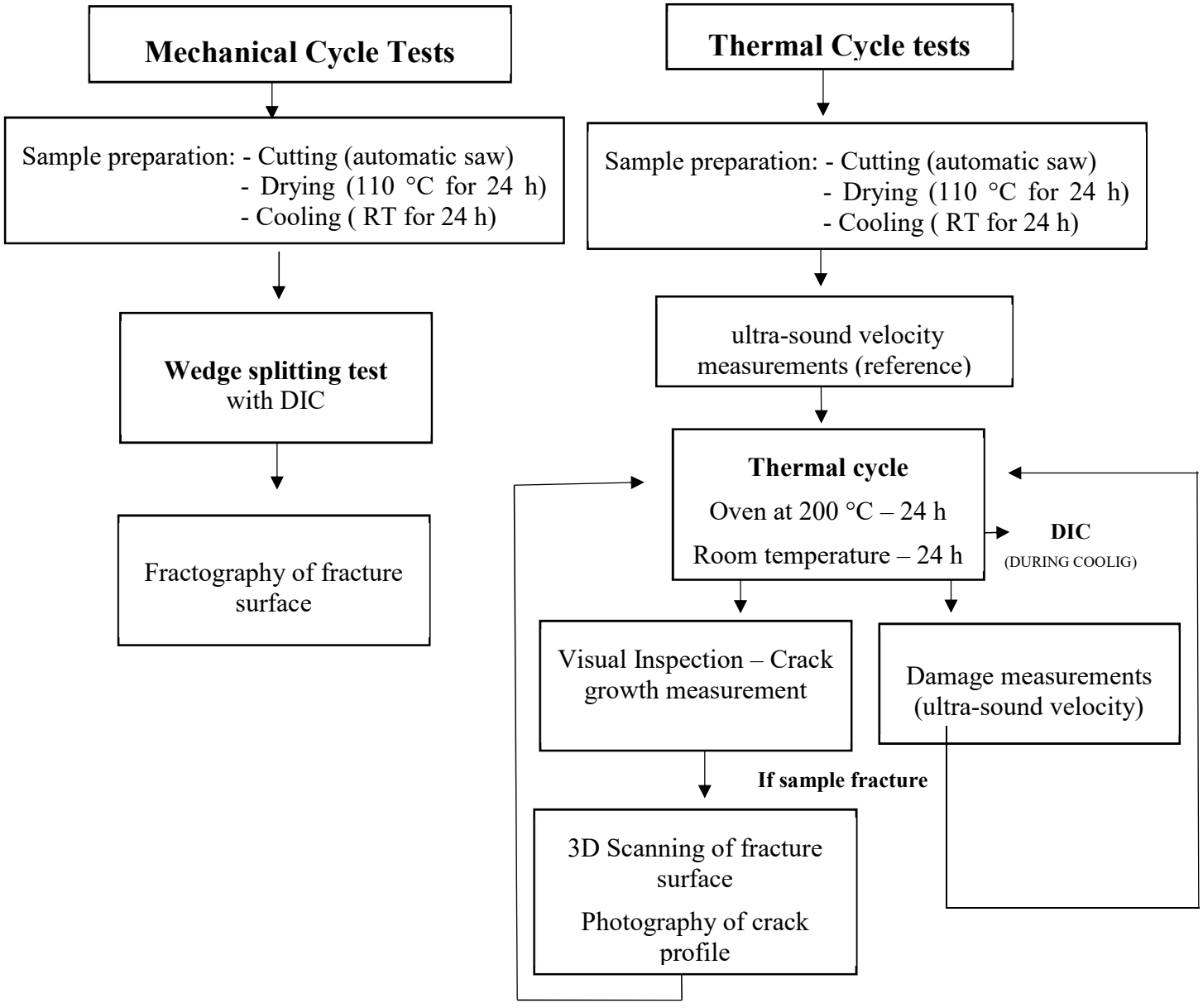

Figure 12 – Scheme of the experimental procedure.

3.1 Thermal Cycle Tests

For thermal cycle test, 5 different sizes were selected: XL, L, M, S and XS (Figure 13). Two samples were tested for each size. The samples were cut according to the dimensions chosen using an automatic circular saw-brillant 285 from ATM. After cutting, samples were dried at 110 °C for 24 hours. Before testing samples were kept at room temperature for 24 hours to ensure complete cooling.

All samples were cut in rectangular shapes with exception of the sample XL which had the dimensions of the commercially bricks. The technical drawing of sample XL is represented in Figure 14 and the respective dimensions of all different sample sizes is described in Table 5.

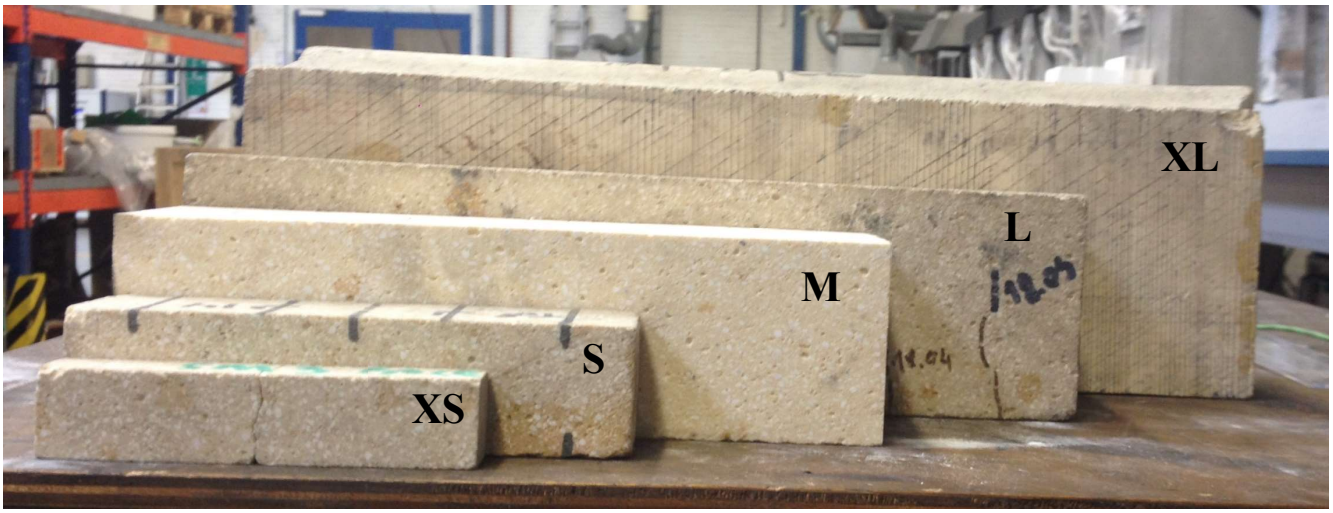

Figure 13 – Different sizes of samples tested.

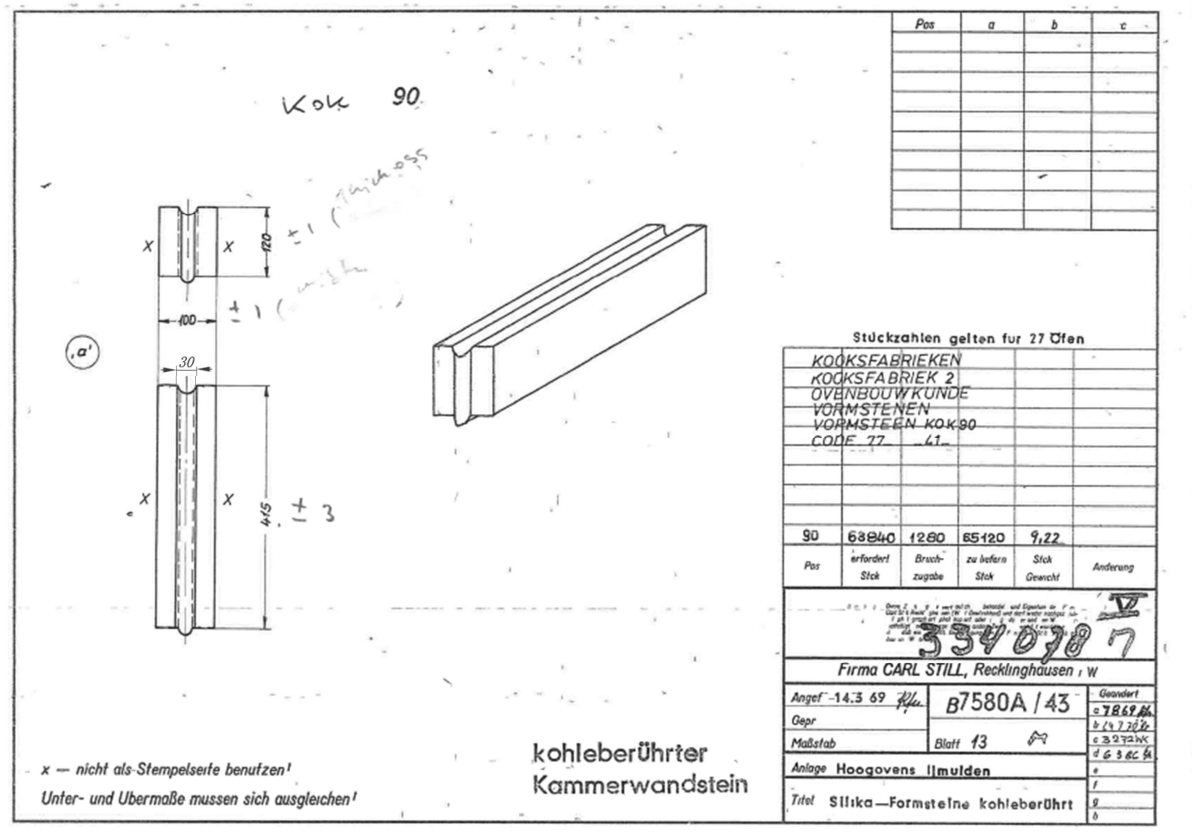

Figure 14 – Technical drawing of the XL samples.

Table 5 – Sizes of the samples used for thermal shock testing.

	XL	L	M	S	XS
Height, mm	121	82	65	41	25
Width, mm	100	83	65	40	20
Length, mm	416	320	250	162	120
Volume, dm^3	5.03	2.16	1.06	0.26	0.06
Surface Area, dm^2	20.78	11.91	7.35	2.94	1.18

The test consists of inducing cyclic thermal shock. The cycle chosen consists of placing the samples in a pre-heated oven at 200 °C for 24 hours, followed by placing the samples in a table for 24 hours at room temperature. The 24 hours cycle was chosen to ensure that the large samples would have enough time to be in thermal equilibrium in both situations (heating and cooling). The temperature chosen was 200 °C since silica bricks are particularly susceptible at this temperature range (Graph 4). Testing at a relatively low temperature also brings advantages since it decreases the costs of the tests (which imply having an oven working continuously for 5 months), decreases significantly the danger when handling the samples and allows to mark and register crack grow in the sample, which at higher temperatures would not be possible since the ink would disappear each cycle.

The position of the samples in the oven was kept the same during all the cycles. The samples were marked with an “x” and “face” to ensure the same positioning. In Figure 15 the oven and the marked faces are illustrated, the “x” faces the oven door and the “face” is orientated upwards.

Figure 15 – Marked surfaces on the samples and oven used for the thermal shock.

The test proceeded even after complete fracture of the samples to study further crack development. After starting a new cycle, the damage and the crack formation and propagation were evaluated.

3.1.1 Damage Measurements

To evaluate the damage the velocity of sound was measured in different directions. The equipment used was an Ip-8 Ultrasonic-multiple-tester from Ultra test, which measures the time a sound signal takes to propagate from one transducer to the other. By placing the transducers in opposite faces and by measuring the distance between the faces, it is possible to calculate the velocity of sound (Figure 16). The damage can be calculated as a percentual ratio of the velocity obtained after N cycles to the initial velocity before the tests. When microcracks are formed, the velocity decreases, since they are a barrier to the sound propagation. For XL samples 12 points were measured: points 1 to 6 – longitudinal direction (x), points 7 to 9 – normal direction (z) and points 10 to 12 – transversal direction (y), as can be seen in Figure 17.

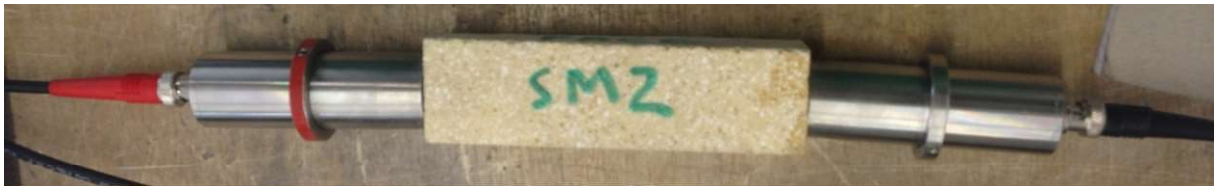

Figure 16 – Damage measurements procedure.

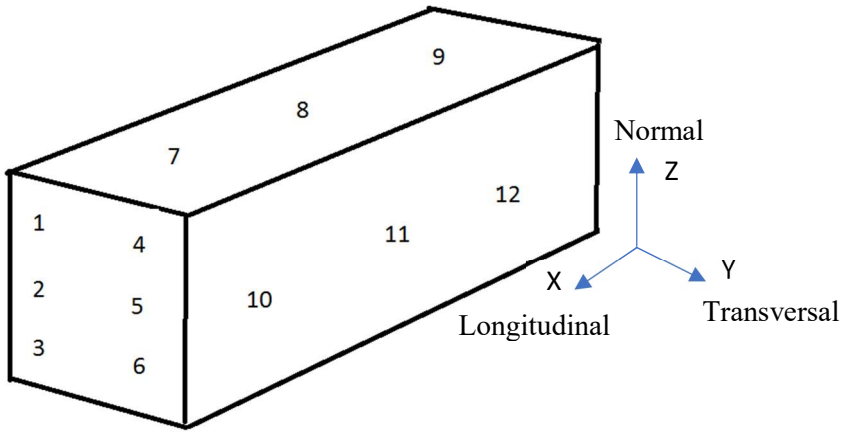

Figure 17 – Measurements points for XL samples.

For L samples, 12 points were measured: points 1 to 4 – longitudinal direction (x), points 5 to 8 – normal direction (z) and points 9 to 12 – transversal direction (y), as can be seen in Figure 18.

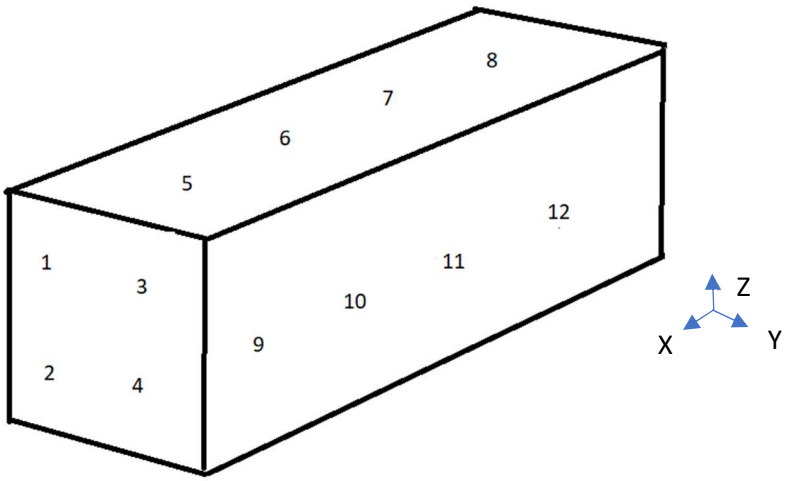

Figure 18 – Measurements points for L samples.

For M samples 10 points were measured: points 1 to 4 – longitudinal direction (x), points 5 to 7 – normal direction (z) and points 8 to 10 – transversal direction (y), as can be seen in Figure 19.

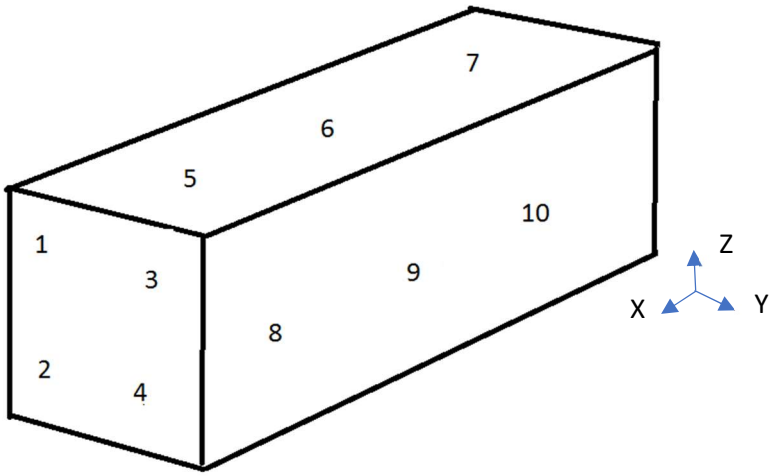

Figure 19 – Measurements points for M samples.

For S and XS Samples only the longitudinal direction was measured – Figure 20.

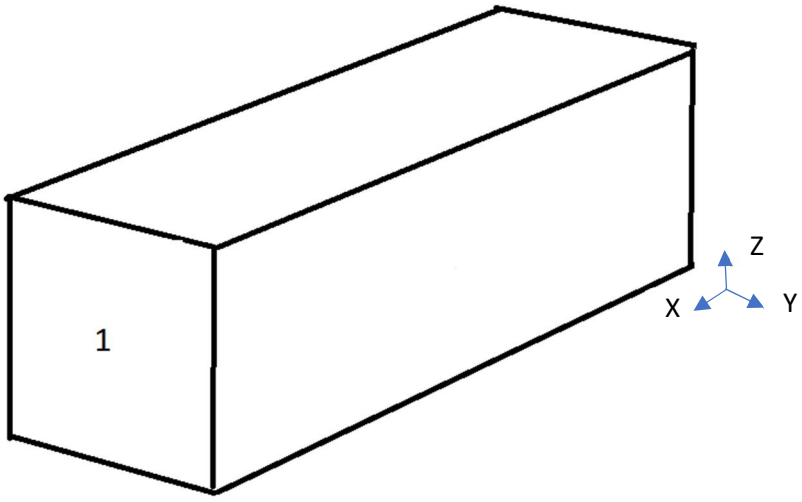

Figure 20 – Measurements points for S and XS samples.

The number of points measured in the samples was selected having into consideration the size of the samples and the size of the measurement equipment. Because of this, large samples enable a higher number of measurement points. For each point, three measurements were conducted.

3.1.2 Fractography

To evaluate the crack formation and propagation a visual inspection of the samples was conducted, and the evolution of the crack was photographically registered and measured using a calliper at the end of every cycle. It is important to mention that the photos were always taken at the same point during the cycle (near the end) in all the samples and in all cycles in order to allow a fair comparison of the crack development.

When samples fractured, the fracture surface was photographed in controlled lighting conditions and, in some samples, the % of white grains in the surface was calculated using Fiji software which is distributed by ImageJ. The white grains are the grains of bigger dimensions in silica bricks which tend to present a white colour that enables their measurement due to the contrast created between the grains and the matrix.

To do this, firstly the images were converted to grey scale and manipulated using Adobe Photoshop 2018, in order to improve the contrast from the grains to the matrix. The parameters used for all the images were:

- Convert image to grey scale (maximum black)
- Contrast: 100%
- Levels: entry (135,5,255)

The images were then open with the Fiji software and converted to 8-bit type and a threshold for grain selection was defined based on Renyi's entropy algorithm (Figure 21). The criteria for selection of this algorithm was based on obtaining images using all algorithms available in the software and choosing the algorithm which allowed a better approximation of the real surface.

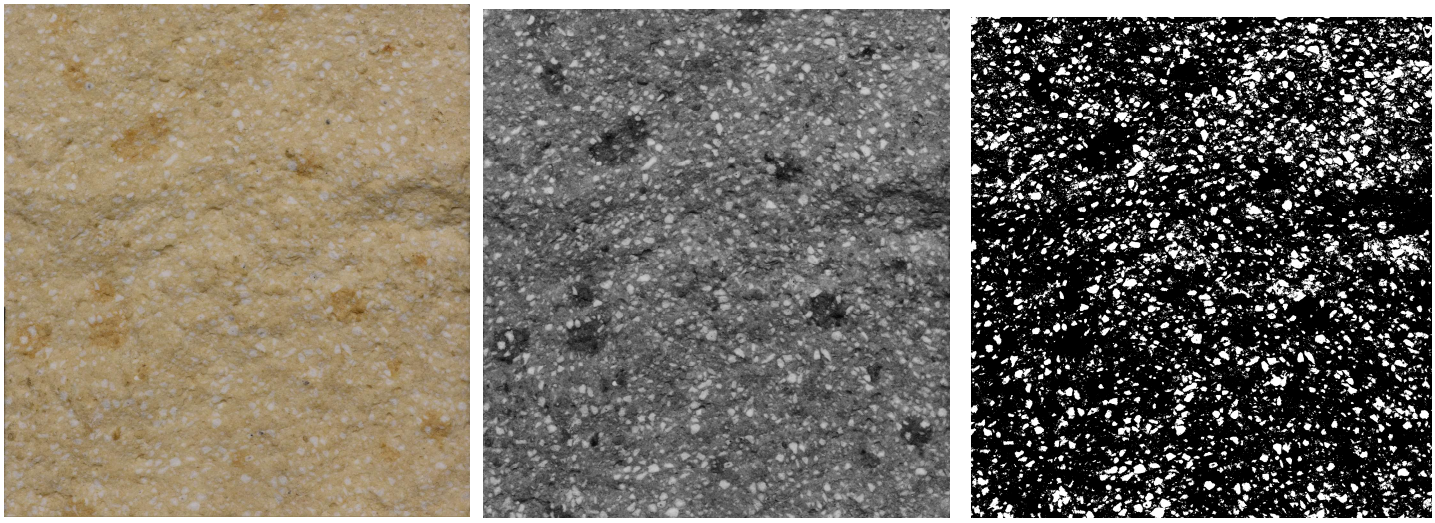

Figure 21 – White grains measurements: Original photo (left), photo after photoshop manipulation (middle), Photo used for the measurements in Fiji software (right).

The fracture surface was also scanned and converted to a .stl file to evaluate the surface roughness. The software Mountains Map from Digital Surf was used to obtain images of the fracture surface with a height scale.

The crack area developed at each cycle was estimated for all cracks of all samples. This was done based on measurements of the growth of the cracks at every cycle. An example of this procedure is presented in Appendix B.

The 2D profile of several cracks was also obtained. This was done using photos of the cracks and by manually retrieving point coordinates throughout the profile using Adobe Photoshop. This procedure is presented with more detail in Appendix C.

The roughness of this profiles was measured using the spectral analysis method, allowing the Hausdorff constant to be calculated.

Digital image correlation was also used for some of the bricks. The surfaces of the samples were marked with a pattern to enable the measurements. In samples with high contrast between grains and matrix, this procedure was not necessary (Figure 22).

Figure 22 –Samples surfaces: samples with low contrast with marks (left and middle), sample with high contrast (right).

A fixed position for the camera and the bricks was defined. The brick was positioned with the same boundary conditions as the ones used in thermal shock – bottom surface in contact with the table. Figure 23 shows the setup for the procedure.

Figure 23 – Set up used to capture the photos for Digital Image Correlation.

The bricks were photographed during cooling. A rate of 2 frames per min was defined. The photos were taken during one / two hours after leaving the oven, depending on the size of the sample. The camera used was a Nikon Coolpix P100, with a resolution of 10 megapixels. The software used for DIC was GOM Correlate 2018.

A brief explanation of the software as well as some tests to assess the accuracy of the measurements are described in Appendix D.

The subset selected for DIC must be based on the typology of the surface pattern. If the subset is to small relatively to the surface pattern it will be governed by the granularity of the speckle pattern; if the subset is too large, it cannot be used to measure heterogenous deformations and will substantially worsen the sub-pixel accuracy. Since GOM Correlate allows to visualize the

quality of the subset selected, in the present work, it was selected the smallest subset which allowed a good quality measurement. The step used was the standard step size. Although a smaller step size would increase the density of the measured points, it would also increase the computation time [41]. The subset size selected for DIC was of 40 x 40 pixels^2, with a step size of 16 pixels.

This technique was also used to compare results from different cycles. In order to be able to obtain valid results it is of extreme importance to place the brick and the camera in the exact same position. To facilitate the position of the brick two fixed perpendicular rulers were used. The camera was locked to the table and kept in the same place throughout the cycles. In order to avoid sliding or minor displacements of the camera, several blocks of Styrofoam were fixed around the camera. The set up used can be seen in Figure 24.

To do this, two new XL bricks were used and photographed from the first cycle until the first complete fracture occurred to enable the analysis of crack appearance and growth.

Figure 24 – Set up used throughout the cycles to capture the photos or DIC.

3.2 Mechanical Tests

3.2.1 Wedge Splitting Test

The test chosen to assess the damage development due to mechanical cyclic loadings was the wedge splitting test. The samples were cut using an automatic circular saw-brillant 285 from ATM.

Two different geometries were used for the wedge splitting test samples which are represented in Figure 25 and Figure 26.

The testing machine used was an Instron 8503 retro line Zwick/ Roell. The horizontal force was calculated from the vertical force. The horizontal displacement was measured by an optical dilatometer.

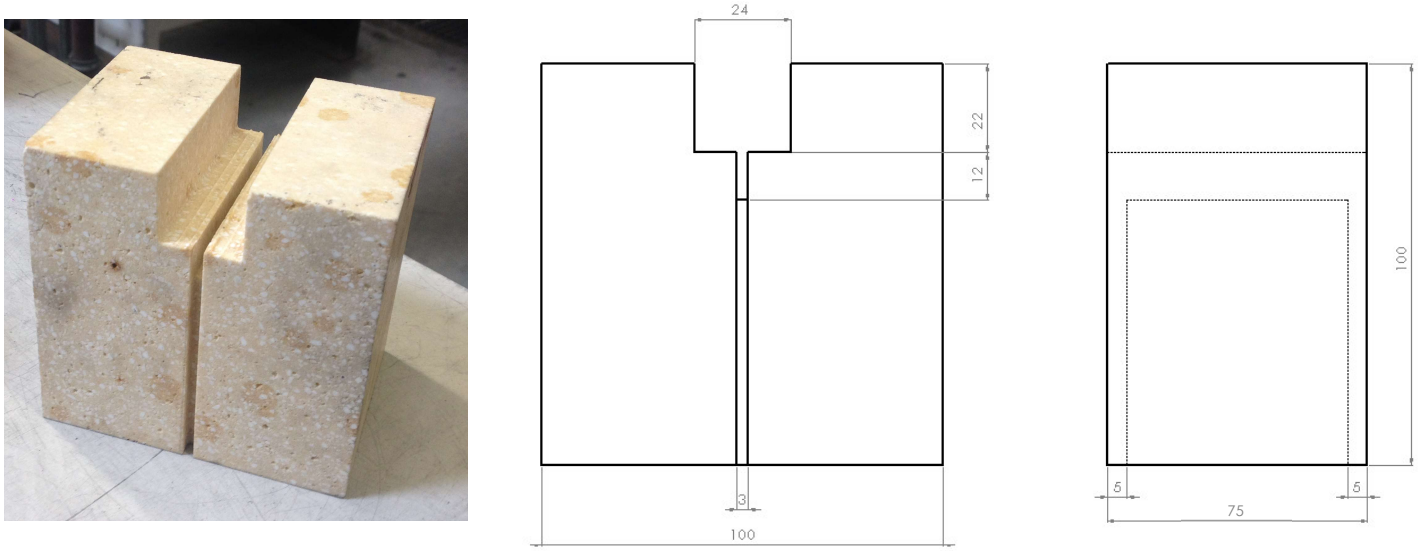

Figure 25 – Sample for wedge splitting test - geometry 1.

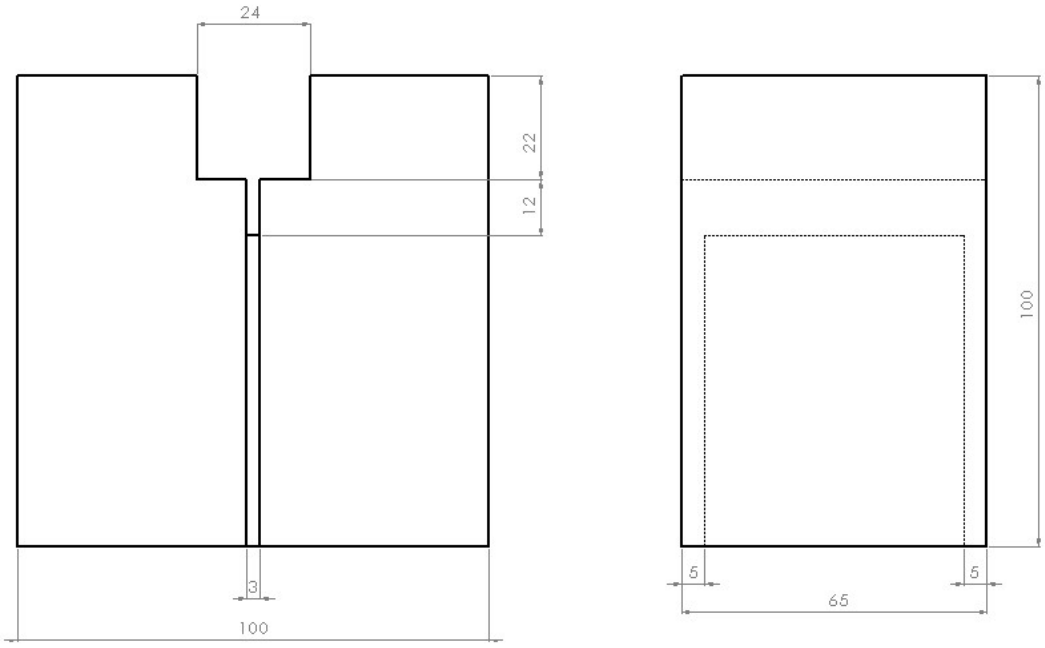

Figure 26 – Sample for wedge splitting test - geometry 2.

In Table 6 and 7, the different loadings applied are described for each tested sample. For cyclic tests the amplitude used, and respective cycle number is also presented. The loading rate for all the tests was 0.5 mm/min and the loading method was Method III (Figure 5).

Several samples were obtained from the same brick. This is interesting since in refractory materials it is common to have a significant spread in the results. The behaviour of these materials is dependent on the initial defects and manufacturing conditions (e.g. position in the oven). Therefore, by using samples from the same brick these effects can be minimized.

It is also important to mention the material of the samples in Table 6 is from a different batch than the material in Table 7, which should be taken into consideration in the analysis of the results.

Table 6 – Types of loading that each sample was subjected in the wedge splitting test for geometry 1.

Brick number	Sample number	Type of test	N° of Cycles	Amplitude
8	A	Mono	-	-
	B	Cyclic	54	0.9 mm
	C	Cyclic	20	1.2 - 1.8 mm
	D	Cyclic	2	1.8 mm

Table 7 – Types of loading that each pair of samples was subjected in the wedge splitting test for geometry 2.

Brick number	Type of test	N° of Cycles	Amplitude
1	Monotonic	-	-
	Cyclic	266	0.63 - 0.75mm
3f	Monotonic	-	-
	Cyclic	26	0.9mm
3	Monotonic	-	-
	Cyclic	194	0.63 - 0.75mm
5	Monotonic	-	-
	Cyclic	155	0.63mm
4	Cyclic	7	0.9
19	Cyclic	115	0.9
23	Cyclic	24	0.9

The wedge system mounted on the sample is represented in Figure 27. In Figure 28 is also possible to see the configuration of the test sample and wedge system mounted on the testing machine.

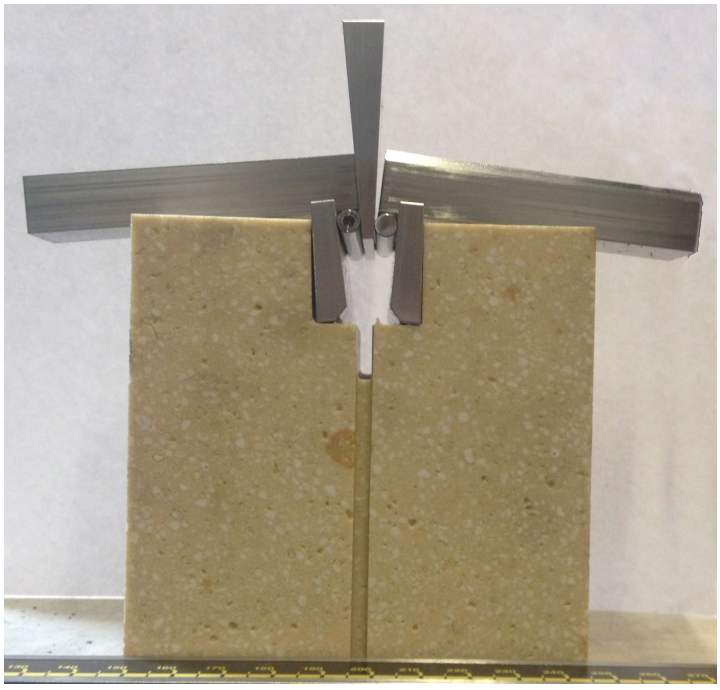

Figure 27 – Sample for wedge splitting test with wedge mounted.

Figure 28 – Configuration of the wedge splitting test.

DIC was also used as an auxiliary technique during the tests. The Camera used was Nikon D750 with a resolution of 24 megapixels. The same parameters and software used for DIC in thermal shock tests were used in this procedure since it is the same material with the same pattern characteristics that is being tested. An artificial pattern had to be created in the surfaces since, as was the case in thermal shock tests, the natural pattern of the surfaces did not enable an accurate feature recognition. In Figure 29, the set up for the test with DIC as well as the artificial pattern in the surface can be observed. Since different amplitudes were used, in order to avoid having to change and predict an appropriate frame rate for each tested, all tests were video recorded with a chosen resolution of 1080p.

Figure 29 – Configuration of the wedge splitting test with DIC.

3.2.2 Fractography

A Wide area 3D Measurement System (VR-300 Keyence) was used to analyse the fracture surface for selected samples after wedge splitting test (Figure 30).

Figure 30 – Wide-Area 3D Measurement SystemVR-300 from Keyence.

Both the roughness (Sa, Sz and Sq parameters) were measured using the Analyser Software VR-H2AE from Keyence. 3D images of the fracture surfaces were also taken for all the samples using the same software.

The Sa parameter expresses the difference in height of each point compared to the arithmetical mean of the surface – eq 3.1 [42]:

$$Sa = \frac{1}{A}\iint_A |z(x,y)|dxdy \tag{3.1}$$

where:

A, is the area
Sa, is the arithmetical mean height

Sq represents the root mean square value of the ordinate values within the definition area. The main difference between Sa and Sq is that Sq amplifies occasional heights or depths while Sa simply averages them– eq 3.2 [42]:

$$Sq = \sqrt{\frac{1}{A}\iint_A z^2(x,y)dxdy} \tag{3.2}$$

where:

A, is the area
Sq, is the root mean square height

The Sz parameter is defined by the sum of the largest peak height and the largest peak depth value within the measured area – eq 3.3 [42]:

$$Sz = max(z(x,y)) + \min(z(x,y)) \tag{3.3}$$

where:

Sz, is the maximum height

The areas of the generated surfaces were also analysed. To do so, the area of either their concave surfaces and the convex surfaces were measured. It was considered that the sum of both concave and convex measures would be a good estimation of the total fracture surface area. In order to have a fair comparison between the samples, the area of the cross section of each sample was also measured. In Figure 31 it is possible to see both concave and convex measurements for one of the samples tested.

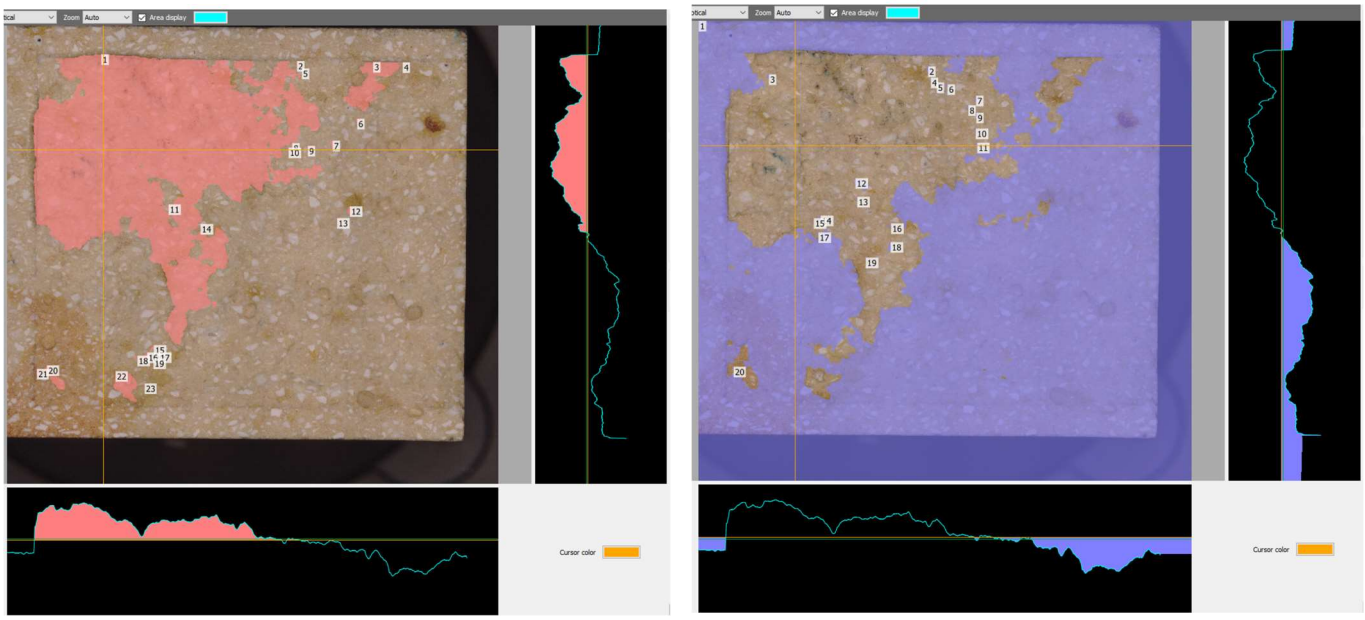

Figure 31 – Surface area measurements for both convex (left) and concave (right) regions of one of the samples tested.

The images obtained from the equipment were also used to determine the % of white grains present in the fracture surface area.

The same procedure used for the white grains measurements in the thermal shock samples was used here to enable a posterior comparison of the results. It is important to notice that the lighting conditions were provided by the 3D scanner used to capture the images and should, therefore, be similar in all samples, thus ensuring the validity of the results. In Figure 32 it is possible to see the image of the fracture surface and the respective image after defining the threshold in Fiji software.

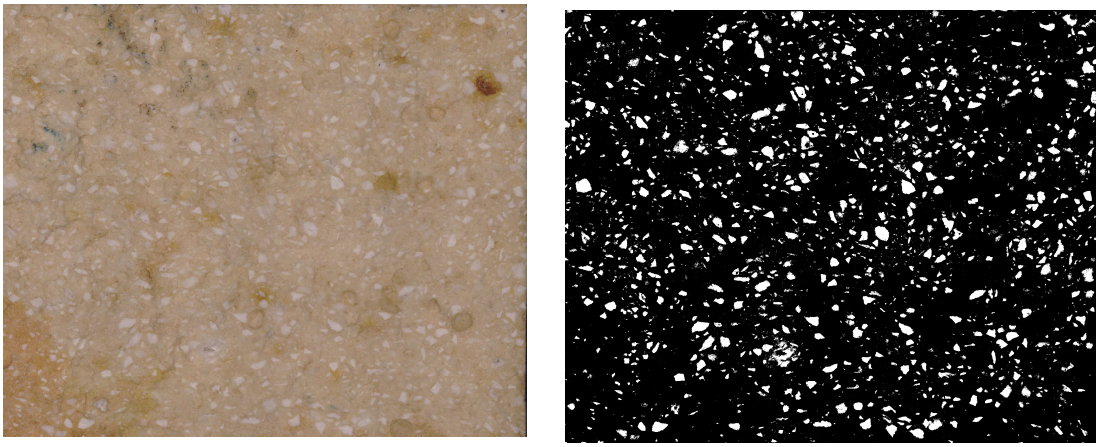

Figure 32 – White grains measurements: Original photo (left) and photo used for the measurements in Fiji (right).

To allow a comparison with the roughness found for thermal shock tests the same parameter used in the latter, Hausdorff constant, was also calculated for these samples. To do so five

equally spaced profile lines of the fracture surface of each sample were obtained (Figure 33), using the Analyser Software VR-H2AE from Keyence. For each profile the Hausdorff parameter was calculated.

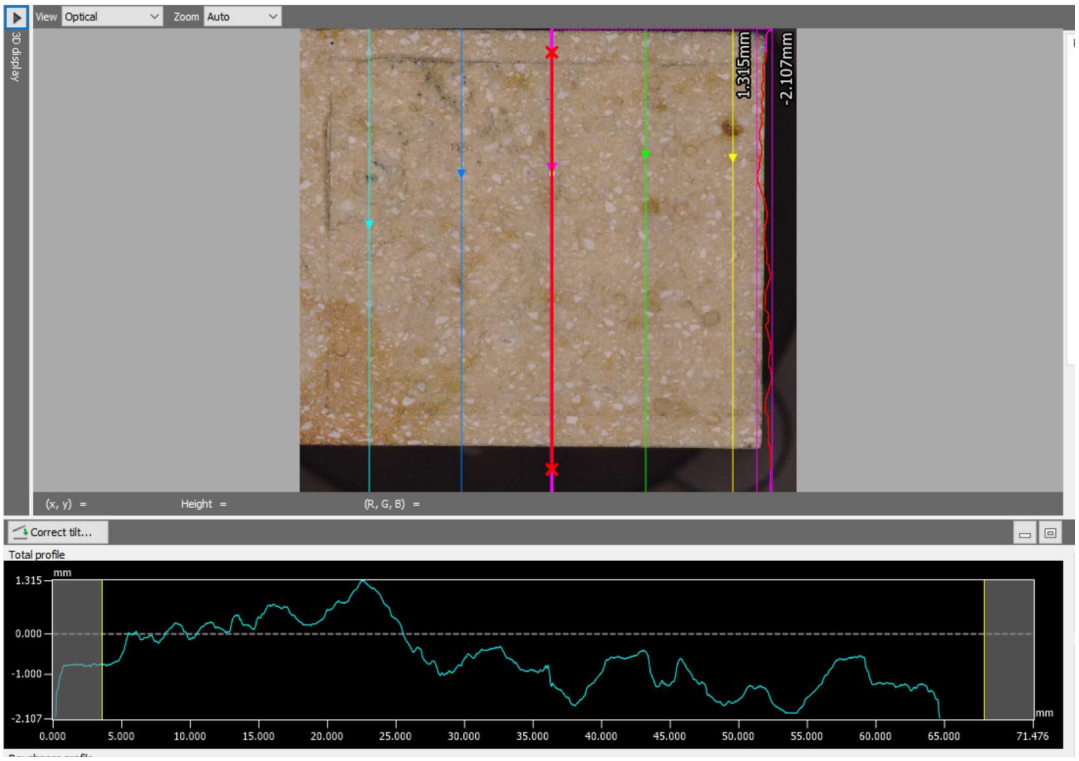

Figure 33 – Selection of three distinct profiles using Analyser Software VR-H2AE from Keyence.

4 Results and Discussion

4.1 Mechanical Tests

4.1.1 Damage Development

In Figure 34 the force displacement curves obtained for several bricks tested in the WST are presented.

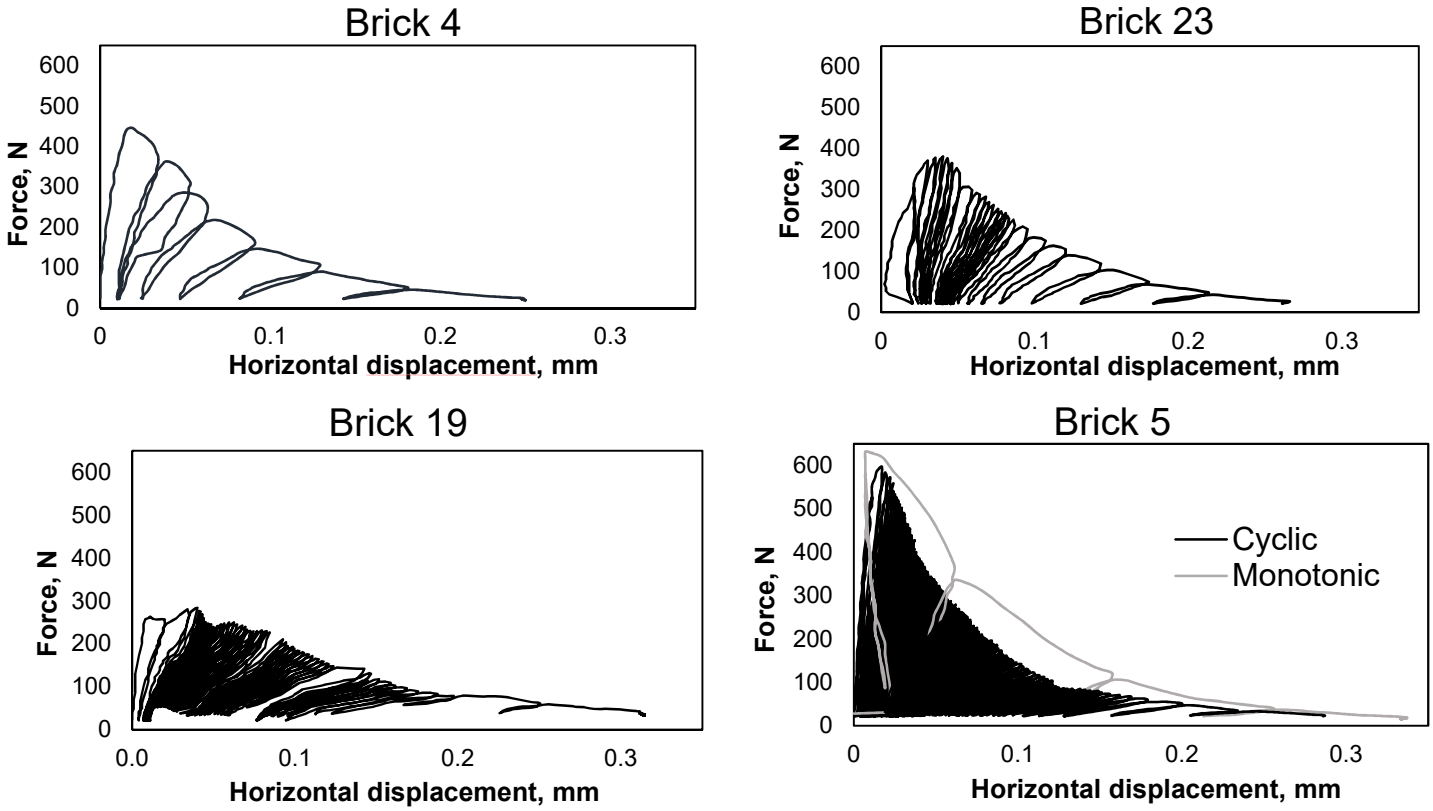

Figure 34 – Force displacement curves for wedge splitting test for different bricks.

To study the damage development, the compliance and irreversible strains were calculated from the force-displacement data. The compliance C is the reverse of the stiffness and was calculated by the formula in eq 4.1.

$$C = \frac{F_t - F_b}{D_t - D_b} \tag{4.1}$$

where:

C, is the compliance
F_t, is the maximum force reached in a given cycle
Fb, is the minimal force reached in a given cycle
D_t, is the displacement correspondent to the maximal force reached in a given cycle

D_b, is the displacement correspondent to the minimal force reached in a given cycle

The irreversible displacements were calculated using the formula:

$$D_{irr} = D_{b\,n} - D_{b\,n-1} \tag{4.2}$$

where:

D_{irr}, is the irreversible displacement for a N cycle
N, is the number of the cycle
D_b, is the displacement correspondent to the minimal force reached in a given cycle

To analyse the damage development, the compliance (Graph 5 and Graph 6) and irreversible strains (Graph 7) were plotted against the number of cycles.

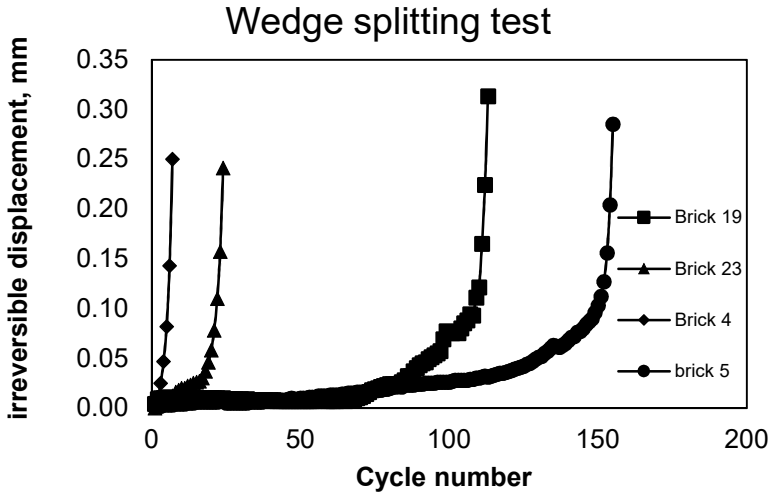

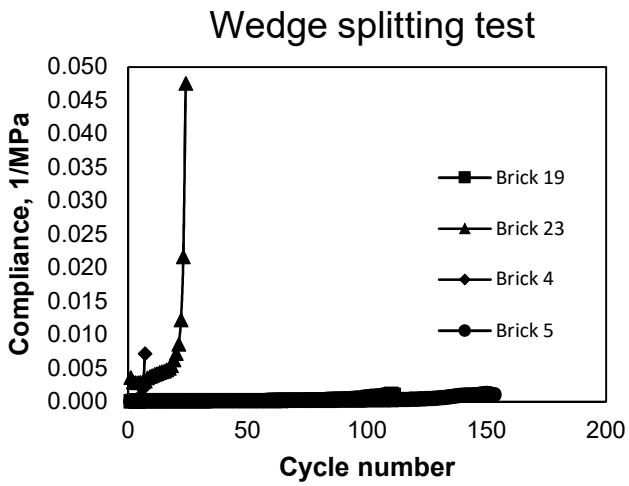

Graph 5 and Graph 6 – Irreversible strain and compliance (left to right) for each cycle.

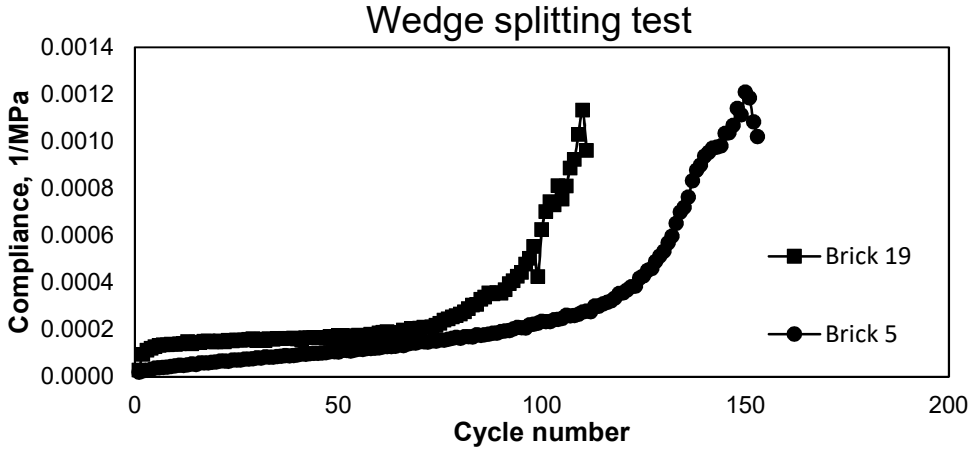

Graph 7 –Compliance for each cycle for the samples with high number of cycles.

By analysing both the compliance and the irreversible strains, it is possible to distinguish two different types of behaviour regarding damage development. An exponential development of the damage was observed in Brick 23 and Brick 4, which failed completely after a small number of cycles. Brick 10 and Brick 5 on the other hand, developed a behaviour similar to a sigmoid, where three different stages were observed. Firstly, an increase in the damage which is followed by saturation and finally a rapid development until failure. This difference in behaviour can be explained by the amplitude used in the tests, since Brick 23 and Brick 4 were tested at bigger amplitudes which promote faster crack development and Brick 19 and Brick 5 were tested at low amplitudes which retards crack initiation.

4.1.2 Fractography

The 3D image of the fracture surfaces of several samples which undergone WST is represented in Figure 35 to Figure 38.

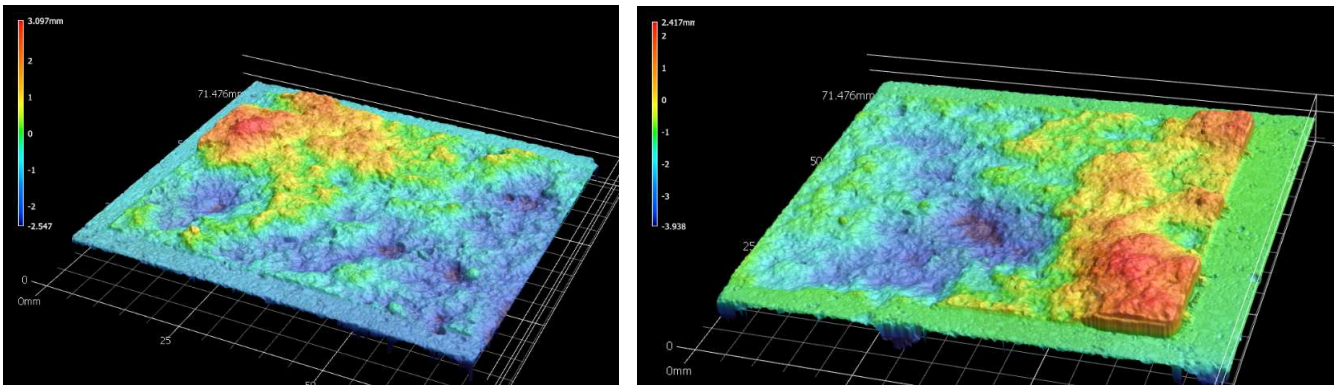

Figure 35 – Fracture surface of the Brick 1- monotonic (left) and cyclic (right).

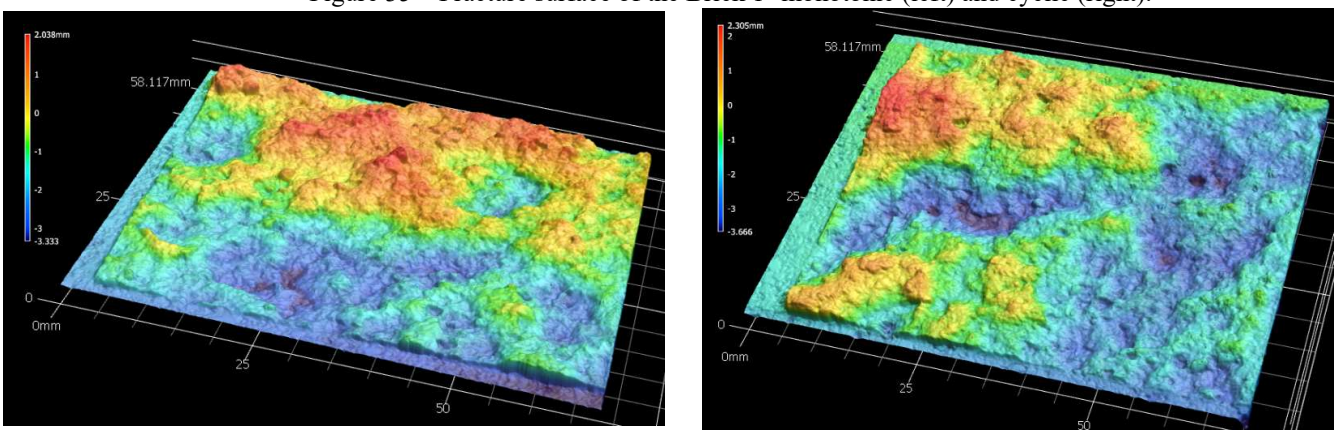

Figure 36 – Fracture surface of the Brick 3f – Monotonic (left) and Cyclic (right).

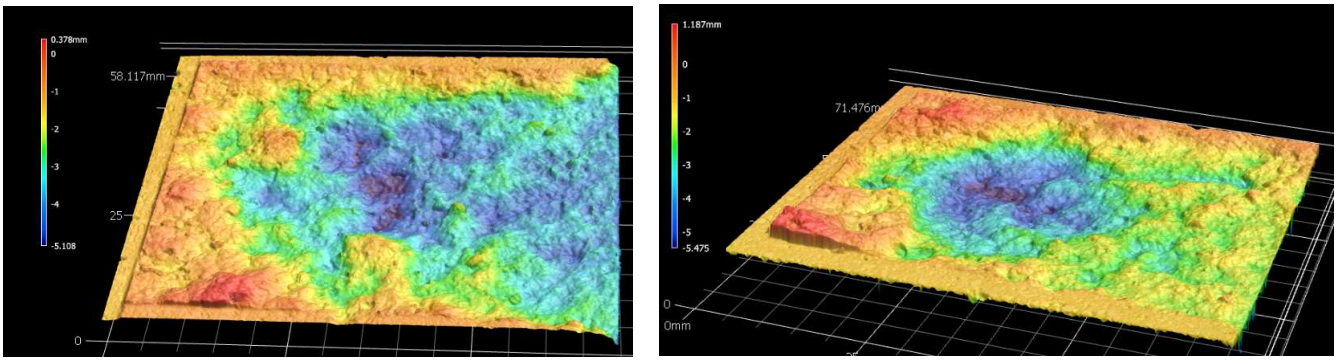

Figure 37 – Fracture surface of Brick 3 – Monotonic (left) and Cyclic (right).

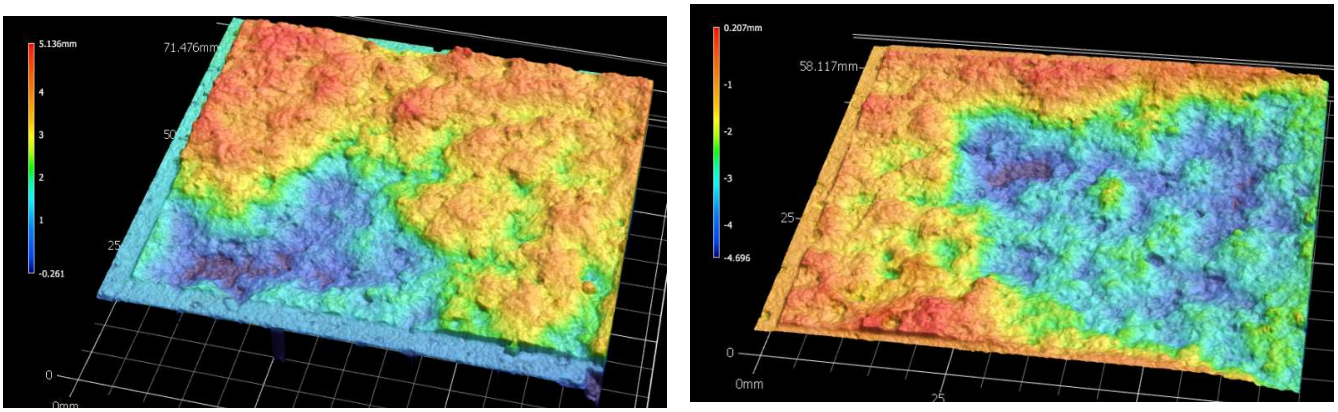

Figure 38 – Fracture surface of the Brick 5 - monotonic (left) and cyclic (right).

The roughness parameters measured for the respective samples Sa, Sq and Sz are presented for each sample from Graph 8 to Graph 10 respectively.

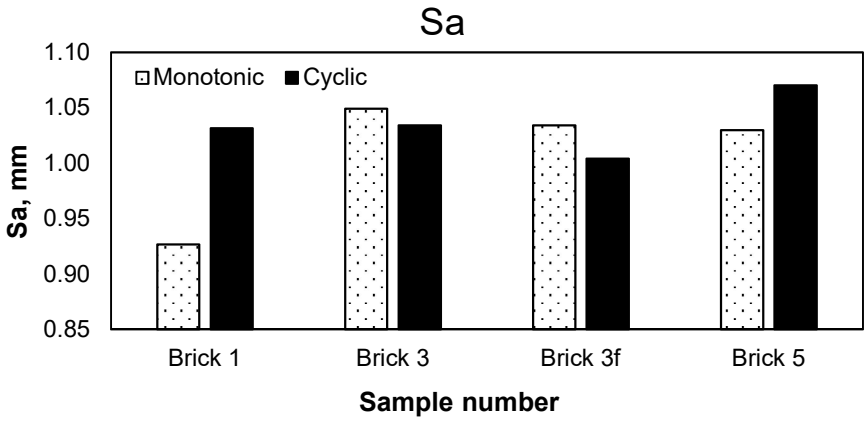

Graph 8 – Roughness (Sa) for the different samples tested.

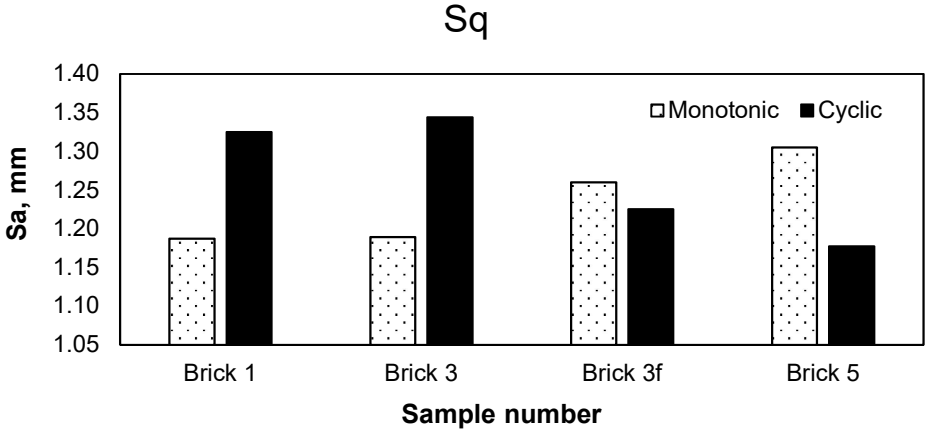

Graph 9 – Roughness (Sq) for the different samples tested.

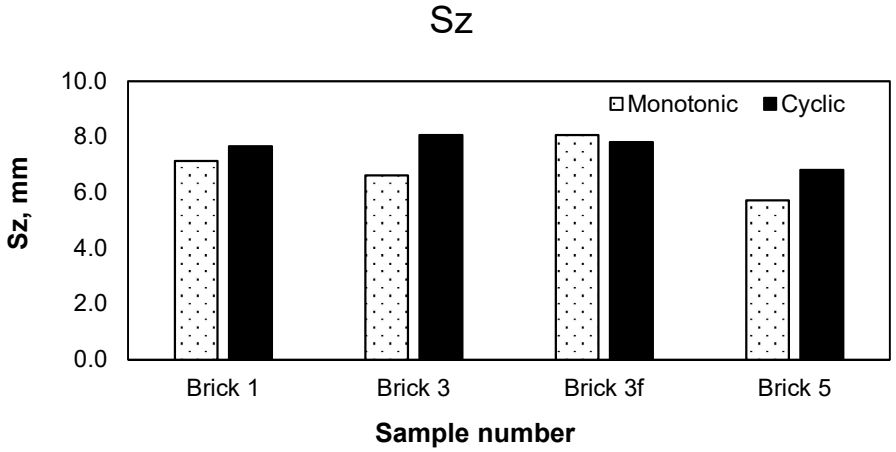

Graph 10 –Roughness (Sz) for the different samples tested.

The Hausdorff dimension was obtained using the Fourier power spectrum (square magnitude of the Fourier transform) method. To calculate the Fourier power spectrum the Fast Fourier Transform was performed in Microsoft Excel. To do this, the input data must have a size that is an integral power of 2. In order to allow comparisons with samples of different sizes and to consider all the data obtained, the criterion selected was adding the necessary zeros to the data points, so that the data size would be a power of two. The Hausdorff can then be calculated from the slope of the straight line fit to the spectral density represented in a logarithmic scale

using equation 2.12 and 2.13. The Hausdorff (D) dimension quantifies the roughness or smoothness of spatial data. Higher values of D means higher roughness and waviness and is

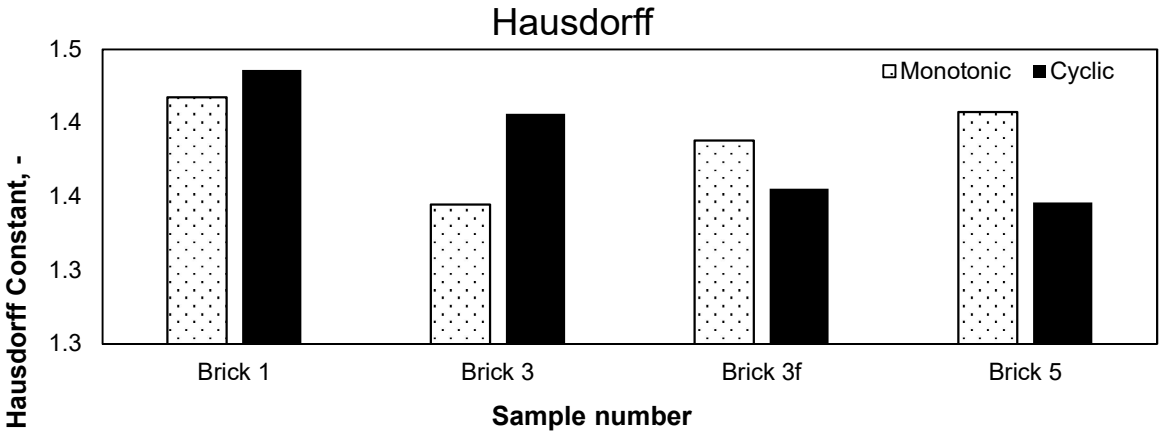

represented for several samples in Graph 11,

Graph 11 –Hausdorff for the different samples tested.

In Graph 12 the ratio of the surface area with the area of the cross section (C.S) measured is represented for several samples.

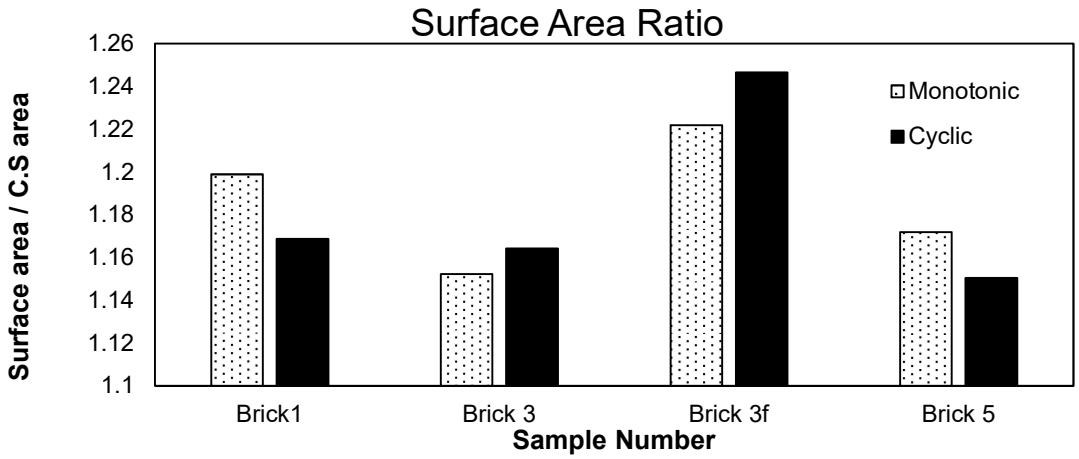

Graph 12 –Ratio of the surface area to the cross-section area for the different pair of samples.

The % of white grains is represented in Graph 13.

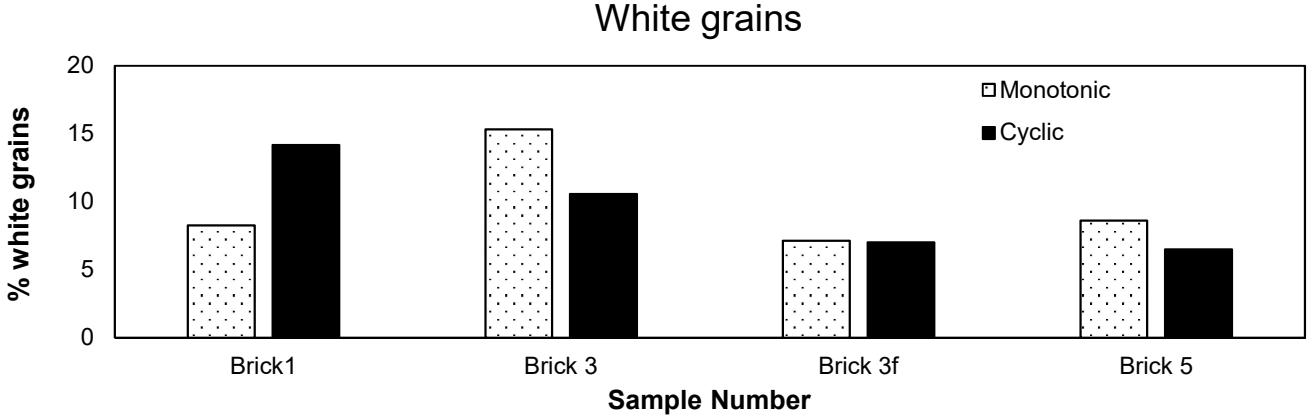

Graph 13 –% of white grains for the different samples.

When comparing the monotonic with the cyclic results no clear trend was observed. For the parameter Sz, the monotonic samples tend to have smaller values with comparison with cyclic

ones with exception of brick 3f where the values of both cyclic and monotonic are similar. This evolution of increasing roughness with the number of cycles is in accordance to X.B. Zhang and J.Li (2008), who correlated the roughness of the fracture surface with the level of stress concentration. It was pointed out that the roughness of the fracture surface decreases as the stress concentration becomes stronger. Since the energy dissipation depends on the net surface creation during the fracture process, increasing roughness of the fracture surface is synonym increasing energy dissipation [43]. However, this trend is not evident in the other parameters evaluated.

The white grains % is relevant since it can indicate how crack propagates, around the grains (lower % of white grains) or transversal to the grains (higher % of white grains). Transgranular crack propagation is usually associated with increase in brittleness, while crack propagation along the grain/matrix interface is more prominent with decreasing brittleness [20]. However, no relevant difference was possible to observe between cycle and monotonic tests.

One justification for these results could be that the cyclic samples undergone a different number of cycles and, therefore, the different bricks are being compared in different circumstances.

In order to overcome this problem these parameters were plotted against the number of cycles from Graph 14 to Graph 18, where the samples that originated from the same bricks are connected by a line.

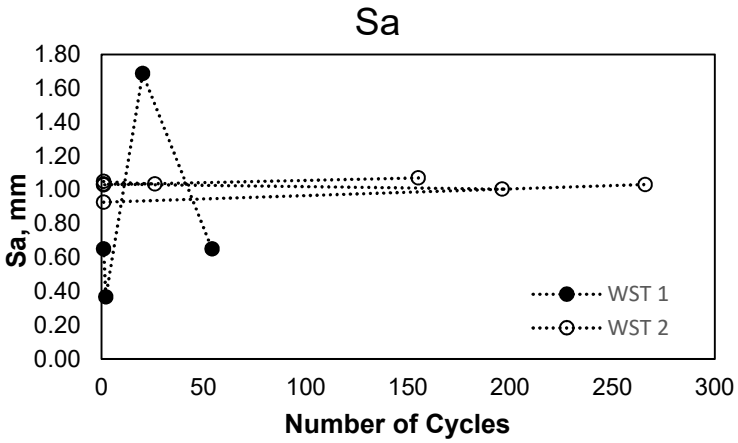

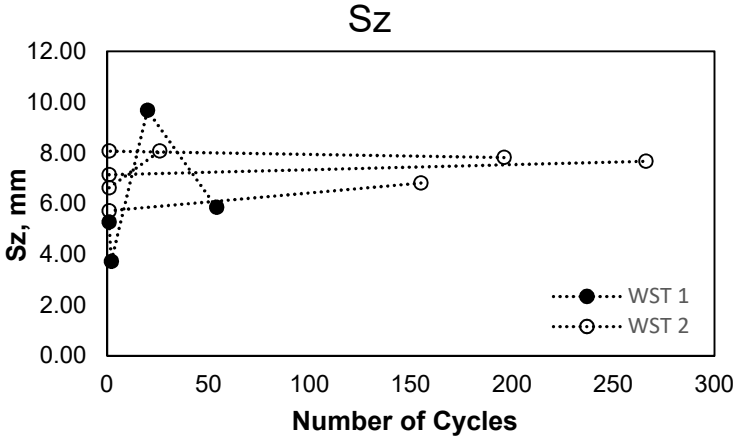

Graph 14 and Graph 15 –Sa (left) and Sz (right) parameter for the different number of cycles.

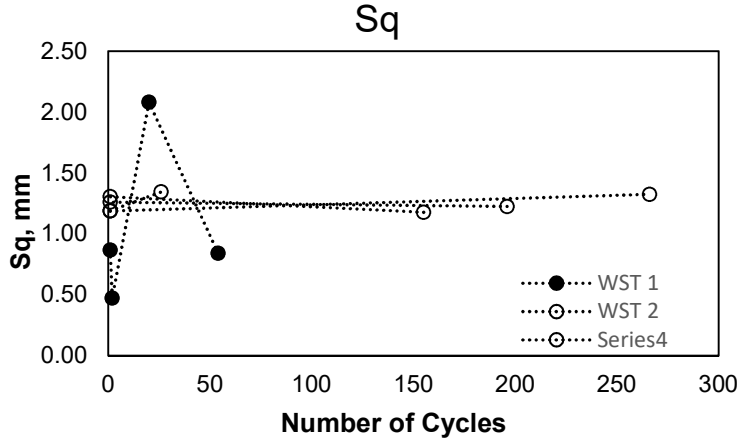

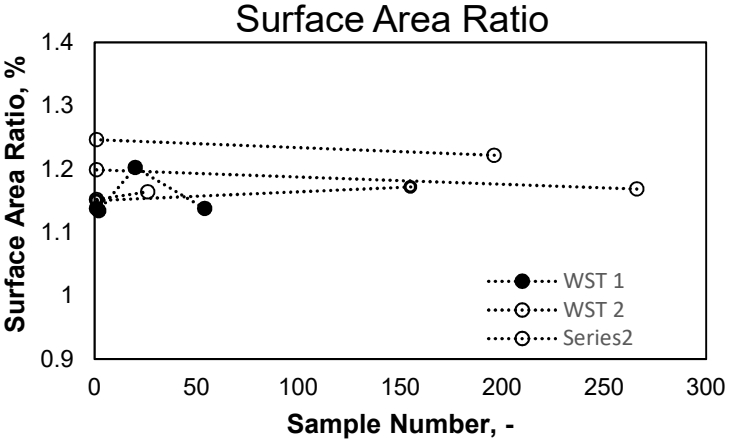

Graph 16 and Graph 17 –Sq parameter (left) and Surface area ratio (right) for the different number of cycles.

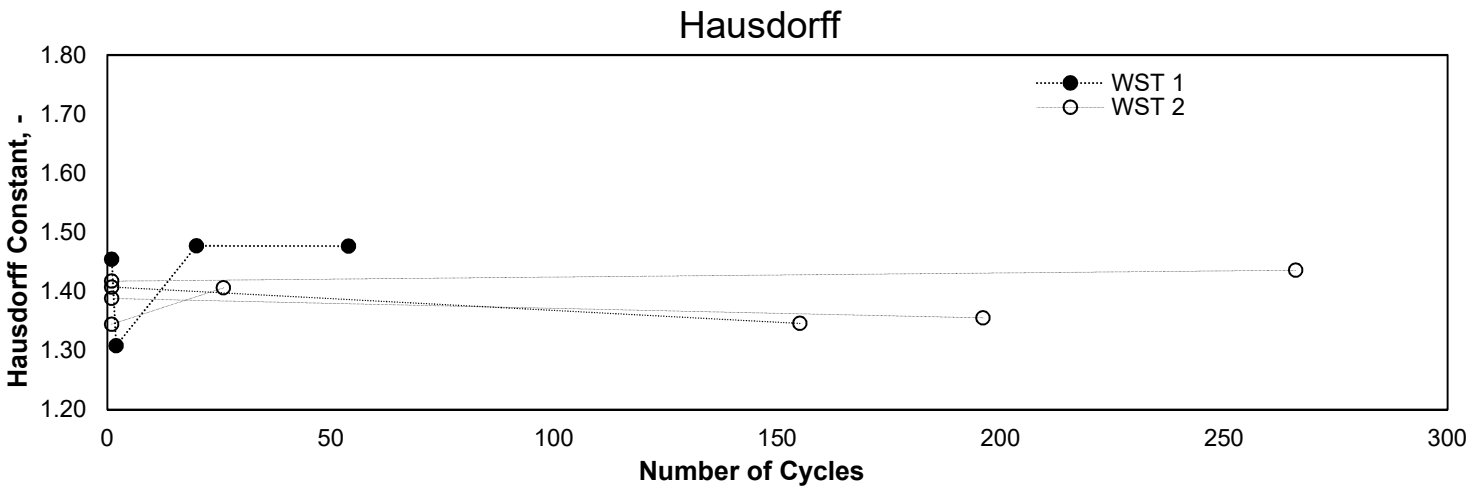

Graph 18 –Hausdorff dimension for samples subjected to wedge splitting test with different number of cycles.

It is possible to observe that for most of the evaluated parameters the roughness tends to increase with the number of cycles until it reaches a peak after which there is a decrease in the roughness. For a high number of cycles, the roughness does not seem to be considerably affected by the number of cycles. However, it is important to mention that the spread obtained in the results is significant, which can be seen in the range of the results obtained for monotonic samples (1 cycle) and therefore more tests should be carried out in order to assess if the results found are not caused by random defects in the samples or if this evolution is observed. Even in samples originated from the brick (samples connected by lines in the Graphs) a significant spread was observed in the results.

This influence can also justify why no trend was observed when comparing monotonic and cyclic bricks, since some of the cyclic bricks were tested in a small number of cycles and other in a high number of cycles.

4.1.3 Digital Image Correlation

DIC was used in two of the tested bricks. The displacements developed throughout the WST in Brick 8 sample D after 5 minutes of testing can be seen in Figure 39. It is possible to observe the presence of a cracks in the sample.

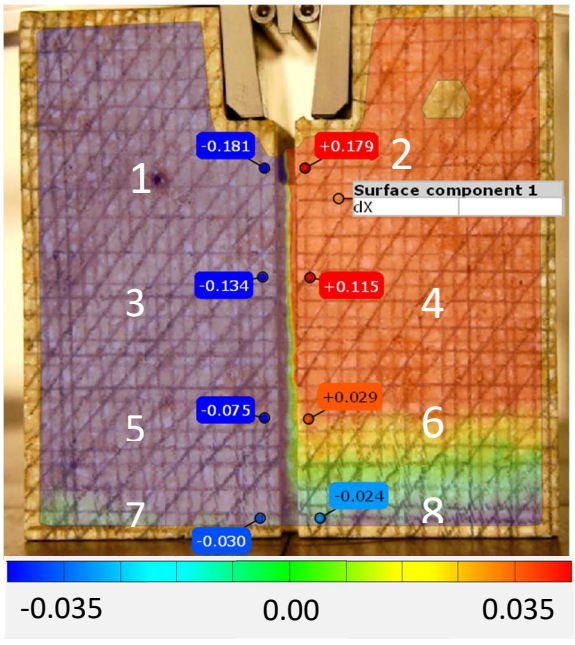

Figure 39 – Points where displacements for crack opening were calculated.

The force displacement curve of these tests can be seen in Graph 19.

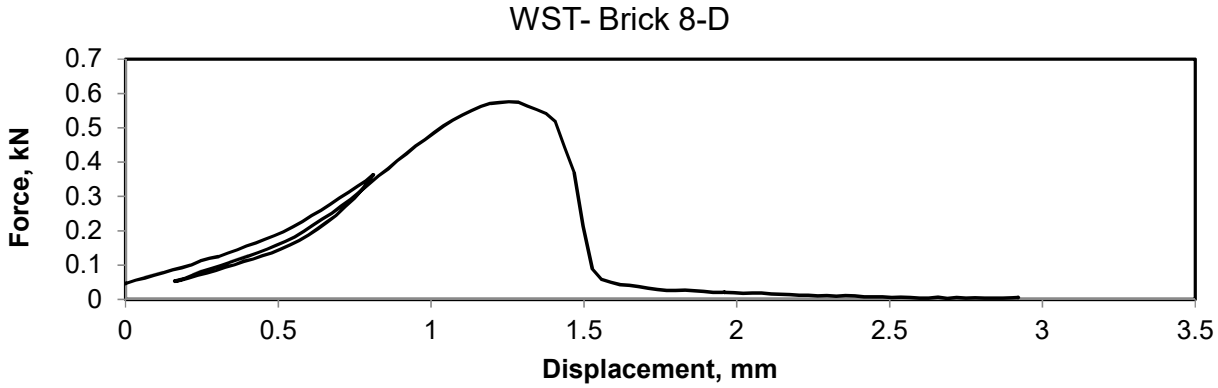

Graph 19 –Force displacement curve of Brick 8 sample D.

The displacement from points 1 to 6 was also calculated and its evolution with time is represented in Graph 20.

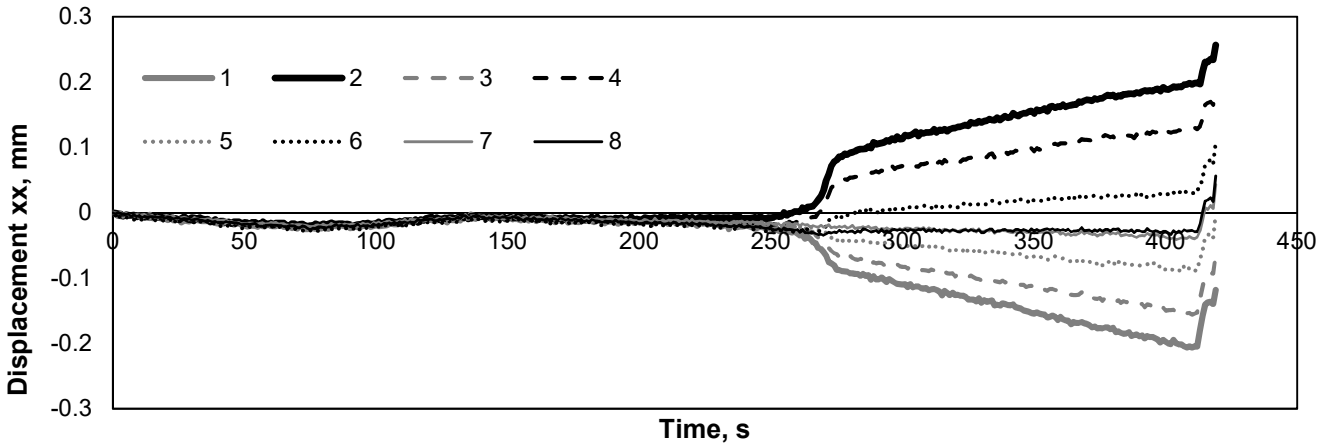

Graph 20 –Displacements of points 1 to 6 in brick 8 sample D during WST.

The points closer to the wedge are the ones which have a higher displacement. The displacement decreases as the points are closer to the bottom of the sample, which was expected given the geometry of the samples. The crack opening was also calculated as the difference between point 1 and 2 since these points are the ones with higher displacement. The crack opening along with the force registered during the tests can be seen in Graph 21.

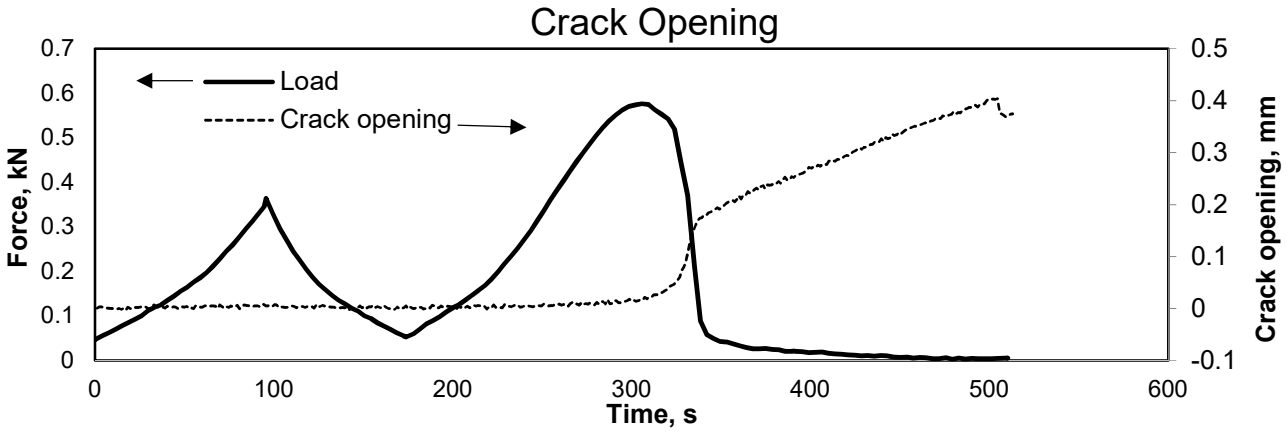

Graph 21 – Crack opening and force developed during WST of brick 8 sample D.

It is possible to observe that a significant increase in the displacement occurs when the maximum force was reached in the second cycle. After this point, the crack development is almost catastrophic, and the sample fails. To understand crack development a zoom to the first stage of the crack opening is presented in Graph 22.

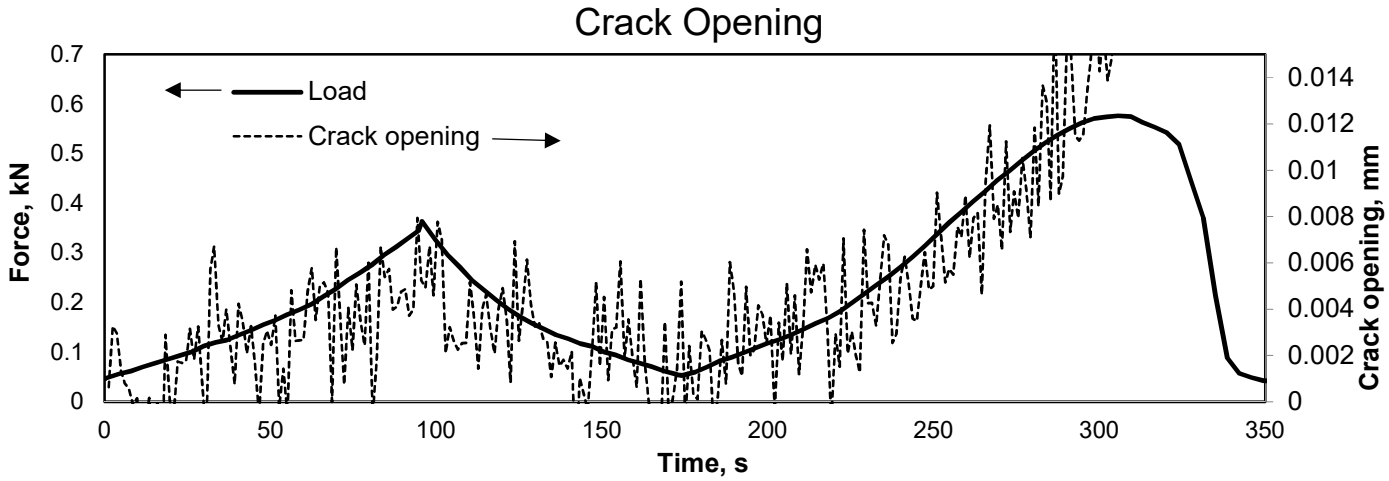

Graph 22 – Crack opening and Force During WST of brick 8 sample D- First stage.

In Graph 22 it is possible to observe that displacement in the first stage follows the force behaviour. In the unloading part of the first cycle the displacement decreases. This is not seen in cycle two where the crack formed continuously grows until failure.

This analysis was also carried out to brick 8 sample C. However, since this was a long test only the first 40 minutes were recorded. In Graph 23 the crack opening, calculated between the points 1 and 2 – Figure 40, is presented as well as the force development. In Graph 24 the loading displacement curve of this brick for the first forty minutes is also presented.

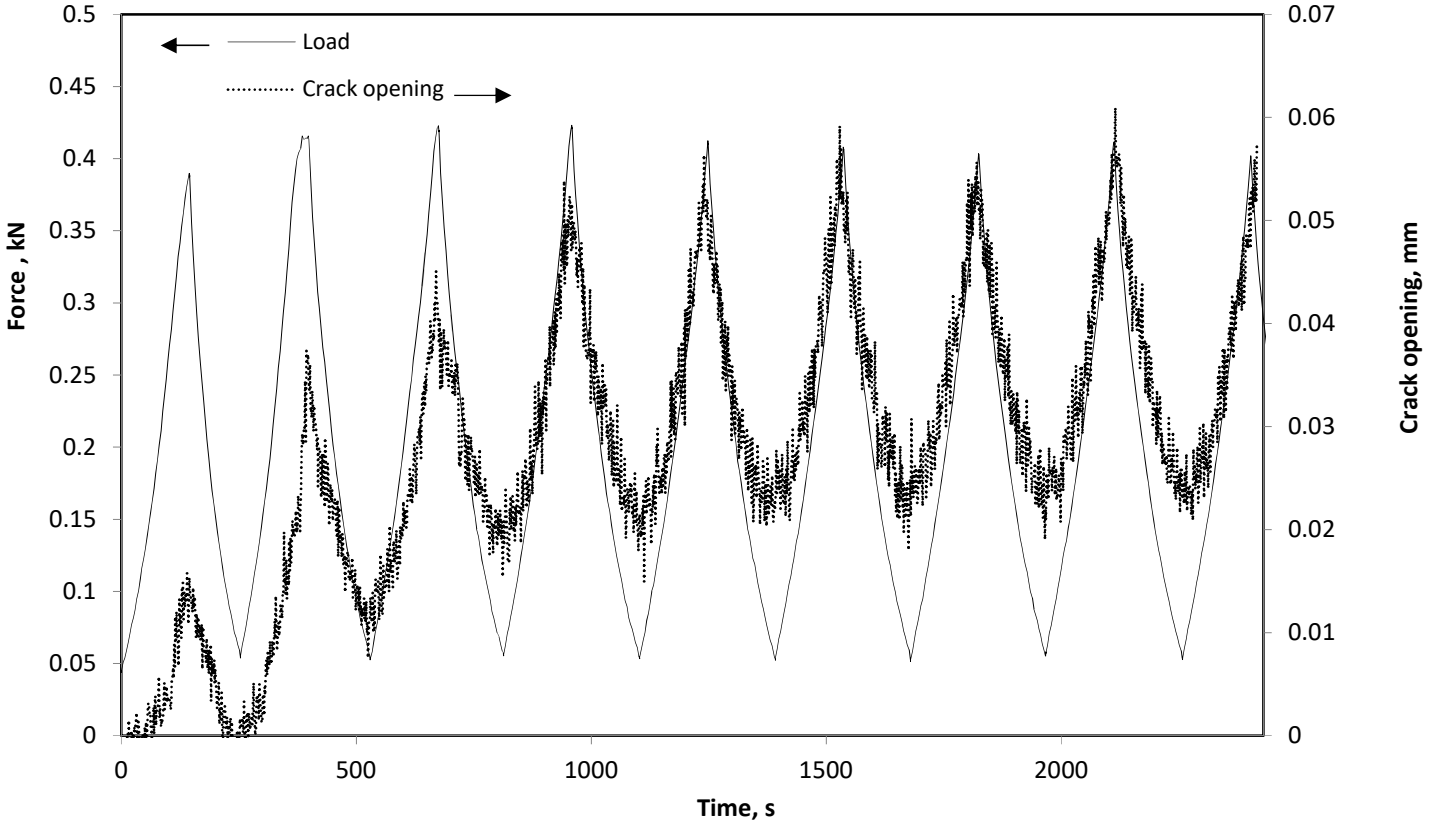

Graph 23 – Crack opening and force registered during WST of brick 8 sample C.

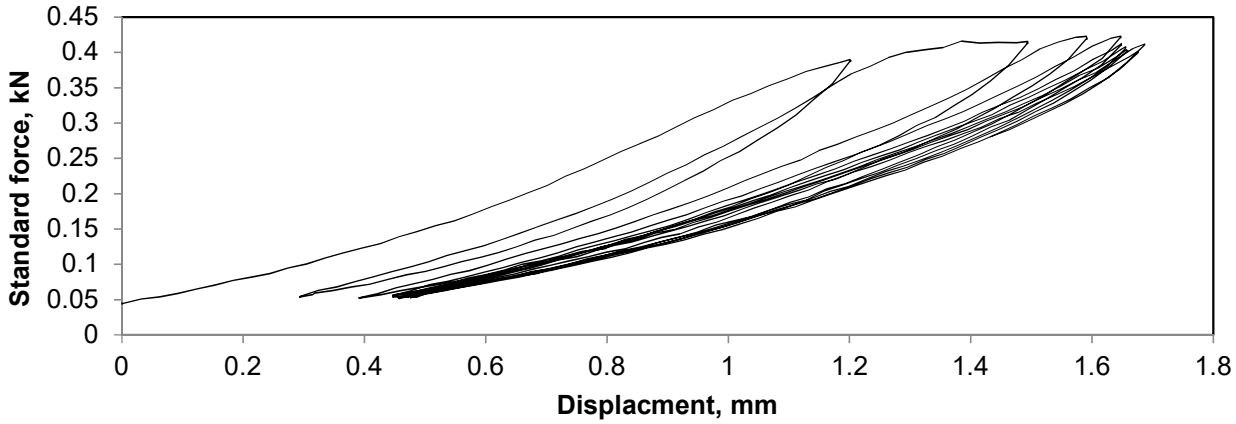

Graph 24 – Force Displacement curve developed in WST of brick 8 sample C.

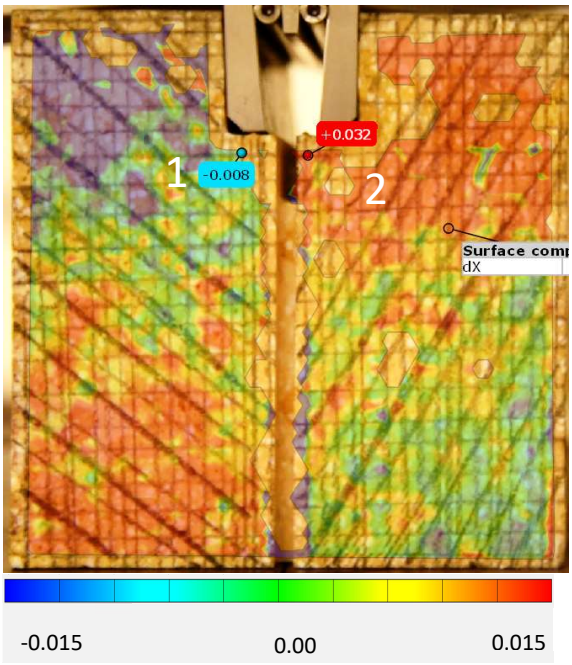

Figure 40 – Reference points used to calculate crack opening. Displacement field (xx) developed at 35 minutes of the beginning of the test.

It is possible to observe that crack opening is synchronized with the force registered during the cycles.

It is also interesting to notice that two different behaviours can be observed in Graph 24. In the first four cycles, it is possible to observe a significant damage accumulation which can be seen by the irreversible strains developed. However, in posterior cycles the irreversible strains stop increasing and damage stabilization is observed.

These two different behaviours are also clearly seen in Graph 23. In the first four cycles crack opening increases at every cycle. It is also observed that the crack opening at the lowest force is increasing which happens due the irreversible displacements. After this, crack opening continues to follow the force behaviour although no growth throughout the cycles is observed and no irreversible displacements are observed.

DIC is proven to be an interesting technique which allows to compare and study the mechanical behaviour found in the wedge splitting tests with the displacement fields developed during the test in the sample. The main limitation of this technique is the image capture device's battery life, which might be insufficient to enable filming tests that take several hours to fail.

The results obtained using DIC were in agreement with what was observed in the mechanical tests. Nevertheless, a study of the parameters used, and an improvement of the patterns selected should be further tested to allow a better accuracy of the measurements.

4.2 Thermal Cycle Tests

4.2.1 Damage Development

4.2.1.1 Extra Large Samples

The initial velocity measured for sample XL1 and XL2 is presented in Graph 25. It is interesting to see that the velocity throughout the different measured points has a similar tendency for both samples. This may indicate that the initial damage may be caused by the manufacturing process. It is also possible to observe that the ultra-sound velocity measured is lower for XL1 than for XL2, which implies a higher initial damage. This might be relevant to understand possible differences in the behaviour of the samples.

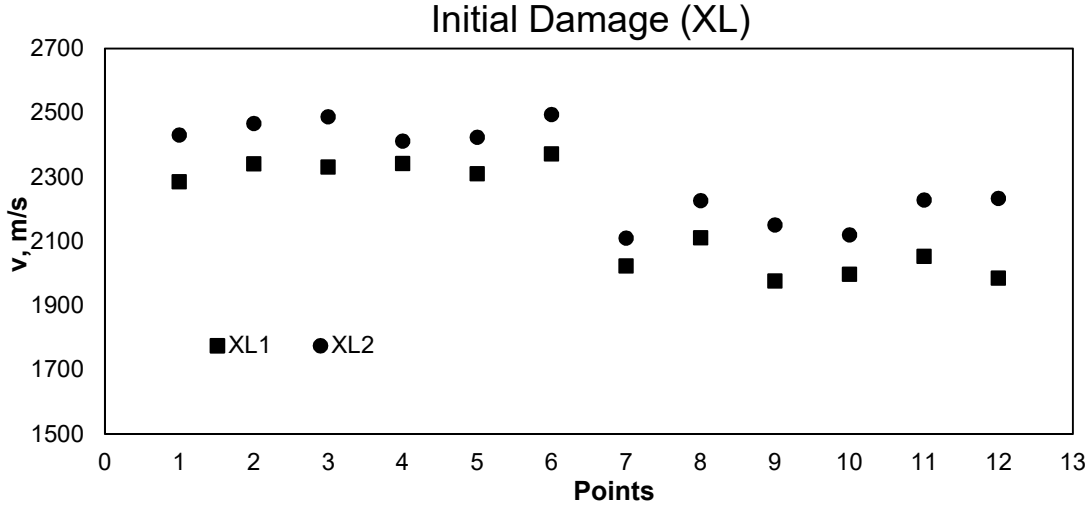

Graph 25 –Initial damage variation throughout the different points of sample XL1 and XL2.

In Graph 26 and Graph 27, it is possible to see the evolution of damage found for XL1 and XL2, in the longitudinal (L) direction. The different directions are explicated in Figure 17.

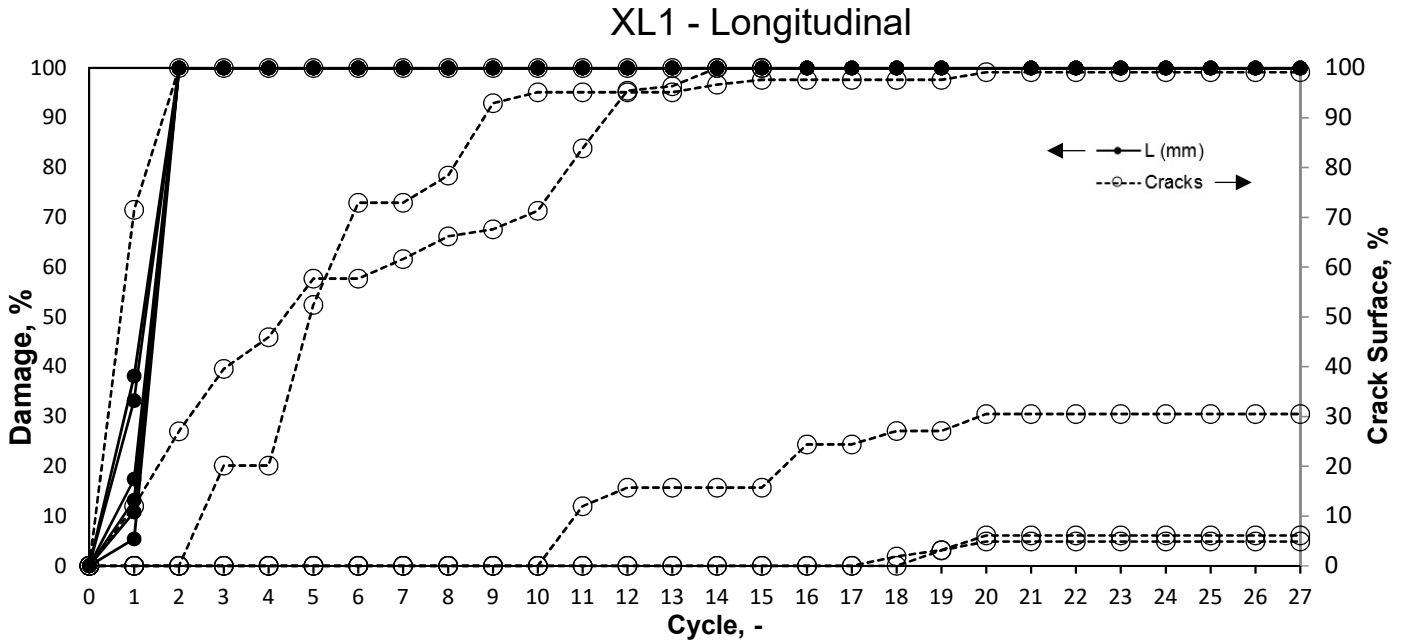

Graph 26 – Damage development in XL1 for the points in the longitudinal direction.

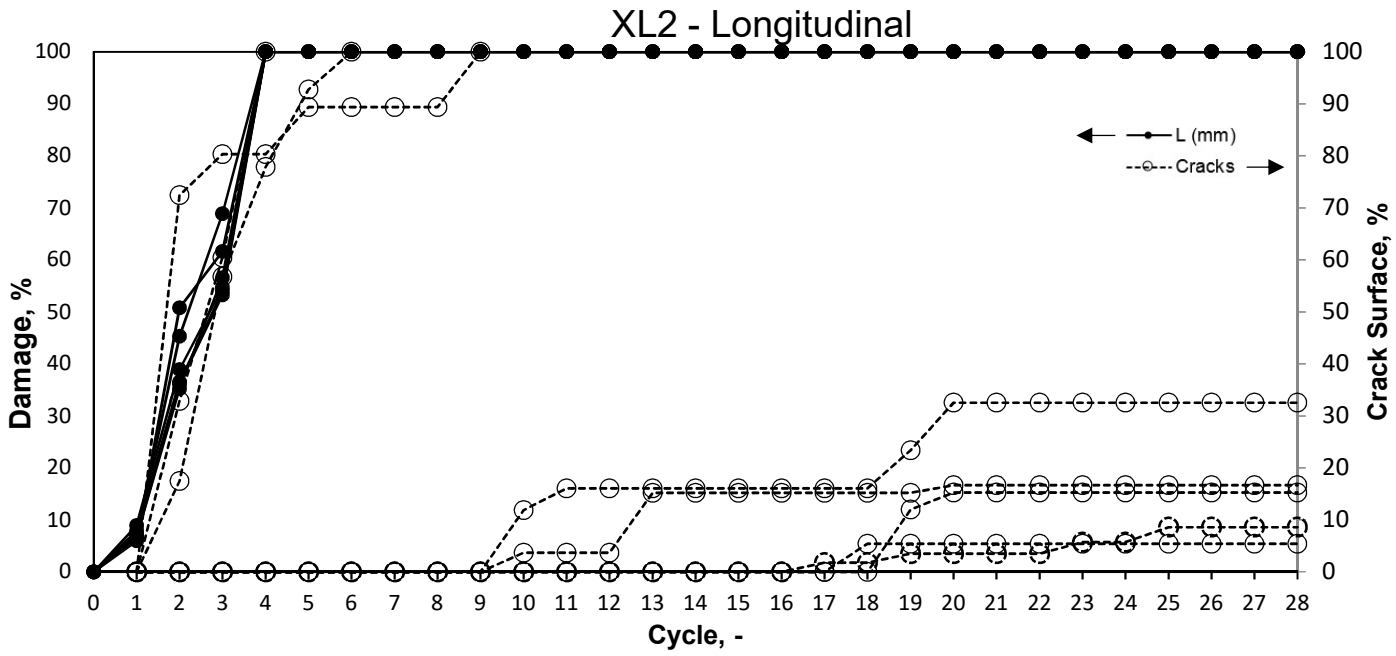

Graph 27 – Damage development in XL2 for the points in the longitudinal direction.

As it can be seen in both samples, the damage developed quickly and failure was achieved (sample fractured) in cycle 2 (XL1) and cycle 4 (XL2). The damage evolution found for both samples is similar to the exponential behaviour found in the wedge splitting test.

It is also possible to observe the development of the cracks formed in the ZY direction, which are the cracks that affect directly the longitudinal measurements. It is possible to see that the appearance of cracks has a direct impact on the damage development. This is easily seen in XL2 where the damage from cycle zero to one only developed 10 %, while from cycle one to two (appearance of first cracks) increased from 10% to approximately 45 %.

The difference of the number of cycles to failure between the samples can also be explained by crack development. As it can be seen, while in XL1 only one significant crack was developed until failure, in XL2 three cracks grew simultaneously and therefore more gradually. By having three cracks developing at the same time, there is less energy for each of them to grow since there will be interaction between the shielding zones of both cracks, which makes them grow more gradually, as it is illustrated in Figure 41. This effect is more significant for cracks of considerable size, since the shielding zone of a crack increases with its length [29]. This effect can also be seen in Graph 27, where it is possible to see a significant decrease in the rate of crack development when the three cracks were already considerably developed (> 70 %). The fact that only one crack was developed in XL1 can be possibly justified by the presence of an initial defect. An indication of this can also be the higher initial damage found for XL1.

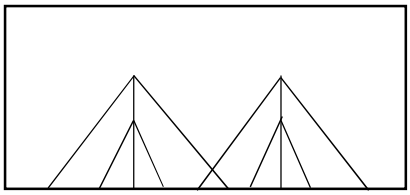

Figure 41 – Interaction of shielding zone for cracks developing at the same time.

In both samples is also possible to notice different waves of crack development. The size of the cracks and the velocity they develop decreases with the number of cycles the wave starts. For the second and third wave it is possible to see that cracks develop gradually and arrest. One explanation for this phenomenon can be the reduction in size of the samples after complete

fracture. The influence of the size of the samples as well as the crack arrest mechanisms will be explored with more detail in the following document sections.

In Graph 28 and Graph 29, it is possible to see the damage development for the measured points in the transversal direction (W) for XL1 and XL2, respectively.

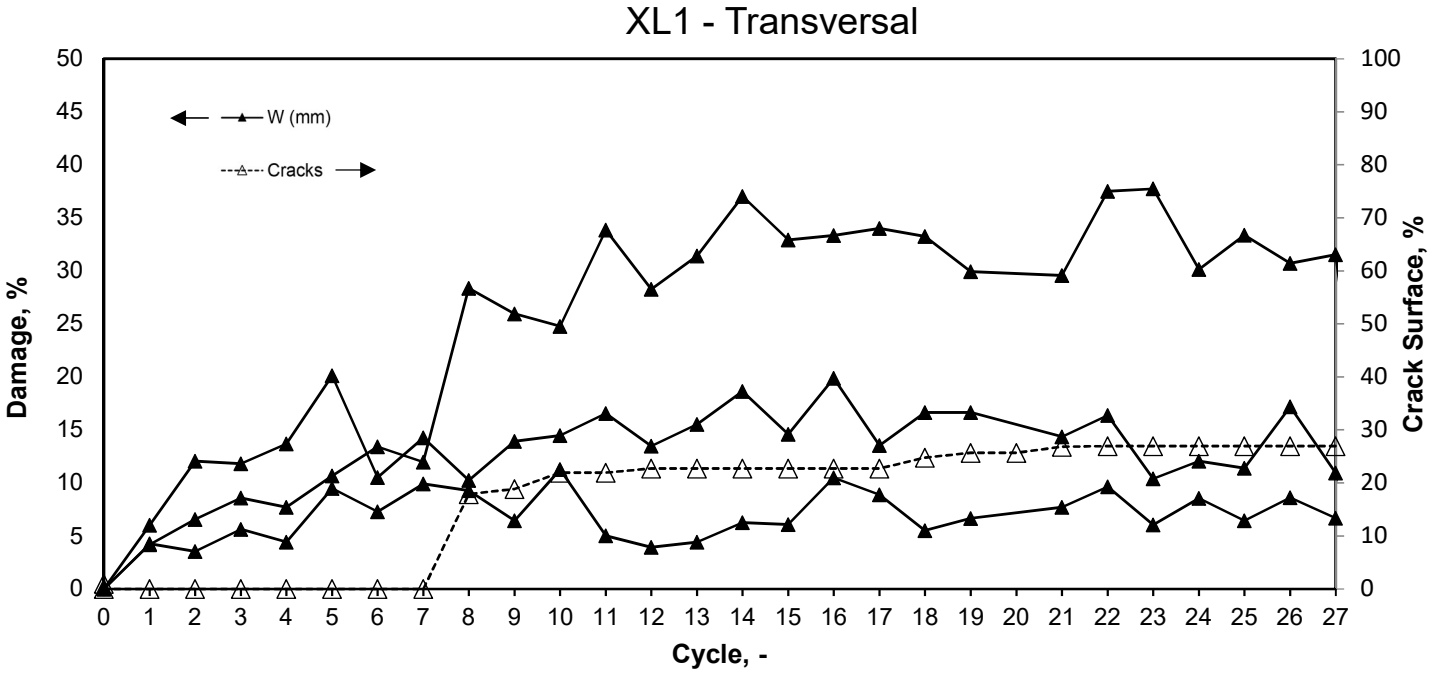

Graph 28 – Damage development in XL1 for the points in the transversal direction.

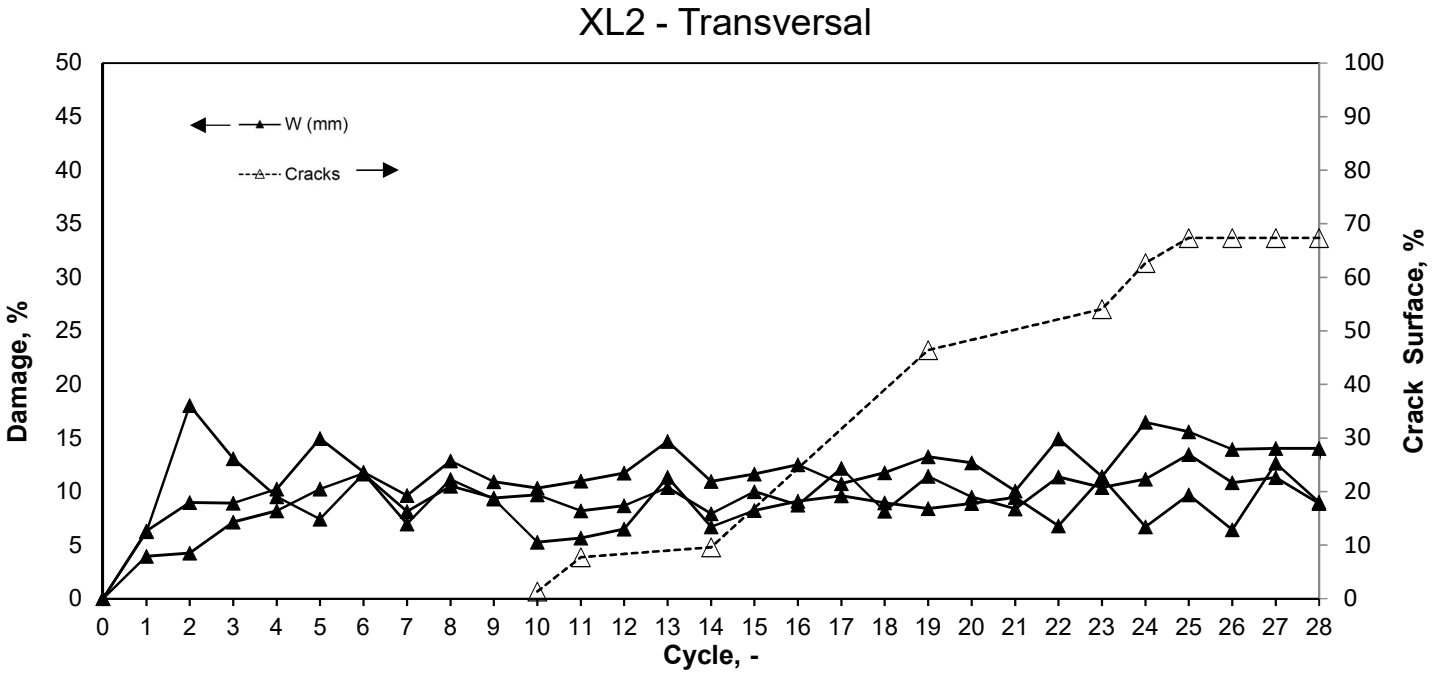

Graph 29 – Damage development in XL2 for the points in the transversal direction.

On the contrary to what was observed for the longitudinal direction, the damage development in the transversal direction was gradual. This can be justified by cracks tendentially form in ZY direction. However, when the first cracks in ZX direction appear, an increase in the damage can be noticed. This is clear in XL1, in cycle 7, when the first crack appears, one of the measured points (the one closer to the crack) has a significant increase in the damage. Cracks in ZY

direction start developing early in XL1 which might have occurred because of the higher initial damage found for this sample.

In Graph 30 and Graph 31, it is possible to see the damage development for the measured points in the normal (N) direction for XL1 and XL2 respectively

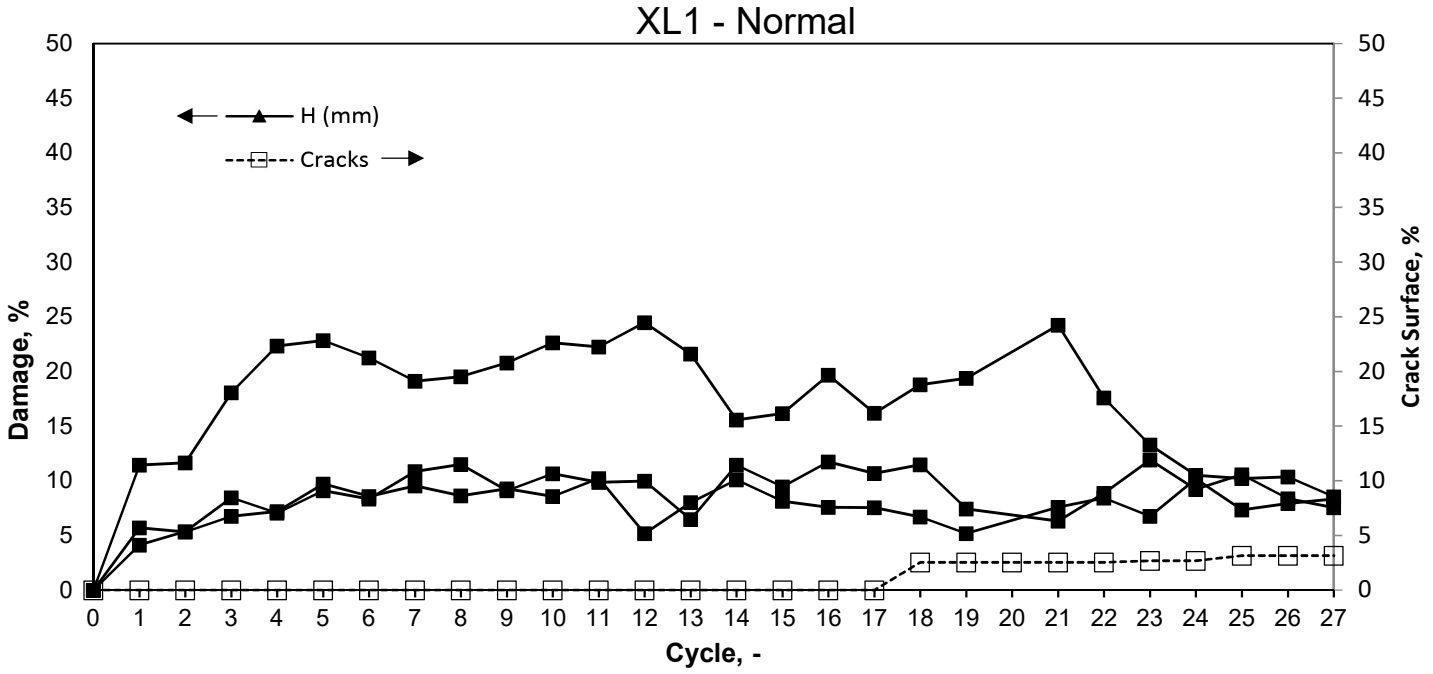

Graph 30 – Damage development in XL1 for the points in the normal direction.

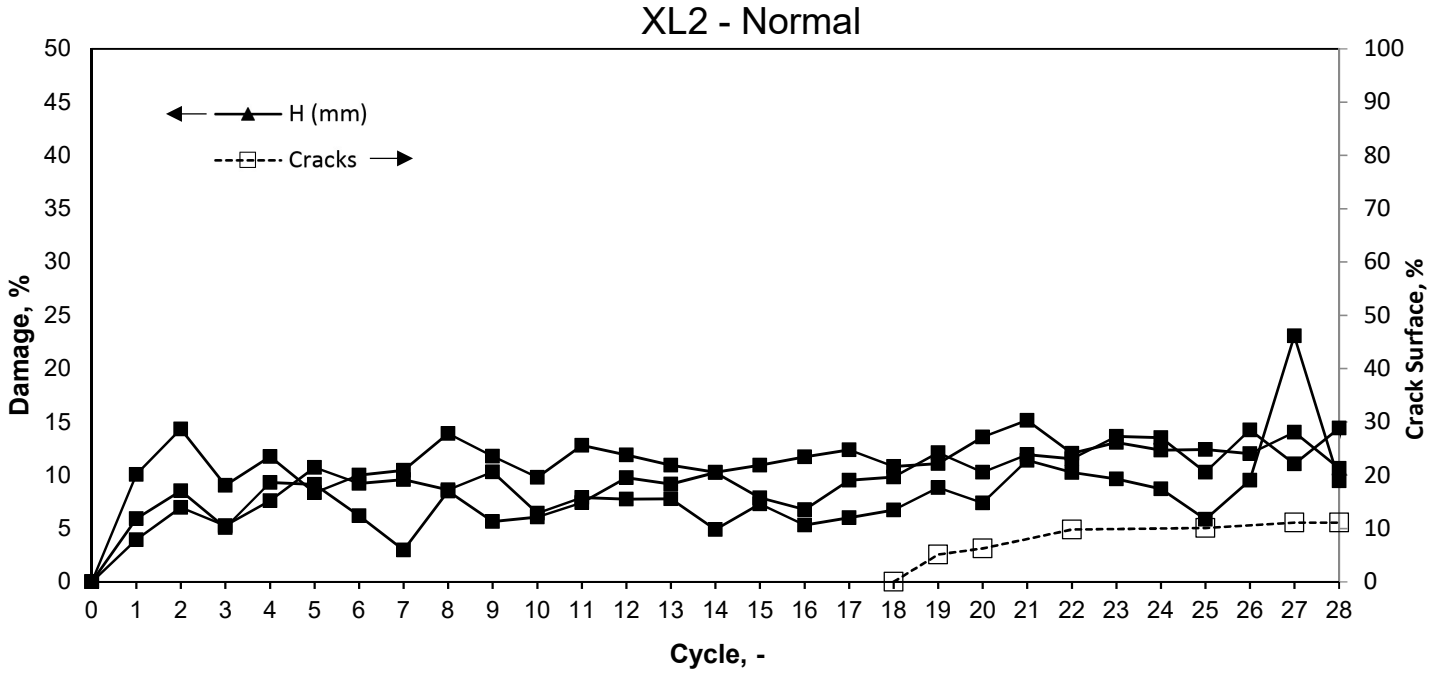

Graph 31 – Damage development in XL2 for the points in the normal direction.

The damage development in the normal direction is similar to the evolution found in the transversal direction. Once again cracks do not tend to form in XY direction. In fact, these cracks only appear after 17/18 cycles and only developed until 5 to 10 %.

4.2.1.2 *Large Samples*

The initial velocity of sound for all the points measured for both L samples is presented in Graph 32. It is possible to observe that L1 has considerably higher initial damage (lower velocity) which might affect the results obtained.

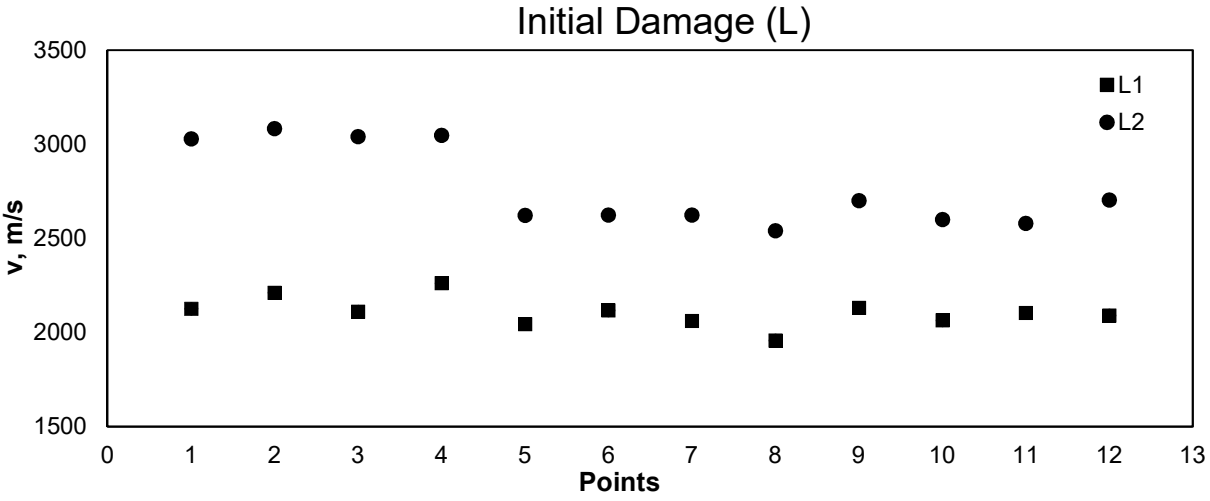

Graph 32 – Initial damage variation throughout the different points of sample L1 and L2.

The development of damage in the longitudinal direction for both L samples, L1 and L2, can be seen in Graph 33 and Graph 34, respectively.

The damage development found for the large samples is significantly more gradual than the behaviour found in the samples of bigger dimensions (XL1 and XL2). This behaviour is similar do the sigmoidal behaviour found in some samples of the wedge splitting test, where three different regions are possible to observe: in the first region there is a fast increase in the damage and the first cracks appear and grow, the second stage the rate of the damage accumulation decreases significantly and cracks stabilize, and the third stage where cracks started growing again and damage develops rapidly until failure. The last phase of the sigmoidal behaviour is not observed for L1. One justification for this could be the higher initial damage of L2. Nevertheless, this phase would probably happen if a higher number of cycles were carried out.

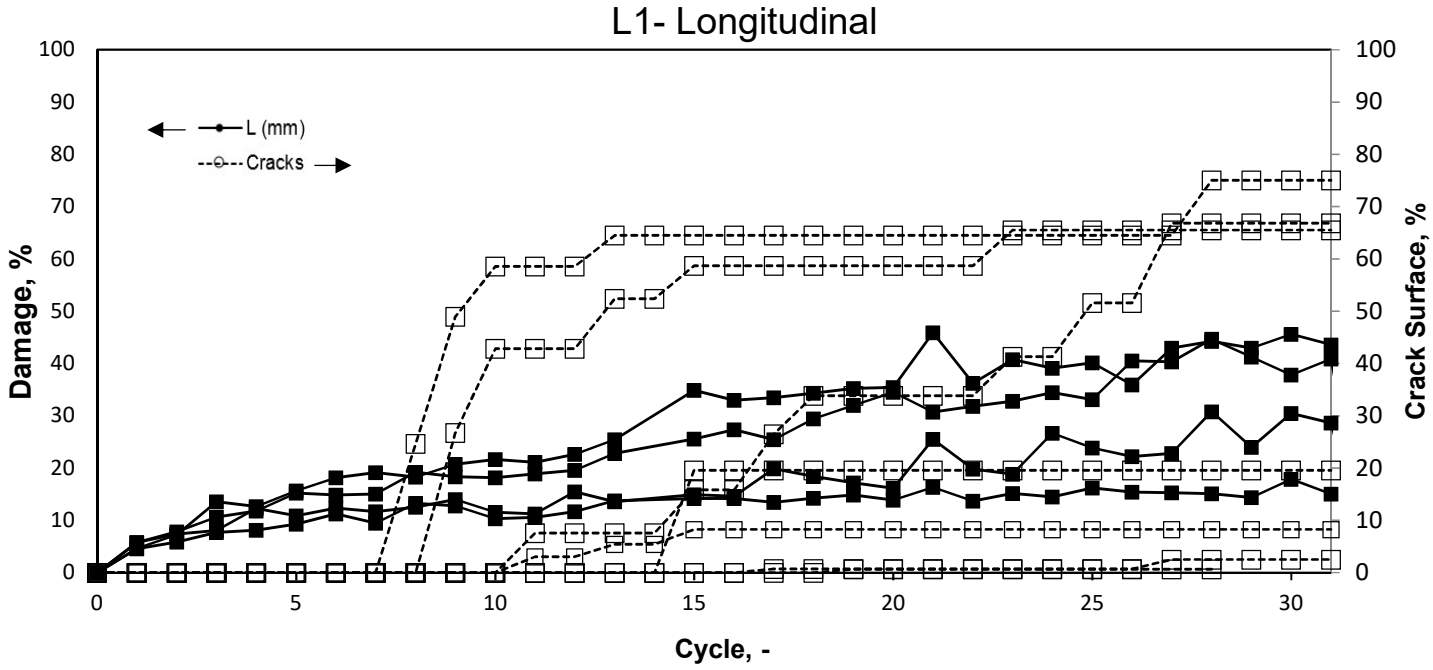

Graph 33 – Damage development in L1 for the points in the longitudinal direction.

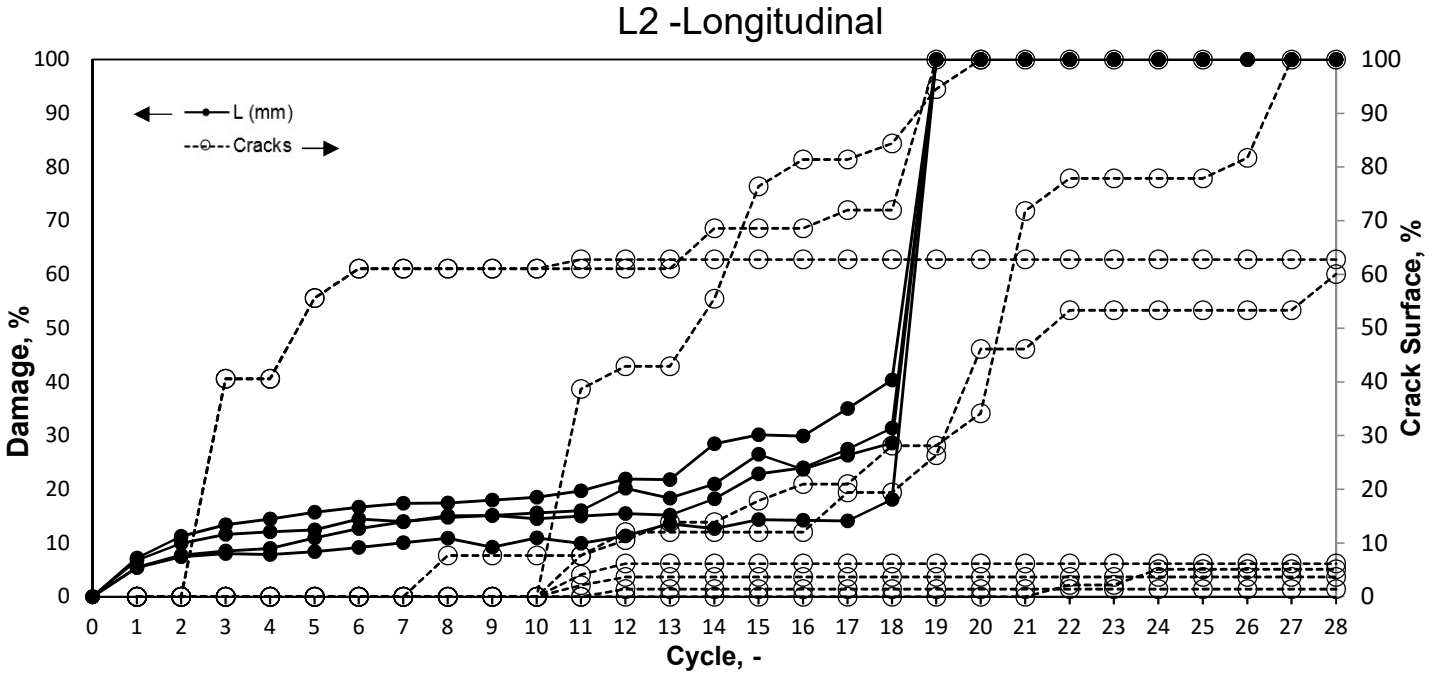

Graph 34 – Damage development in L2 for the points in the longitudinal direction.

Comparing the crack development with the one found for XL samples, it is possible to observe that in L samples cracks develop later, more gradually, and in some cases stop growing (crack arrest), which resembles the crack development seen in the second and third waves in the XL samples. It is therefore possible to see that the size of the sample is highly influential on the damage formation and propagation.

In Graph 35 and Graph 36 it is possible to see the damage development for the measured points in the transverse direction for L1 and L2, respectively

Once again, it is possible to see that the damage is less significant in the transverse direction, and that cracks formed in this direction developed at later stages. In sample L2 it is possible to see the development of a crack affecting considerably the damage in the point near this crack.

In Graph 37 and Graph 38 it is possible to see the damage development for the measured points in the normal direction for L1 and L2, respectively.

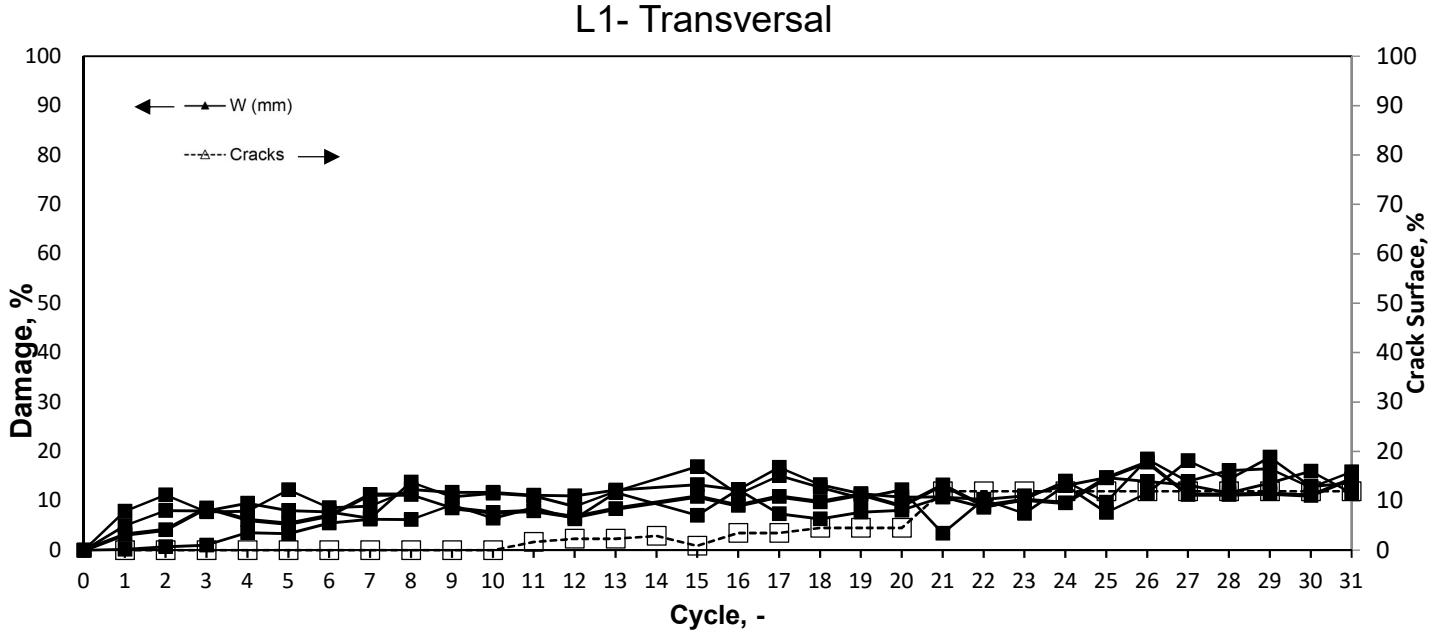

Graph 35 – Damage development in L1 for the points in the transversal direction.

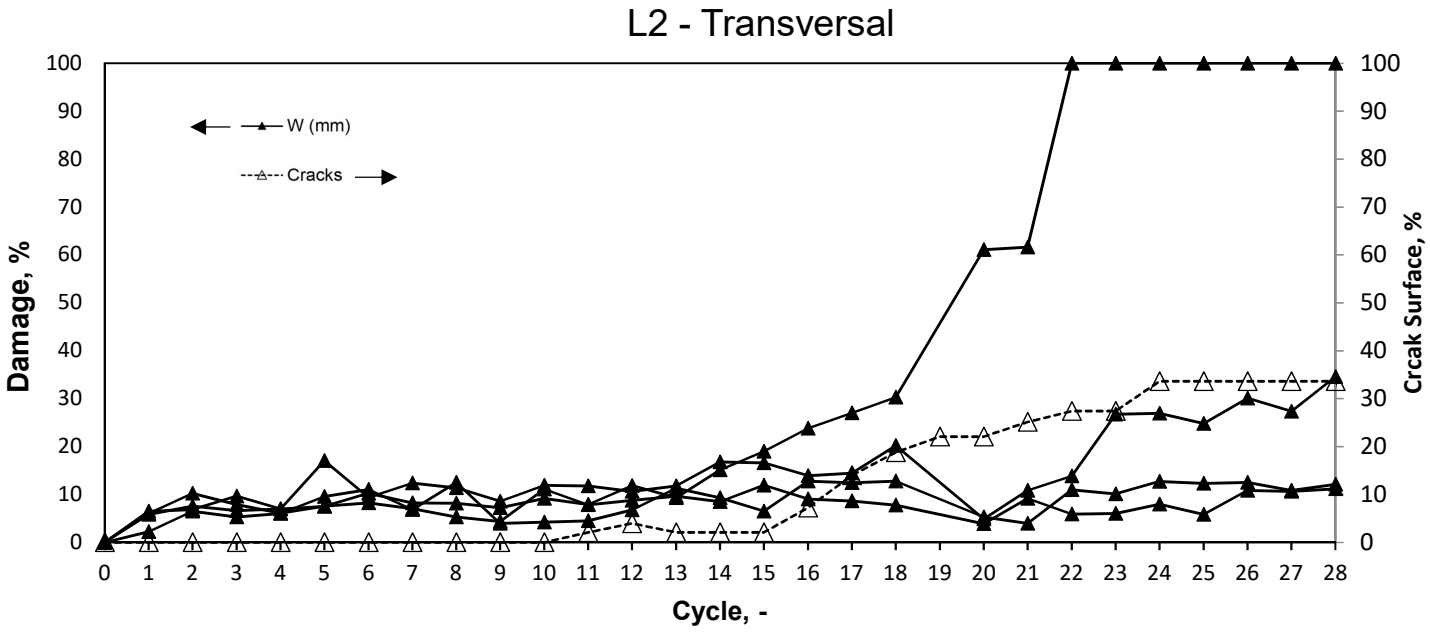

Graph 36 – Damage development in L2 for the points in the transversal direction.

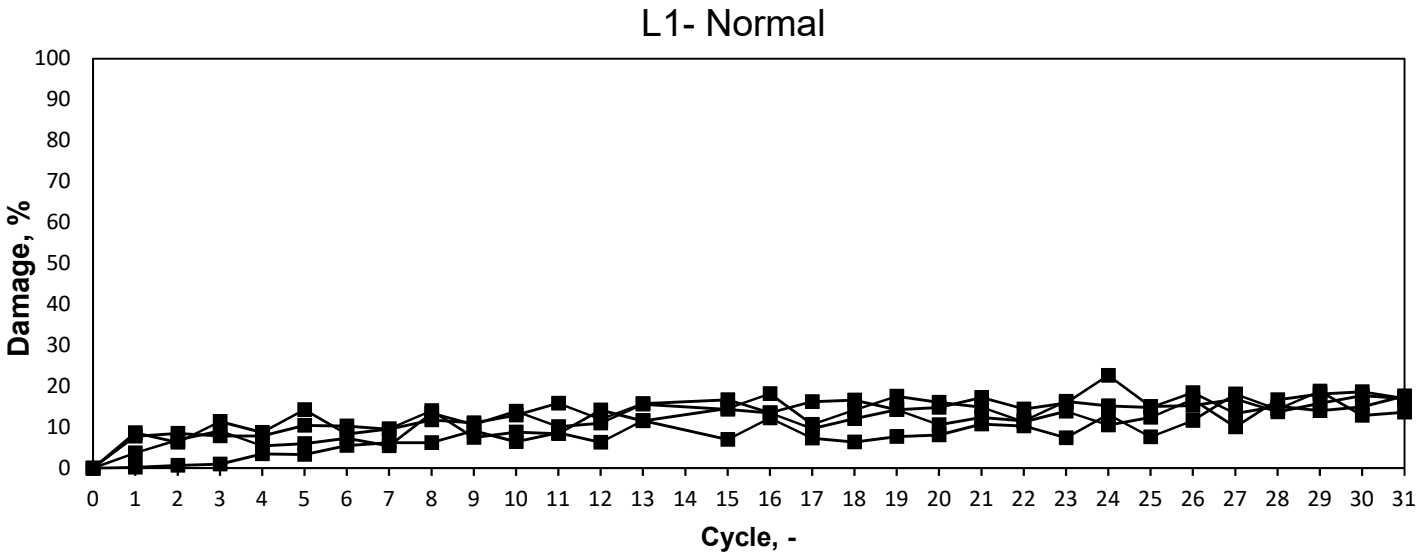

Graph 37 – Damage development in L1 for the points in the normal direction.

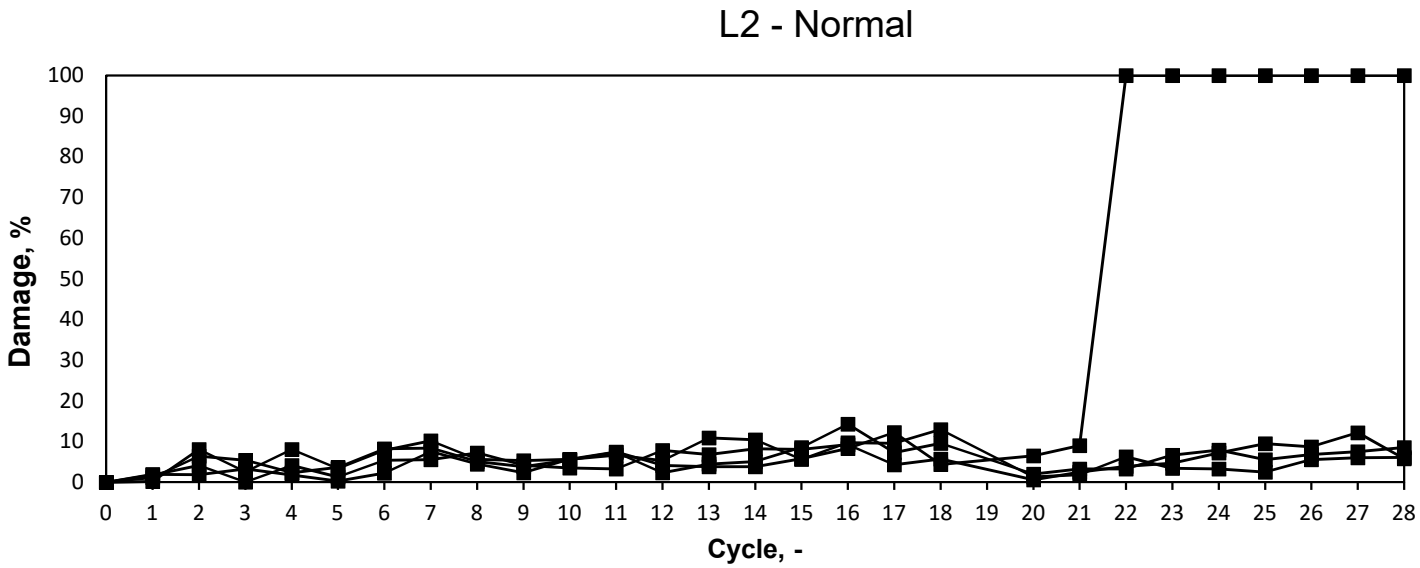

Graph 38 – Damage development in L2 for the points in the normal direction.

Both transversal and normal directions behave similarly. No crack was formed in the normal direction. However, it is possible to see that, when crack opened in the transversal direction, the points closer to the crack were also affected by this direction.

4.2.1.3 Medium Samples

In Graph 39 and Graph 40 it is possible to observe the damage development in the longitudinal direction for the medium samples. As it can be seen, for both samples the number of cycles tested is considerably smaller than the number of cycles carried out for the other sample sizes. This happened because this size was added at later stages of the tests and, therefore, the analysis presented is limited.

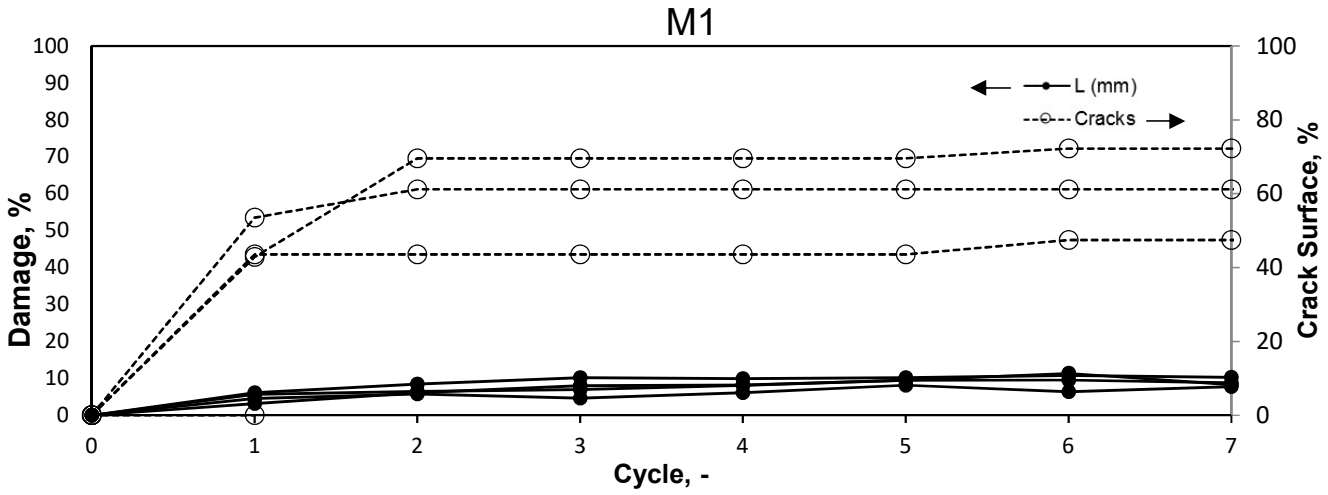

Graph 39 – Damage development in M1 for the points in the longitudinal direction.

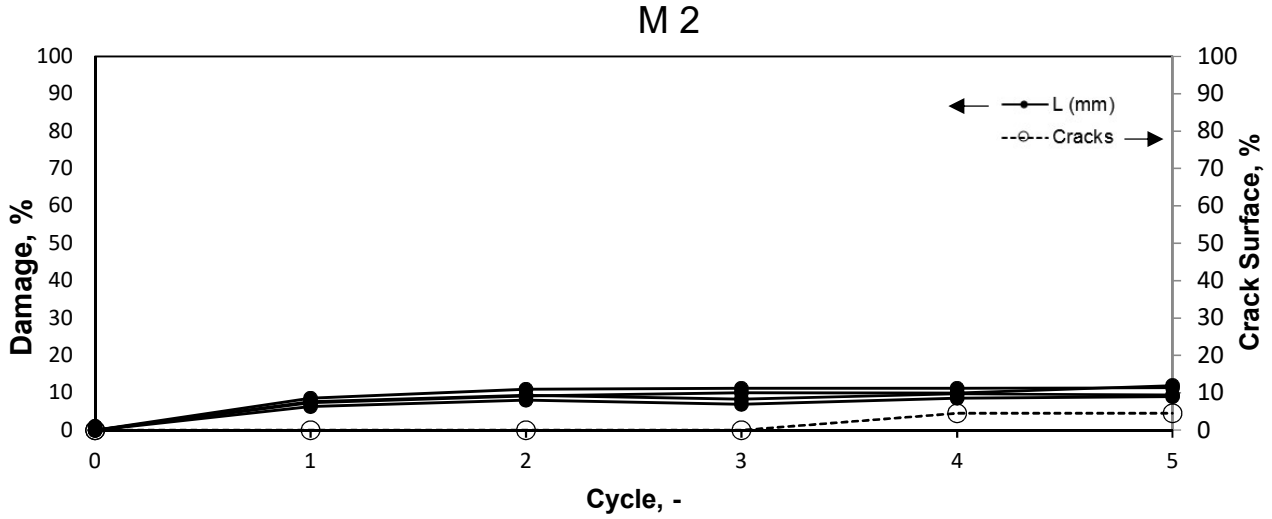

Graph 40 – Damage development in M2 for the points in the longitudinal direction.

Despite the development of three cracks in sample M1 at the first cycle, the damage development in both samples was gradual and seems to start stabilizing. For this analysis, it is crucial that a higher number of cycles are carried out. The presence of this cracks in M1 might be justified by the presence of defects in the sample due to pressing. These defects were observed before beginning the cyclic tests and are illustrated in Figure 42

.

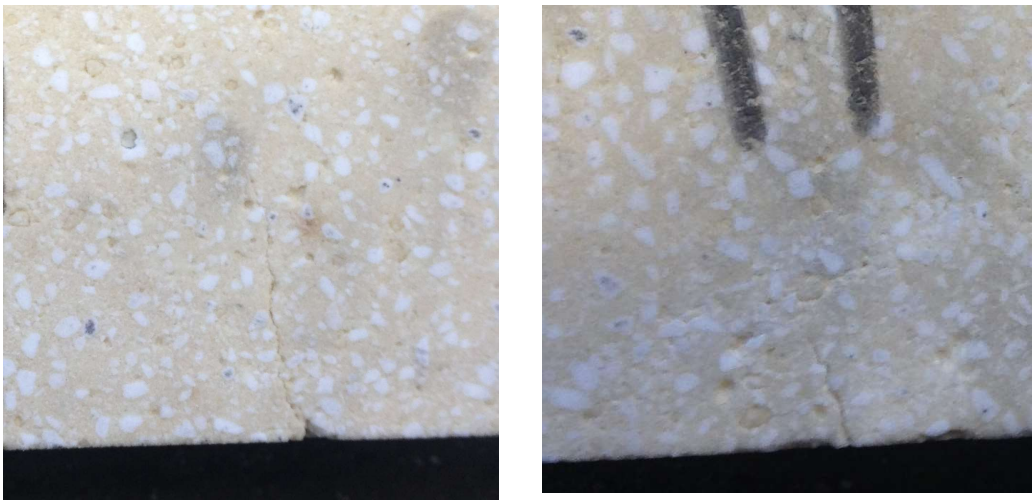

Figure 42 – Manufacturing defects observed in M1 before cyclic thermal shock tests.

Even though three cracks developed, these rapidly stabilized. It is also possible to observe that the damage developed in these samples is generally inferior to the one developed at the same cycles in the L samples.

Although the damage developed in the other directions was also measured, the number of cycles was low, and no crack formed in the other directions. Because of this fact, it was considered that would be too repetitive to present these results.

4.2.1.4 Small and Extra Small Samples

In Graph 41 the damage development throughout the cycles is plotted for all of the samples of smaller dimensions (S, XS).

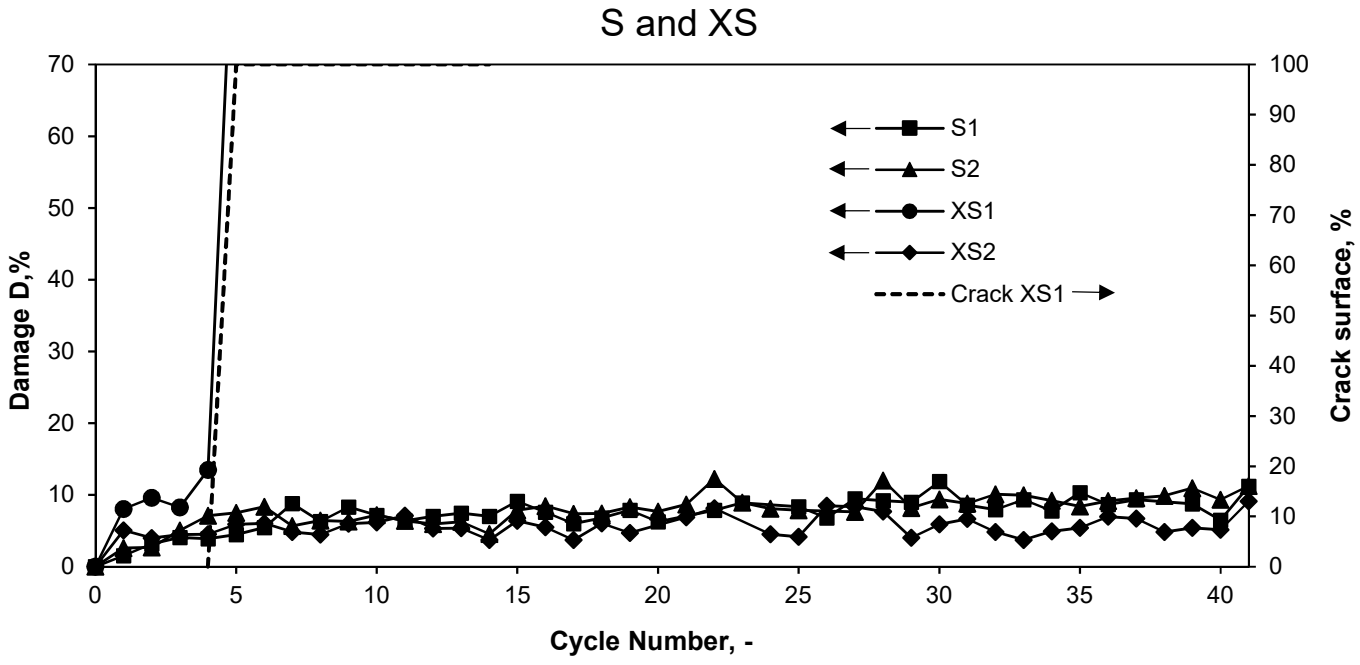

Graph 41 – Damage development in samples of smaller dimensions for the points in longitudinal direction.

All samples of smaller dimensions, with exception of XS1, had a similar behaviour. No cracks were developed throughout the cycles and the damage saturation was observed after approximately six cycles. In sample XS1 the behaviour was quite different and presented three different phases. Firstly, a significant increase in the damage (cycle 0 to cycle 1), then a stabilization (cycle 1 to 3) and finally an abrupt increase in the damage until failure (cycle 3 to

5). This behaviour is similar to the one found for some samples in the wedge splitting tests, sigmoidal behaviour and might be justified by an initial defect.

By comparing the damage in the longitudinal direction (which was already established as the most significant direction for the present analysis), it is possible to conclude that the size of the sample is a detrimental factor on how the damage develops, since the damage increases significantly with the increase in the size of the sample.

Firstly, large samples have a higher probability of having a bigger initial defect and, therefore, a decreasing resistance is expected with the increase in volume of the sample. This concept is used in the Weibull model [10].

Furthermore, since smaller samples will cool faster, the thermal gradient inside the small samples will be lower and, therefore, the stress generated will also be lower [1, 24].

The different behaviours found for the damage development in thermal shock were similar to the ones found in the wedge splitting test. For XL samples, an exponential behaviour was observed. In L samples and in one XL samples a behaviour similar to a sigmoid was observed (three distinct phases). For the XL and L, since the third phase of the sigmoidal behaviour was not observed, it remains to be determined if the damage saturated or if a higher number of cycles would lead to failure. For M samples the number of cycles was reduced and therefore it was not possible to verify how the damage would have developed.

4.2.1.5 T. Fleck Analysis

To validate the results found in the thermal shock tests, the algorithm developed by Lu and Fleck (1998)[1] was used. To implement it, two characteristic lengths were calculated using equation 4.3 and 4.4, which represent the theoretical and the effective characteristic length, respectively. Although the theoretical characteristic length is the general formula used in heat transfer, this parameter is highly subjective, and it was considered that half of the height could better represent the scale of the problem, since heat transfer will occur mainly in vertical direction.

$$Leff = b/2 \tag{4.3}$$

$$Lth = V/A \tag{4.4}$$

where:

$Leff$, is the effective characteristic length
Lth, is the theoretical characteristic length
V, is the volume
A, is the area
b, is the height

The characteristic length as well as the Biot number for all of the different sizes of samples used in the thermal shock tests is represented in Table 8 (considering theoretical characteristic length) and Table 9 (considering effective characteristic length).

Table 8 – Theoretical characteristic length (Lc), Biot (Bi) and the inverse of Biot (1/Bi) for all the samples.

	XL	**L**	**M**	**S**	**XS**
Lth (m)	0.024	0.018	0.014	0.0089	0.0051
Biot	0.322	0.244	1.192	0.116	0.058
1/Biot	3.10	4.098	5.215	8.65	14.706

Table 9 – Effective characteristic length (Leff), Biot (Bi) and the inverse of Biot (1/Bi) for all the samples.

	XL	L	M	S	XS
Leff (m)	0.060	0.041	0.033	0.02	0.0125
Biot	0.800	0.547	0.433	0.267	0.167
1/Biot	1.250	1.829	2.371	3.750	6.000

Since the size of the initial defects is unknown, two different situations, depending on this parameter, were considered. Equation 4.5 represent the dimensionless maximum stress achieved when considering random distribution of flaws. In Equation 4.6 is represented the dimensionless maximum stress intensity factor when considering a large pre-existing flaw (flaw with the same scale length as the thickness). Both equations are for the case of cold shock.

$$\sigma^* = \left\{1.5 + \frac{3.25}{Bi} - 0.5e^{-\frac{16}{Bi}}\right\}^{-1} \tag{4.5}$$

$$K^* = 0.222\left(1 + \frac{2.12}{Bi}\right)^{-1} \tag{4.6}$$

where:

σ^*, is the normalized maximum stress
K^*, is the normalized maximum stress intensity factor
Bi, is the biot

For the case of hot shock, the applicable equations based on Lu and Fleck (1998) are represented in eq 4.7 and eq 4.8.

$$\sigma^* = \frac{0.3085}{1+(\frac{2}{Bi})} \tag{4.7}$$

$$K^* = 0.177\left(1 + \frac{2.12}{Bi}\right)^{-1} \tag{4.8}$$

Graph 42 shows the dimensionless maximum stress as a function of the inverse of Biot for both hot and cold shock. Using the calculated Biot for the samples, it is possible to estimate the maximum stress for each of the samples. Once again, it is possible to see the dependence of the stress generated with the geometry of the sample. With the increase of the Biot number, there is an increase in the magnitude of the stress which is more significant for higher values of Biot.

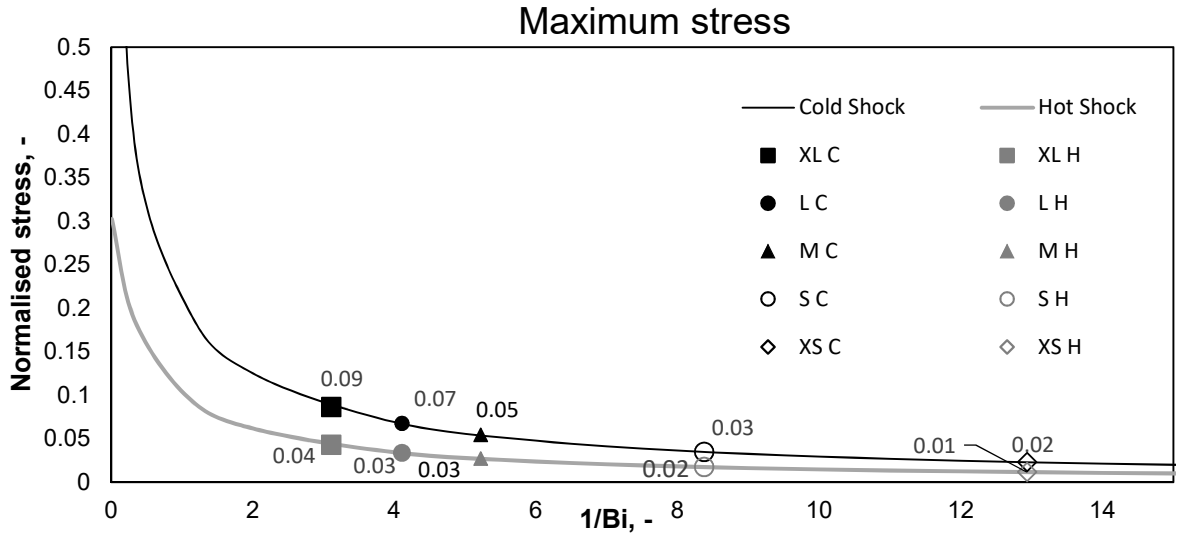

Graph 42 – Evolution of the dimensionless maximum stress with the inverse of the Biot and location of the samples analysed in this function.

This can explain why small samples (even with different biot numbers) had a similar behaviour, since within this range the function is almost constant. It is also possible to see that the stress achieved in cold shock is always superior to the hot shock situation.

In Graph 43, it is also possible to see the dimensionless stress intensity factor plotted against the inverse of the Biot for both cold and hot shock. A similar trend to the one found for the maximal stress can be observed. However, when comparing the values, it is possible to see that the magnitude for all of the samples in analysis is lower for the case of considering the stress intensity factor criteria.

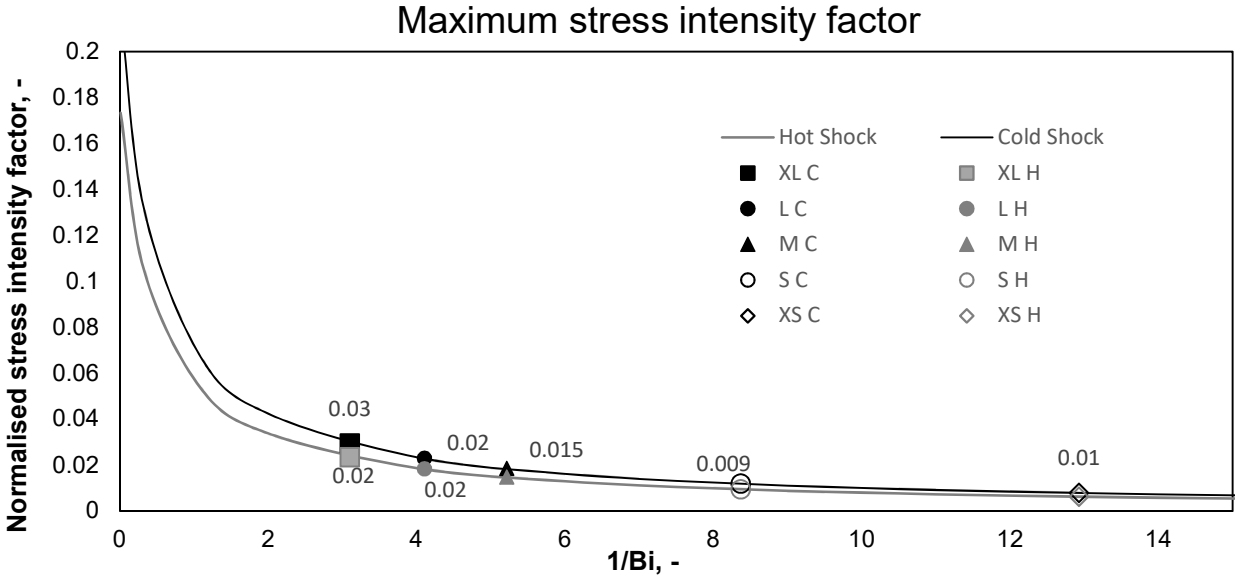

Graph 43 – Evolution of the dimensionless maximum stress with the inverse of the Biot. Size of the samples analysed displayed.

The dimensionless time to achieve the maximum stress/stress intensity factor in cold shock can also be obtained from eq 4.9 and 4.10 respectively

$$t_\sigma^* = 0.08 + \frac{0.4}{1+1.4Bi} \tag{4.9}$$

$$t_k^* = \frac{0.48}{1+1.8Bi} \tag{4.10}$$

where:

t_σ^*, is the dimensionless time of occurrence of σ^*
t_k^*, is the dimensionless time of occurrence of K^*

The same analysis can be conducted for hot shock. Eq 4.11 and eq 4.12 represent the dimensionless time for maximum stress and for maximum stress intensity factor, respectively.

$$t_\sigma^* = 0.115 + \frac{0.45}{1+2.25Bi} \tag{4.11}$$

$$t_k^* = \frac{0.48}{1+1.8Bi} \tag{4.12}$$

The dimensionless time to achieve maximum stress/stress intensity factor is plotted against the inverse of Biot in Graph 44 and Graph 45, respectively. It is possible to observe that, for the stress intensity factor criteria, the normalized time to achieve maximum stress is higher than the one found for the tensile stress criteria. The normalized time of occurrence of maximum stress, in both cases, is higher for samples with lower Biot. Additionally, when considering the

stress intensity factor criteria, the time to achieve maximum stress sintensity factor is the same considering hot or cold shock.

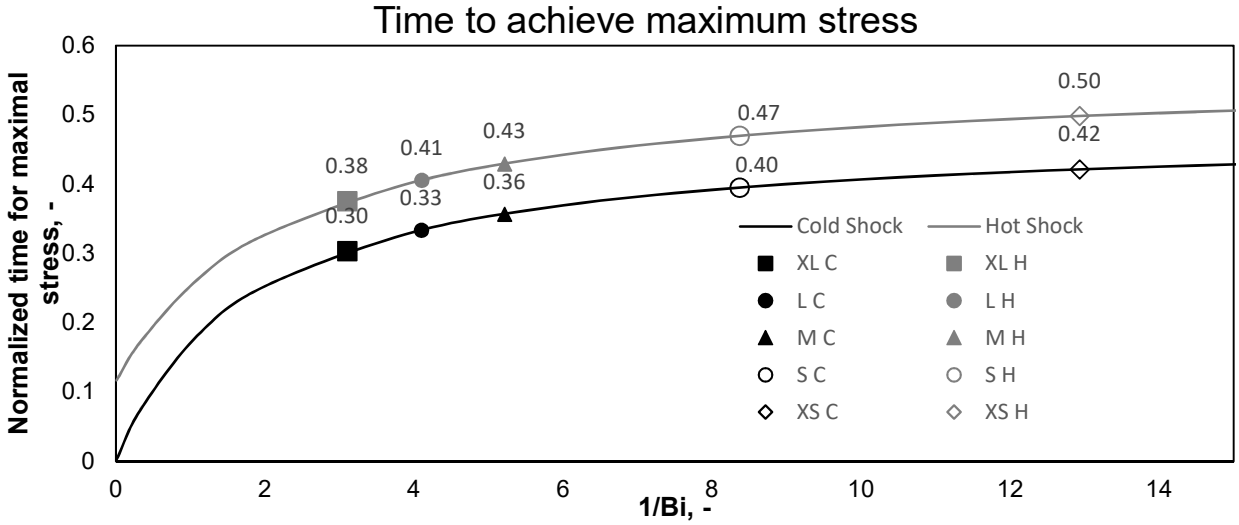

Graph 44 – Evolution of the dimensionless time to achieve maximum stress with the inverse of the Biot and location of the samples analysed in this function.

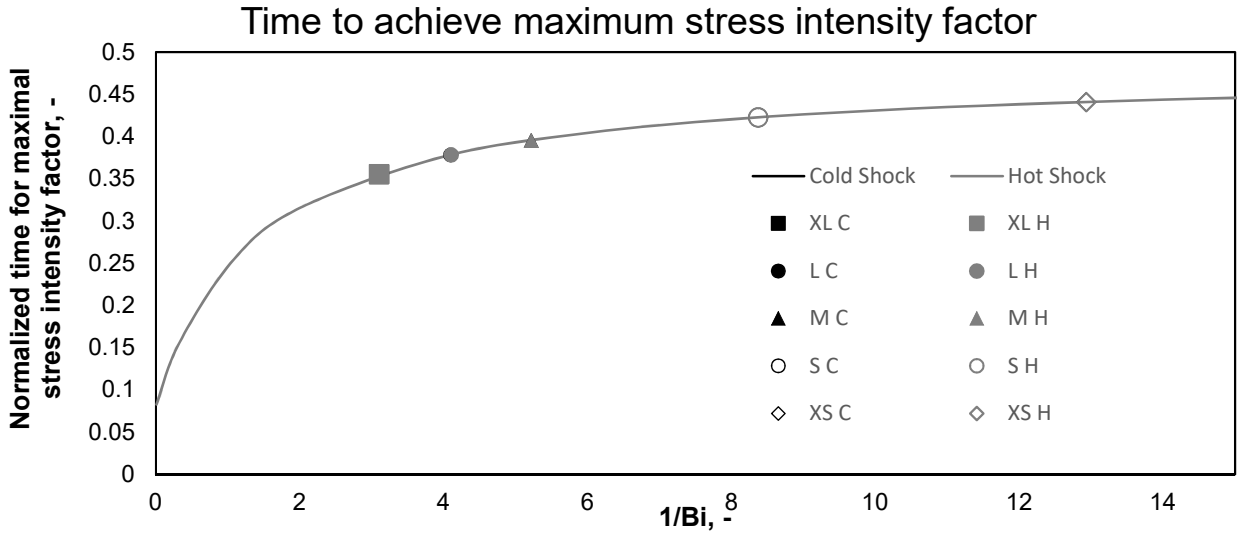

Graph 45 – Evolution of the dimensionless time to achieve maximum stress intensity factor with the inverse of the Biot and location of the samples analysed in this function for hot and cold shock (coincidence curve).

In order to be able to compare the theoretical approach presented with the results found in the thermal shock tests, the real stress and the real stress intensity factor were calculated based on eq 4.13 and 4.14 respectively. The strain correspondent to the maximum stress was calculated instead of the real maximum stress, since the strain to failure (STF) is a known parameter of the material in analysis.

$$\sigma_m = \sigma^* E \alpha \Delta T \ <=> \ \varepsilon = \sigma^* \alpha \Delta T \tag{4.13}$$

$$K_m = K^* E \alpha \Delta T \sqrt{\pi * Lc} \tag{4.14}$$

where:

σ_m, is maximum strain
K_m, is the maximum stress intensity factor
ε, is the real strain
α, is the linear coefficient of thermal expansion

The real strain, considering different characteristics length, is presented for the different sizes of samples used in cold and hot shock in Graph 46, where the strain to failure (STF) of the material is also plotted. It is possible to see that the characteristic length chosen highly influences the results obtained. When considering the theoretical characteristic length, no samples are expected to fail, while on the contrary, when considering the effective characteristic length both samples XL1 and XL2 are above the strain to failure of the material. Furthermore, when comparing with the results from the thermal shock tests, where both samples XL1 and XL2 fractured in the initial cycles, it is possible to conclude that using the effective characteristic length allows a more realistic approach to the problem.

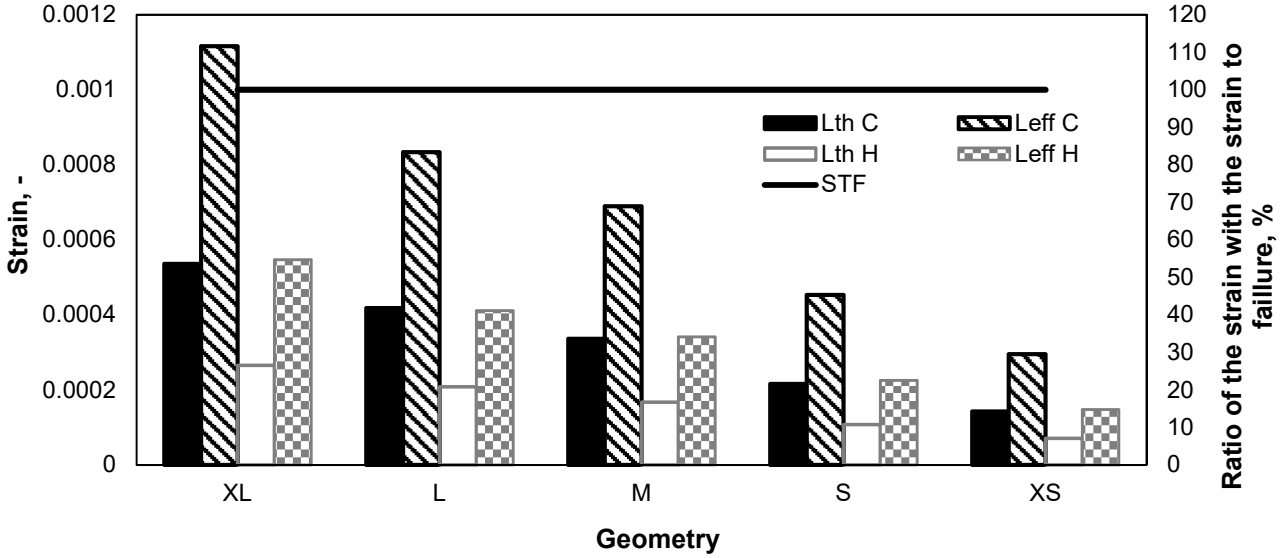

Graph 46 – Real strain calculated with theoretic characteristic length (Lth) and effective characteristic length (Leff) for the different samples.

The same analysis was conducted for the stress intensity factor criteria. As can be seen in Graph 47, independently of the characteristic length considered, no sample surpasses the fracture toughness of the material. As expected, the higher values were achieved for the larger samples, although they did not surpass 60 % of the fracture toughness of the material. Since the samples of larger dimension fractured, it's unlikely that they were governed by this criterion.

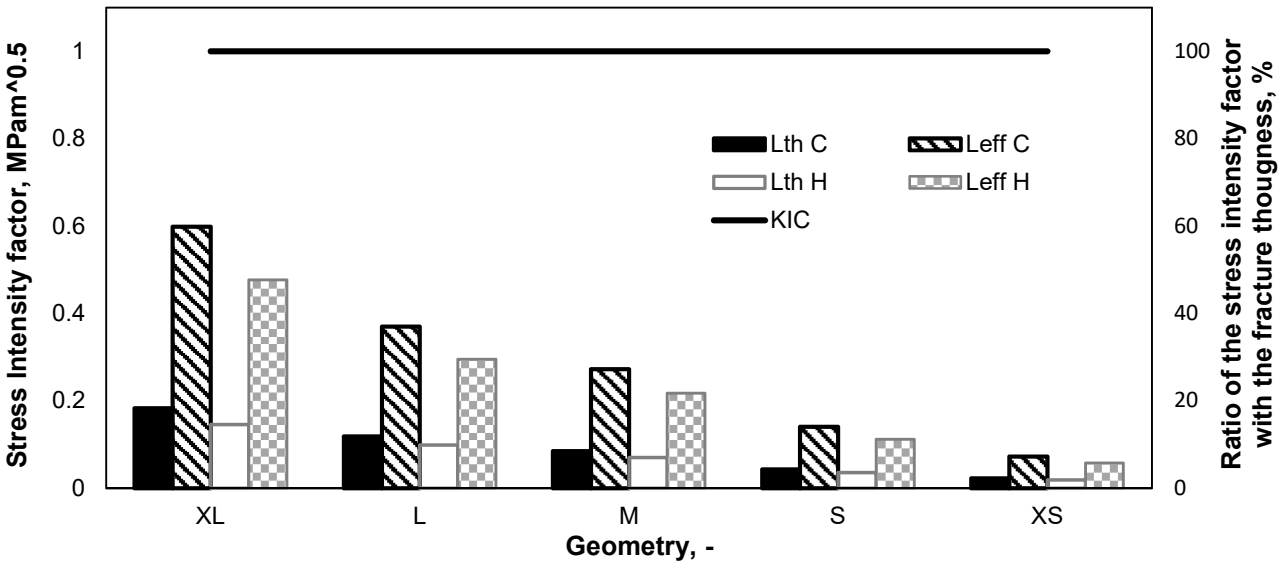

Graph 47 – Real stress intensity factor calculated with theoretic characteristic length (Lth) and effective characteristic length (Leff) for the different samples.

The real time can also be calculated for both cases using equations 4.15 and 4.16

$$t = \alpha t_{\sigma}^{*}/Lc \tag{4.15}$$

$$t = \alpha t_{k}^{*}/Lc \tag{4.16}$$

In Graph 48 and Graph 49, it is possible to observe the real time to achieve maximum stress and stress intensity factor respectively for all of the samples using both characteristic lengths. As opposed to what was found in the evolution of the dimensionless time, the real time increases with the size of the sample for both criteria and characteristic lengths. The time to achieve maximum stress in the samples of bigger dimensions is approximately 18 minutes (considering the effective characteristic length) while in small samples is approximately 2 minutes.

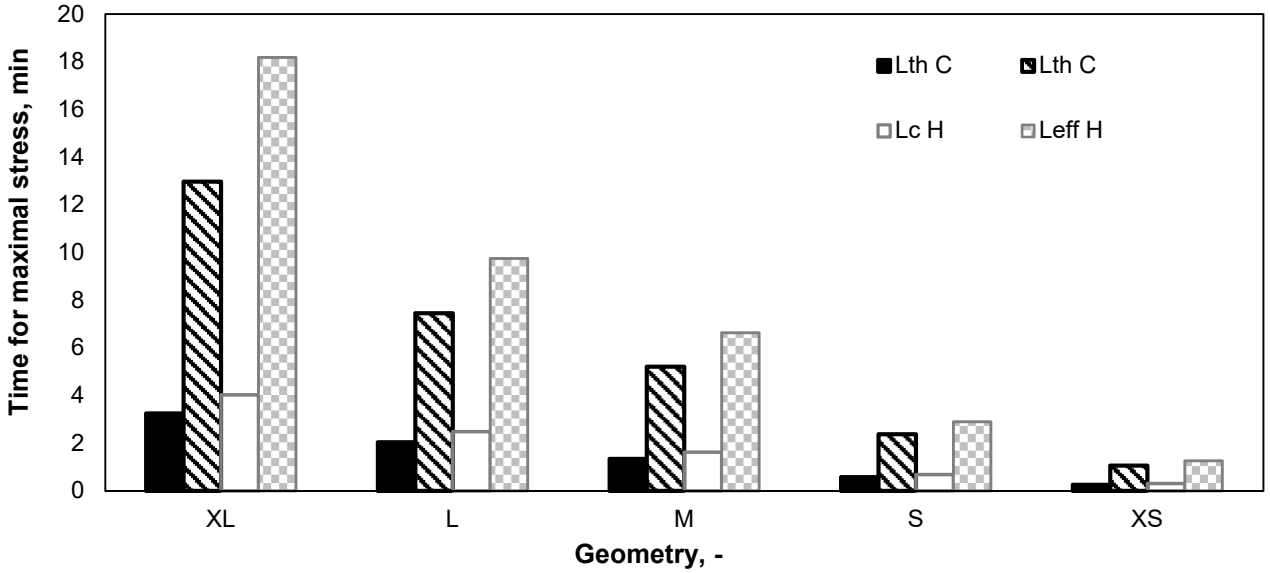

Graph 48 – Real time to achieve maximum stress calculated with theoretic characteristic length (Lth) and effective characteristic length (Leff) for the different samples.

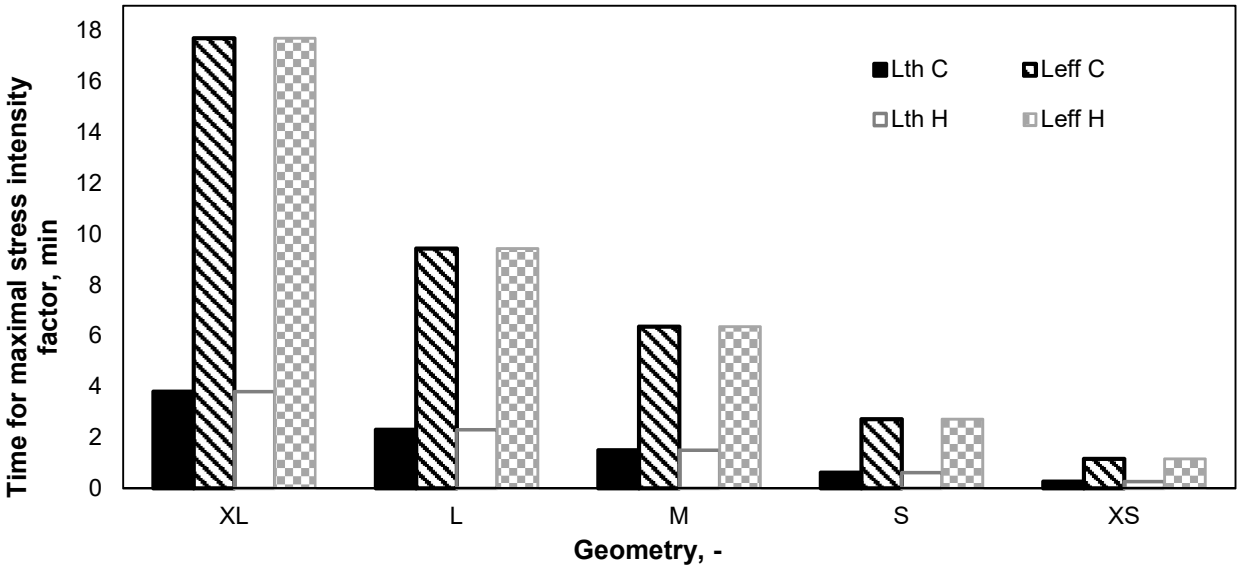

Graph 49 – Real time to achieve maximum stress intensity factor calculated with theoretic characteristic length (Lth) and effective characteristic length (Leff) for the different samples.

This analysis corroborates what was observed in the thermal cyclic tests regarding the size of the samples used. Since the size of the sample determines the load, completely different behaviours were observed in cyclic tests depending on the size of the sample tested.

It is, therefore, of extreme importance to correctly choose the size of the samples to characterize thermal shock resistance. DIN CEN/TS 993 -11 indicates a sample size of 140 x 64 x 64 (a) or 230 x 64 x 54 (b) to study the thermal shock resistance in refractories [44]. To understand the implications of these dimensions, the respective normalized strain using Lu and Fleck (1998) approach explained above was estimated for both geometries defined by the standard and are displayed in Graph 50 to allow a comparison with the samples studied.

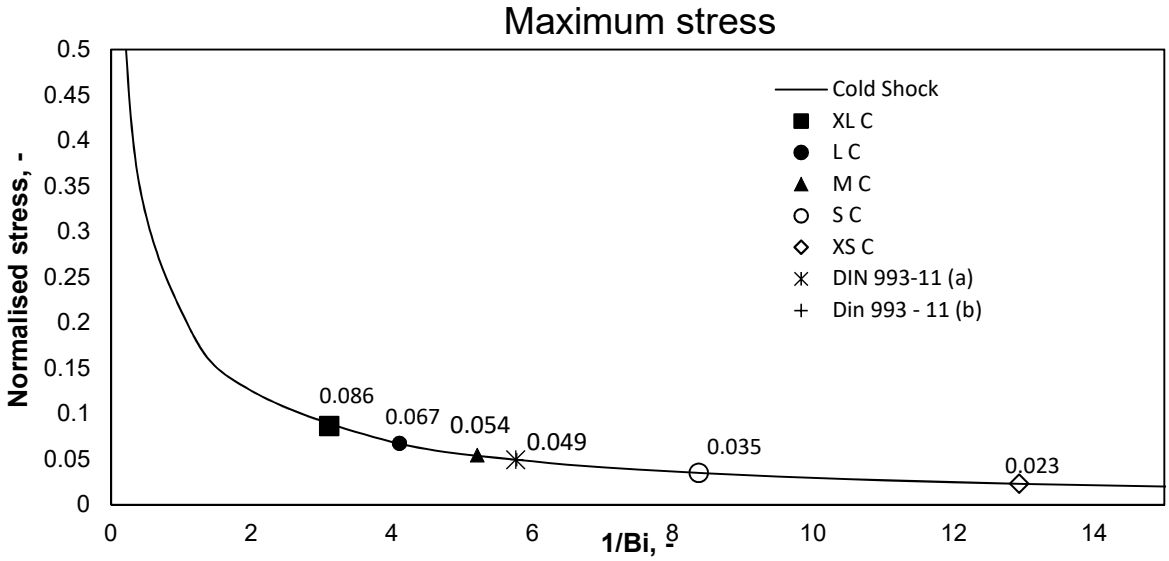

Graph 50 – Evolution of the dimensionless maximum stress with the inverse of the Biot. Size of the samples tested, and samples indicated in DIN 993–11 displayed.

As it can be observed, the dimensions defined by the norm are between the M and S size of the samples tested in thermal shock. Therefore, the expected behaviour for this dimension would be either saturation of damage (found for S) or three distinct phases of damage development (found for M/L). This behaviour is very distinct from the one found for the XL samples which are the most representative of the service conditions since they represent the size of the commercial bricks. In this samples high values of stress are generated, which leads to an exponential increase in the damage and, therefore, failure is achieved in a small number of cycles. The study of thermal shock tests with samples similar to the XL dimension were not found in the literature, which explains why the thermal shock tests in refractories are usually associated with damage saturation in literature. This fact proves the importance of considering a sample size representative of the service conditions.

In order to correlate this analysis with the experimental results obtained for the thermal shock tests, the predicted strain for each different size of samples is plotted against the damage developed in the first cycle for each sample in Graph 51. As was already expected, the damage increases with the increase of the predicted maximum strain. The unfilled points are points in which the ultrasound measurements were affected by the presence of a crack and, therefore, where higher damage is expected and observed, with the exception of the case of M samples (strain = 0.0069). However, this samples had a higher initial damage and therefore the presence of internal defects may explain the higher damage for points where no crack was observed.

The damage developed in the first cycle where a crack was observed is shown in Graph 52. This analysis is interesting since it enables to determine the value for the critical damage. It can be seen that for damage levels higher than 10 % cracks are expected to appear. It can also be seen that the measured damage for samples of bigger dimensions tends to be higher, which can be explained since these cracks developed faster in these samples.

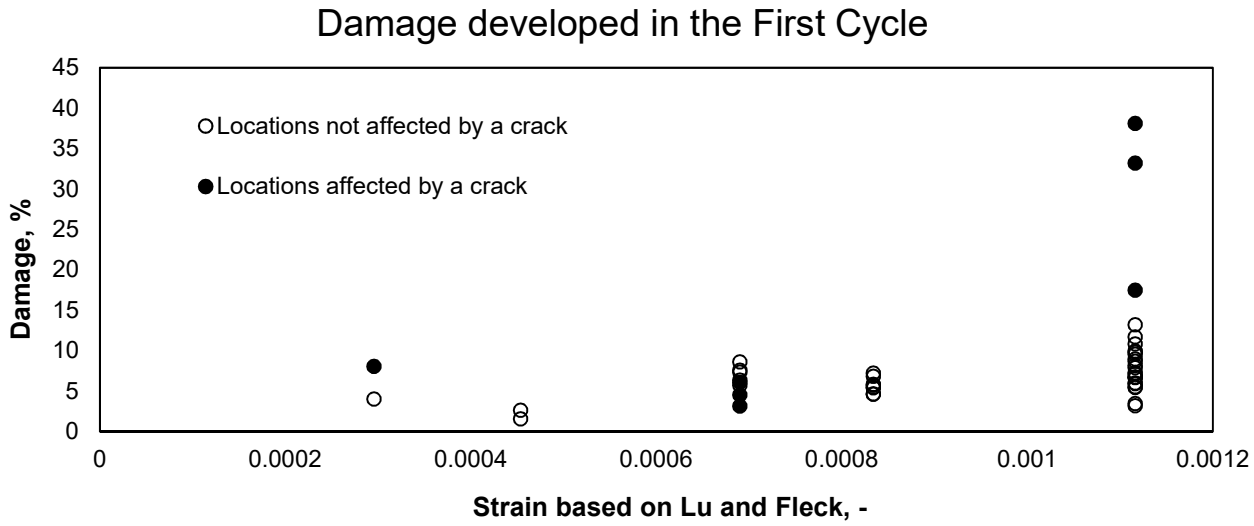

Graph 51 – Damage developed in the first cycle for the predicted strain by Lu and Fleck.

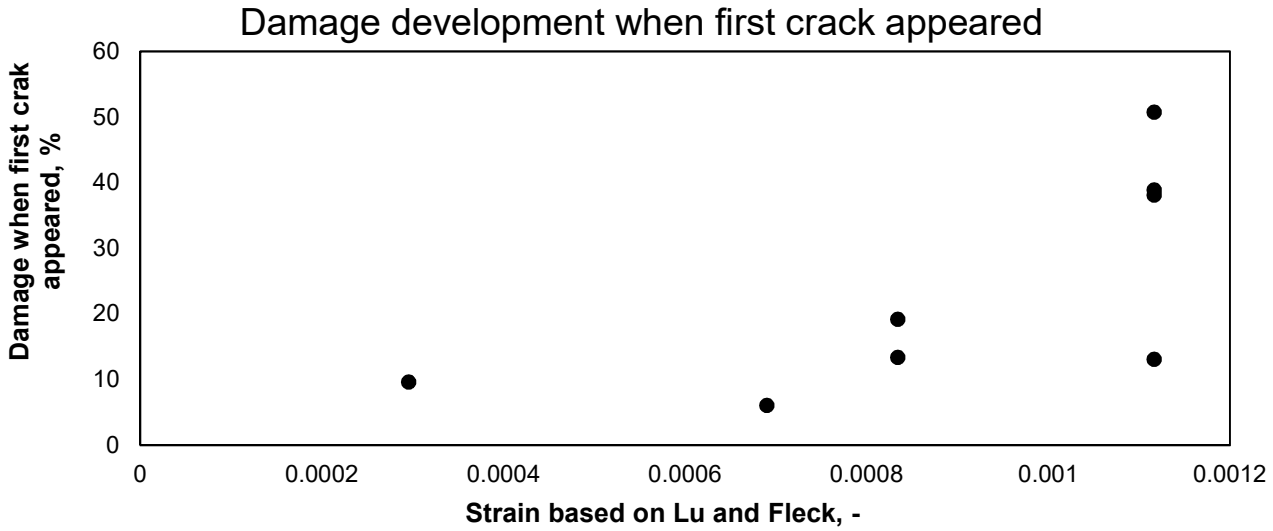

Graph 52 – Damage developed in the first cycle where a crack was observed for the predicted strain by Lu and Fleck.

4.2.2 Fractography

4.2.2.1 Crack growth

The crack development is schematized for all samples throughout all the cycles where visual changes were registered, in Appendix E. From Figure 44 to 46, it is possible to see the cracks observed after the last thermal cycle carried out for the different samples. Different line thicknesses were used when representing the cracks to help interpreting the results. The thickness decreases with the number of cycles in which the profile was registered: the crack development registered within the first cycles is displayed with thicker lines and the one registered in the last cycles is displayed with thinner lines. The criteria used for the thickness selection is represented in Figure 43.

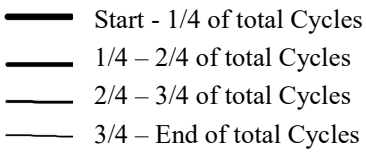

Figure 43 –Scale used for thickness distinction in the different cracks

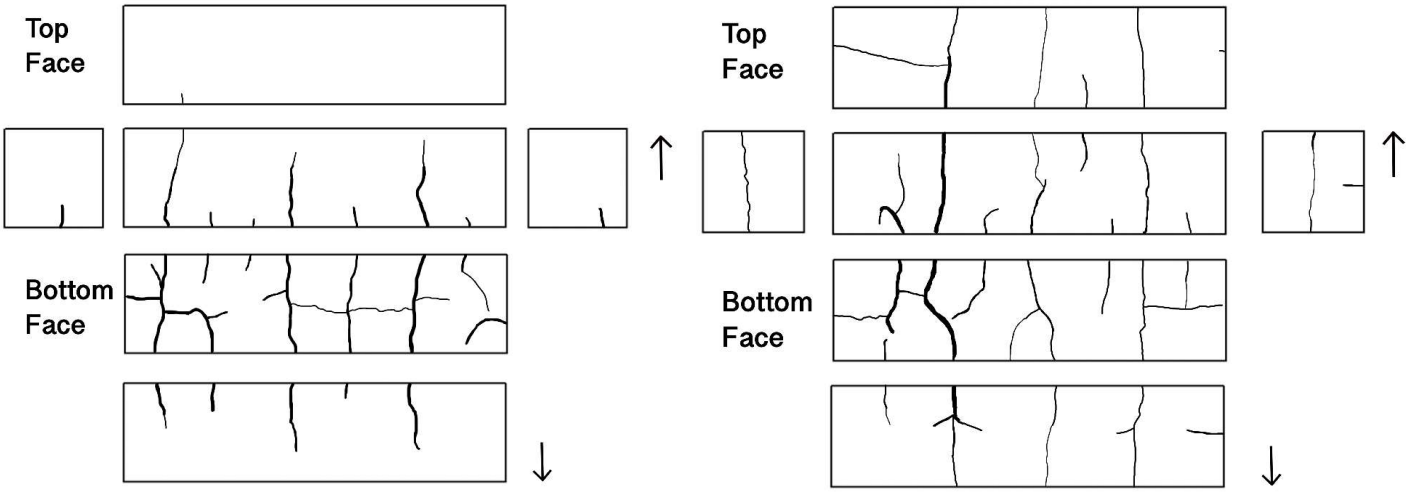

Figure 44 – Cracks at the end of the last thermal cycle for XL samples.

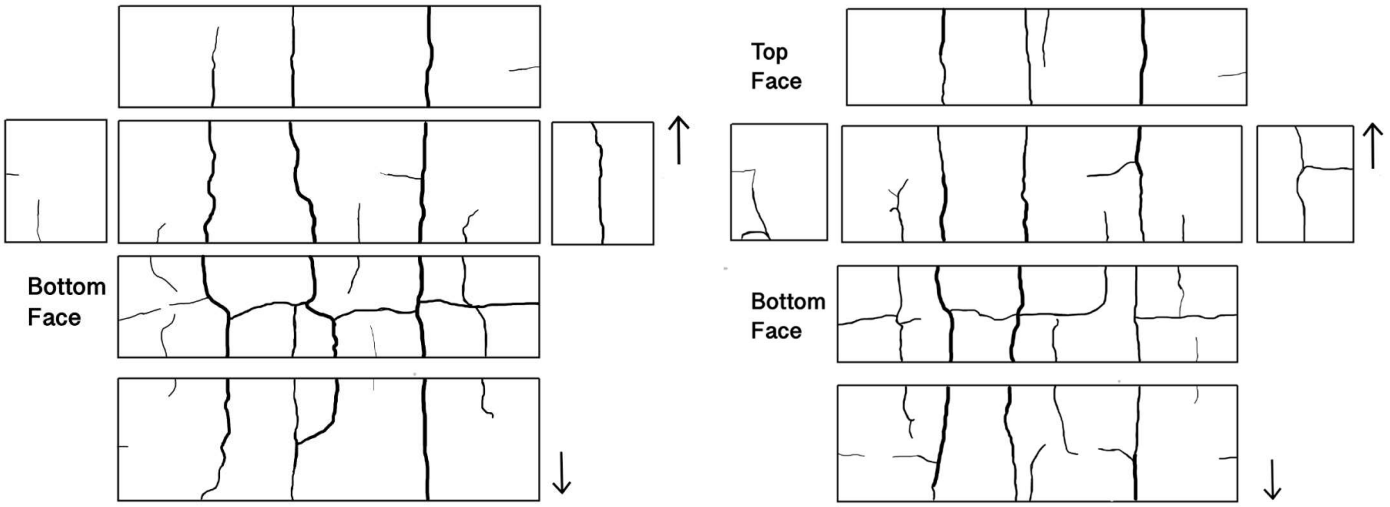

Figure 45 – Cracks at the end of the last thermal cycle for L samples.

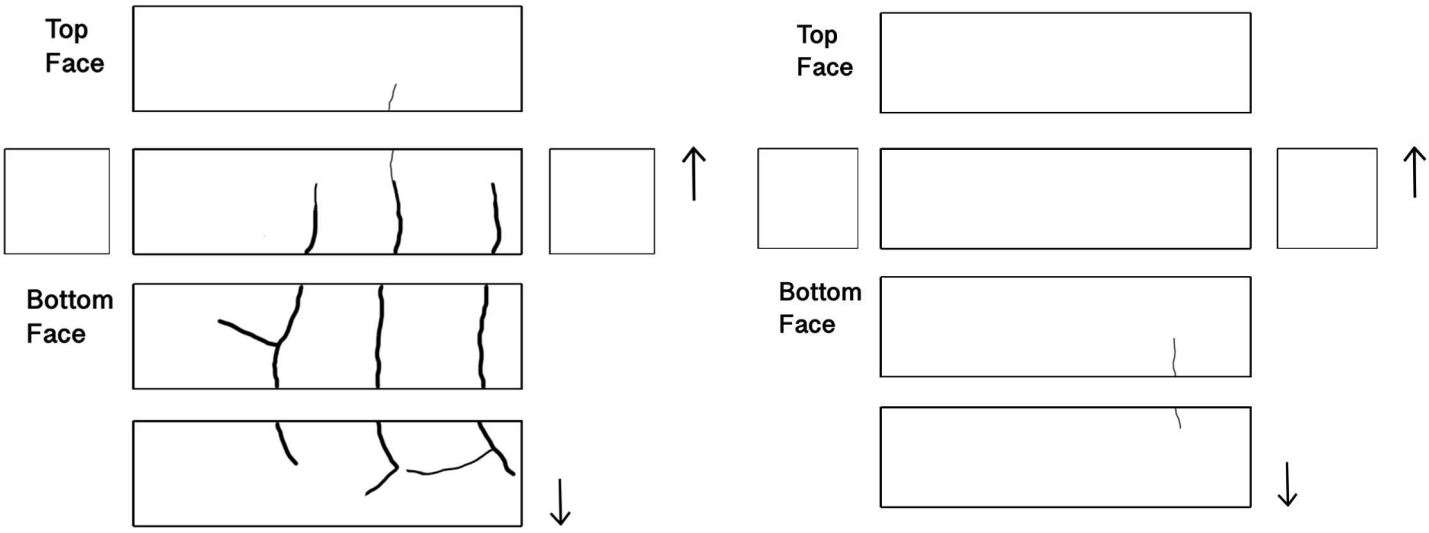

Figure 46 – Cracks at the end of the last thermal cycle for M samples.

Cracks tend to form in ZY direction and start growing in most of the cases from the bottom (Figure 47). This can be easily explained since the bottom surface is in contact with a metal table, which has a higher thermal conductivity, and therefore induces a fast heat transfer which increases the stress in this region.

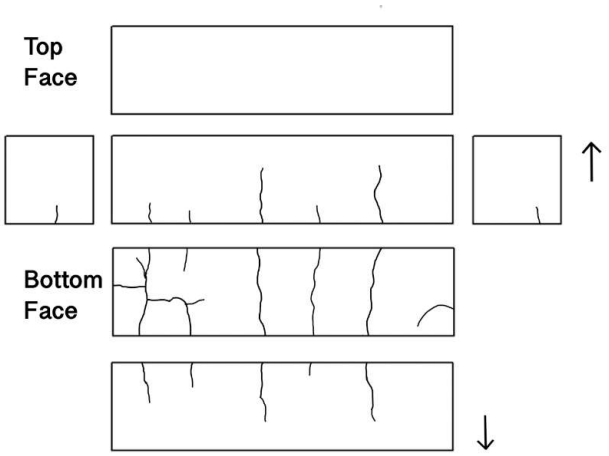

Figure 47 – Crack development in L1 after 6 cycles.

It is also possible to observe that cracks tend to be symmetric, and equally spaced. The bricks tend to be divided in equal parts, which can be observed throughout the different waves of crack development. One example can be observed in Figure 48, representing the different waves of cracks in XL1.

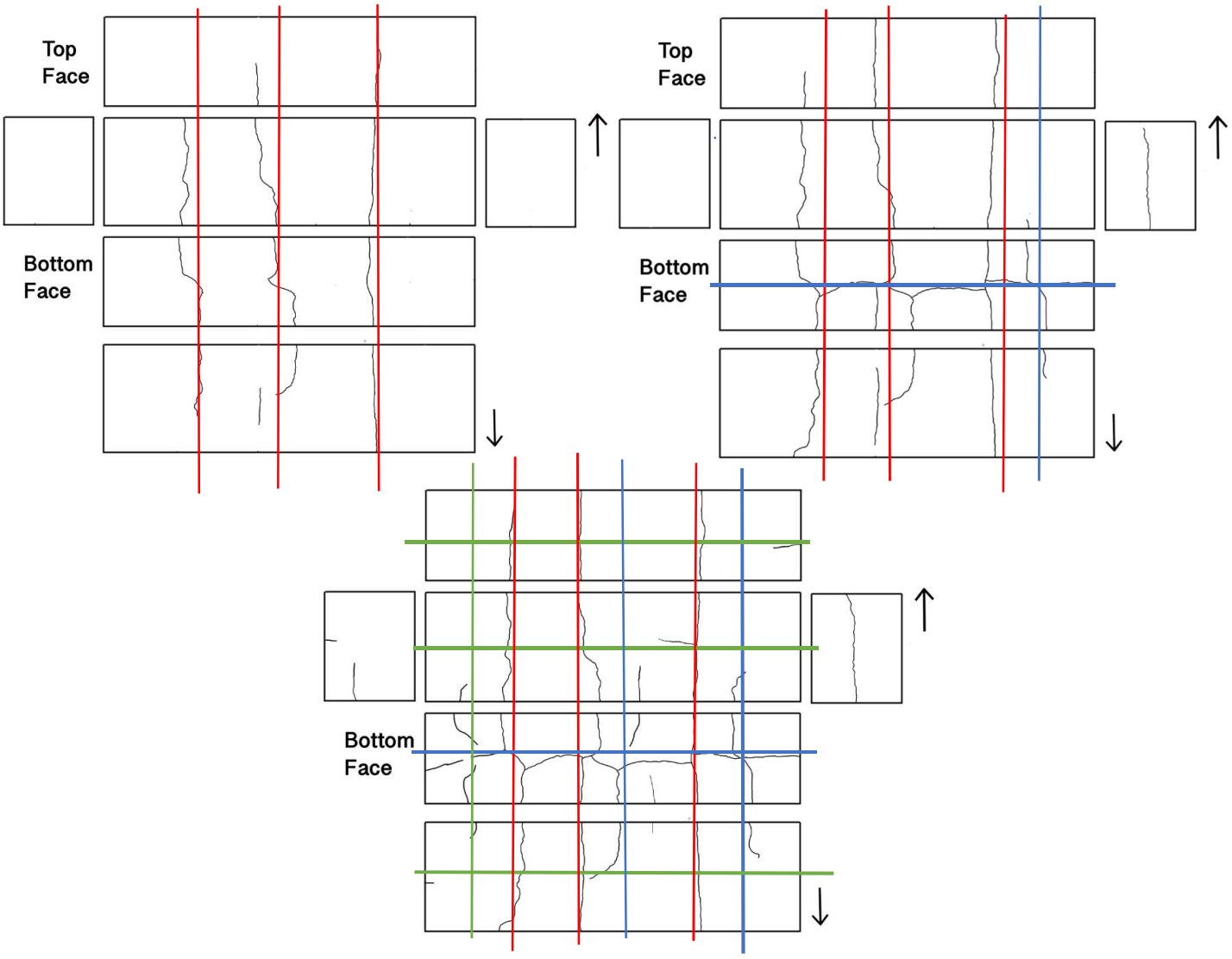

Figure 48 – Crack development in XL1 after 7 cycles (top left), 13 cycles (top right) and 26 cycles (bottom). Red represents the cracks that appeared in the first wave, blue the cracks in the second wave and green the cards in the third wave.

Three parallel almost equidistant cracks were developed in the first wave which divided the brick in four different sections. These sections, in the second and third wave, tend to be equally divided again. While in some bricks it is more evident than others, this symmetry was seen in the majority of the bricks studied.

In the second wave of cracks in the XL and L samples, it is possible to see cracks being deflected and arresting. This phenomenon can be explained also by the boundary conditions. When cracks start developing, the distance from the bottom increases and therefore the stress generated decreases and cracks arrest. Other motive that promotes crack arrest is the fact that the interior of the brick in cold shock (most critical) is in compression while the surface is in tension. Therefore, cracks tend to initiate at the surface and arrest when enter the central compressive region. Other reason can also be the change in length of the sample since, as more cracks develop, less volume for crack development (and shielding zone) exists and therefore cracks do not have enough energy to grow. Other phenomenon observed is that due to the difference in heat transfer of the surfaces, the bricks will tend to bend, which can also cause the cracks to deflect. Examples of crack arrest and deflection are identified with arrows in Figure 49.

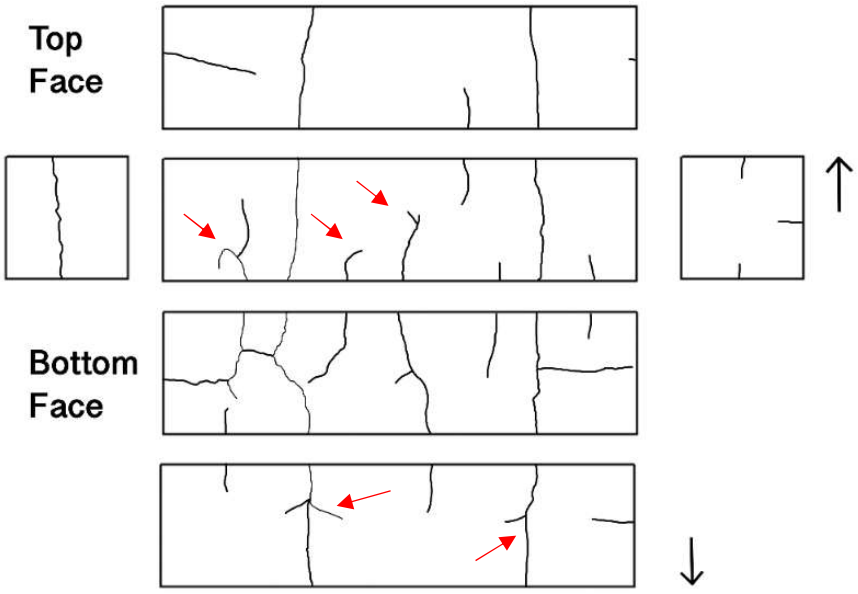

Figure 49 –Crack development in sample L2 after 20 cycles. Arrows indicate cracks which deflect and arrest.

The effect of the influence of the available length with the crack development can be observed on Graph 53, in which the crack surface developed in the first cycle where the crack appeared is plotted against the length available for crack development. In the first cycles, since no prior cracks existed, the length considered was the total length and the crack surface of all the cracks that appear in this cycle were summed, since it would be impossible to know which cracks developed first.

As was already expected, it is possible to see that with the increase in length there is an increase in crack development. This is reasonable since higher lengths represent a higher volume in the vicinity of the crack. Therefore, a bigger shielding zone may be developed, as is illustrated in Figure 41. The unloading of this zone, which is elastic and uncracked, releases the elastic energy into the cracking zone and promotes further growth of the crack [45]. While in the Lu and Fleck analysis the thickness was the main geometry parameter which affected the load (considering the effective characteristic length), it is possible to observe that the length is also an important factor for the crack development.

In XL samples it is also possible to observe the symmetry in crack development as can be seen in the second and third waves of cracks which divided the brick in 4 (400/100) and in 8 (400/50) parts.

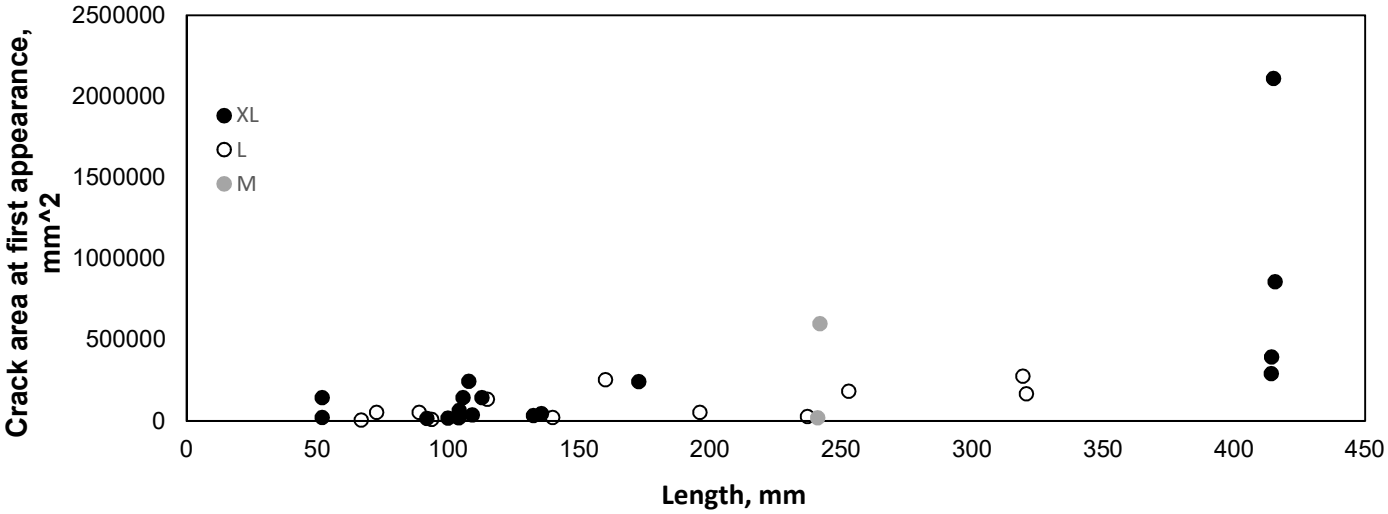

Graph 53 –Influence of the length (volume) available for crack development with the crack area developed at first appearance in mm^2.

The fracture surfaces of several complete fractures that occurred in the XL samples can be seen from Figure 50 to 53, where the crack growth registered at each cycle is marked with lines (different colours represent different cycles) and the cycle in which the crack growth was observed is indicated. It is interesting to notice that different areas of crack propagation were developed throughout the cycles, which tend to coincide with the crack development registered (visual inspection) during the cycles. This can validate the considerations used to estimate the surface of crack development (Appendix B). These different regions can be clearly seen in the fracture XL2 ZY1 or XL1 ZY1, while in other fractures such as XL2 ZY2 it is more difficult to define these regions of crack development. It is also possible to notice that when the number of cycles to fracture is high, such as in XL2 ZY2 (15 cycles) these regions are less obvious to observe. This can be an indication of the influence of the number of cycles in the fracture surface.

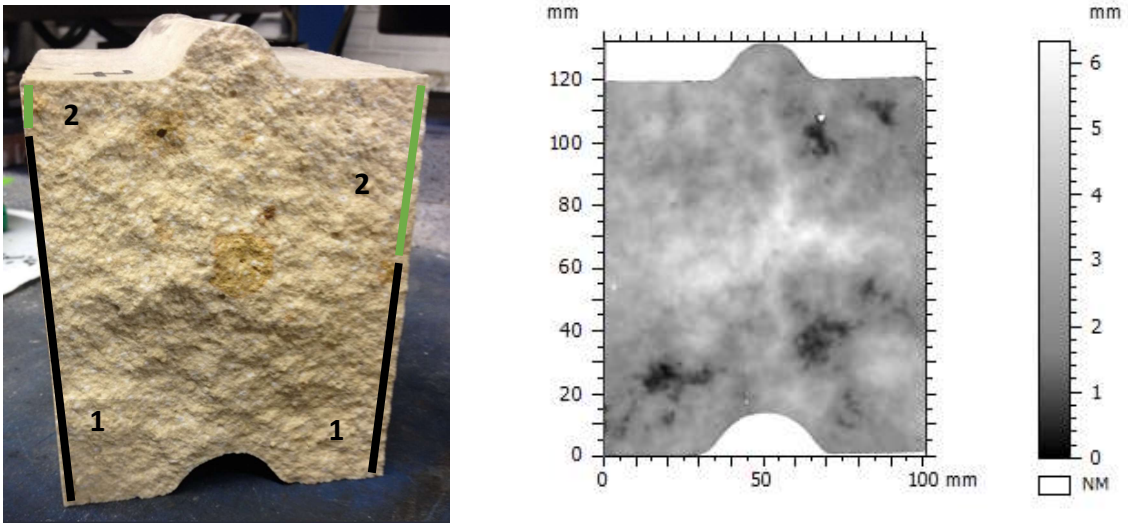

Figure 50 – Fracture surface of XL1 ZY1.

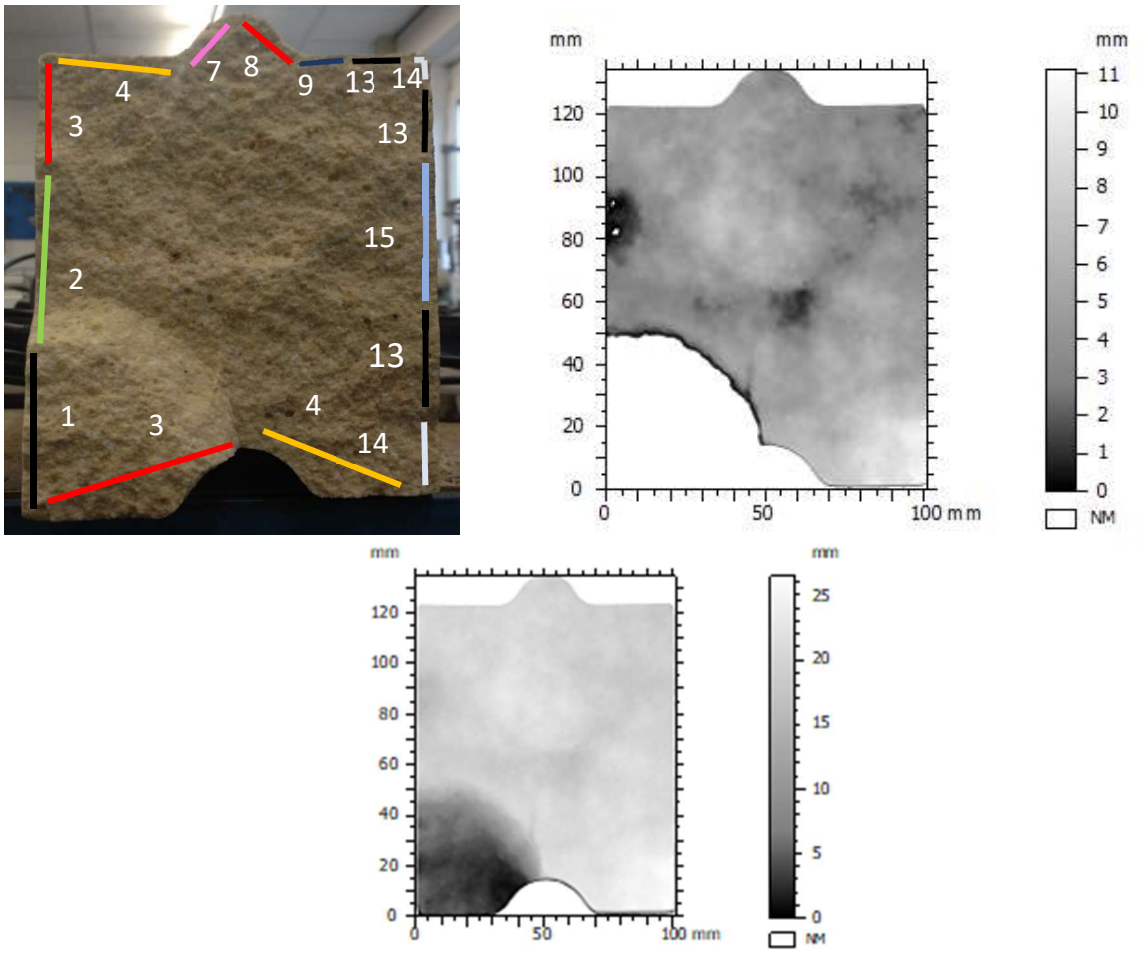

Figure 51 – Fracture surface of XL1 ZY2.

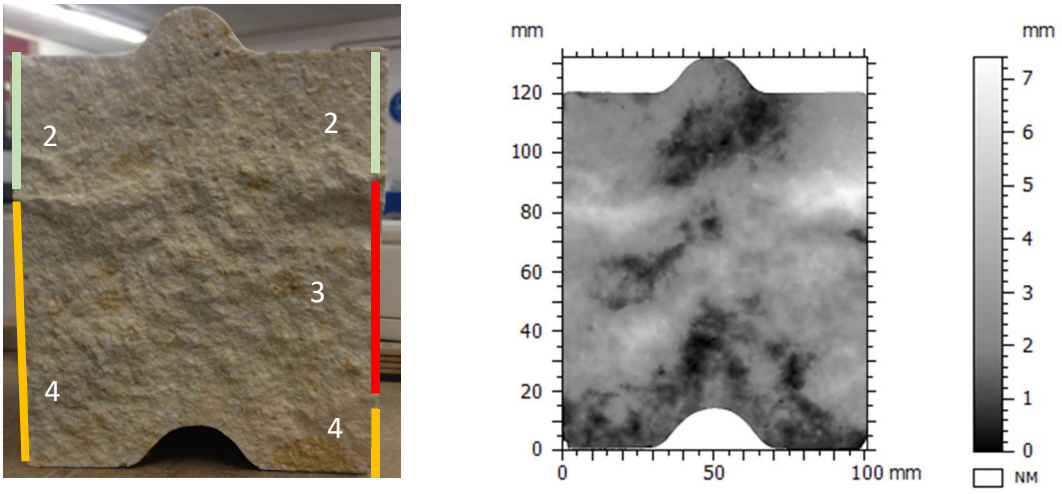

Figure 52 – Fracture surface of XL2 ZY1.

The measured % of white grains is plotted against the number of cycles necessary for complete fracture (since crack first appeared until the sample fractured) in Graph 54. Only the results obtained for the XL samples were considered since the ratio of the grains to the size of the sample changes with the change in size and, therefore, a percentual evaluation of this parameter would not enable a fair comparison.

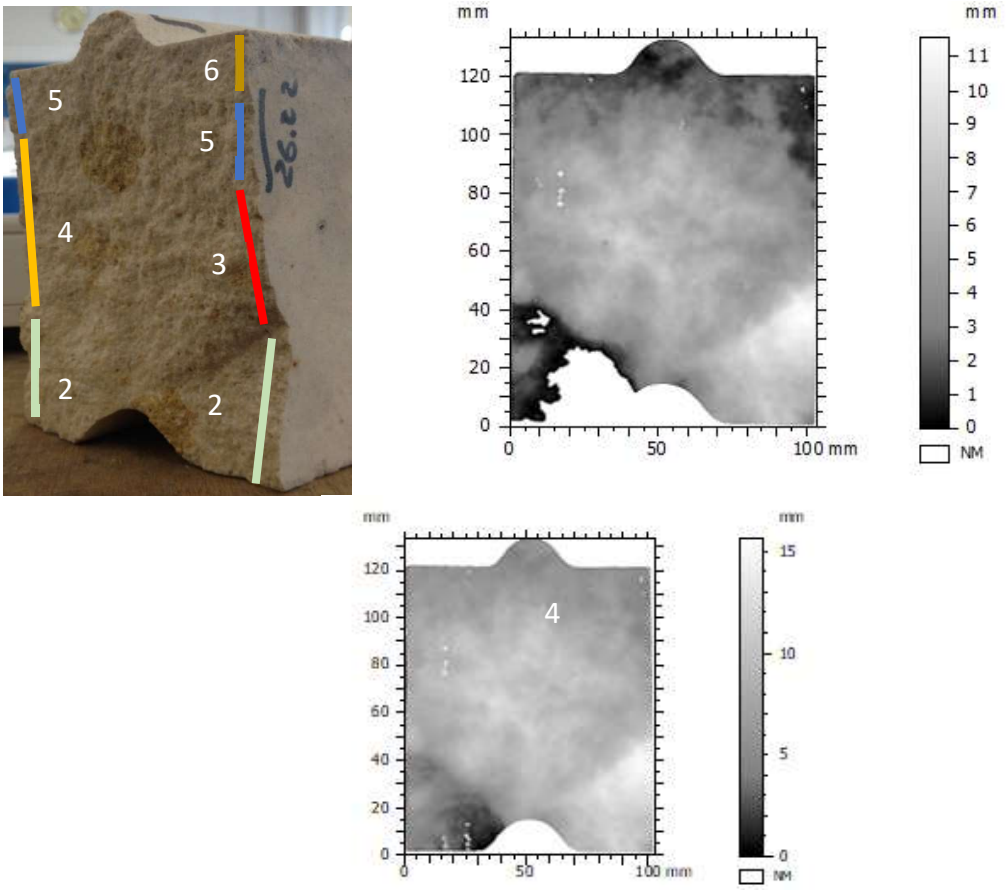

Figure 53 – Fracture surface of XL2 ZY2.

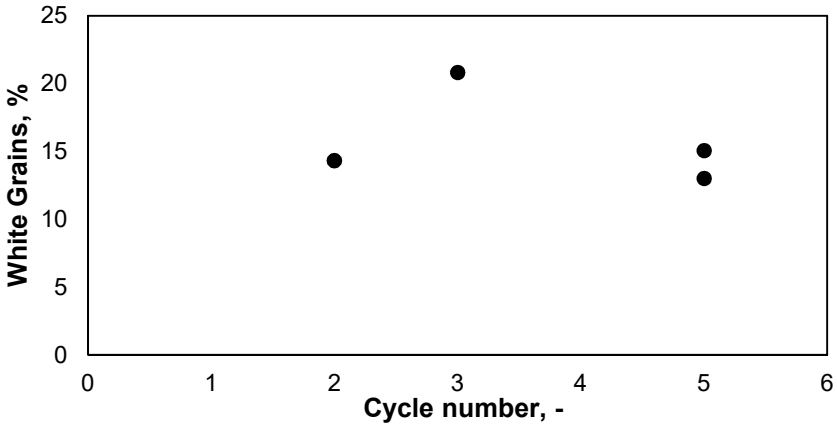

Graph 54 – White grains % with the number of cycles to fracture.

The number of fracture surfaces where white grains were analysed was low, which limits the interpretation of the results. However, no trend was observed for the % of white grains throughout the cycles. It is expected that, with the increase in the number of cycles, reduced brittleness is observed [7]. This can be seen in the thermal shock results where the crack development measured at first appearance reduces significantly with the number of cycles. Less brittle failure is usually associated with crack propagation around the grains since more energy is dissipated [7]. However, other motives can explain why reduced brittleness is observed, such as the development of more distributed failure process with increasing number of cycles which promotes more tortuous cracks [7].

In literature, the crack propagation trajectory (transgranular or intergranular) is usually evaluated for different materials with different grain matrix coherences and properties [9, 20, 22] and, therefore, it is possible that this factor is not significant when considering reduced

brittleness in the same material since the interaction between grains and matrix may not be particularly affected by the number of cycles.
Other limitation with this measure resides in the fact that even if the crack propagation occurs between the grains and the matrix, the grains will still be visible in one of the sides of the fracture surface and therefore not all grains measured in the surface imply straight crack propagation.

4.2.2.2 Roughness Profile

The results of the profiles of cracks ZY1 and ZY2 of XL1 can be seen in Figure 54, where it is also possible to see in which cycle the section of the profile was developed. As was already seen, crack ZY1 developed considerably fast, since it developed completely in the second cycle. This fast development can justify why, by analysing the profile, it is not possible to see significant deviations of the crack trajectory. On the other hand, by analysing crack ZY2, which was developed in later cycles, it is possible to observe a more significant deviation of the crack trajectory. However, when comparing both sides of this crack, it can be observed that the side where less cycles occurred to achieve the top (side A) is where the deviations are more prominent.

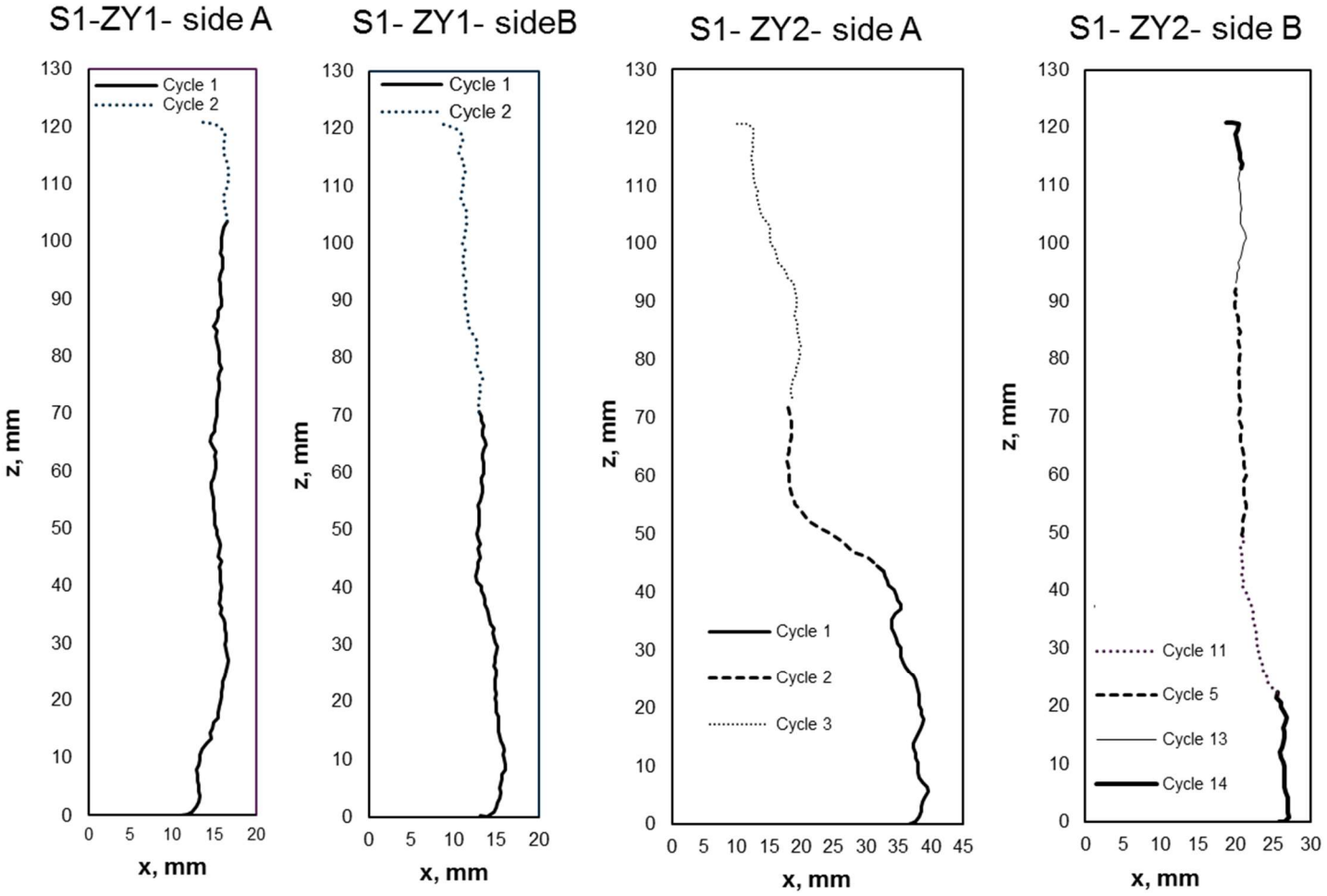

Figure 54 – Profile of both sides of cracks ZY1 and ZY2 from XL1.

In Figure 55 and Figure 56, it is possible to observe the profile of cracks developed in XL2. As was previously seen, when cracks developed in few cycles (1 or 2) there is almost no deviations of the crack path (ZY3 – side b). This is also seen when a large portion of the crack profile is developed only in one cycle (ZY1 – side B - cycle 4).

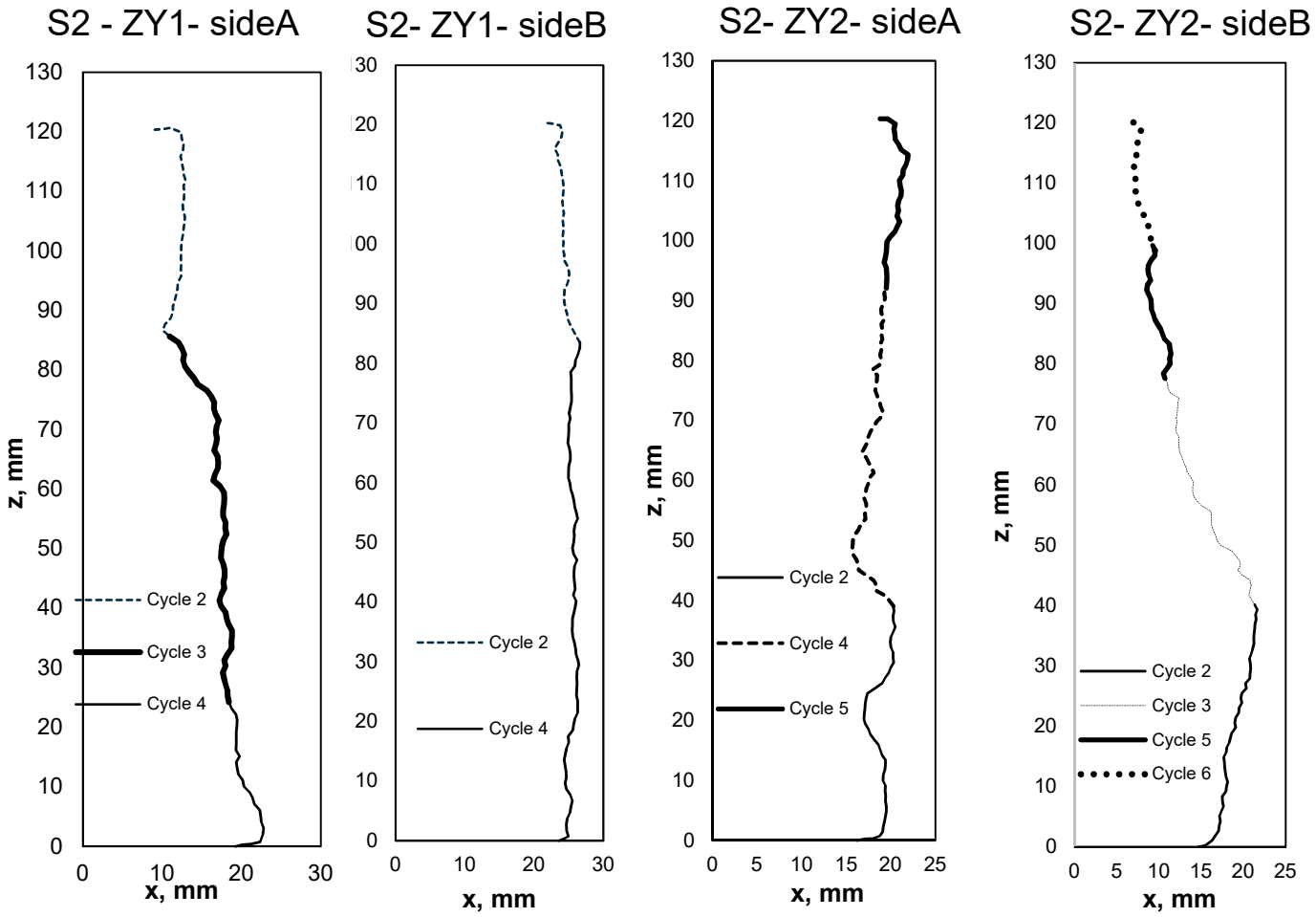

Figure 55 – Profile of both sides of cracks ZY1 and ZY2 from XL2 sample.

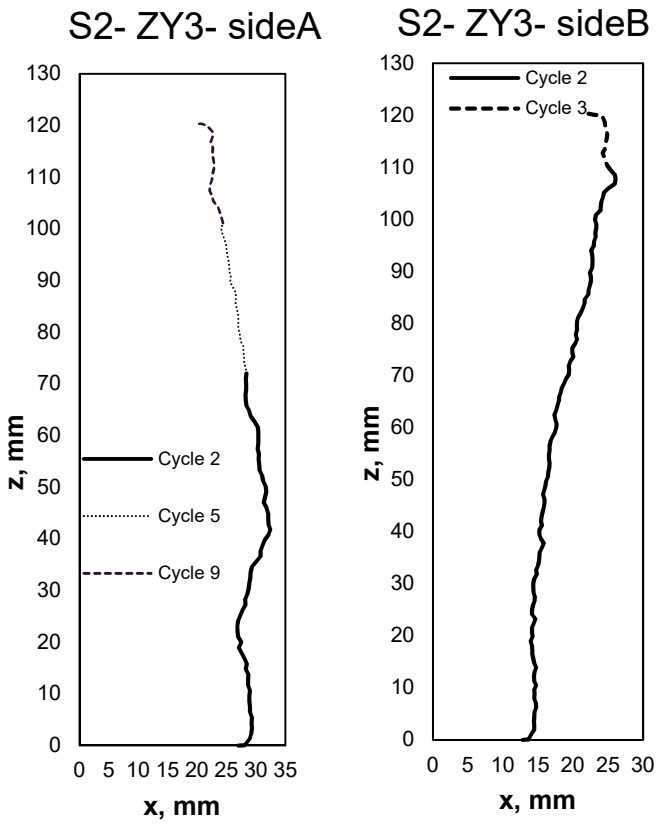

Figure 56 – Profile of both sides of crack ZY3 from S2 sample.

When cracks are developed in an intermediate number of cycles (3 to 8), it is possible to see rougher profiles with noticeable trajectory deviations. However, this trend changes when the number of cycles is higher. For cracks developed throughout many cycles, for example XL1 ZY2 – side B and XL2 ZY3 – side A, the deviations in trajectory are not as significant as the ones observed for crack developed in an intermediate number. This can be explained since a small portion of the crack is developed in each cycle. It should be noted that the crack ZY3 in S2 starts growing from the top of the brick which is an exception from the behaviour found in the remaining cracks.

To have a quantitative analysis of the roughness of the profiles, the fractal analysis of the profiles was carried out. The fractal parameter used was the Hurst and Hausdorff dimension which allows the measurement of the extent of the ‘’tortuosity’’ or irregularity of the surface (roughness). For a curve the Hausdorff dimension can vary between 1 (for smooth curve) and 2 (rough curve) [39].

The method used was the same described for the mechanical tests to enable a fair comparison of the results. In Graph 55, it is possible to see the Fourier Power Spectrum obtained for XL2 ZY1 side b with the straight line fit. Using equation 2.12 and 2.13 is possible to calculate both fractal parameters using the slope of the line.

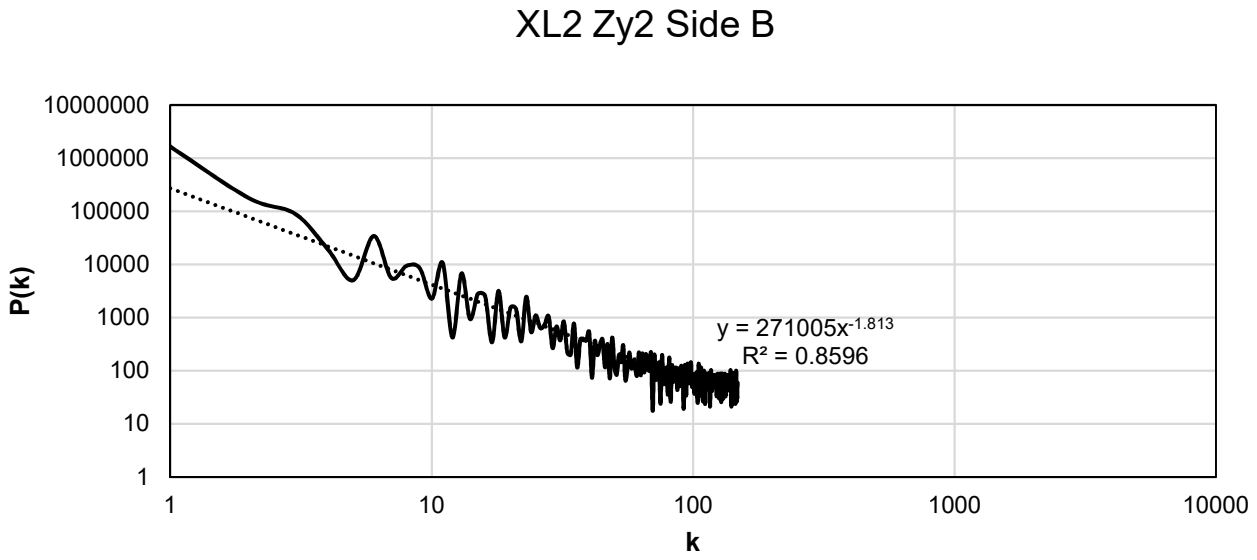

Graph 55 – Fourier Power spectrum of XL2 ZY2 – side B.

This analysis was conducted for all cracks that developed completely in all samples. In Graph 56, the Hausdorff dimension is represented as a function of the number of cycles necessary for the profile to fully develop (number of cycles that occurred since the crack appear until it fully developed in that face). The two different sides of the crack were considered since in some cases a different number of cycles was necessary to fully develop the crack in each side.

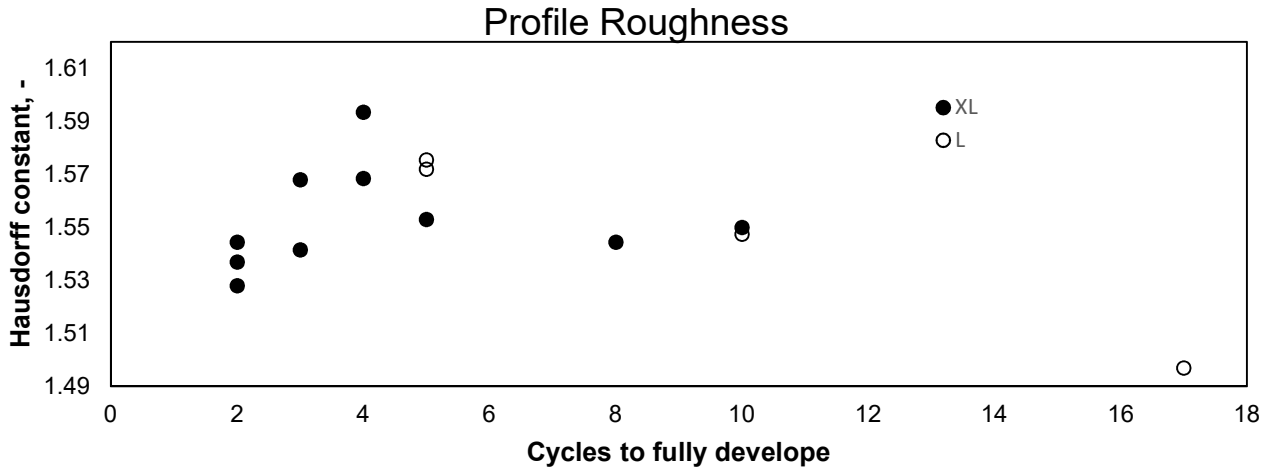

Graph 56 – Hausdorff constant obtained for samples which undergone thermal-shock tests.

It is possible to see that the roughness increases with the number of cycles until a peak is reached at approximately 4 cycles. After this there is a decrease in the roughness. The roughness is intrinsically related with the energy dissipation. Therefore, it would be expected that it would increase with the number of cycles since it would imply a more gradual loading. However, with the increase of the cycles, more cracks are present in the samples and the length available for crack development decreases, which means that the energy for a crack to propagate is lower resulting in cracks developing small lengths throughout a high number of cycles.

4.2.2.3 Digital Image Correlation

The results of the displacements in x direction measured using DIC during cooling of S1 can be seen in Graph 57. The location of the points measured are represented in Figure 57.

It is possible to distinguish two phases during cooling in both samples. In the first minutes, the heat transfer in the vertices near the bottom (2 and 6) is higher, after which this difference stabilizes. This can also be clearly seen in Figure 58. One reason that can explain the faster cooling in the bottom vertices is the fact that they are in contact with a metal table, which has a higher conductivity than the air.

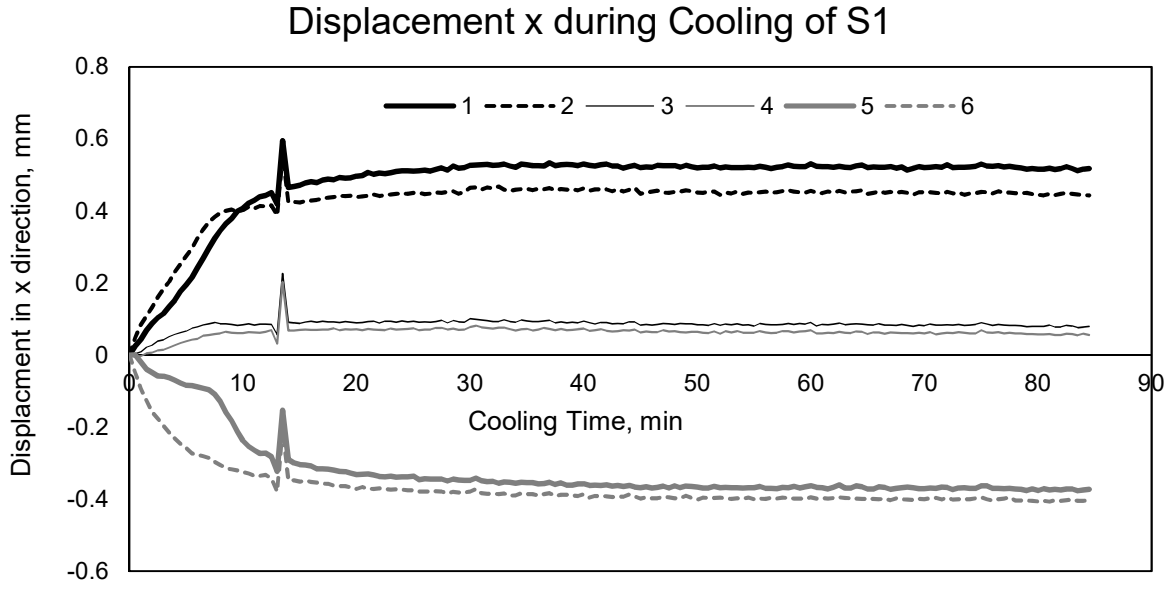

Graph 57 – Displacements in x direction in different areas of the sample S1.

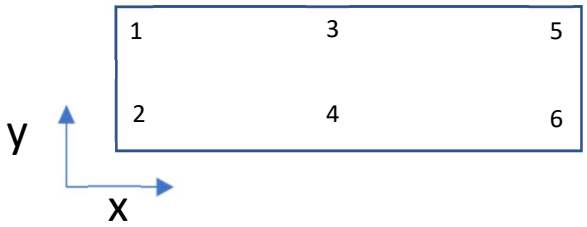

Figure 57 – Location of the points where displacements were measured during cooling

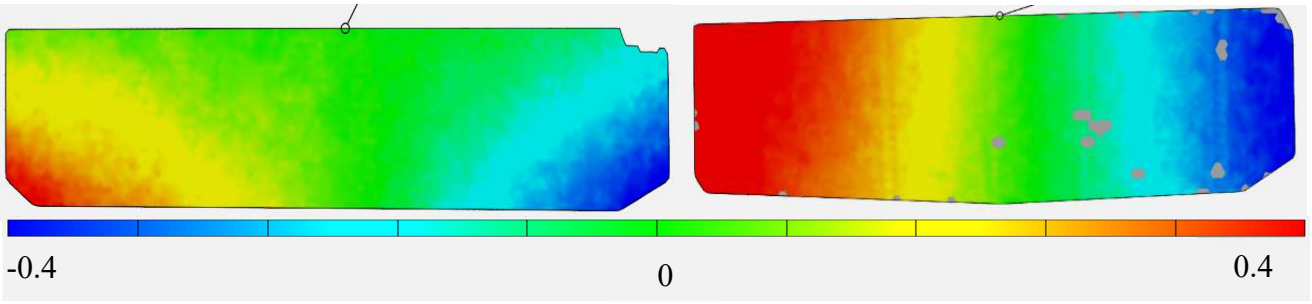

Figure 58 – Displacement x during cooling of XS1: First phase (left), Second phase (right).

The maximum displacement occurring during cooling can be calculated as the difference from point 1 to 5 or point 2 to 6 and is approximately 0.92. The maximal displacement can also be theoretically calculated using eq 4.17.

$$\Delta x = \alpha . \Delta T . L \tag{4.17}$$

where:

Δx, is the displacement in the x direction
α, is the linear coefficient of thermal expansion
ΔT, is the thermal gradient
L, is the length

The theoretical Δx considering a ΔT of 180 °C is approximately 1, which is in agreement with what was measured.

The displacements in the y direction for S1 is represented in Graph 58. As was expected, the magnitude of the displacement in this direction is less significative. Because of this, the results present significative variations and jumps, which can be justified by the fact that, during cooling, the bricks are in contact with a table used for other experiments. Since the magnitude measured is very small, the results are very sensitive to small vibrations in the table.

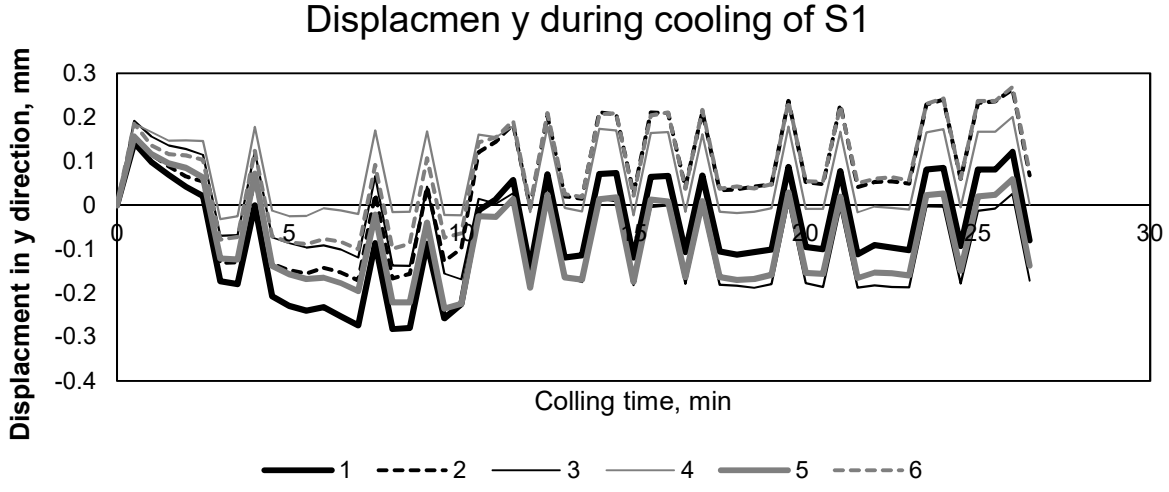

Graph 58 – Displacement y during cooling of S.

Nevertheless, it is possible to see that both bricks tend to bend. Point 1 and 5 (top vertices) are the ones with higher negative displacement. This is also illustrated in Figure 59 and 60.

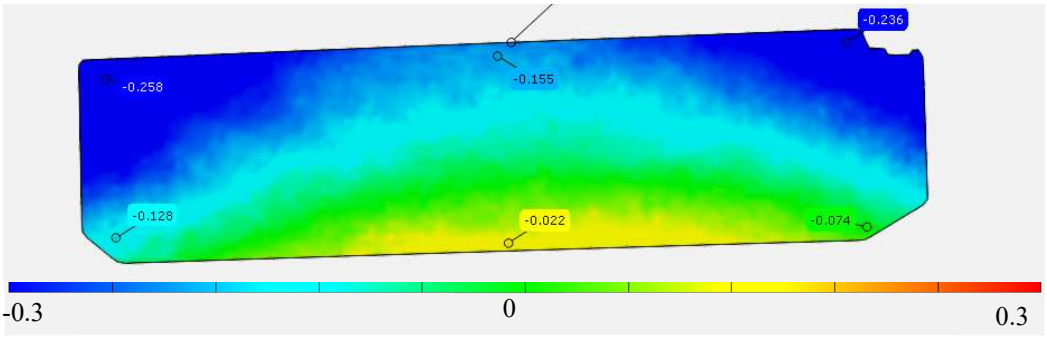

Figure 59 – Displacement y during cooling of S1

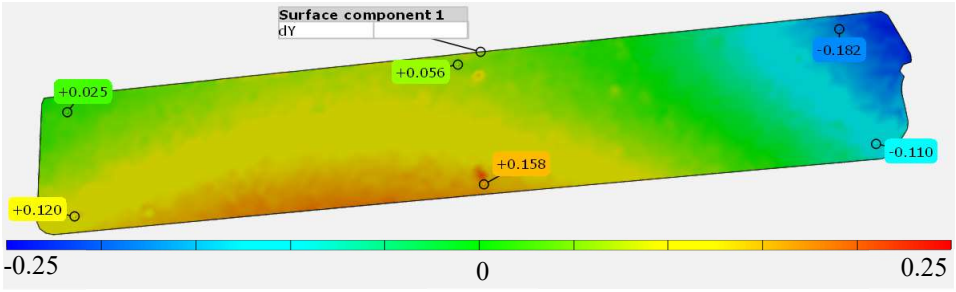

Figure 60 – Displacement y during cooling of XS1

To study the crack opening an area of the L sample was also photographed. As illustrated in Figure 61 several points situated near the crack were measured. The displacements in the x direction can be seen in Graph 59.

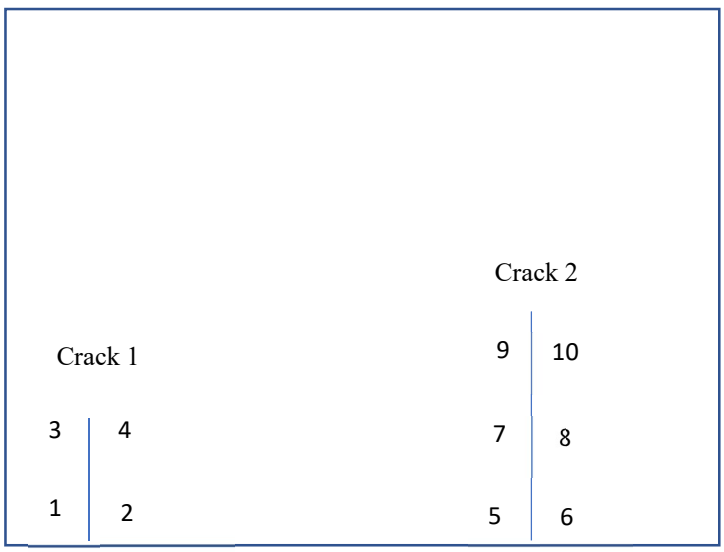

Figure 61 – Location of the points where displacements in x direction were calculated in sample SI1.

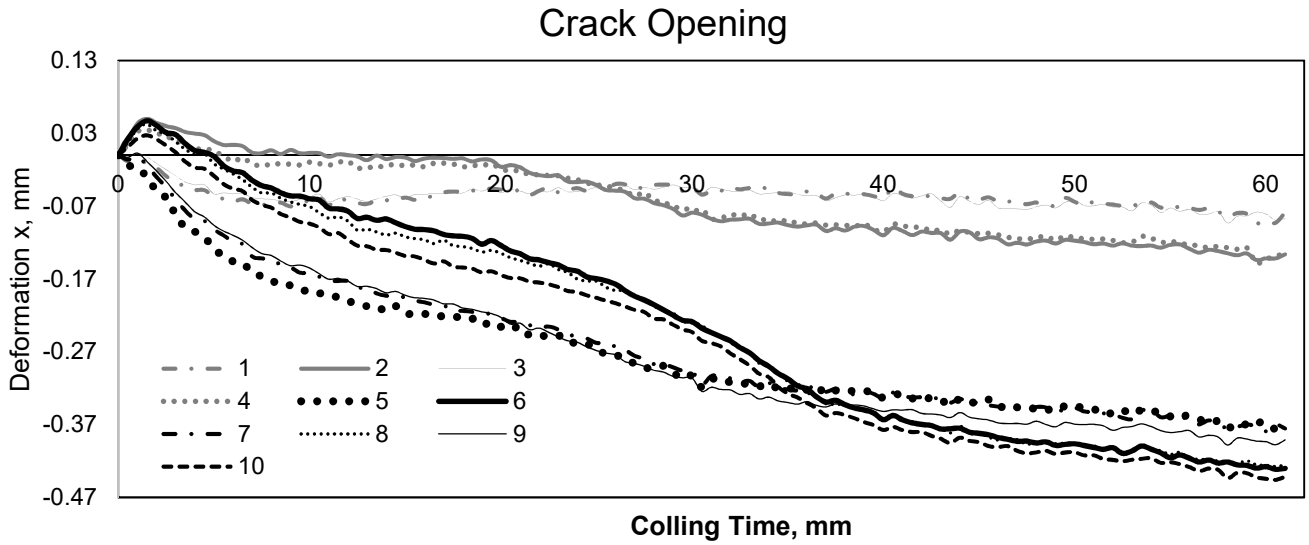

Graph 59 – Displacements in x direction in the defined points of the sample L1.

To better interpret the results obtained the crack opening was calculated. To do so eq 4.18 and 4.19 were used.

$$\Delta x\ crack1 = \Delta x2 - \Delta x1 \tag{4.18}$$

$$\Delta x\ crack2 = \Delta x5 - \Delta x6 \tag{4.19}$$

where:

Δxi, is the displacement in x direction in crack i

$\Delta x\ crack$, is the crack opening

Only the points near the bottom were considered to calculate crack opening, since it is where the displacement is higher. In Graph 60, it is possible to see the evolution of crack opening for two cracks during cooling.

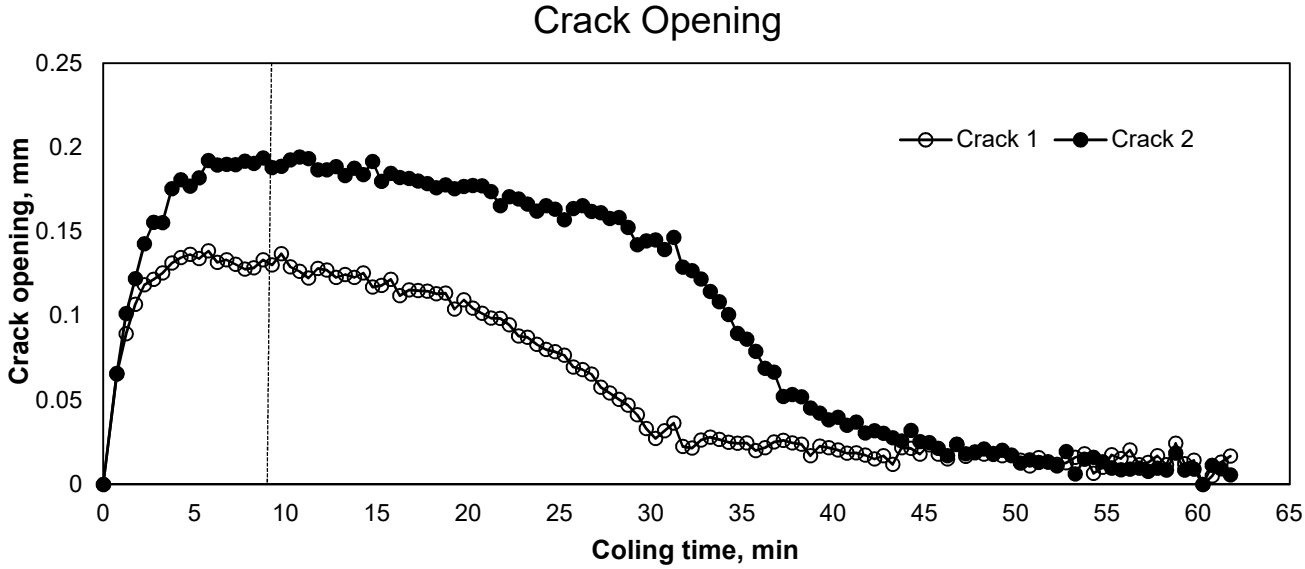

Graph 60 – Crack opening of two cracks in L1. Dashed line represents the time where maximum stress intensity factor is expected to occur based on Lu and Fleck analysis.

Different phases of crack opening can be distinguished during cooling. In the first moments the cracks are opening. After this, it is possible to see a stabilization of crack opening and finally both cracks tend to close. Based on Lu and Fleck (1998)[1] approach the maximum load for

cold shock, considering the stress intensity factor criteria since there are cracks present, would be reached in approximately 9 minutes for L samples. The estimated time for maximal stress coincides with the beginning of the stabilization of the crack opening measured, which indicates the validation of the results, since maximum load is expected to happen near this time.

This phenomenon was also visually observed since in the first minutes of cooling cracks were much easily visually detected that at the end of the cycle (Figure 62)

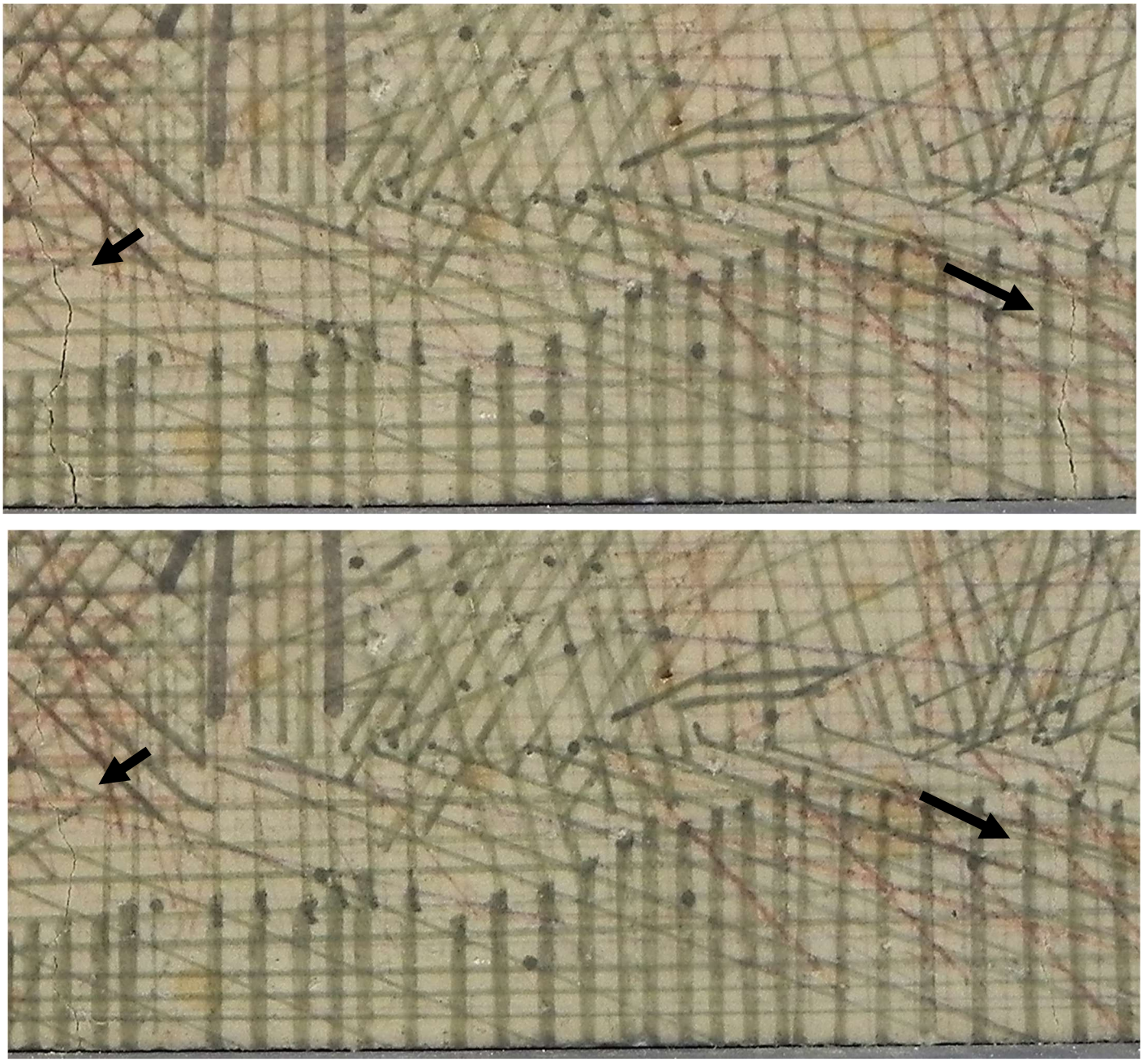

Figure 62 – Crack appearance at the beginning of the cooling phase – after 9.5 min (top) and crack appearance at the end of the cooling phase – after 2 hours and 40 minutes (bottom).

To study how cracks appear and develop throughout the cycles, the same analysis presented above was carried out throughout different cycles. In Graph 61 the crack opening for sample XL3 is calculated. The first cycle is not represented in this graph since the photos taken during this cycle were affected by changing lighting conditions. However, to understand what happens during this cycle one image from the first seconds of the cooling stages and one image from the last seconds of the cycle were used. It was possible to observe that the difference in the points between these frames was smaller than 0.05 mm, and therefore, the growth of the crack was not

considered. This consideration is in agreement with the visual inspection where no cracks were possible to observe after the first cycle. The reference image used for the measurements was the image taken in the first seconds of the first cycle.

This analysis was conducted to sample XL4 from cycle 4 to cycle 9 and the calculated crack opening is represented in Graph 62.

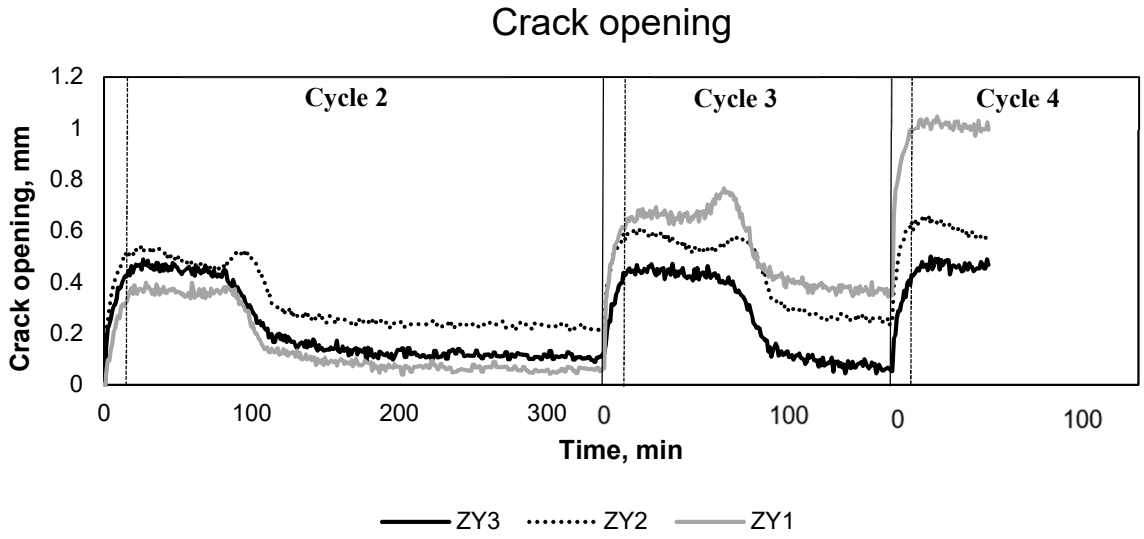

Graph 61 – Crack opening in sample XL3 during cycle 2, 3 and 4. Lines represent the beginning of a new cycle and dashed lines represent the time where maximum stress intensity factor is expected to occur based on Lu and Fleck analysis.

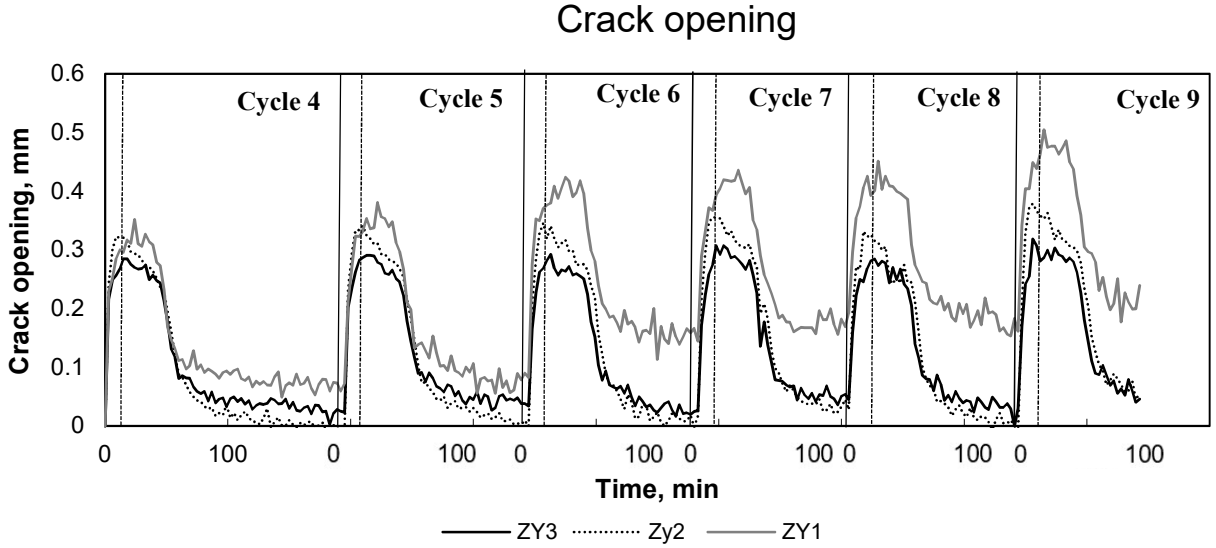

Graph 62 – Crack opening in sample XL4 during cycles 4 to 9. Lines represent the beginning of a new cycle and dashed lines represent the time where maximum stress intensity factor is expected to occur based on Lu and Fleck analysis

It is possible to observe that cracks tend to open and close during the cycles, as was already seen in Graph 60. The opening of the cracks is caused by the increase in load, due to the strains developed during cooling. The cracks then stabilize once the maximum load is reached, which would be at approximately 18 minutes for the XL samples, considering the Lu and Fleck approach (for cold shock with the stress intensity factor criteria). The 18 minutes predicted by Lu and Fleck are in accordance with the crack opening measured using DIC (marked in the Graph 61 and Graph 62 with dashed lines). It is also interesting to notice that after reaching the maximum load, crack stabilization is seen during approximately one hour. After this, the

temperature gradient has already decreased significantly and, therefore, the load is reduced and cracks tend to close. However, a complete crack closure is never observed due to friction and interlocking [46]. Crack opening at the relaxed state (end of cooling stage) tends to increase with the cycle number. This happens because of the increase in the irreversible displacement with the number of cycles [46]. This irreversible strain build-up was also observed in the crack development in the wedge splitting tests ensuring the correlation of the crack development mechanisms in both test methodologies.

It is also possible to observe that while a crack grows significantly (ZY1in XL3 and ZY1 XL4), the other cracks tend to stabilize.

Another interesting application of DIC is the easier and more accurate visualization of the cracks. It was proven that cracks are seen at later cycles when using visual inspection comparing to the results from DIC, where cracks are detected sooner. This is illustrated in Figure 63, where it is possible to see a photo taken after 16 minutes of cooling in the first cycle of sample XL4 and the respective images at the same time using DIC (reference photo was the first photo taken during cooling in the first cycle). While in the regular photo no crack is detected, using the DIC, it is possible to notice three different areas where displacements/strains have a different behaviour than in the rest of the brick. This is an indication of the beginning of crack formation. It is also possible to observe the development of a crack process zone. However, further studies should be carried to locate the crack tip to enable measurements of the crack process zone.

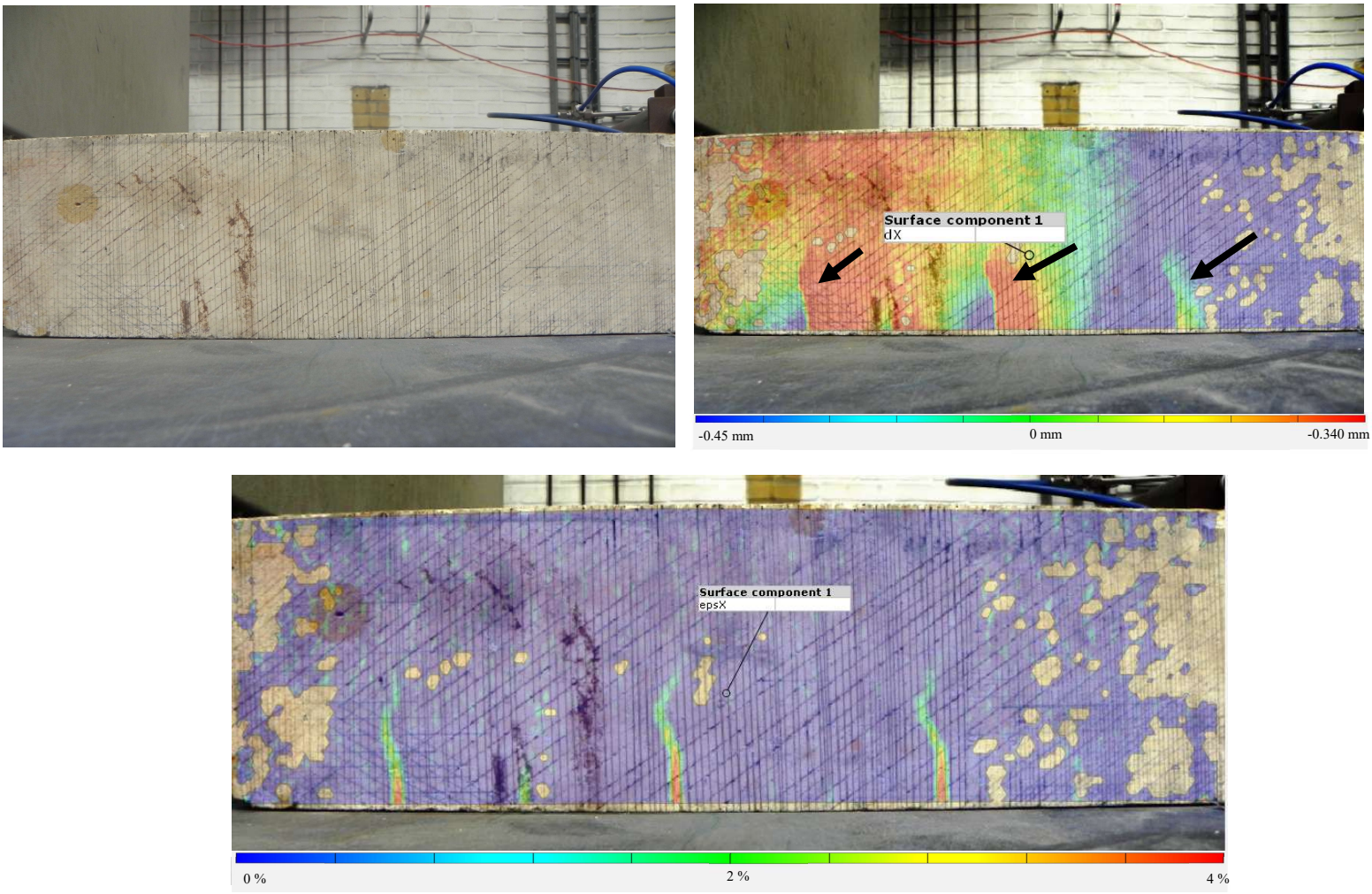

Figure 63 – Photo and respective DIC image of displacements x for XL4 in the first cycle after 16 minutes in the cooling stage.

This could be confirmed with the results obtained from the following cycles. In Figure 64 a photo taken after 30 minutes of the cooling stage in cycle 8 is presented, in which the cracks detected using DIC in Figure 63 can now be visually detected.

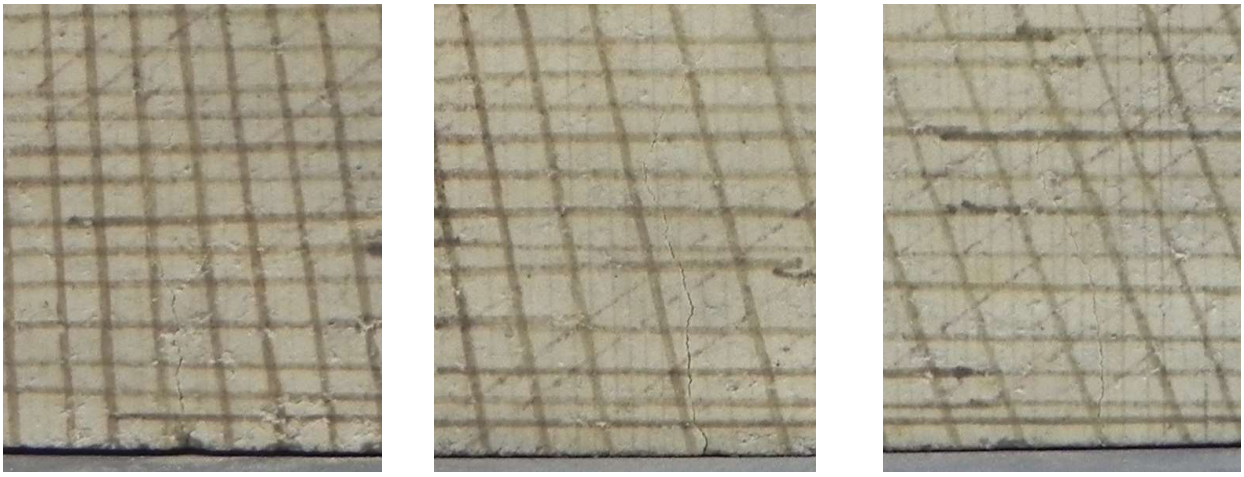

Figure 64 – Photo and respective DIC image of displacements x for XL4 in the x cycle after x minutes in the cooling stage.

This can also be seen in sample XL3, where the crack path observed in DIC in cycle 2 was coincident with the crack path observed when the sample fractured in Cycle 5. This is illustrated in Figure 65. It is also possible to see that by visual inspection only the beginning of the crack was detectable in cycle 2 whereas when using DIC the complete trajectory of the crack was possible to observe. This indicates that DIC not only allows to detect potential cracks that are not visually observed but also allows to predict the crack trajectory before it is visually noticeable.

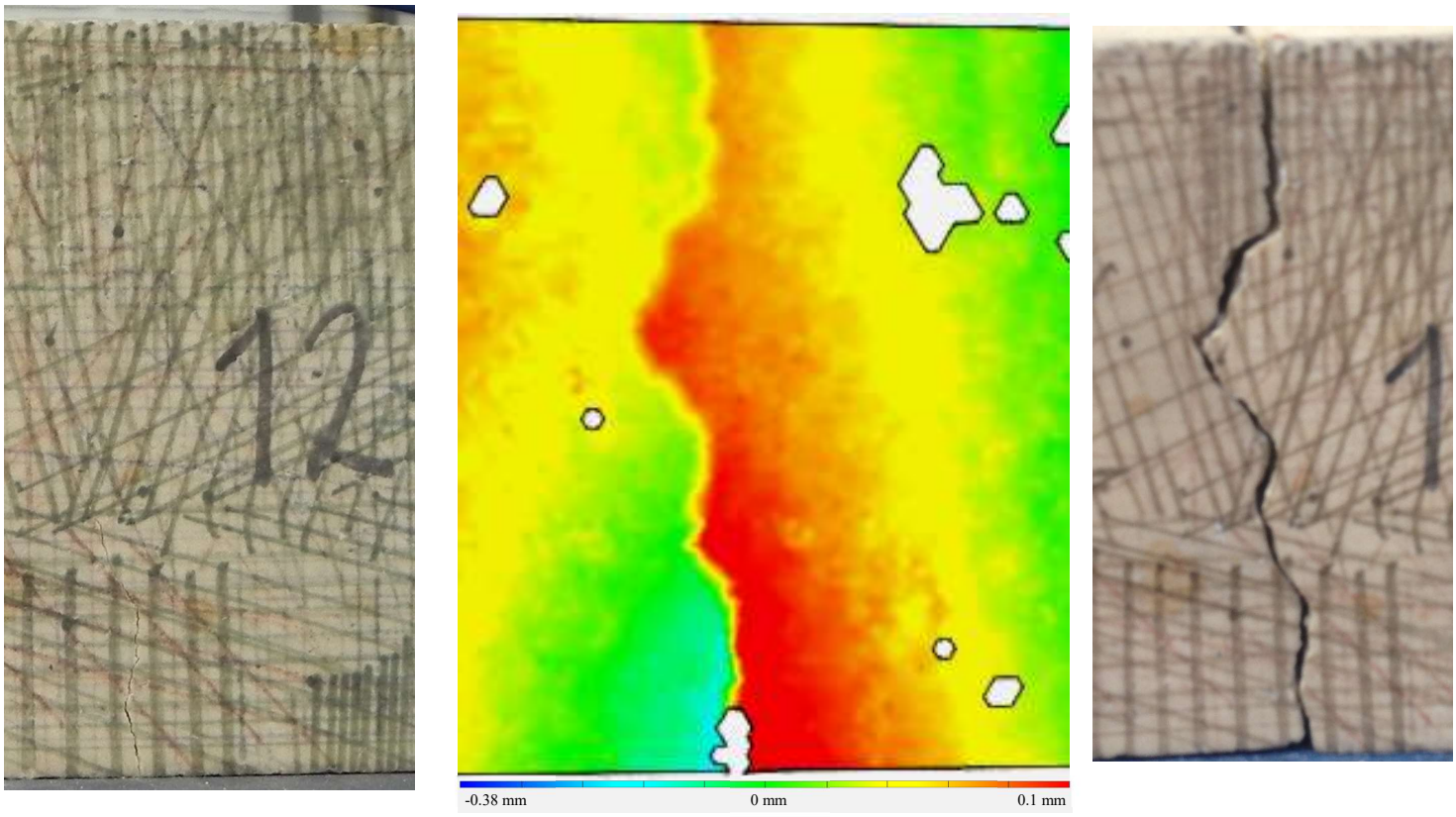

Figure 65 – Photo (left) and respective DIC (middle) of the displacements x for XL3 in the cycle 2 after 36 minutes in the cooling stage. Photo of sample after fracture, cycle 5 (right)

4.2.3 *Thermal Cycles*

Since one of the limitations of the thermal shock cyclic tests is the time necessary for each cycle, it was considered that studying the cooling and heating of the sample would be of the utmost importance to understand the optimal testing time.

In order to do so, a finite element model already developed in Ceramic Research Centre at Tata steel in Ansys R19.0 was adapted to the boundary conditions of the problem at hand and the temperature profiles were calculated for both cooling and heating situations. This analysis was only carried out for XL samples since they represent the most critical situation (more time to cool or heat). The boundary conditions considered were natural convection in the vertical walls and in the top horizontal wall. No boundary condition was considered in the bottom face, which represents in both cases a conservative approach since conduction happens either between the sample and the table or between the sample and the oven and reduces, in both situations, the cooling/heating time. Radiation and conduction in the sample was also considered. The room temperature considered was 20°C.

In Figure 66 it is possible to observe a section of the sample with the profiles of the temperatures developed after two hours of cooling and heating respectively. Symmetry in all planes was considered. The origin is situated in the centre of the sample.

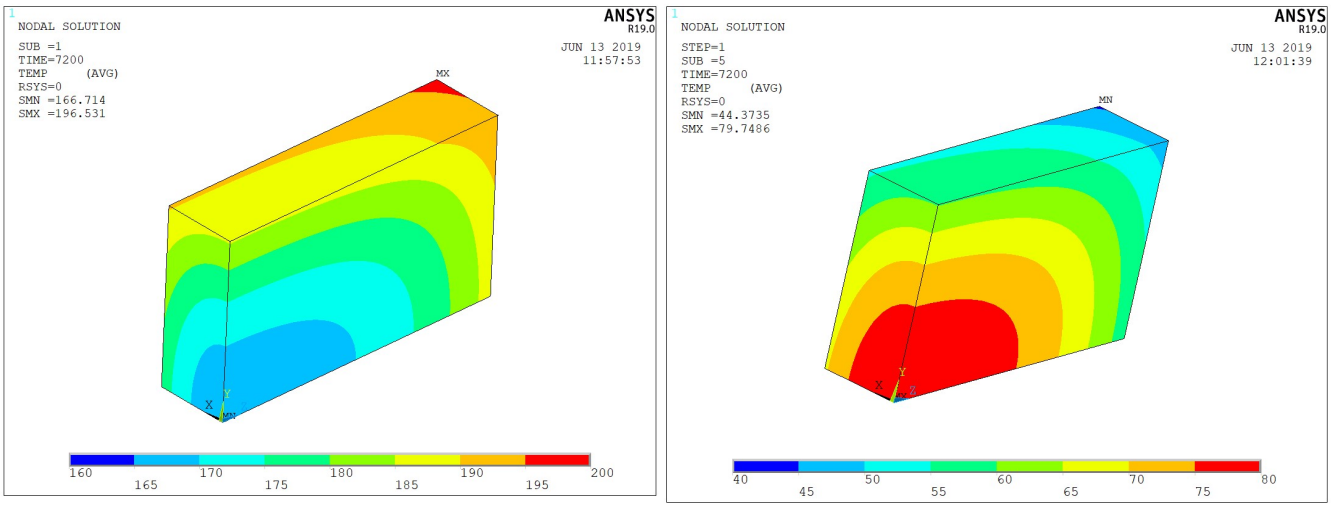

Figure 66 – Results of the simulation for both heating (left) and cooling (right) conditions.

In Graph 63 and Graph 64 the temperature evolution in the centre of the samples is plotted against the time for heating and cooling respectively.

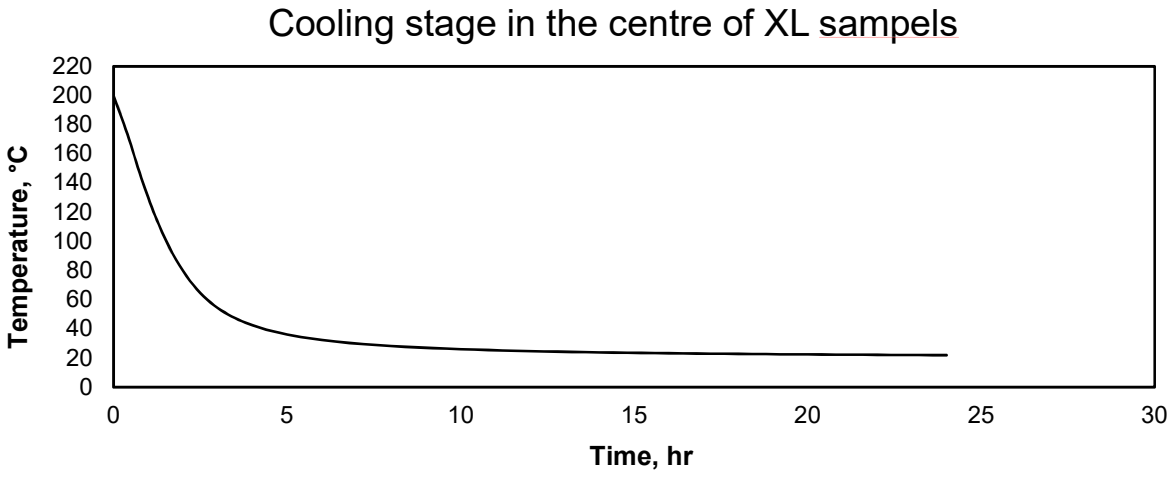

Graph 63 –Temperature profile in the centre of XL samples during heating.

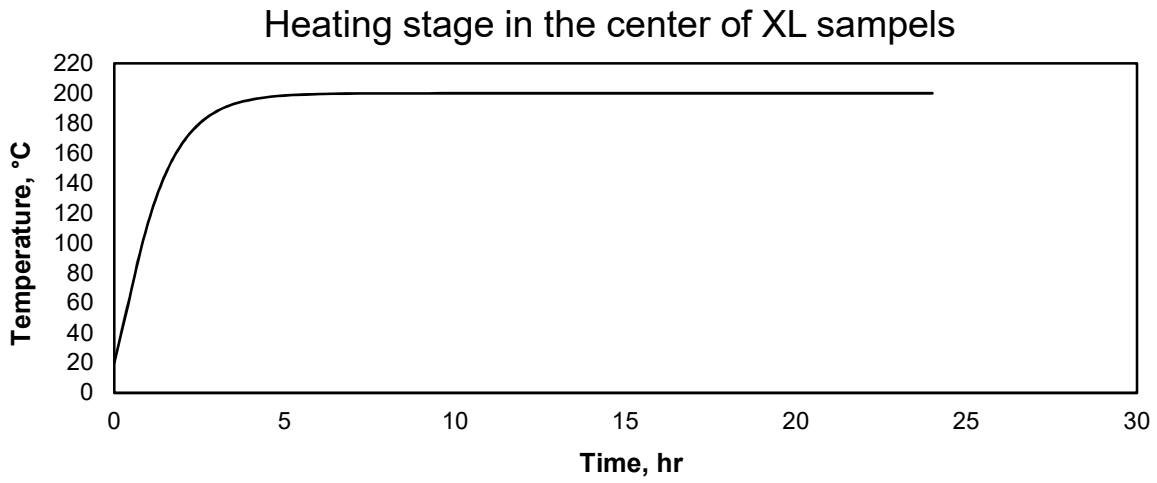

Graph 64 –Temperature profile in the centre of XL samples during cooling.

It is possible to observe that, even when neglecting the conduction mechanism in the bottom face, after 5 hours the temperature in the samples starts stabilizing. During heating, the temperature of 200 °C is reached at 12 hours. In cooling the temperature reached after 24 hours is 21.9 °C which is a higher temperature than the room temperature considered. With the results obtained, it can be concluded that the 24-hour cycles selected for the tests seem to be excessive.

Moreover, the model used is not considering conduction, which is even more relevant in the cooling stage, the one limiting the cycle test time. Other indications that this time may be excessive are the crack opening observed in DIC which, after less than three hours, had already closed and stabilized, indicating the reduction of the strain in the brick. Even with the results from the model the temperature after twelve hours in the centre would be 24 °C which would represent an almost insignificant difference.

A model considering the conduction mechanism should be developed to confirm the results observed.

4.3 Comparison between mechanical and thermal cycle tests

4.3.1 Damage Development

As was already seen throughout the analysis of mechanical and thermal shock results, despite the different nature of the results, similar behaviours were observed. The exponential behaviour was found for both bigger samples in thermal shock and samples tested at high amplitudes in mechanical cycles. A sigmoidal behaviour with three different phases of damage development was seen in both mechanical and thermal tests, for low amplitudes and lower sizes respectively. Although the saturation behaviour found for the samples of small dimensions in thermal shock was not seen in mechanical tests, the number of cycles in thermal shock is very reduced in comparison with the mechanical tests and therefore more cycles should be done to assess this phenomenon.

To compare both mechanical and thermal shock tests, the strain predicted by Lu and Fleck for each size tested is plotted in Graph 65 against the number of cycles for first crack appearance and in Graph 66 against the number of cycles to complete fracture. It is possible to observe that both graphs have the same trend – with the increase in the strain, there is a decrease in the number of cycles. This is more abrupt when considering the number of cycles to failure, as was expected since cracks usually take several cycles to fracture. To have a better interpretation of

the results, it would be necessary to test more sizes and to achieve a higher number of cycles since, for several sample sizes tested, failure was not achieved.

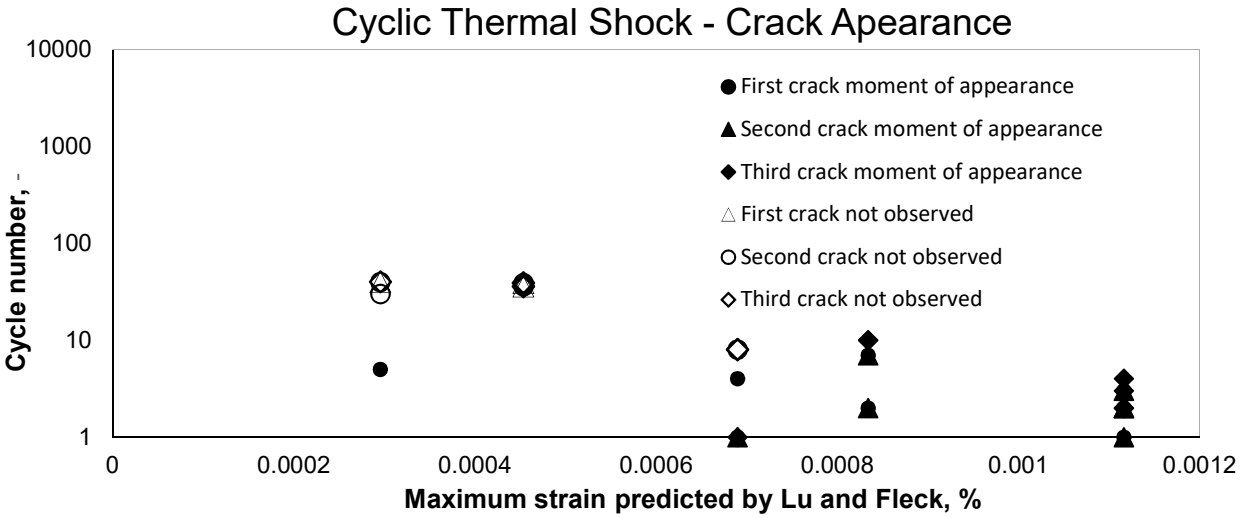

Graph 65 – Influence of the cycle number where first, second and third crack appear on the predicted Lu and Fleck strain, for each size of samples tested in thermal shock.

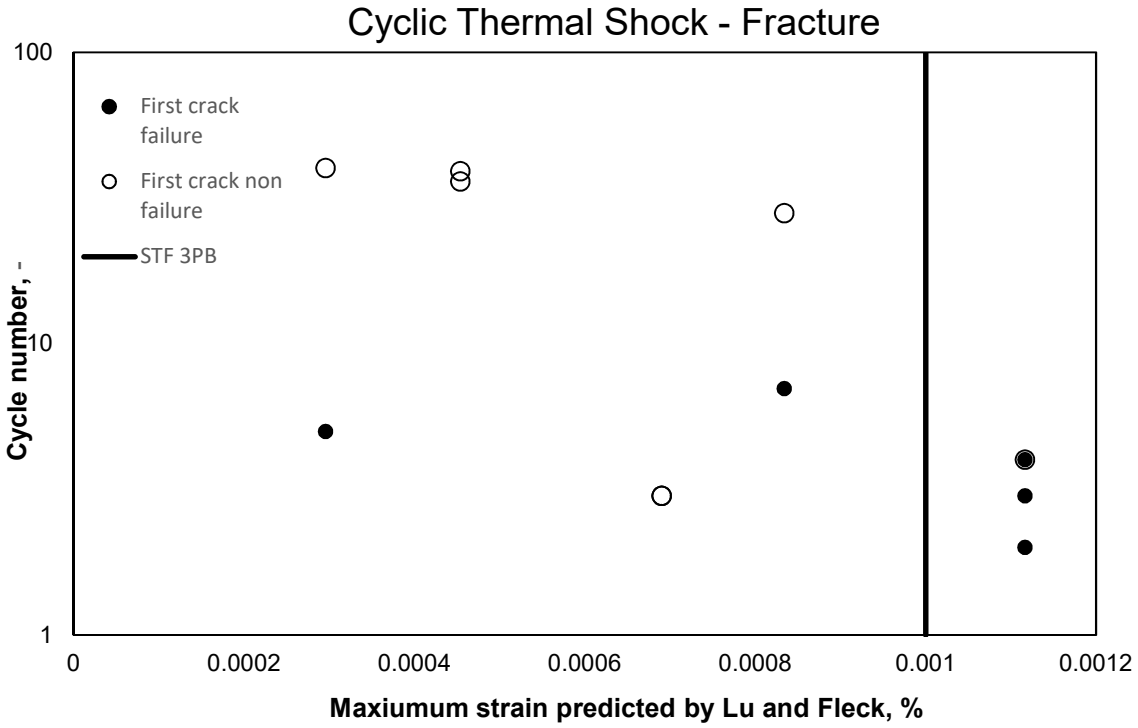

Graph 66 – Influence of the cycle number where first fracture occured on the predicted Lu and Fleck strain for each size of samples tested in thermal shock.

In Graph 67, it is possible to see the fatigue curve obtained in different mechanical tests for the same material. These tests were conducted previously to the present work by Andreev Kirill (2017) [7]. It is possible to observe that the number of cycles to failure increases in a linear way with strain amplitude. This trend is not applicable below 50 % of the strain amplitude to failure since failure is not achieved within the number of cycles tested.

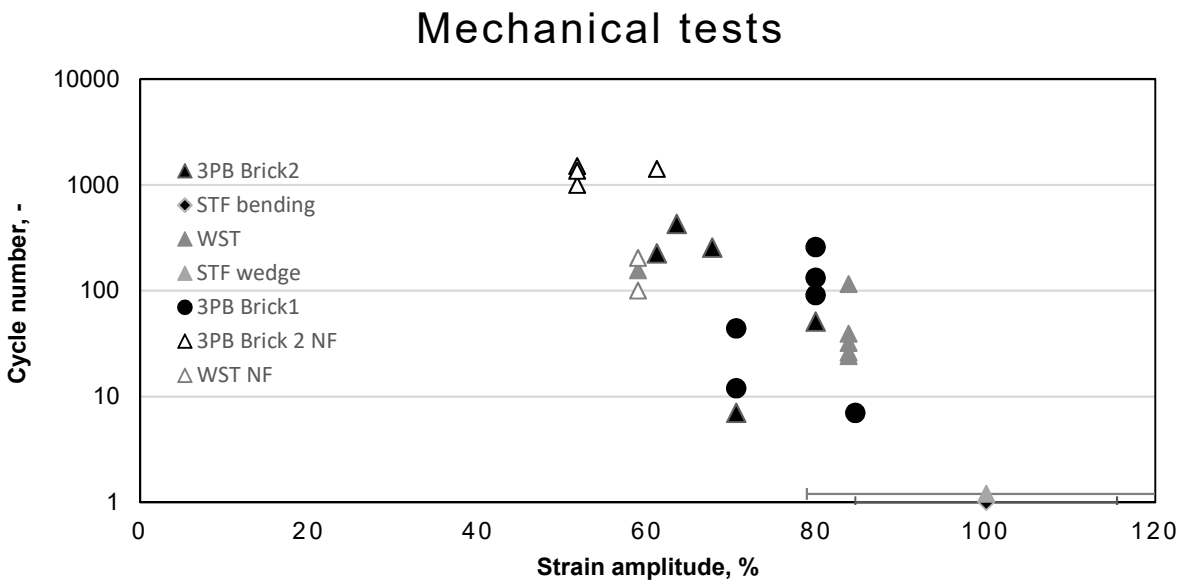

Graph 67 – Fatigue behaviour at room temperature for silica bricks obtained with different mechanical tests. 3PB - three point bending tests, WST – Wedge splitting test.

Graph 66 and Graph 67 could be compared since both refer to complete failure of the sample. However, the main limitation in this comparison is that the considered strain to failure (STF) of the material is highly dependent on the test methodology used to obtain it. The STF for the thermal shock tests is unknown. However, to enable a comparison the STF obtained for the three-point bending test is marked in Graph 66. Despite the few results available, it is possible to see a similar behaviour between mechanical and thermal shock results.

The thermal shock tests should be continued to enable a better comparison of the results. It could also be interesting to study more sizes of samples. Other important factor that should be considered is the fact that the strain calculated is estimated by the Lu and Fleck analysis, which agreed with the experimental results. However, this analysis does not consider all boundary conditions of the real tests and, therefore, variations from the estimated values can be expected. A Finite Element module could be developed to predict with better accuracy the strains developed during the cycles.

4.3.2 Roughness

The Hausdorff parameter obtained in both mechanical and thermal cycle tests was plotted against the respective number of cycles to failure. Due to the different nature of the tests, the number of cycles has a broad range of values. Thermal shock tests are very limited in the number of cycles achieved, since one cycle takes two days to be completed, while more than 100 cycles can be easily carried out in mechanical testing in a few hours.

It is also important to mention that the methodology used to measure the roughness, despite based on the same principle (spectral analysis), has differences which can influence the results obtained. In mechanical tests the profiles were obtained from the Analyser Software VR-H2AE. On the other hand, in thermal shock samples, it was not possible to use the same equipment due to the larger dimensions of the samples used. Therefore, the profiles were obtained using Adobe Photoshop (Appendix C).

Other motives that may affect the results can be the size effects and the nature of the tests. The wedge splitting test is a notched test and, therefore, a lower roughness can be expected when comparing with unnotched specimens.

Having this in consideration, it is possible to see that samples subjected to thermal-shock tests tend to have a higher roughness in comparison with samples from mechanical tests. The peak

observed in the thermal-shock samples is not verified in the mechanical tests due to the lack of data in the range where the peak was expected. Mechanical tests carried at high amplitudes to enable failure in 3 to 5 cycles should be carried out to determine whether this trend is observed or not.

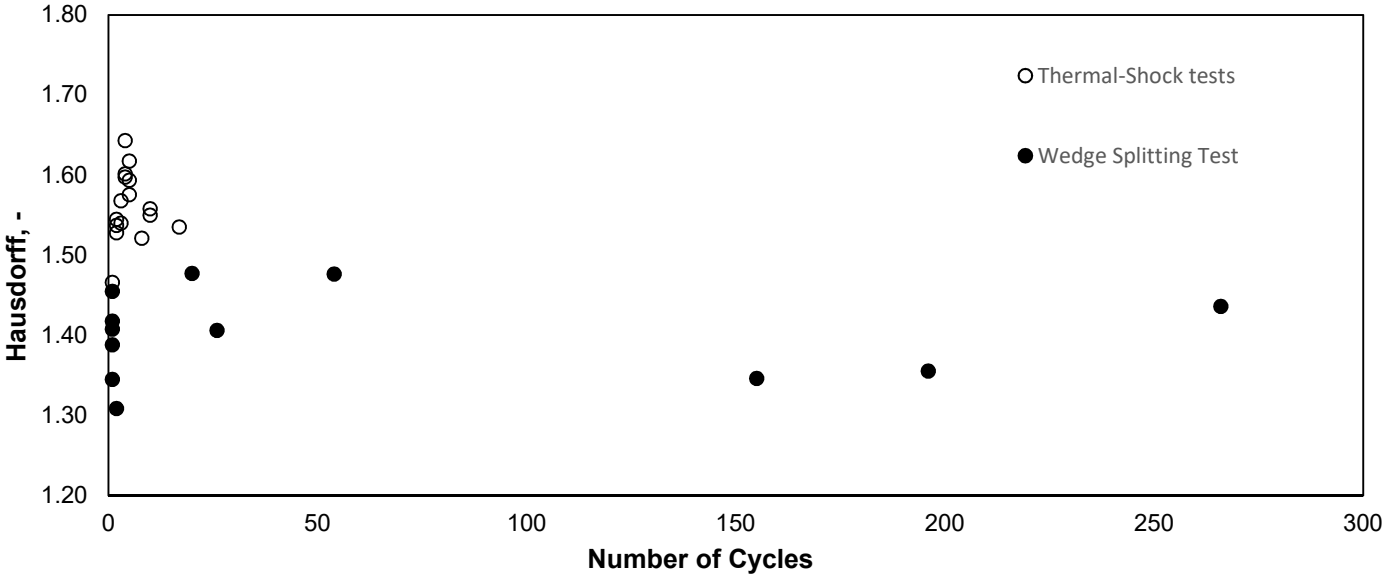

Graph 68 – Influence of number of cycles in the roughness for both mechanical and thermal-shock tests.

5 Conclusions

In the present work two methodologies were used to assess the resistance of silica bricks to thermal-mechanical loadings: mechanical and thermal-shock cyclic tests. These loads are one of the principal motives of failure of refractories in service conditions. The main parameters analysed in both testing methodologies were the roughness and the damage development. DIC was also used as an auxiliary technique in both approaches.

For the roughness analysis several parameters were studied: Sa, Sz, surface area and Hausdorff constant. The Hausdorff constant was considered to be the most representative parameter for this analysis. In thermal shock tests, it was possible to observe a peak in the roughness of the fracture surfaces, which was reached after 3-4 cycles. After this, the roughness decreases and starts stabilizing for a high number of cycles. For the samples which undergone mechanical tests, due to the lack of relevant data, this peak was not clear. More tests with higher amplitudes (low number of cycles) should be carried out to validate the presence of the trend found for thermal shock in mechanical cyclic degradation. It was also possible to observe that the roughness found in thermal shock tests was higher than that found in mechanical tests.

Similar behaviours were found for the damage development in mechanical and thermal tests. In both cases exponential behaviour was observed. This happened for large samples in thermal shock tests and for samples tested at high amplitudes in mechanical tests. For thermal shock tests of similar regimes, the size of the sample determines the intensity of the load. A sigmoidal behaviour was also observed for intermediate samples in thermal-shock tests and samples tested at lower amplitudes in mechanical tests. In thermal-shock tests for the samples of smaller dimensions damage stabilization occurred.

Regarding the crack growth, stabilization was observed in thermal shock tests, which is not seen in mechanical tests where cracks grew continuously. A correlation between the strain loads and the number of cycles to failure for both tests was also found and should be used for assessing the criticality of the service loads for the degradation of materials.

A theoretical algorithm was used to corroborate the results found. Both the maximum strain and the time at which it happened were predicted. The results obtained were in approximate agreement with what was observed in the experimental procedures.

Digital image correlation (DIC) enabled to observe how cracks form and the displacement fields developed during the test. This technique was proven to be useful since it allows measurements of the crack opening and strains occurring throughout the process to be made. In thermal shock tests, it was possible to observe that cracks could be detected at earlier stages and that the crack trajectory could be predicted when using DIC.

Other phenomenon observed was that in the first minutes of cooling cracks open, after which they stabilize and finally, after some time, depending on the size of the samples, cracks close. However, due to the irreversible strains, cracks never close completely and, therefore, start growing. This irreversible strain build-up is also observed in the cracks formed in the wedge splitting tests and, therefore, it is possible to correlate both crack development mechanisms.

The DIC technique should be further explored and optimized. In the present work the goal was not to study thoroughly DIC but for it to be used as an auxiliary technique to corroborate the results observed and to study the possibility and interest of its application in the tests conducted.

It was possible to observe that the thermal shock tests are highly influenced by the size of the samples selected and that the standard size might not be the most representative of the behaviour during the service conditions. Therefore, selecting a representative sample size for the testing methodologies is of extreme importance.

.

6 Future Work

The research conducted in the present dissertation raised some questions that should not be left unexplored.

On the one hand, the thermal-shock cyclic tests should be continued to all samples which failure was not achieved. This is important to enable a better comparison with the mechanical tests and to assess if damage stabilization is still observed for a higher number of cycles. Samples with intermediate sizes could also be studied in thermal shock to have a better understanding of the size influence on the strains developed. It would also be important to increase the number of samples studied for each size to have a more representative analysis.

In the present work the maximum strains developed in thermal shock cycles for each size were estimated using a theoretical algorithm. However, a better estimation could be obtained if a Finite Element model is developed considering all the boundary conditions of the tests. This model could also help accessing whether the 24-hour cycles are confirmed to be excessive for the testing methodology used. Tests at different temperatures could also be interesting to understand the influence of this parameter in the damage and crack development.

Due to the large size of the samples in the thermal shock tests, the methodology used to measure the roughness was not the same for these samples and for samples which undergone mechanical tests. It would be interesting to define a methodology which allowed to measure the roughness parameters in both sample types in the same way.

On the other hand, mechanical tests with higher amplitudes (low number of cycles) should be carried out to validate the trend found in the roughness and to determine the location of its peak. The samples used for wedge splitting tests were notched, which has a high influence on the roughness of the fracture surface and, therefore, repeating the tests with unnotched samples is proposed. This would enable to understand the influence of the notch and to have a better comparison with the roughness found for fracture surfaces in thermal shock tests. Mechanical tests at high temperature could also be carried out to understand the influence of this parameter in the damage development.

Digital Image Correlation should be further explored and optimized. The ideal parameters and surface pattern should be studied to allow a better accuracy of the results. DIC was used to measure crack opening. However, other measurements such as the crack process zone developed at each cycle could be measured and further studied.

References

1. Lu, T.J. and N.A. Fleck, *The thermal shock resistance of solids.* Acta Materialia, 1998. **46**(13): p. 4755-4768.
2. Sarkar, R., *Refractory technology : Fundamentals and Applications*, ed. C. Press. 2016.
3. Lee, W.E., *4.12 - Refractories*, in *Comprehensive Composite Materials*, A. Kelly and C. Zweben, Editors. 2000, Pergamon: Oxford. p. 363-385.
4. Taikabutsu Gijutsu, K., *Refractories handbook*. 1998, Tokyo: Technical Association of Refractories, Japan.
5. Schacht, C., *Refractories Handbook*. 2004: CRC Press.
6. Damhof, F., W.A.M. Brekelmans, and M.G.D. Geers, *Non-local modeling of thermal shock damage in refractory materials.* Engineering Fracture Mechanics, 2008. **75**(16): p. 4706-4720.
7. Andreev, K., et al., *Cyclic fatigue of silica refractories – effect of test method on failure process.* Journal of the European Ceramic Society, 2017. **37**(4): p. 1811-1819.
8. E. Lee, W., S. Zhang, and M. Karakus, *Refractories: Controlled microstructure composites for extreme environments: SPECIAL SECTION: Characterisation of Ceramics (Guest Editor: M. H. Lewis)*. Vol. 39. 2004.
9. García-Prieto, A., et al., *Influence of microstructural characteristics on fracture toughness of refractory materials.* Journal of the European Ceramic Society, 2015. **4**.
10. Lamon, J., *Introduction*, in *Brittle Fracture and Damage of Brittle Materials and Composites*, J. Lamon, Editor. 2016, Elsevier. p. xi-xiv.
11. Šavija, B., et al., *Modelling of deformation and fracture for a model quasi-brittle material with controlled porosity: Synthetic versus real microstructure*. 2018.
12. Lino Alves, F.J., *Effect of the bridging mechanism on ceramics toughness.* Revista da Sociedade Portuguesa de Materiais, 2000. **12**(2): p. 10-15.
13. Cornetti, P., et al., *Finite fracture mechanics: A coupled stress and energy failure criterion.* Engineering Fracture Mechanics, 2006. **73**(14): p. 2021-2033.
14. Griffith, A.A., *The Phenomena of Rupture and Flow in Solids.* Philosophical Transactions of the Royal Society of London. Series A, Containing Papers of a Mathematical or Physical Character, 1921. **221**: p. 163-198.
15. Hou, C., et al., *A generalized maximum energy release rate criterion for mixed mode fracture analysis of brittle and quasi-brittle materials.* Theoretical and Applied Fracture Mechanics, 2019. **100**: p. 78-85.
16. Mirsayar, M.M., et al., *Tangential strain-based criteria for mixed-mode I/II fracture toughness of cement concrete.* Fatigue & Fracture of Engineering Materials & Structures, 2018. **41**(1): p. 129-137.

17. Xie, H., et al., *Energy analysis and criteria for structural failure of rocks.* Journal of Rock Mechanics and Geotechnical Engineering, 2009. **1**(1): p. 11-20.

18. Pique, J., *Fracture process zone of quasi-brittle materials : a model material approach*. 2002, Technische Universiteit Eindhoven: Eindhoven.

19. Hasselman, D.P.H., *Unified theory of thermal shock fracture initiation and crack propagation in brittle ceramics.* J. Amer. Ceram. Soc., 1969. **52**: p. 600-604.

20. Harmuth, H. and R.C. Bradt, *Investigation of refractory brittleness by fracture mechanical and fractographic methods*. Vol. 62. 2010. 6-10.

21. Nakayama J, I.M., *Experimental evidence for thermal shock damage resistance.* Am. Ceram. Soc. Bull. **64**(11): p. 671-675.

22. Andreev, K., et al., *Thermal and mechanical cyclic tests and fracture mechanics parameters as indicators of thermal shock resistance – case study on silica refractories.* Journal of the European Ceramic Society, 2019. **39**(4): p. 1650-1659.

23. Damhof, F., et al., *A Novel Experimental Approach to Investigate Thermal Shock Damage in Refractory Materials*. Vol. 84. 2007.

24. Case, E.D., *The saturation of thermomechanical fatigue in brittle materials*. 2002. 137-208.

25. Rendtorff, N. and A. Esteban, *Thermal Shock Resistance (TSR) and Thermal Fatigue Resistance (TFR) of Refractory Materials. Evaluation Method Based on the Dynamic Elastic Modulus*. 2014. p. 5119-5128.

26. Schneider, G.A. and G. Petzow, *Thermal Shock and Thermal Fatigue Behavior of Advanced Ceramics*. 2013: Springer Netherlands.

27. Hino, Y. and Y. Kiyota, *Fatigue Failure and Thermal Spalling Tests to Evaluate Dynamic Fatigue Fracture of MgO–C Bricks.* ISIJ International, 2011. **51**(11): p. 1809-1818.

28. Manson, S.S., *Thermal stress and low-cycle fatigue*. 1966: McGraw-Hill.

29. Fissolo, A., et al., *Predicton of crack initiation and growth under thermal fatigue*, in *Thermomechanical Fatigue and Fracture*, M.H. Aliabadi, Editor. 2002.

30. Andreev, K., N. Shetty, and E. Verstrynge, *Acoustic emission based damage limits and their correlation with fatigue resistance of refractory masonry.* Construction and Building Materials, 2018. **165**: p. 639-646.

31. Thummen, F., C. Olagnon, and N. Godin, *Cyclic fatigue and lifetime of a concrete refractory.* Journal of the European Ceramic Society, 2006. **26**(15): p. 3357-3363.

32. Harmuth, H., et al., *Investigation of the nonlinear fracture behaviour of ordinary ceramic refractory materials.* Materials Science and Engineering: A, 1996. **214**(1): p. 53-61.

33. Brühwiler, E. and F. Wittmann, *The wedge splitting test, a new method of performing stable fracture mechanics tests*. Vol. 35. 1990. 117-125.

34. Allaoui, S., et al., *Digital Image Correlation measurements of mortarless joint closure in refractory masonries.* Construction and Building Materials, 2018. **162**: p. 334-344.

35. McCormick, N. and J. Lord, *Digital Image Correlation.* Materials Today, 2010. **13**(12): p. 52-54.

36. Higuchi, T., *Approach to an irregular time series on the basis of the fractal theory*. Vol. 31. 1988. 277-283.

37. Sahoo, P., *1 - Surface topography*, in *Tribology for Engineers*, J.P. Davim, Editor. 2011, Woodhead Publishing. p. 1-32.

38. A. Majumdar, A. and B. Bhushan, *Role of Fractal Geometry in Roughness Characterization and Contact Mechanics of Surfaces*. Vol. 112. 1990. 205-216.

39. Militky, J. and V. Bajzik, *Surface Roughness and Fractal Dimension*. Vol. 92. 2001. 91-113.

40. Seismology, G., et al., *Fault slip distribution and fault roughness*. Vol. 187. 2011. 959-968.

41. Caporossi, P., P. Mazzanti, and F. Bozzano, *Digital Image Correlation (DIC) Analysis of the 3 December 2013 Montescaglioso Landslide (Basilicata, Southern Italy): Results from a Multi-Dataset Investigation*. Vol. 7. 2018. 372.

42. Keyence. *Area Roughness Parameters*. Introduction to Roughness 2019 [cited 2019 March].

43. Zhang, X.B. and J. Li, *A failure criterion for brittle and quasi-brittle materials under any level of stress concentration.* Engineering Fracture Mechanics, 2008. **75**(17): p. 4925-4932.

44. DIN, *Methods of test for dense shaped refratory products* in *Part 11 : Determination of the resistance to thermal shock (CEN/TS 993-11)*. 2003.

45. Reinhardt, H.W., *2 - Factors affecting the tensile properties of concrete*, in *Understanding the Tensile Properties of Concrete*, J. Weerheijm, Editor. 2013, Woodhead Publishing. p. 19-51.

46. Dai, Y., D. Gruber, and H. Harmuth, *Determination of the fracture behaviour of MgO-refractories using multi-cycle wedge splitting test and digital image correlation.* Journal of the European Ceramic Society, 2017. **37**(15): p. 5035-5043.

Appendix A: Technical drawing S1 and S

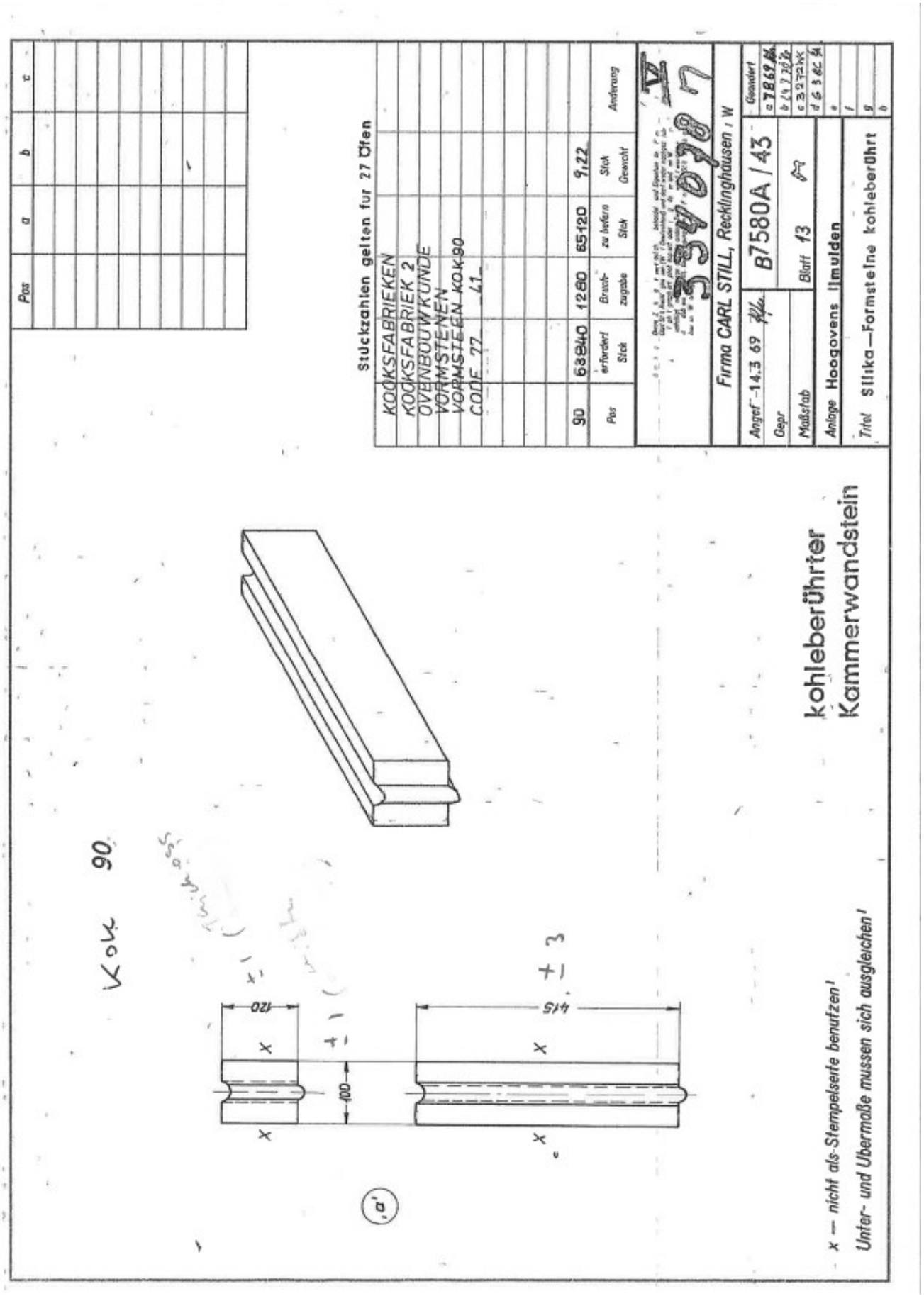

Figure A1 – Technical Drawing of XL samples

Appendix B: Crack Development (Area Calculation)

The area of crack development throughout the cycles was estimated based on the visual development registered at each cycle. For example, examining Figure B1, it is possible to see a crack that developed throughout different cycles.

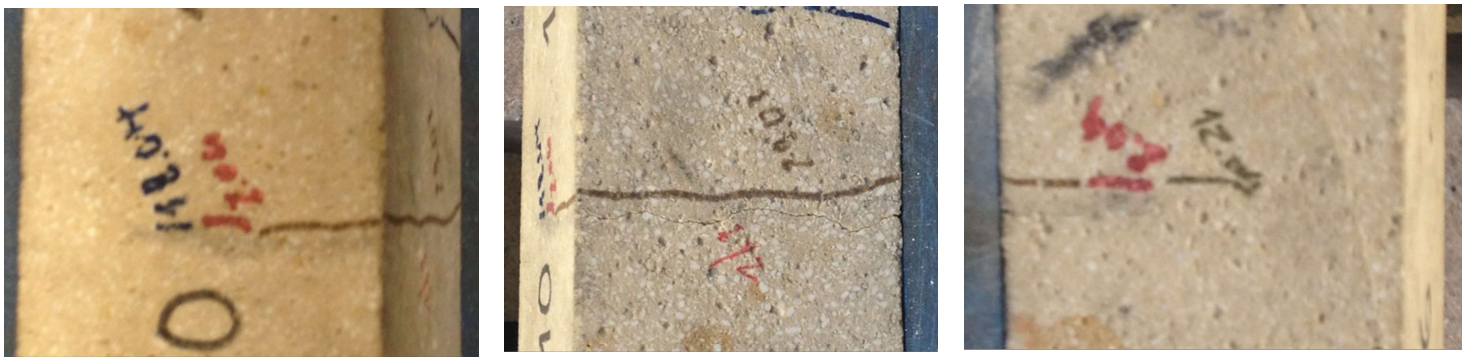

Figure B1 – Crack zy2 in SI1 in different faces: Side A, bottom and side b (left to right)

By measuring the distance grown at each cycle and by approximating the area to simple geometric figures (squares, rectangles, triangles) it is possible to define areas of crack development for each cycle – Figure B2.

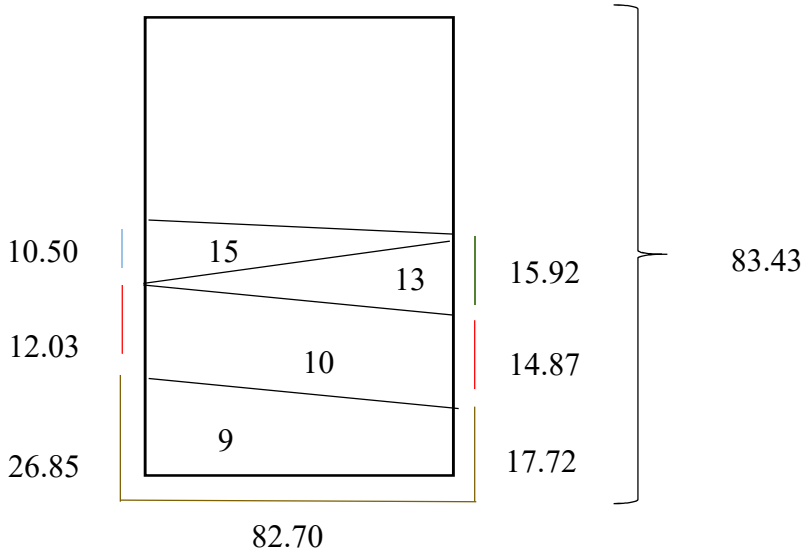

Figure B2 – Scheme of crack development throughout the different cycles

The percentual grow in each cycle can then be easily calculated by eq B.1 to B.5.

$$A\ total = W * H = 83.43 * 82.70 = 6898.83\ \text{mm}^2 \quad \text{(B.1)}$$

$$A\ 9 = \frac{\left(\frac{dh1+dh2}{2} * dw\right)}{A\ total} * 100 = \frac{\left(\frac{26.85+1\ .720}{2} * 82.70\right.}{A\ total} * 100 = 26.73\ \% \quad \text{(B.2)}$$

$$A10 = \frac{\left(\frac{dh1+dh}{2} * dw\right)}{A\ total} * 100 = \frac{\left(\frac{14.87+12.03}{2} * 82.70\right.}{A\ total} = 16.12\ \% \quad \text{(B.3)}$$

$$A13 = \frac{\left(\frac{dh}{2} * dw\right.}{A\ total} * 100 = \frac{\left(\frac{15.92}{2} * 82.70\right)}{A\ total} * 100 = 9.54\ \% \quad \text{(B.4)}$$

$$A15 = \frac{\left(\frac{h}{2} * w\right)}{A\ total} * 100 = \frac{\left(\frac{10.50}{2} * 82.70\right)}{A\ total} * 100 = 6.30\ 5\% \quad \text{(B.5)}$$

where:

An, is the percentual increase in the area in the respective n cycle.
dh, is the distance grown in the normal direction
dw, is the distance grown in the transversal direction
A total, is the total area created if crack fractured.

Appendix C: Crack Profile

Photographs of the crack were used and manipulated using Adobe Photoshop in order to obtain a graphic representation of the crack profile. Firstly, the boundary of the profile was outlined using the magic wand tool. After selecting all the boundary area, the contrast was changed to the maximum to allow an easy visualization of the boundary of the crack. One of the processed images can be seen in Figure C1.

Figure C1 – Crack profile highlighted.

Afterwards, a grid was created to allow the measurement of the points in the profile. The size of the grid was 0.5x0.5 cm in the photograph which, after applying a scale factor, represented a grid of 0.8 x 0.8 mm. This grid can be seen in Figure C2 (the size of the grid was selected based on the resolution of the photographs taken).

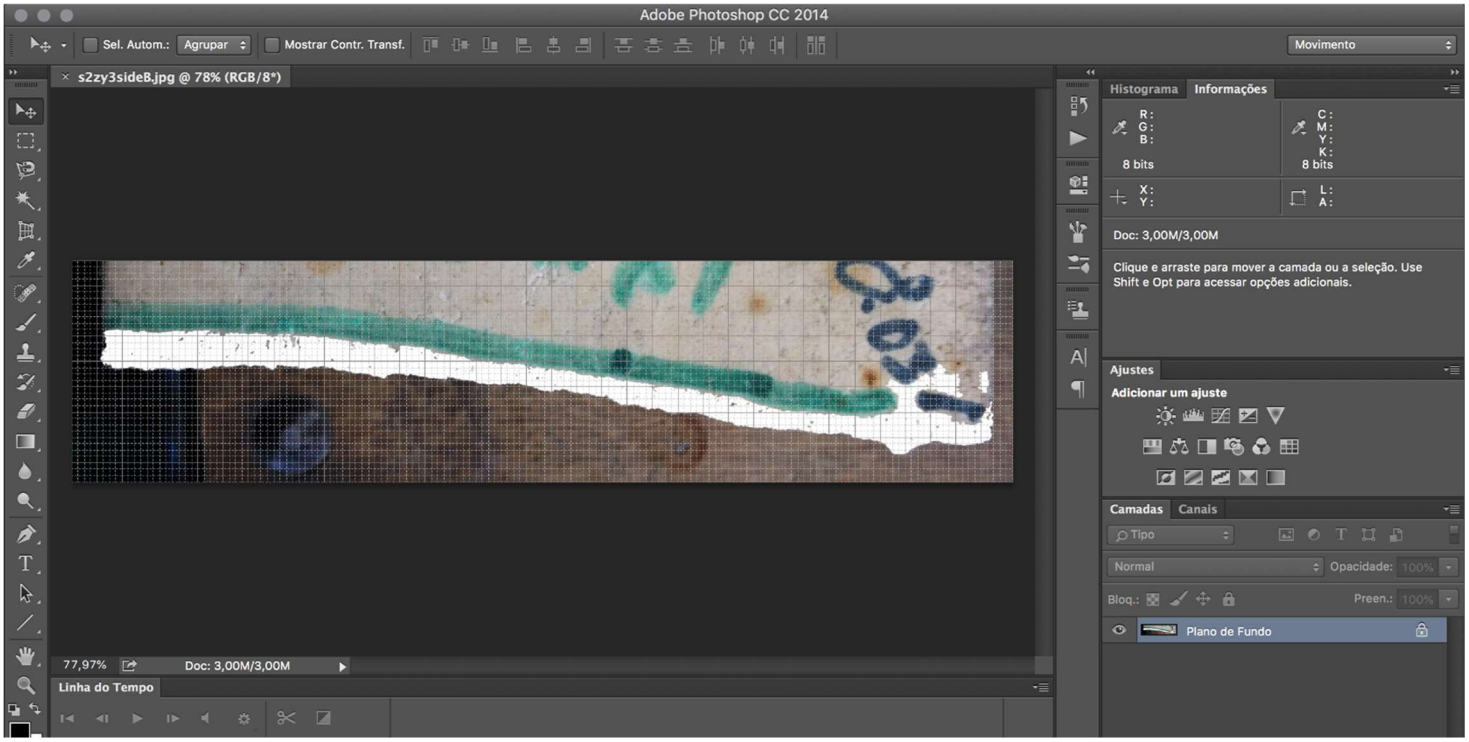

Figure C2 – Grid created using Adobe Photoshop.

By selecting one point in which the grid intersects with the profile, it is possible to define the xy coordinates. This procedure was done manually to all points that intersected with the profile. The coordinates obtained are referenced to the zero of the grid, and therefore a translation of the coordinates was done in order to consider the zero in the bottom of the crack. A scale factor was also applied to obtain the corrected values.

After recording the coordinates, the profile can easily be plotted in a xy graph. In Figure C3, it is possible to see the profile calculated for sample s2 crack zy1 and the respective photo of the real profile of the crack.

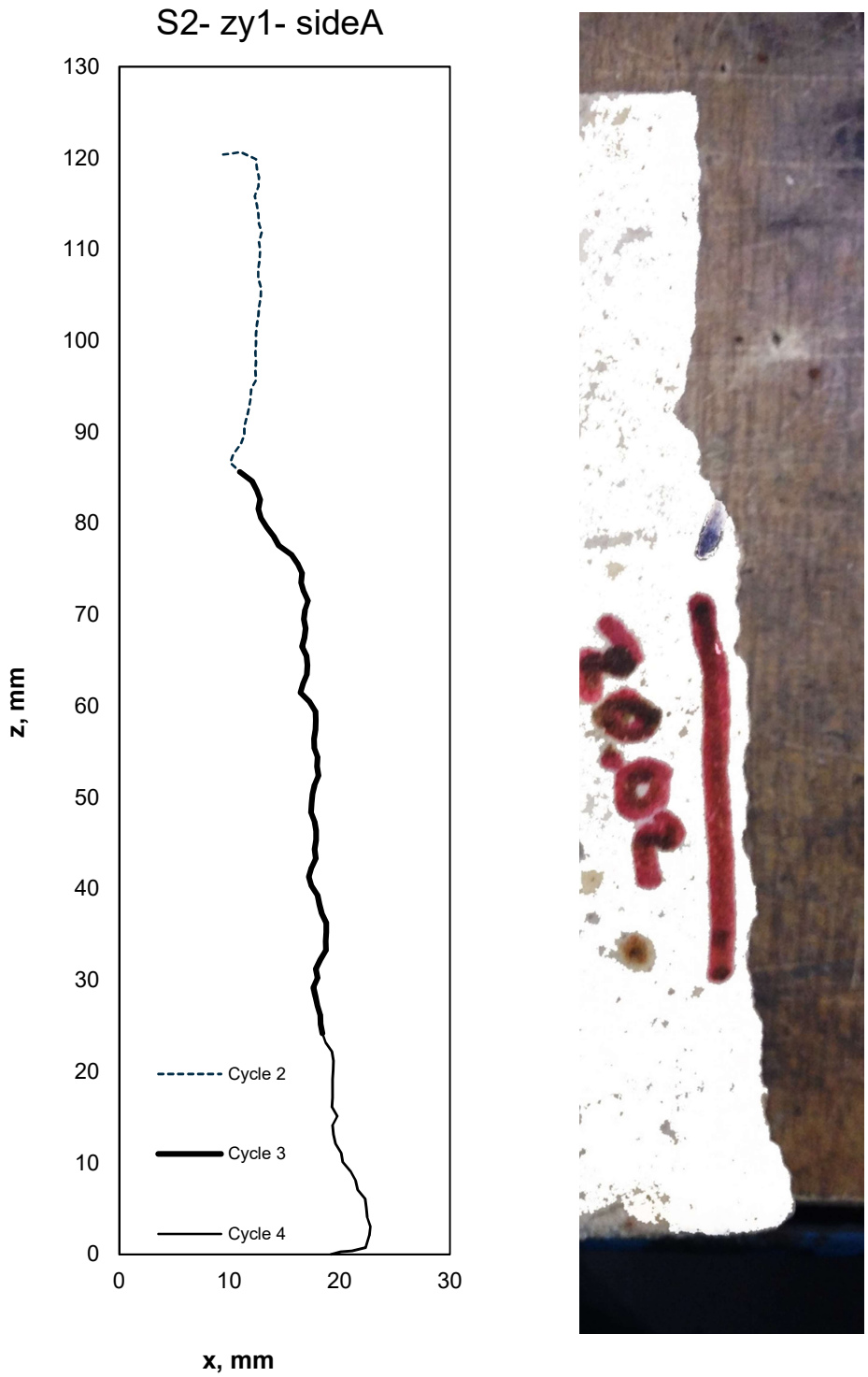

Figure C3 – Comparison between real profile and calculated profile

Appendix D: Digital Image Correlation

The software used for digital image correlation was GOM Inspect 2018. The software allows to import a succession of photos, which should be numbered chronologically. By default, the first photo is considered as the reference photo and, therefore, all the measurements will be relative to it. The photos imported should be taken with the camera and the sample in the exact same position to allow accuracy in the measurements. After importing the pictures, it is necessary to define desired area for the measurements- Figure D1.

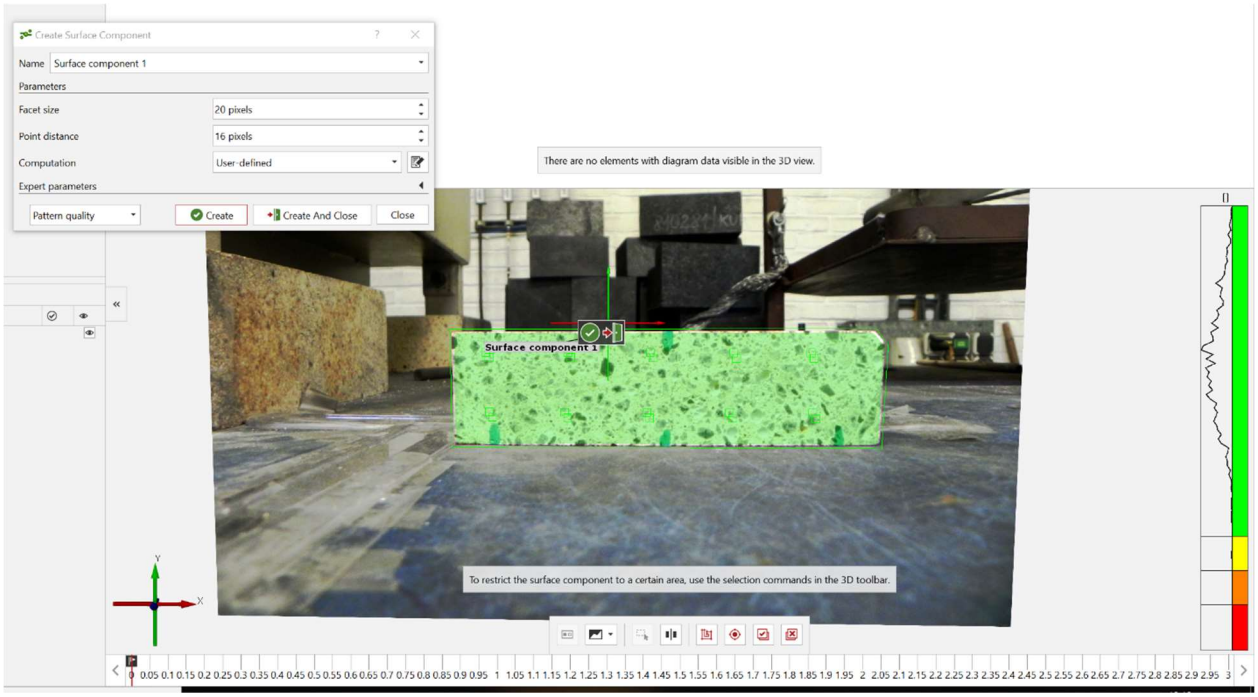

Figure D1 – Definition of the Surface Component and assessment of Pattern quality.

The software allows to see the quality of the surface selected (good measurement quality is represented in green). When the surface does not present a natural pattern that allows a good quality measurement, it is necessary to create an artificial pattern in the surface, Figure D2.

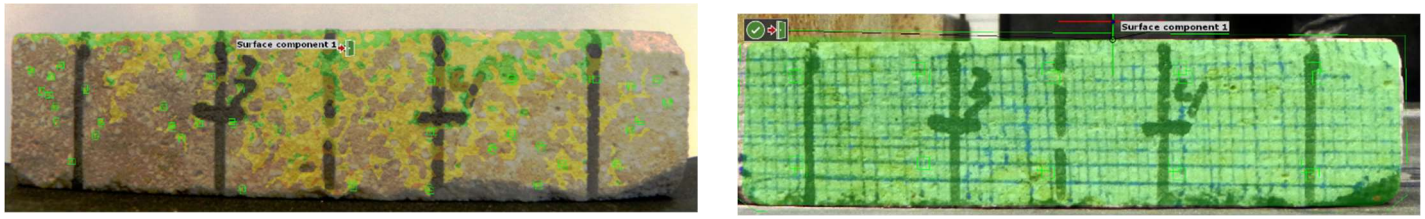

Figure D2 – Quality of pattern for natural surface (left) and artificial pattern in surface (right).

After defining the surface, it is necessary to define a scale, which can be done by defining the real distance between two points in the picture - Figure D3. The scale is automatically applied to all photos.

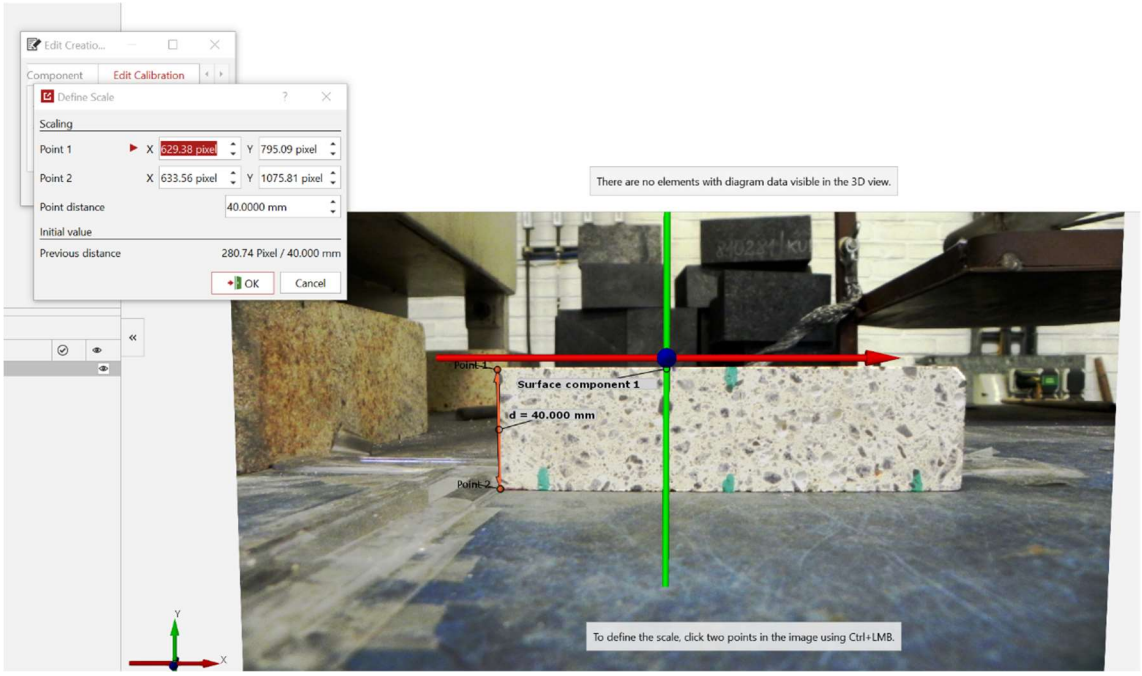

Figure D3 – Definition of a scale in GOM Inspect Software.

Afterwards, the desired measuring parameter can be selected and automatically calculated.

The setup chosen to allow the same positioning of the bricks after leaving the oven is illustrated in Figure D4 and consists of two fixed perpendicular rulers which allow the alignment of two faces of the brick. The camera was kept in the same position during the cycles.

A test was carried out to assess the accuracy of the set up and the measurements. A brick, which was already fractured, was positioned using the same set up. Two different displacements were then applied to one of the parts of the brick and measured using a calliper, as can be seen in Figure D5.

Figure D4 – Set up used for DIC.

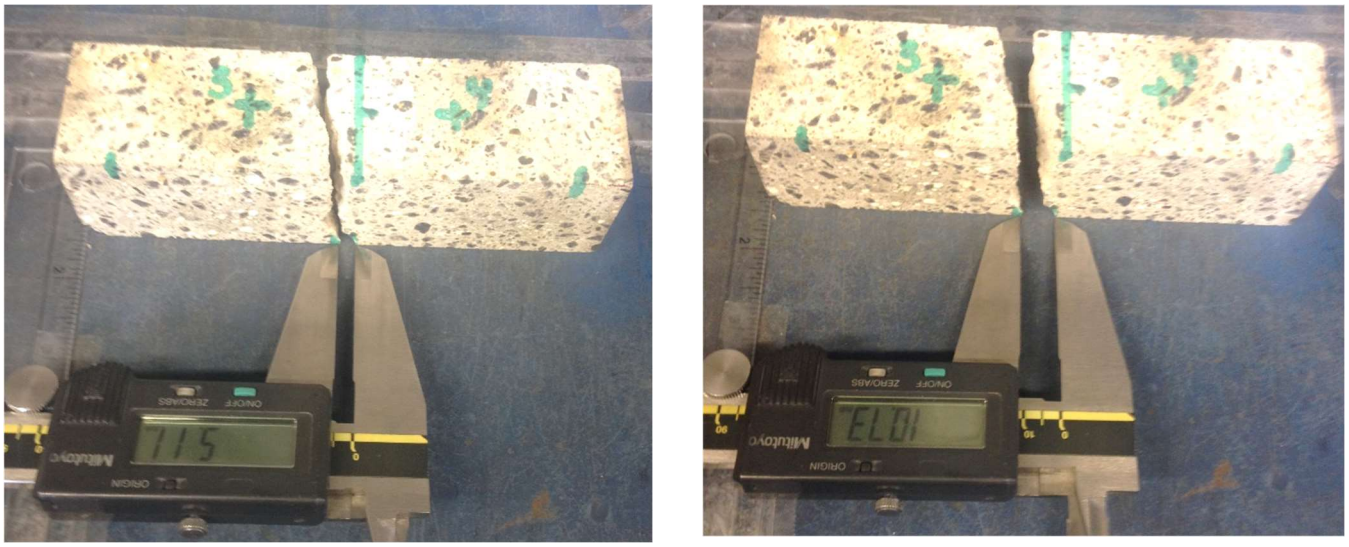

Figure D5 – Measurements of two different displacements, d2 and d3 (from right to left).

The results obtained using the GOM inspected software are represented in Figure D6.

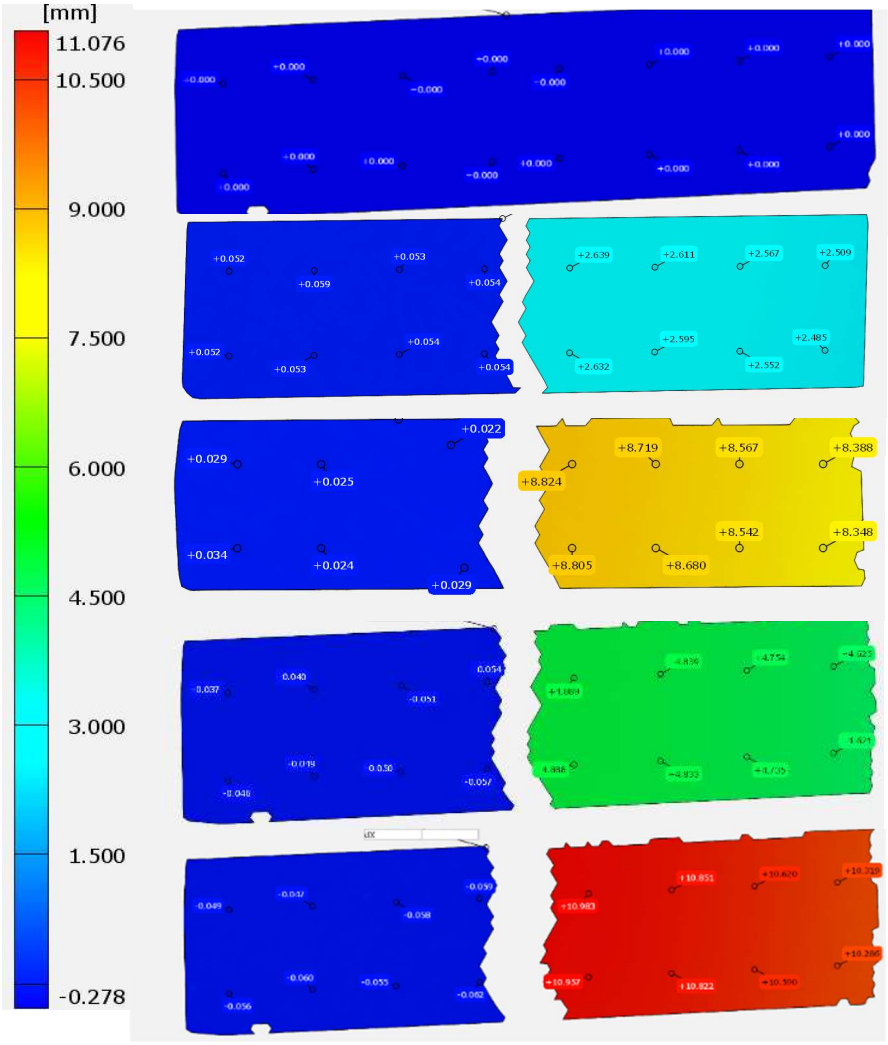

Figure D6 – Displacement in x direction: reference photo, d1 to d4 (from top to bottom).

In Table D1, the average of the measured displacements using digital image correlations as well as the standard deviations and the error when comparing the DIC results with the calliper measured are presented.

Table D1 – Displacement in x direction: Reference photo, d1 and d2 (from top to bottom)

Displacement	Average DIC, mm	STD DIC, mm	Calliper measurement, mm	Error, %
d1	2.70	0.14	2.29	17.90%
d2	4.77	0.11	5.11	6.65 %
d3	8.60	0.18	8.16	5.39%
d4	10.68	0.27	10.73	0.47 %

The maximum error found was 6.6 %, which could have been aggravated since between the pictures the calliper was used to measure the displacement, possibly affecting the positioning of the brick. This might also be the reason why the values have a slight variation trough the length of the sample. Even so the standard deviation of the measurements was inferior than 0.3 mm which corresponds approximately to less than 3 % of the displacement measured.

Even with this error, it was considered that this methodology could be of interest for the present work since it allows to evaluate the deformation during cooling as well as many possibilities to study crack opening.

In Graph D1, it is possible to observe accuracy of the measurements obtained.

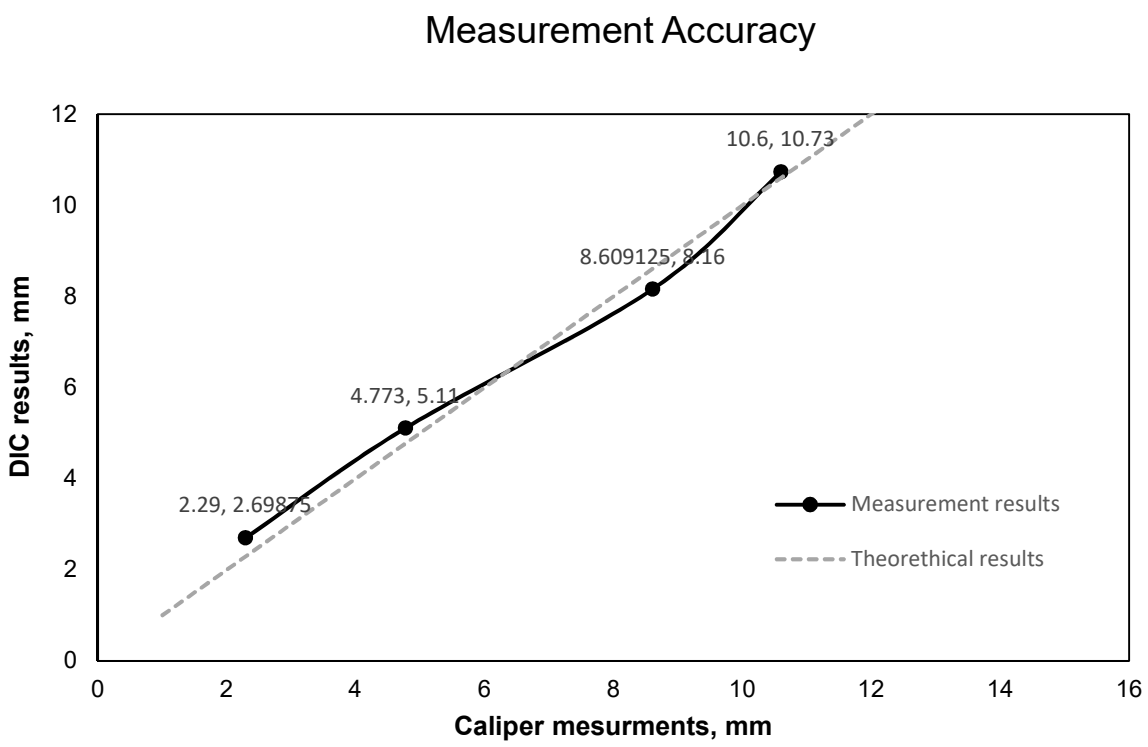

Graph D1 – Measurement comparison between results obtained from DIC and from a calliper.

Appendix E: Crack Development

- XL1

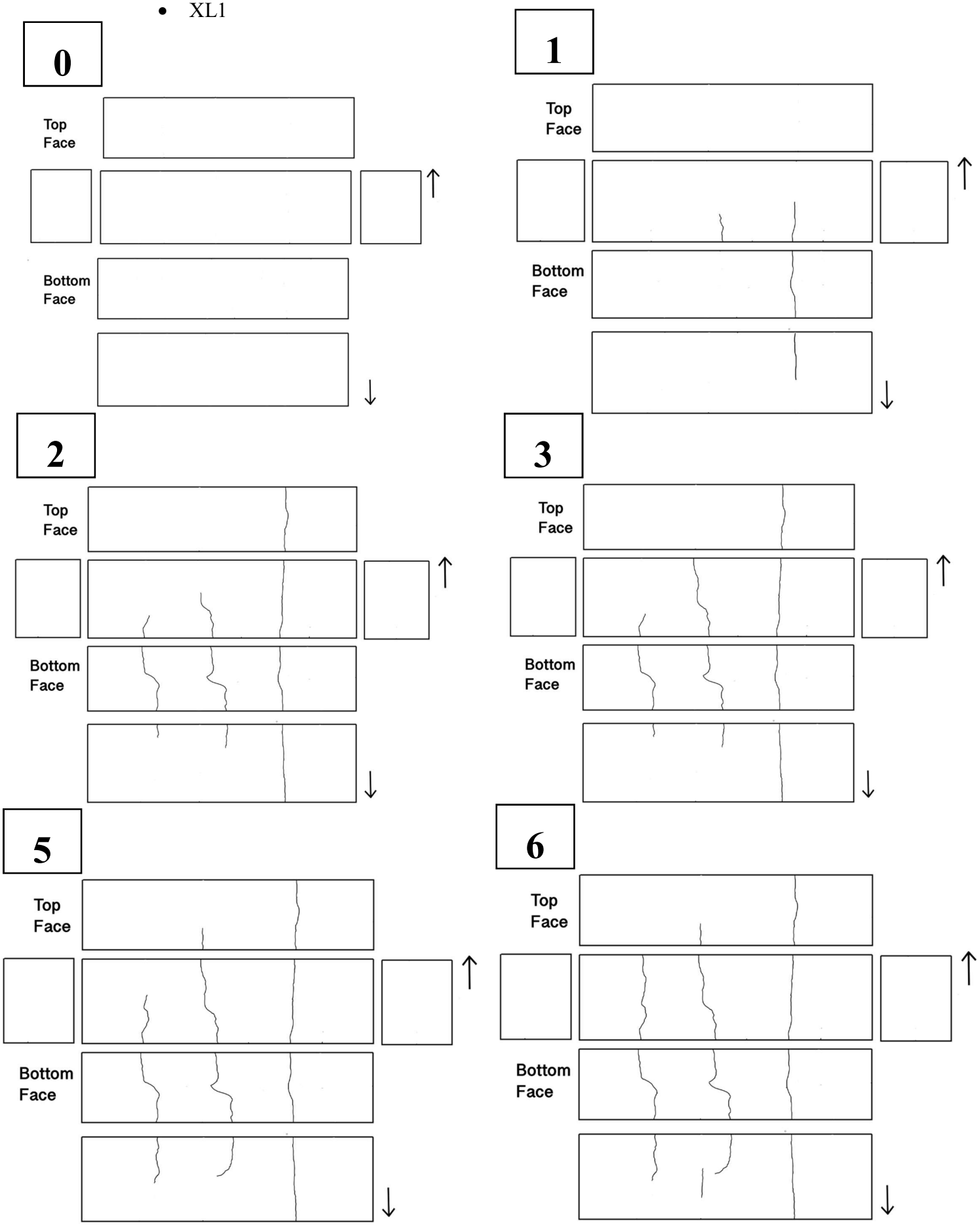

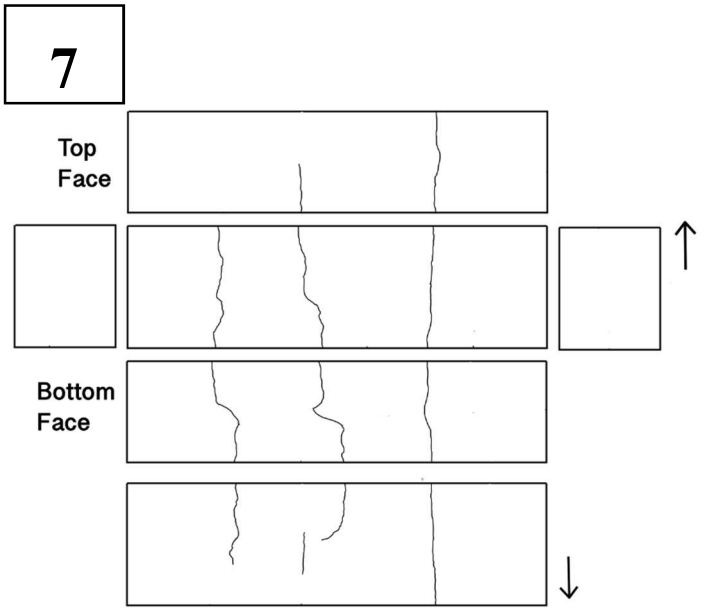
7
Top Face
Bottom Face

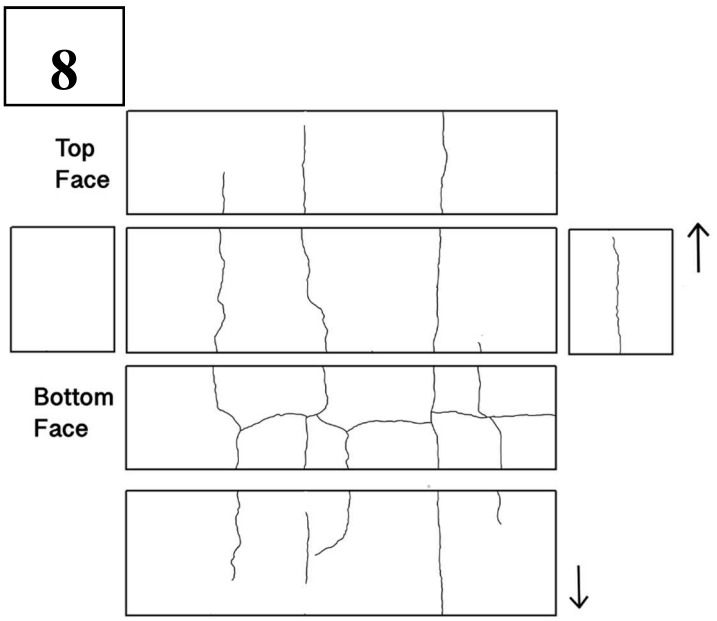
8
Top Face
Bottom Face

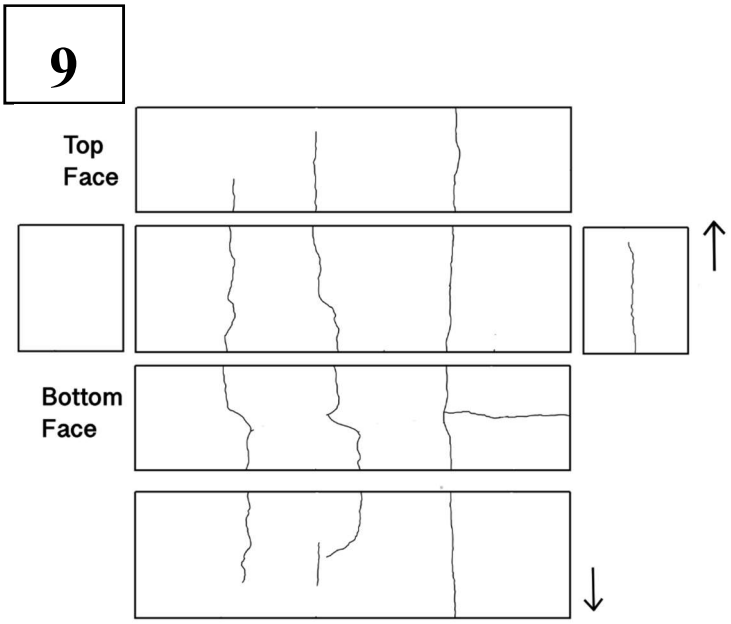
9
Top Face
Bottom Face

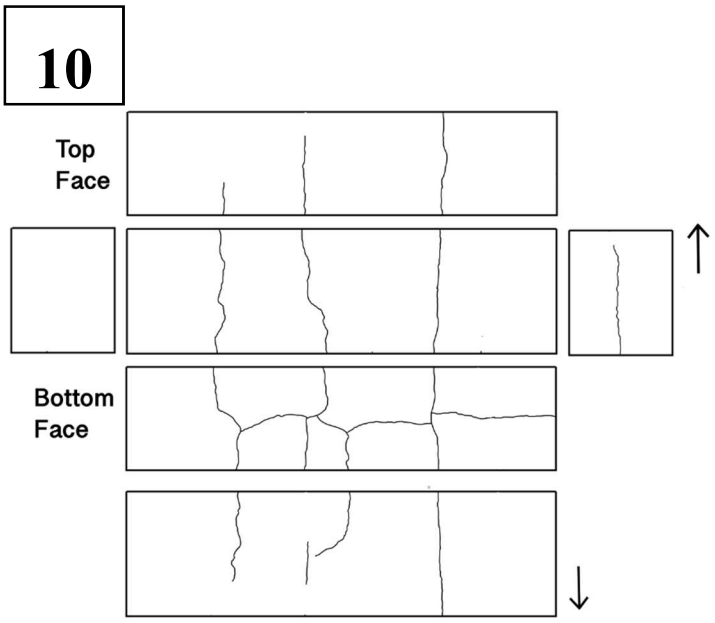
10
Top Face
Bottom Face

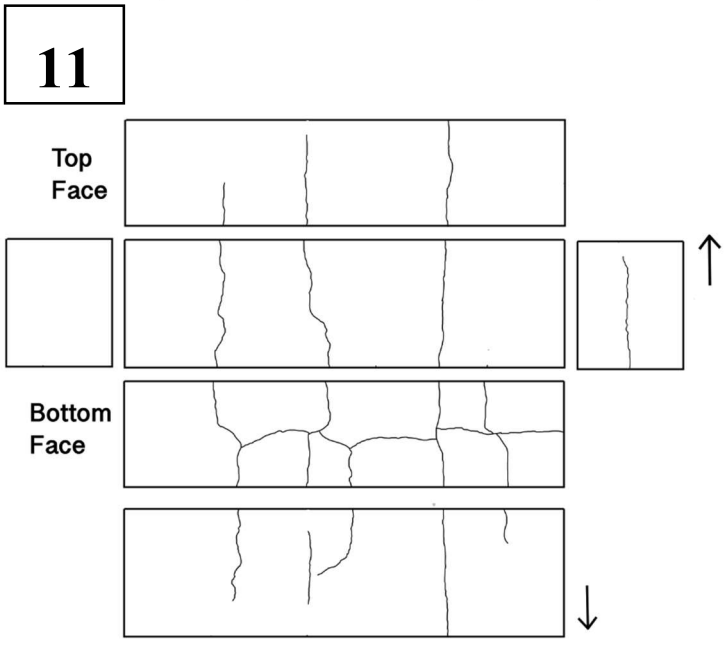
11
Top Face
Bottom Face

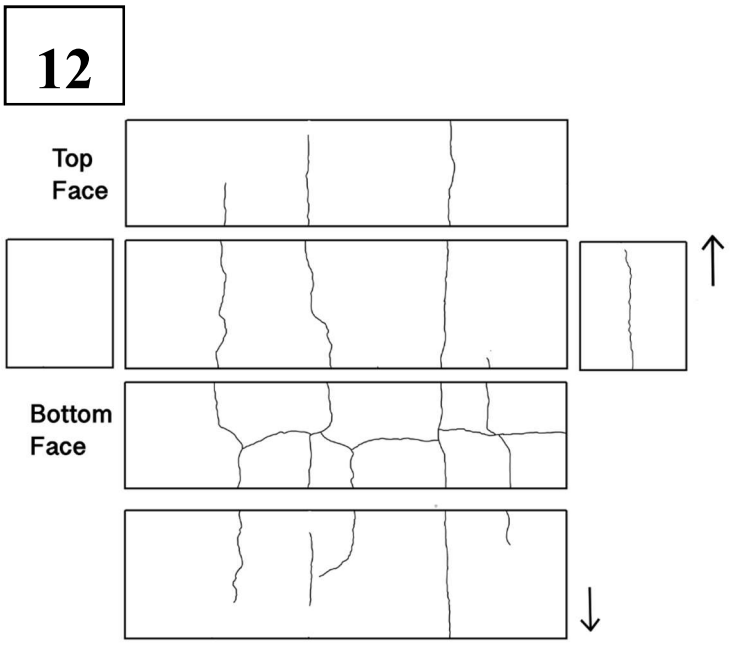
12
Top Face
Bottom Face

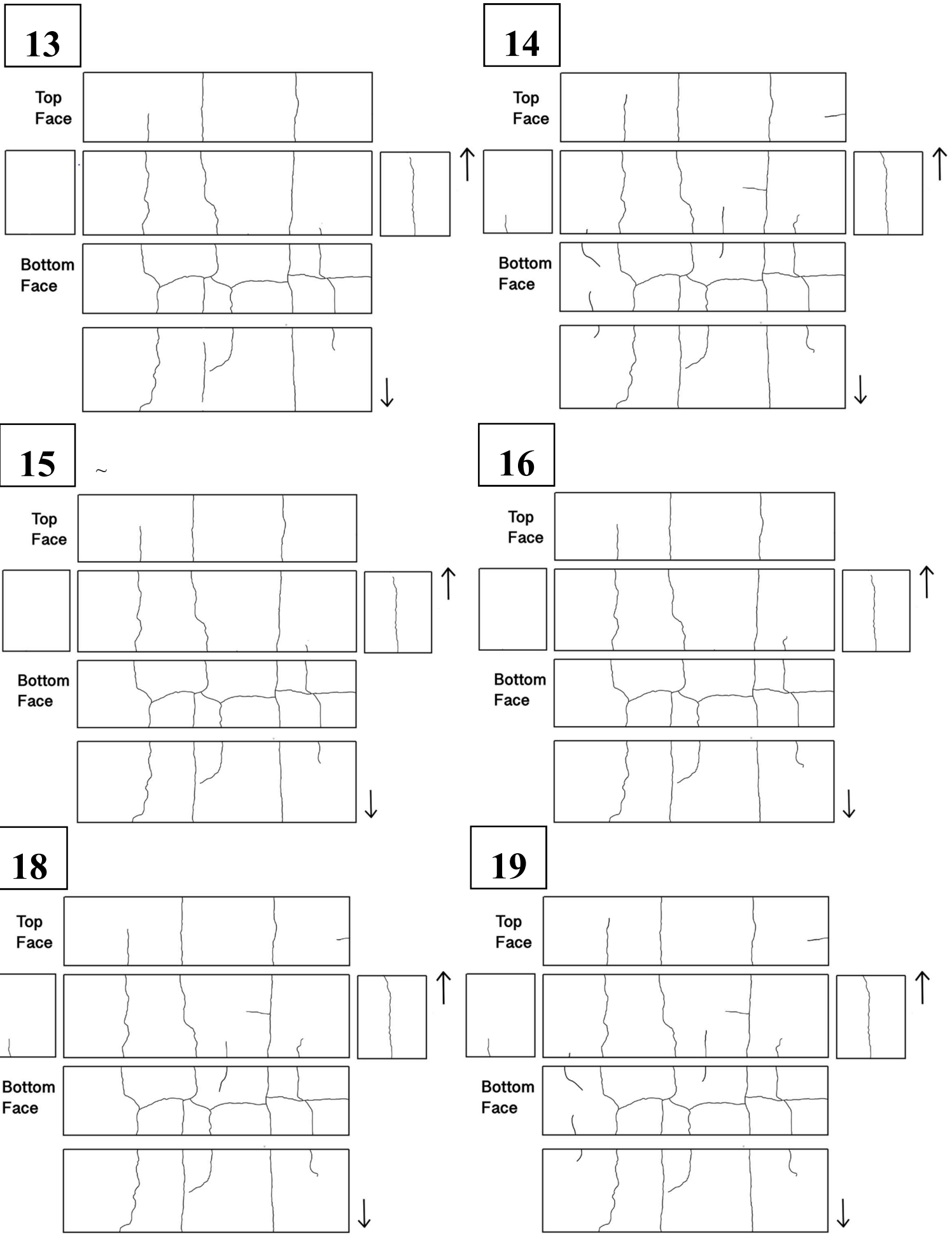
13
Top Face
Bottom Face
14
Top Face
Bottom Face
15
Top Face
Bottom Face
16
Top Face
Bottom Face
18
Top Face
Bottom Face
19
Top Face
Bottom Face

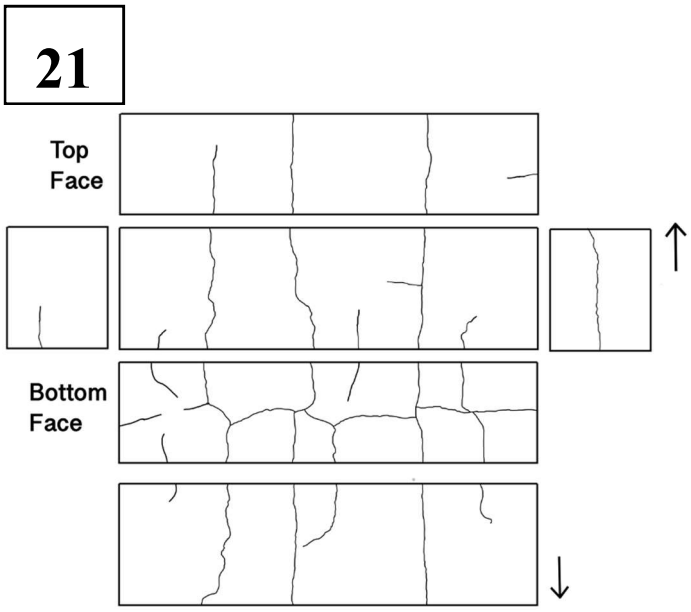
21
Top
Face
Bottom
Face

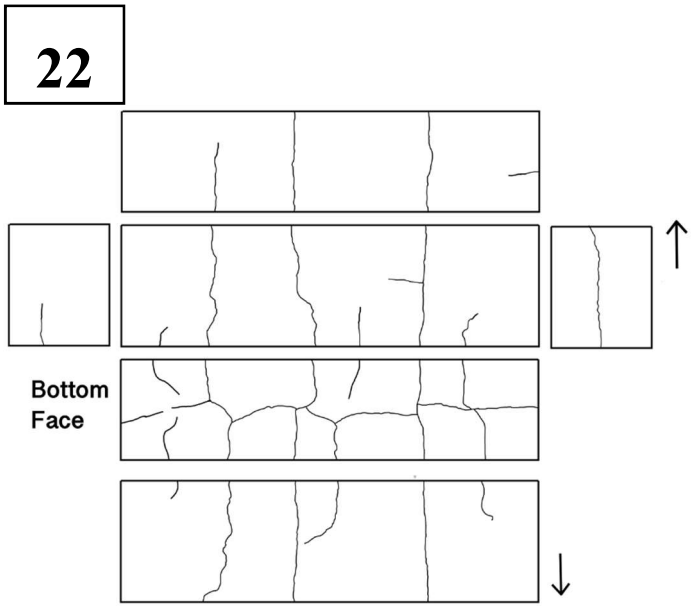
22
Bottom
Face

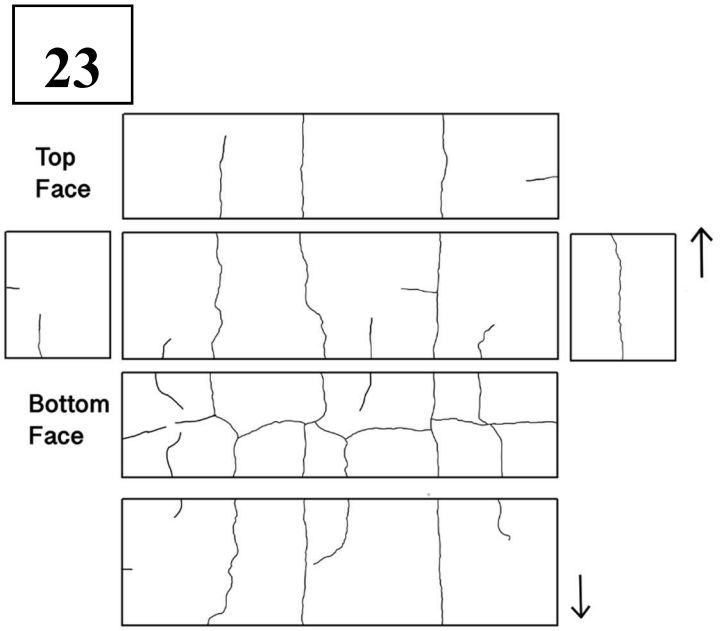
23
Top
Face
Bottom
Face

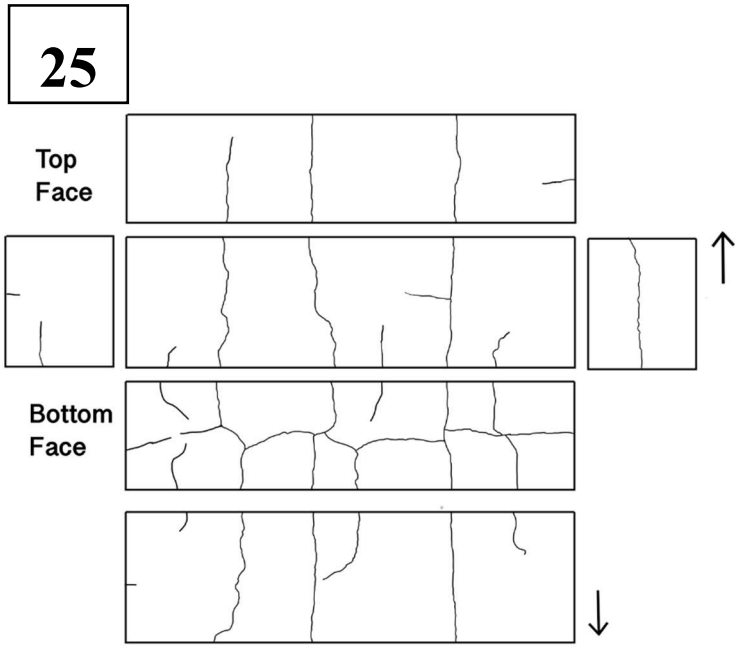
25
Top
Face
Bottom
Face

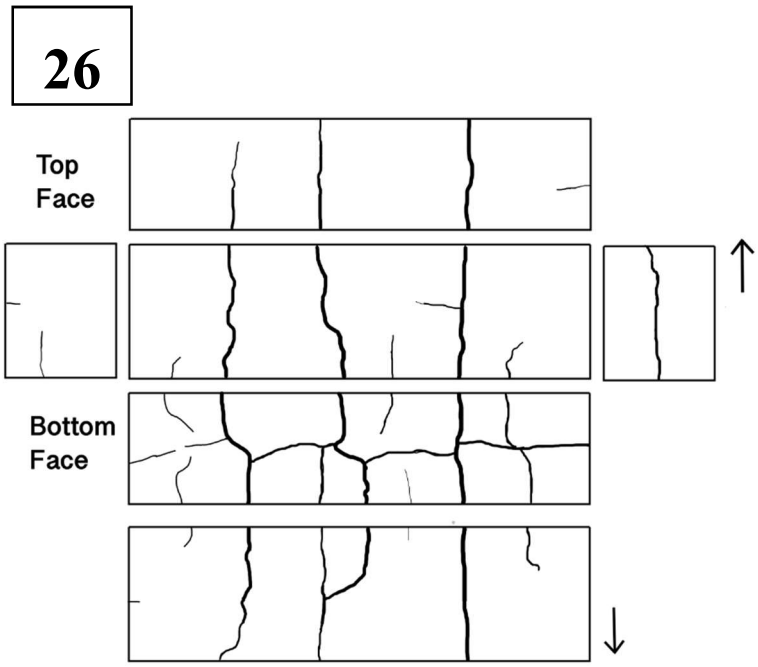
26
Top
Face
Bottom
Face

- XL2

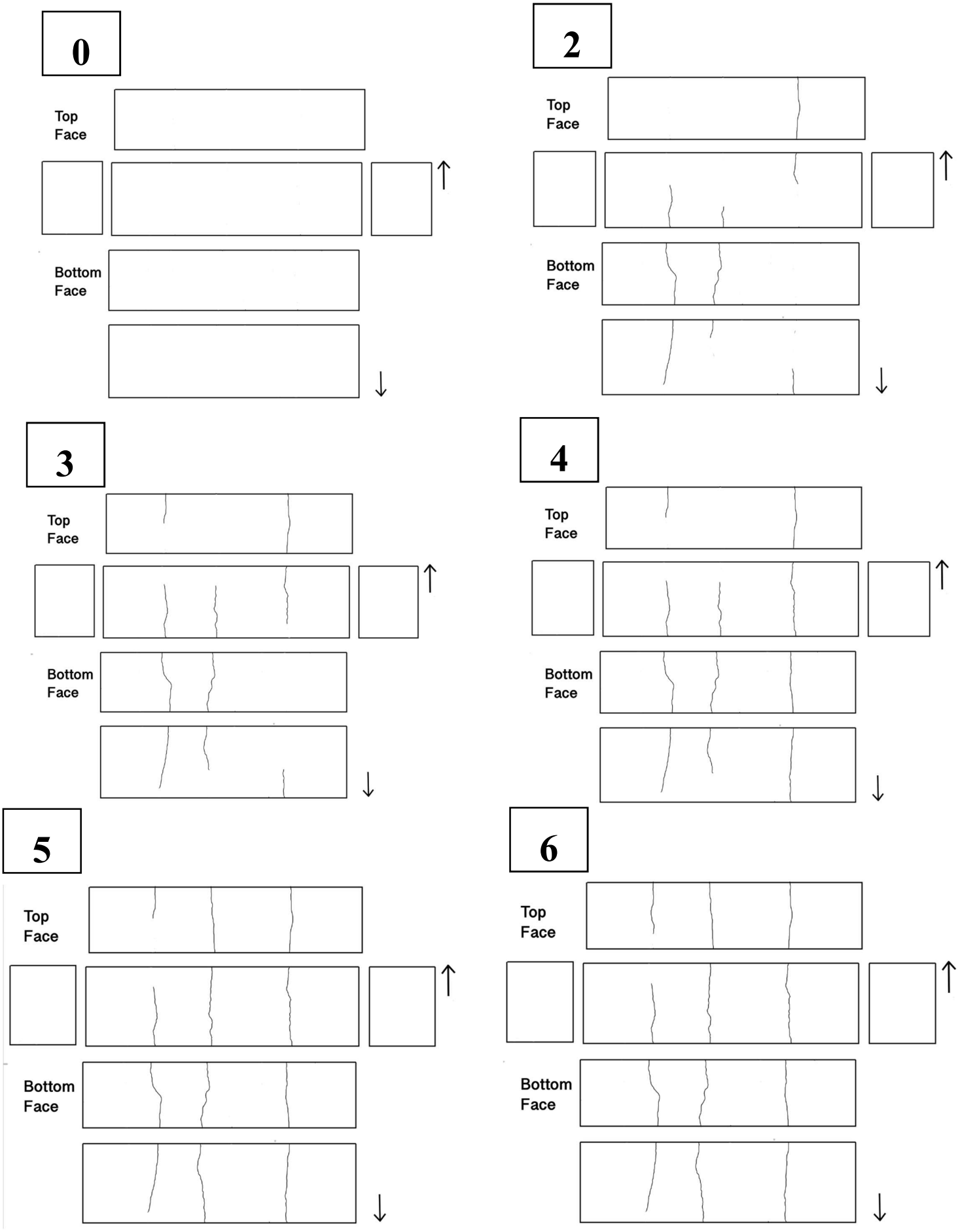
0
Top Face
Bottom Face
2
Top Face
Bottom Face
3
Top Face
Bottom Face
4
Top Face
Bottom Face
5
Top Face
Bottom Face
6
Top Face
Bottom Face

7

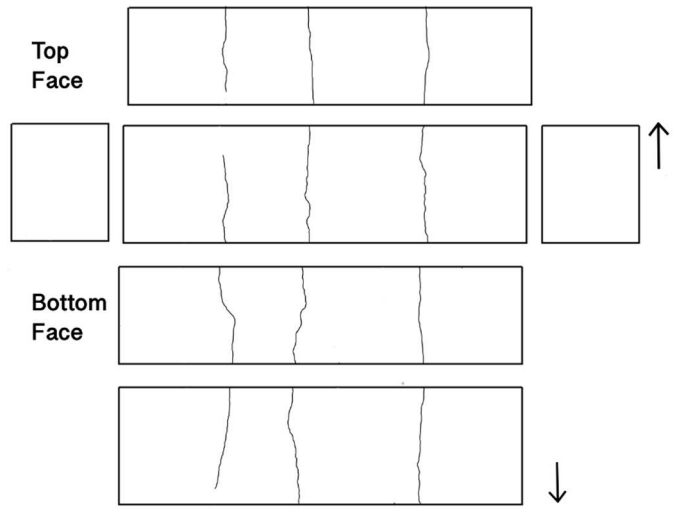

10

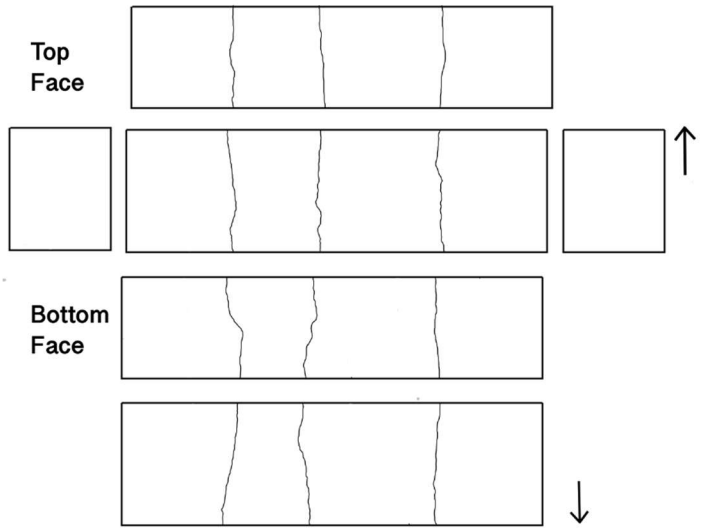

11

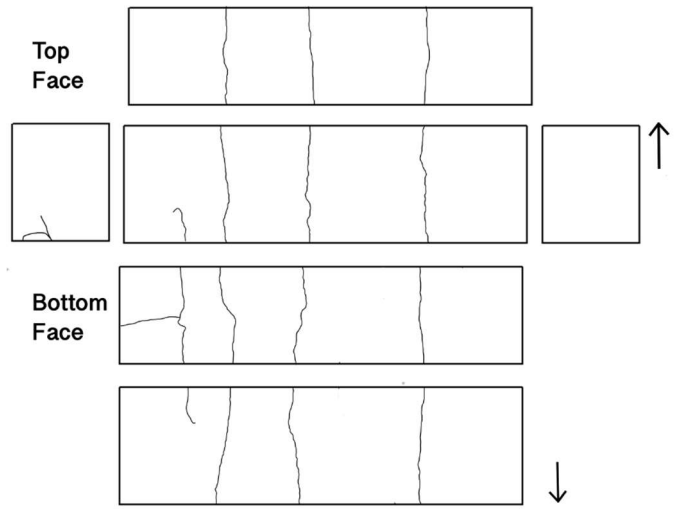

12

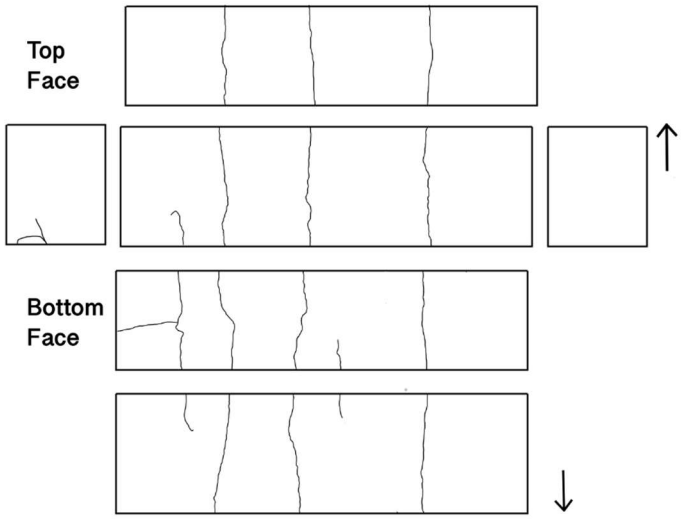

13

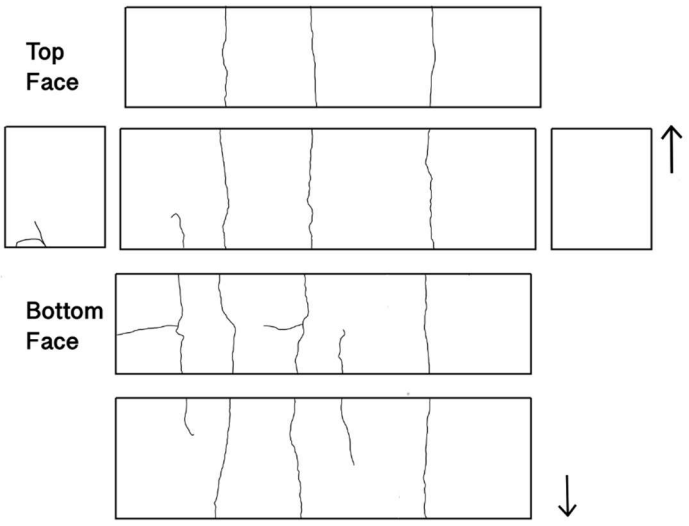

17

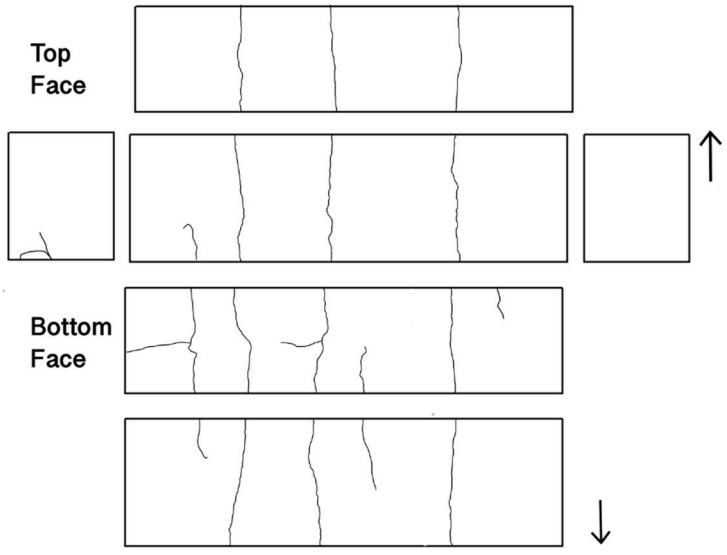

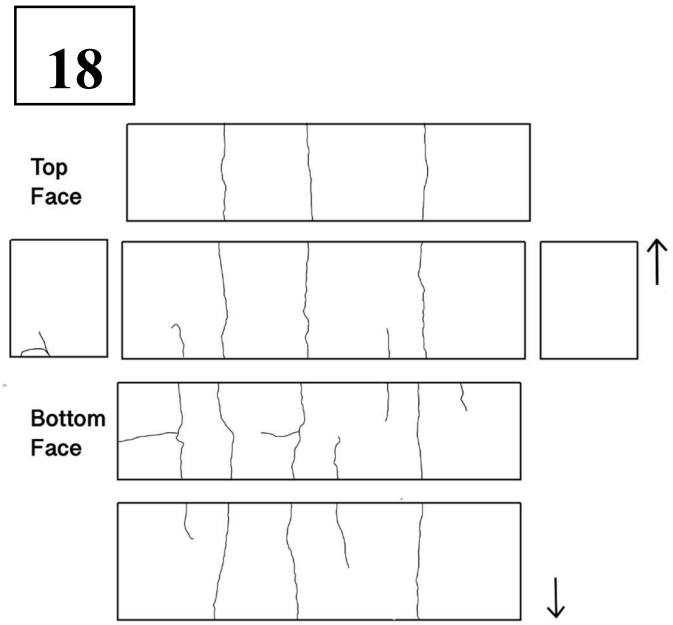
18
Top
Face
Bottom
Face

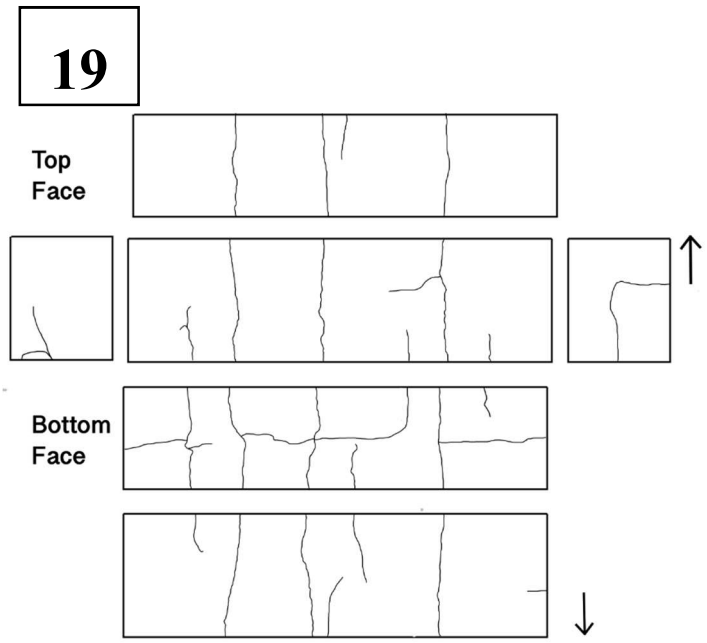
19
Top
Face
Bottom
Face

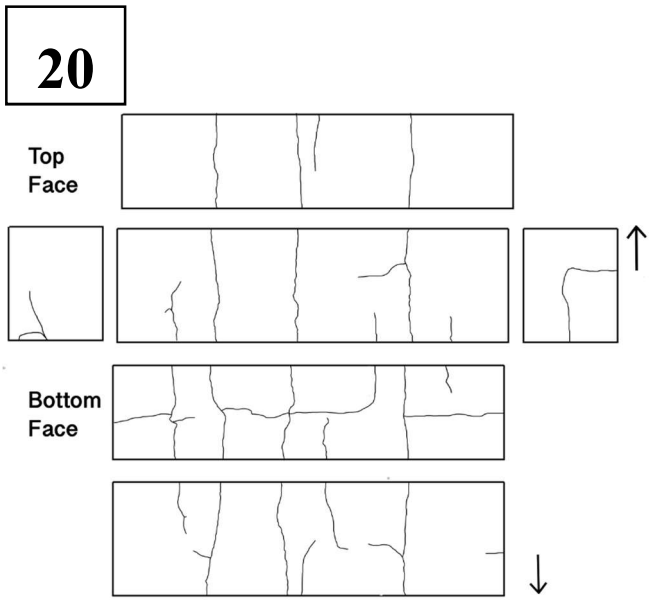
20
Top
Face
Bottom
Face

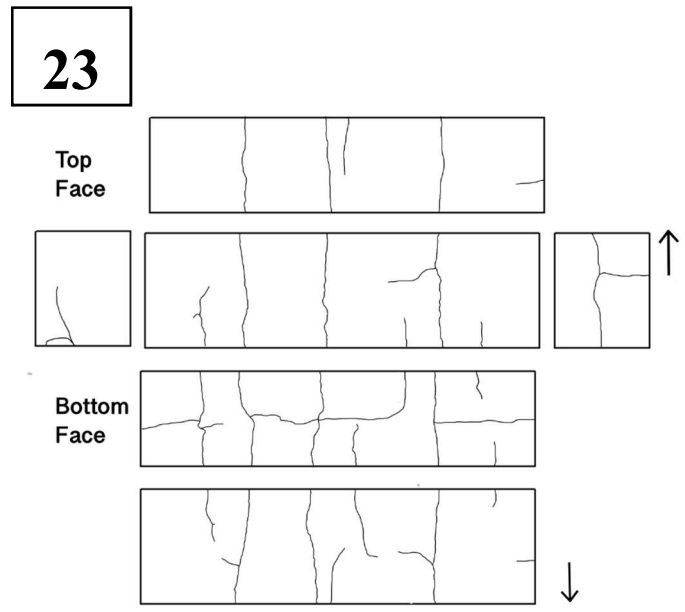
23
Top
Face
Bottom
Face

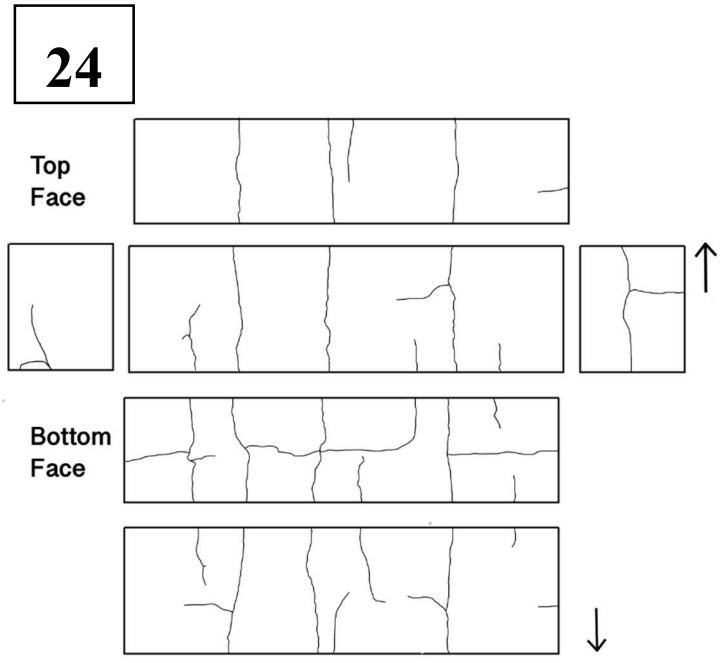
24
Top
Face
Bottom
Face

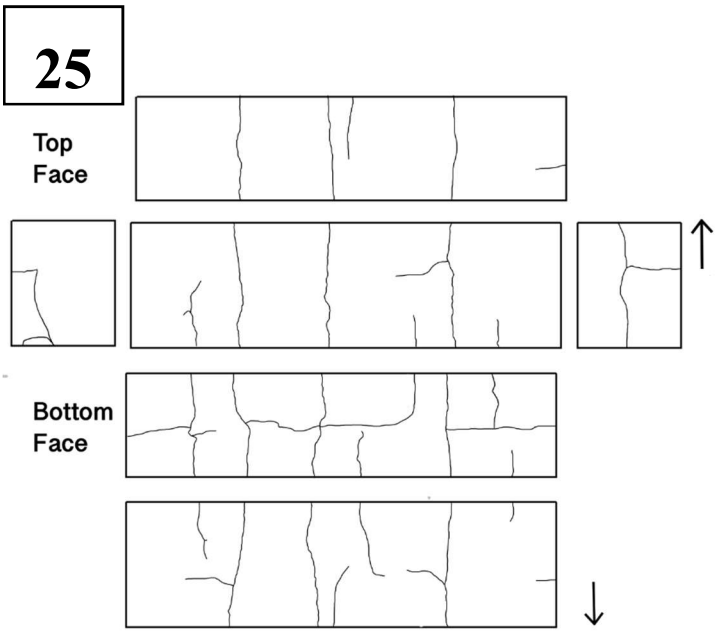
25
Top
Face
Bottom
Face

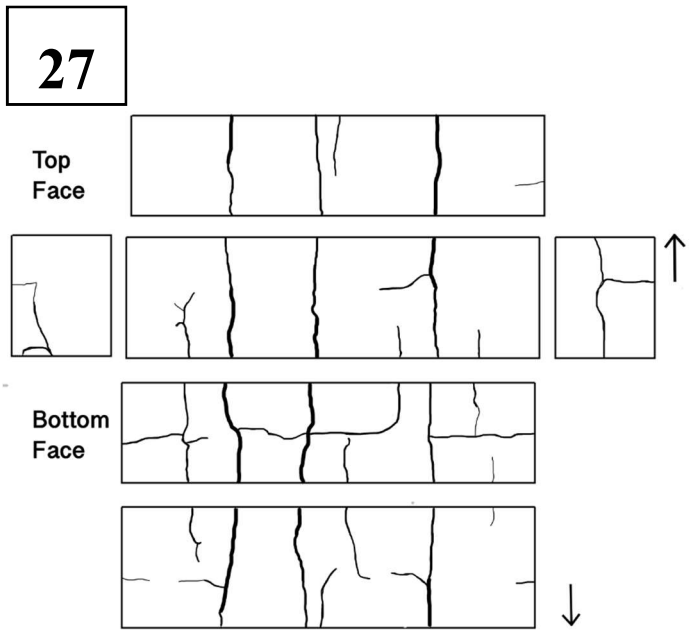
27
Top
Face
Bottom
Face

- L1

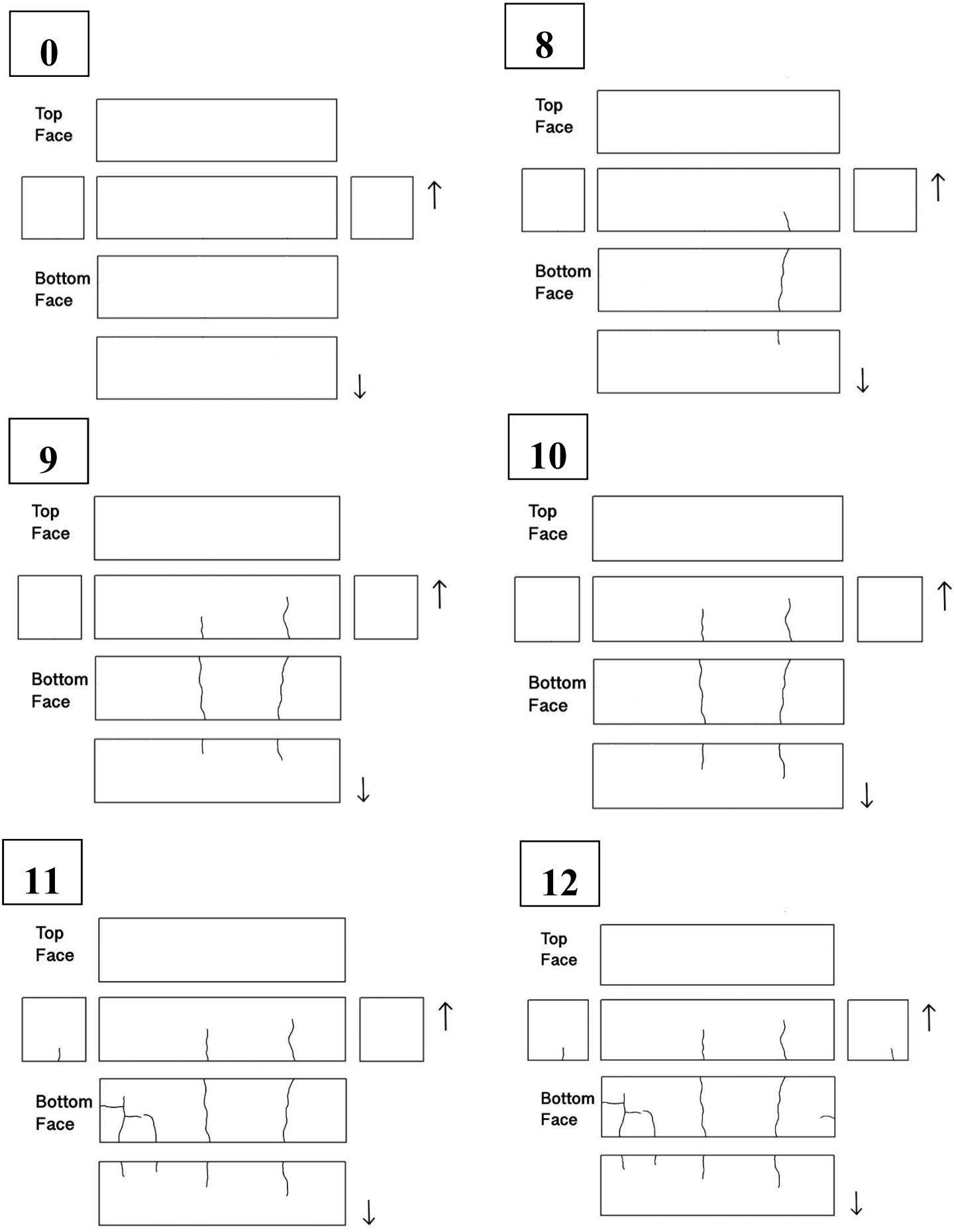
0
Top Face
Bottom Face
8
Top Face
Bottom Face
9
Top Face
Bottom Face
10
Top Face
Bottom Face
11
Top Face
Bottom Face
12
Top Face
Bottom Face

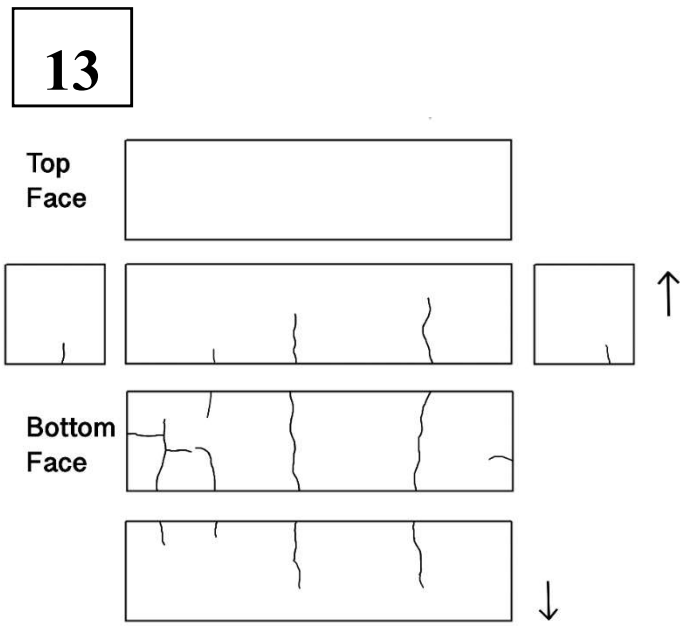
13
Top
Face
Bottom
Face

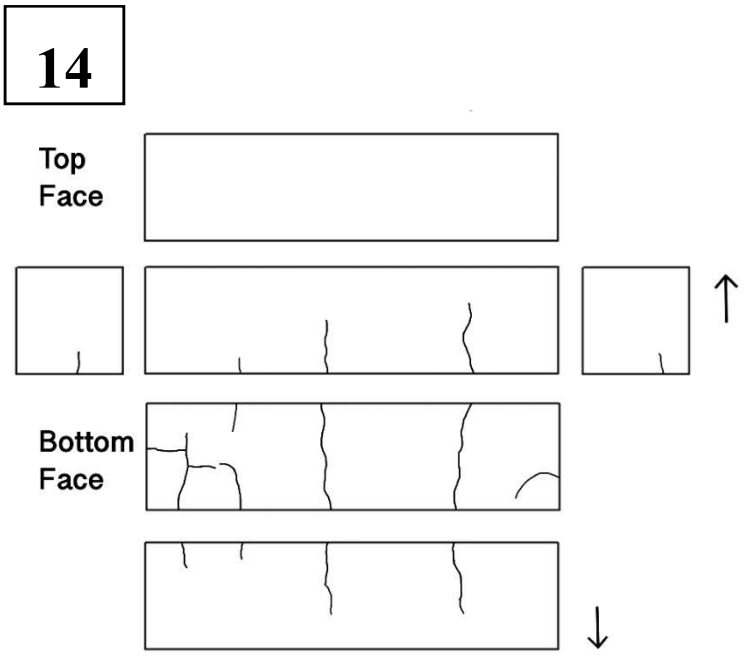
14
Top
Face
Bottom
Face

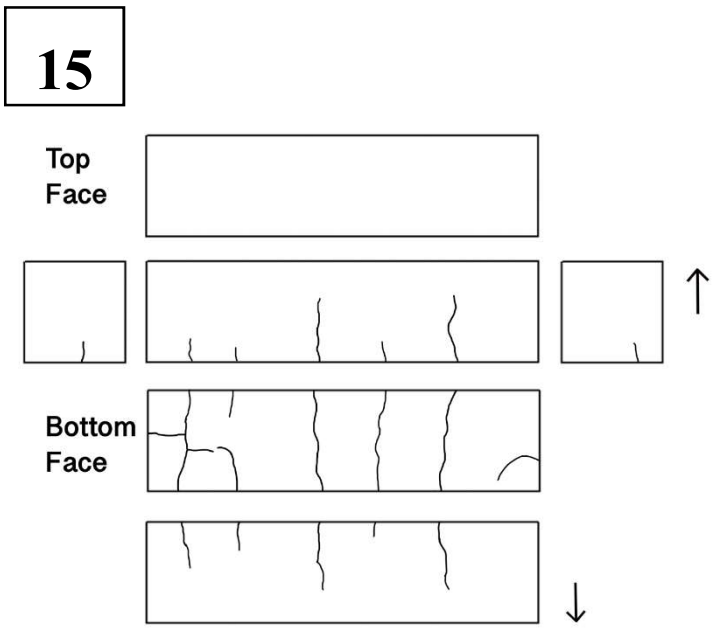
15
Top
Face
Bottom
Face

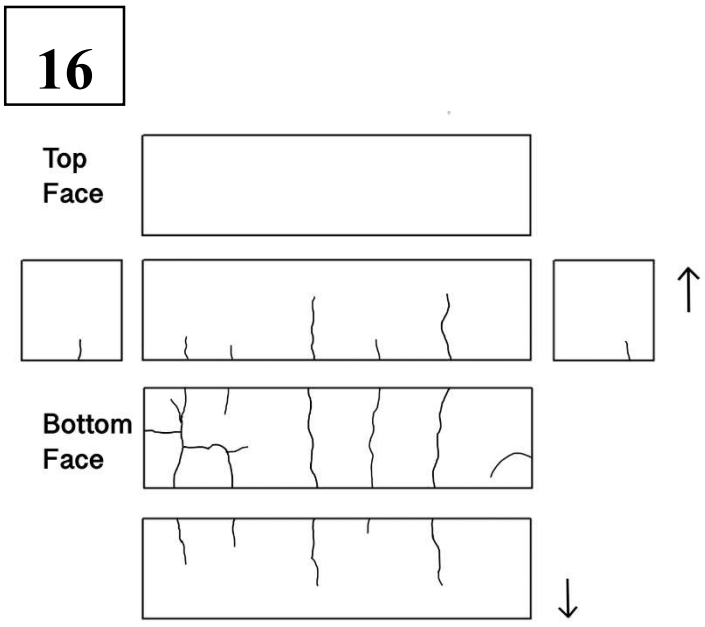
16
Top
Face
Bottom
Face

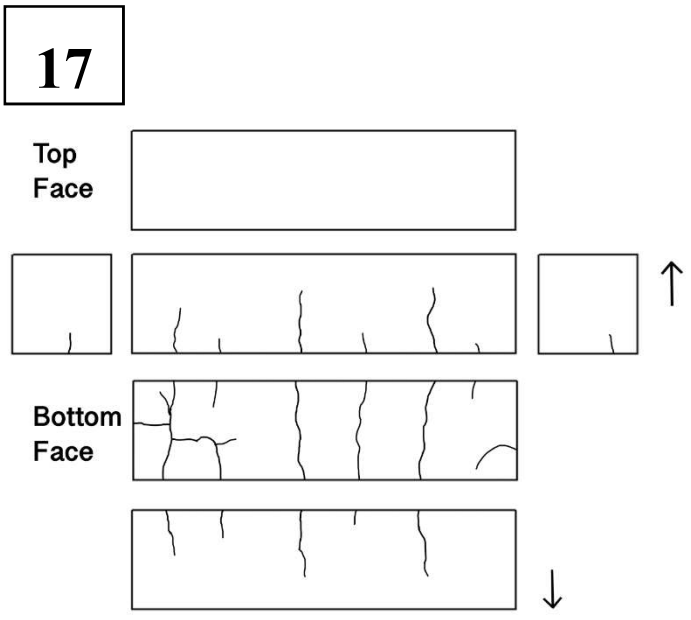
17
Top
Face
Bottom
Face

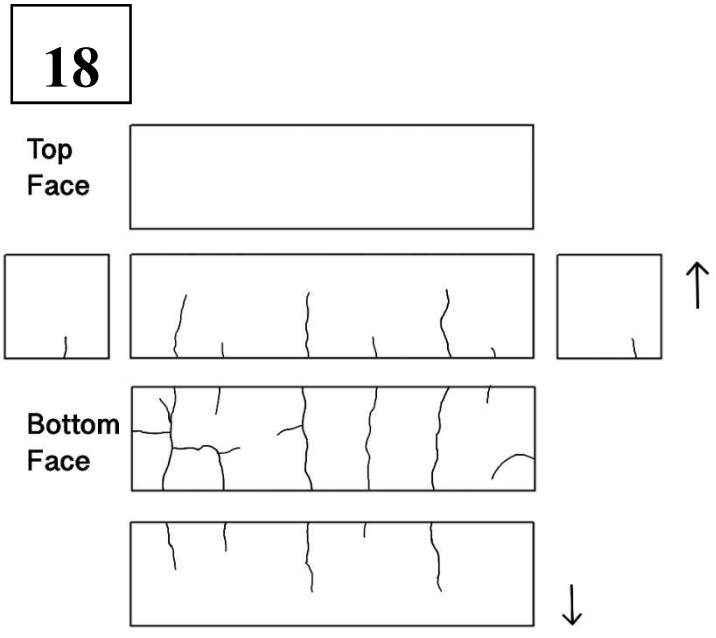
18
Top
Face
Bottom
Face

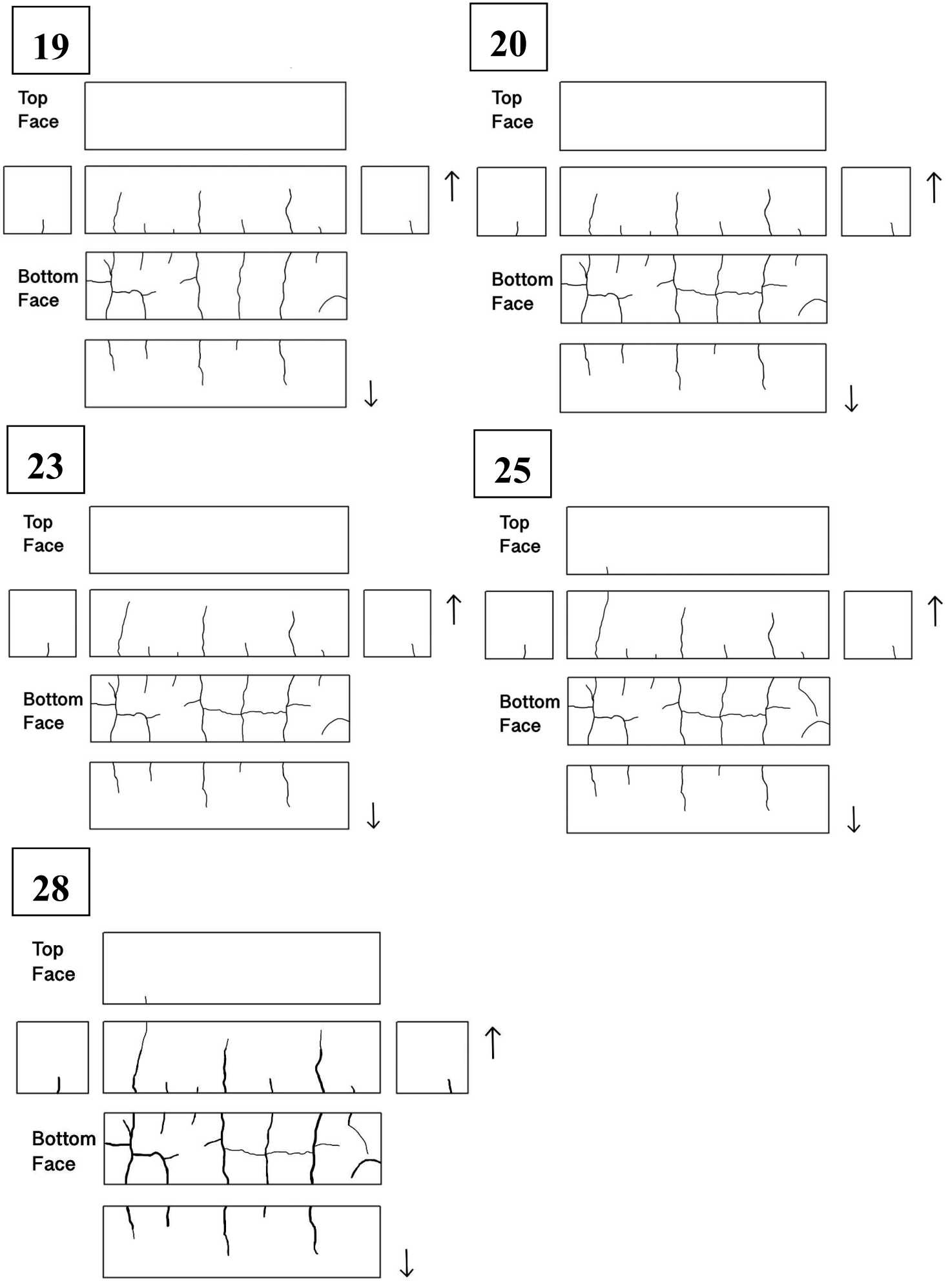
19
Top Face
Bottom Face
20
Top Face
Bottom Face
23
Top Face
Bottom Face
25
Top Face
Bottom Face
28
Top Face
Bottom Face

- L2

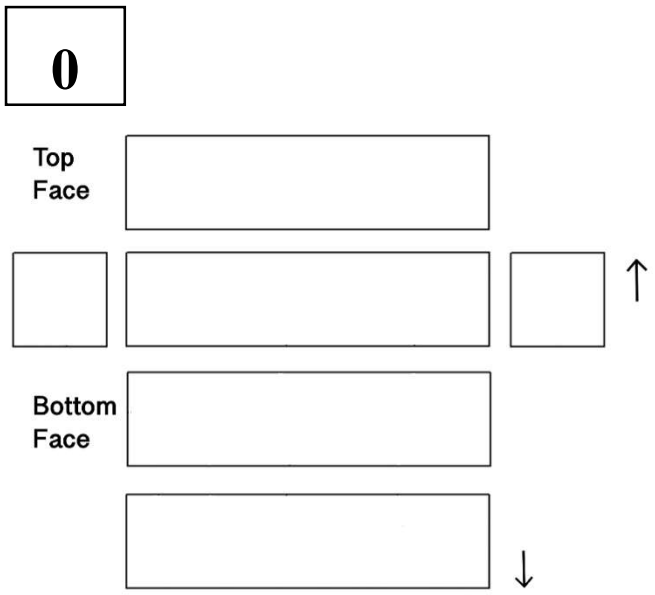
0
Top Face
Bottom Face

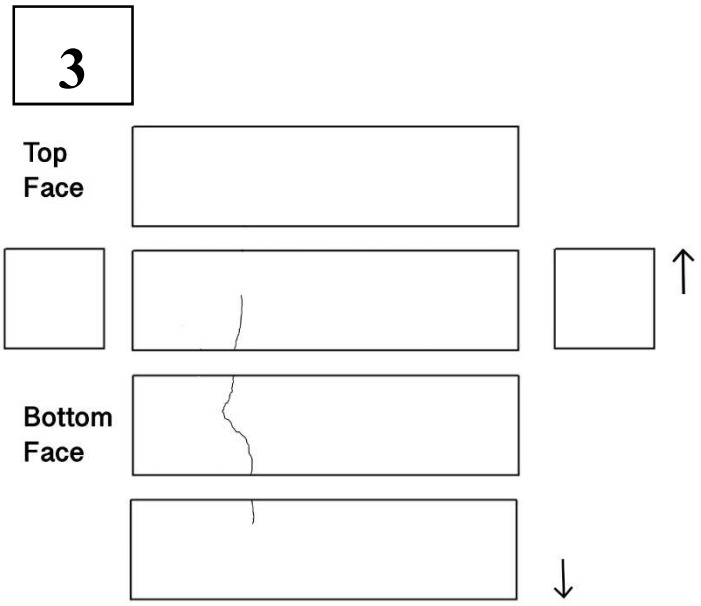
3
Top Face
Bottom Face

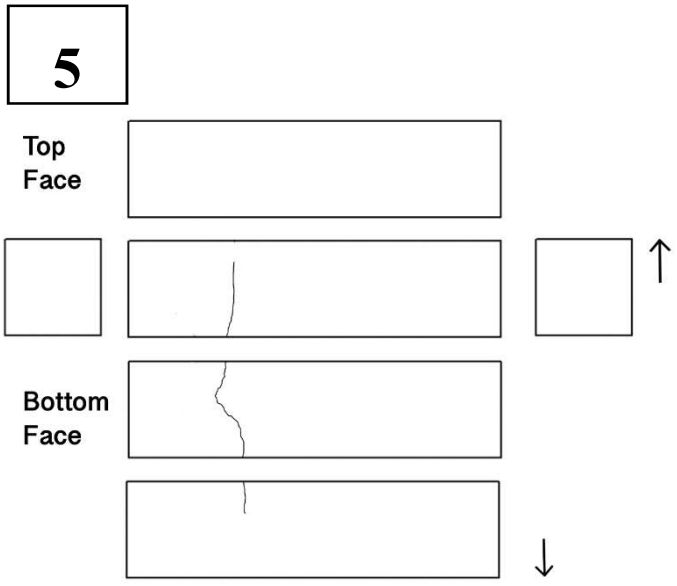
5
Top Face
Bottom Face

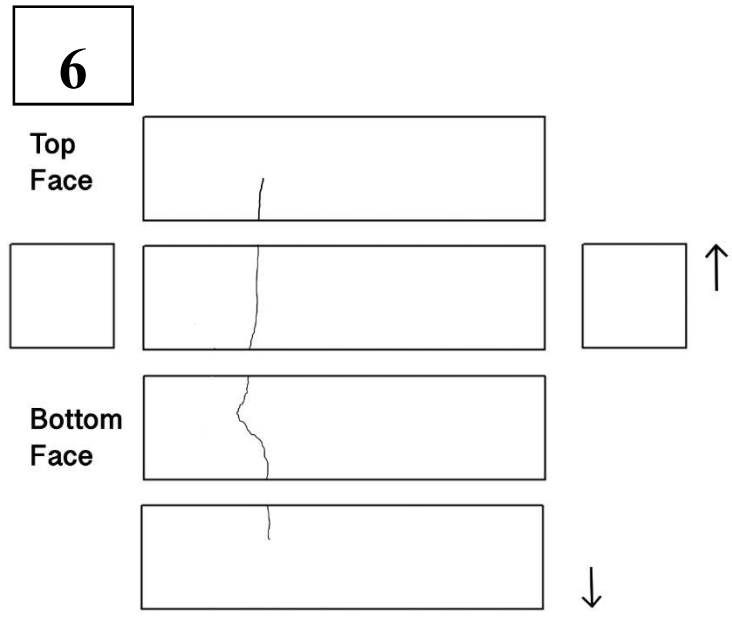
6
Top Face
Bottom Face

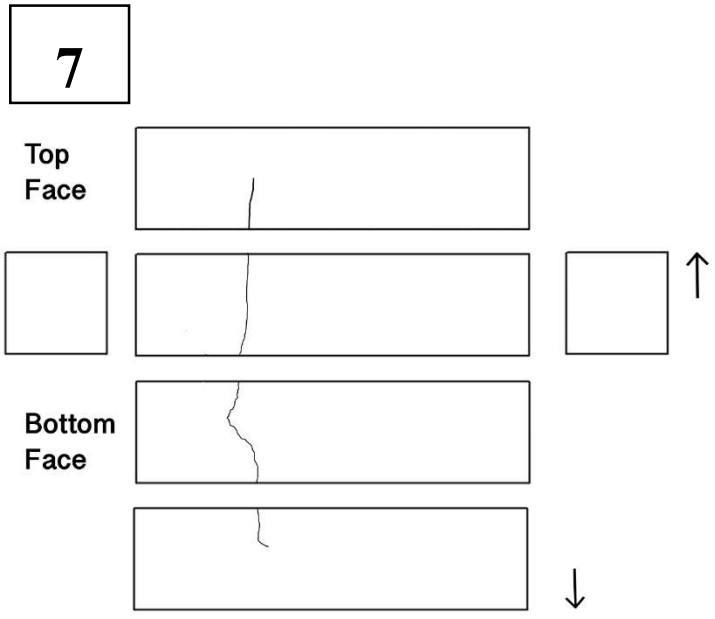
7
Top Face
Bottom Face

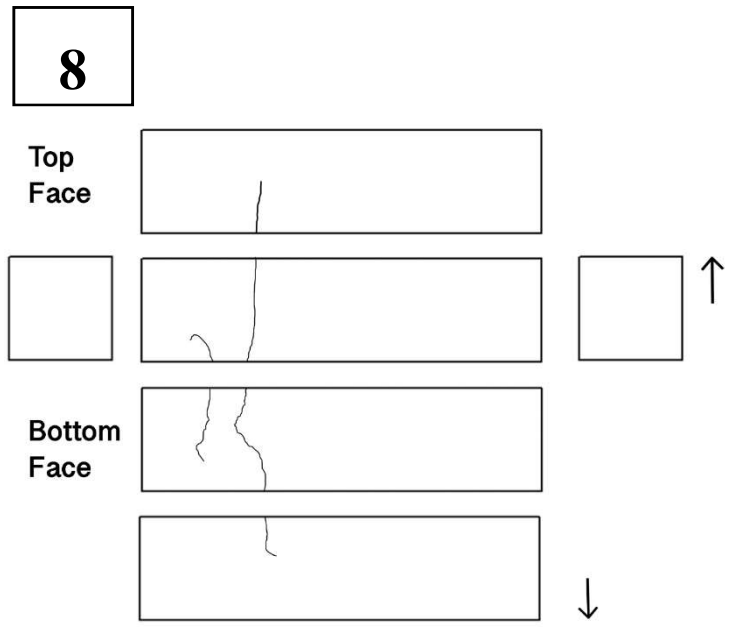
8
Top Face
Bottom Face

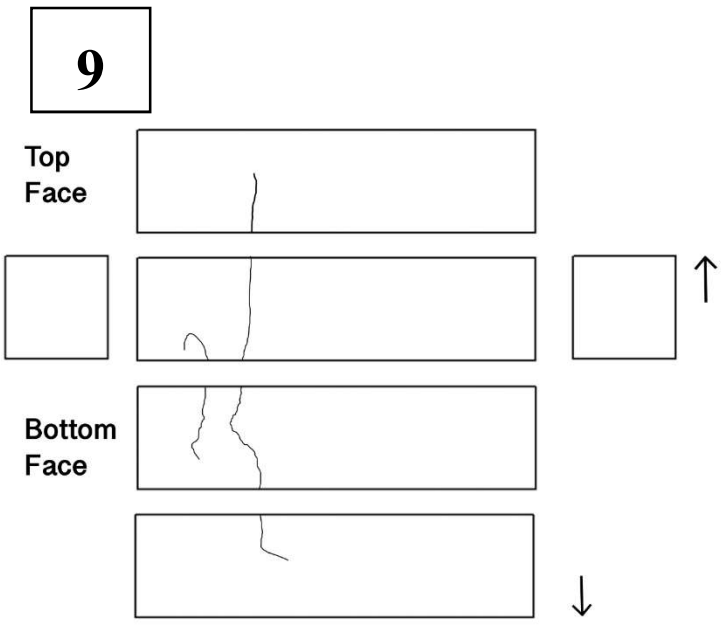
9
Top
Face
Bottom
Face

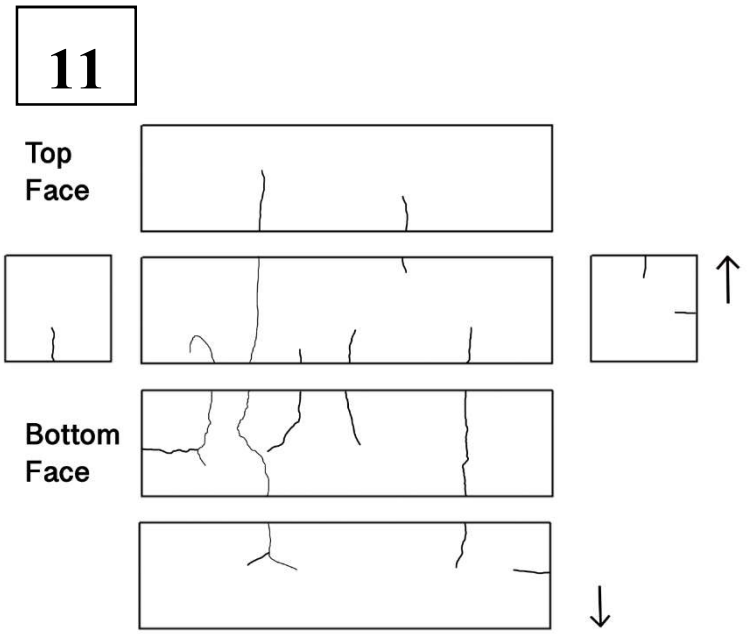
11
Top
Face
Bottom
Face

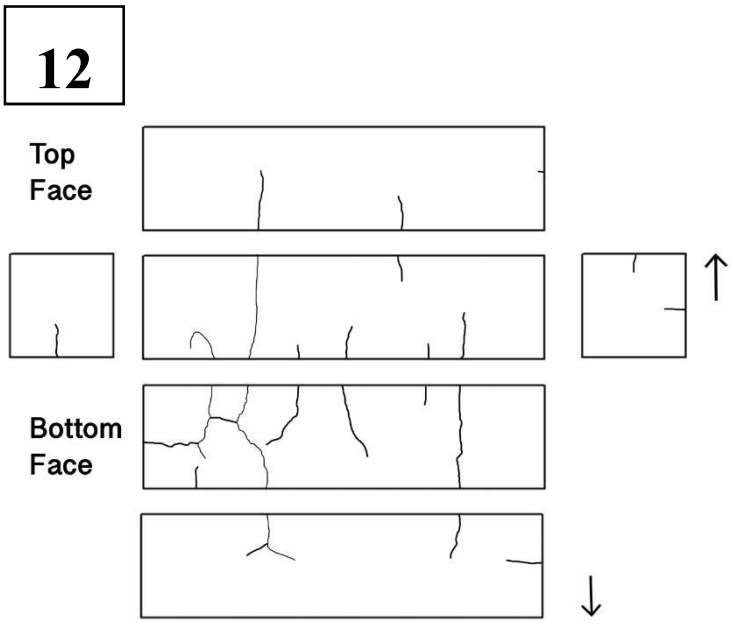
12
Top
Face
Bottom
Face

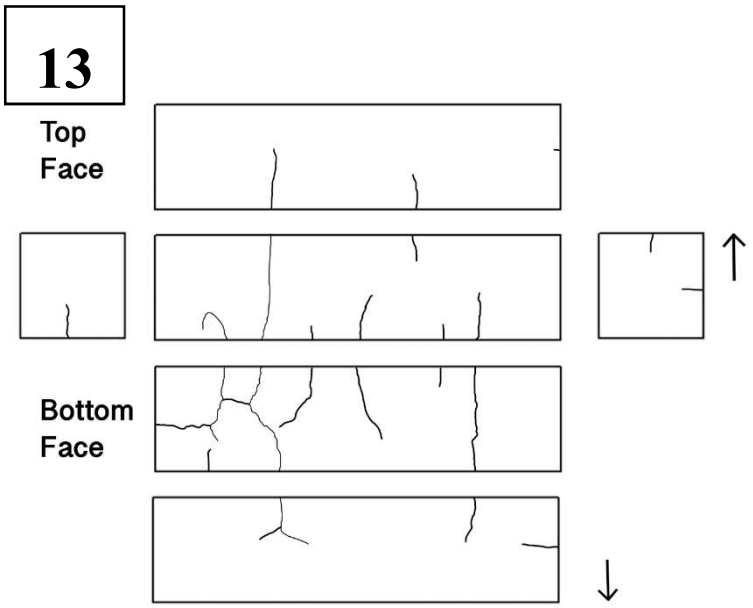
13
Top
Face
Bottom
Face

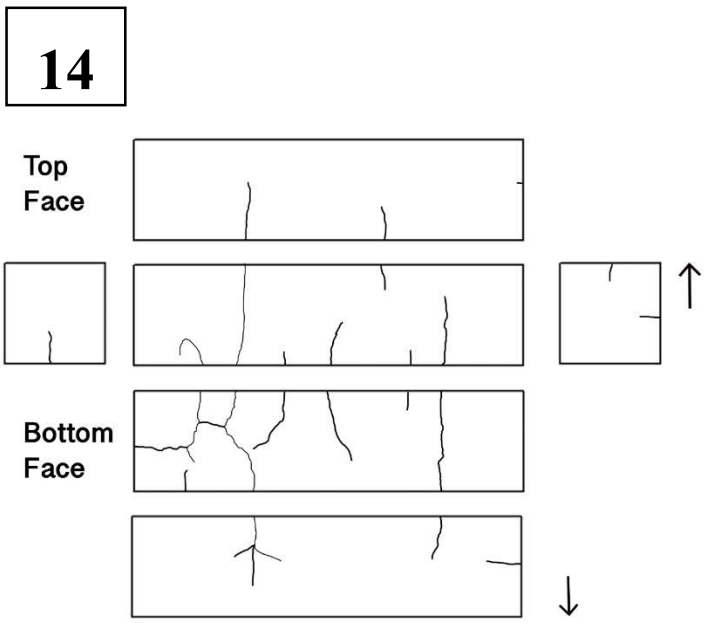
14
Top
Face
Bottom
Face

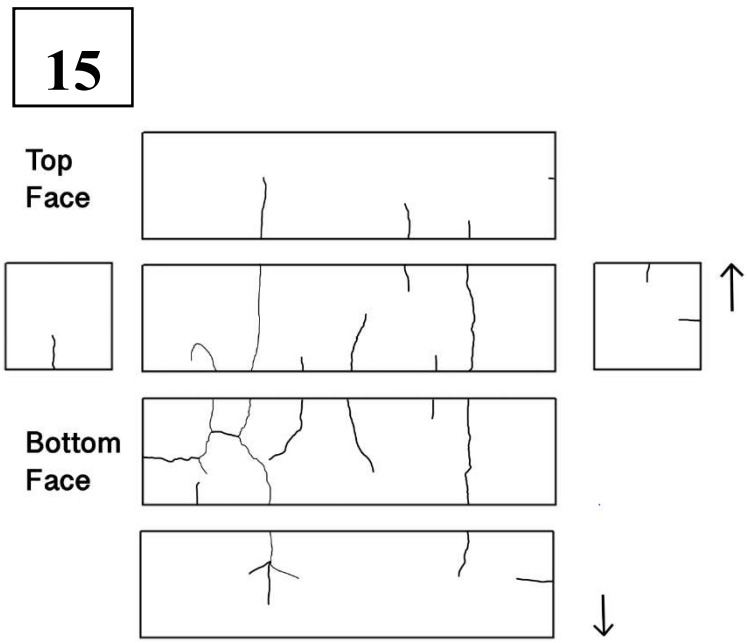
15
Top
Face
Bottom
Face

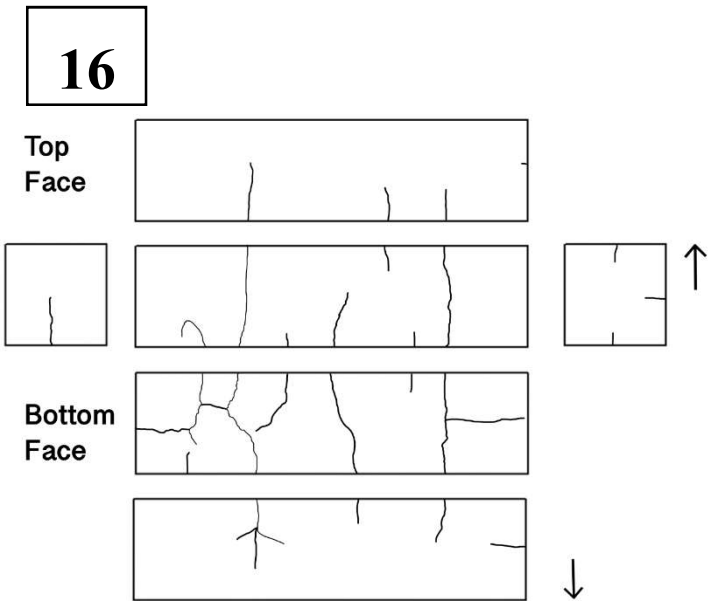
16
Top
Face
Bottom
Face

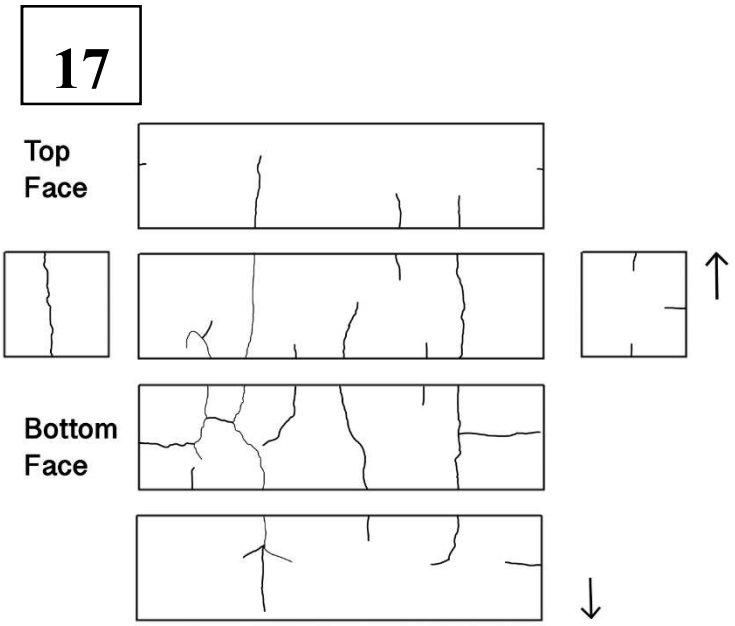
17
Top
Face
Bottom
Face

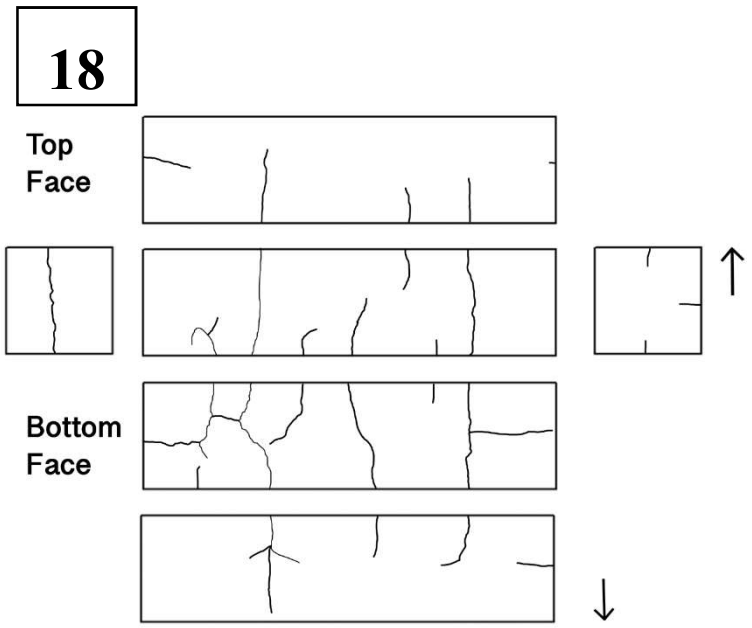
18
Top
Face
Bottom
Face

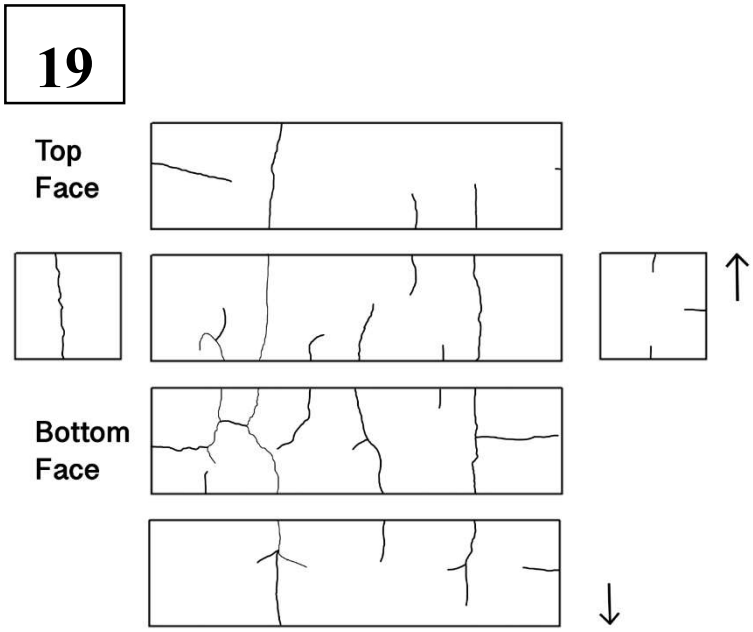
19
Top
Face
Bottom
Face

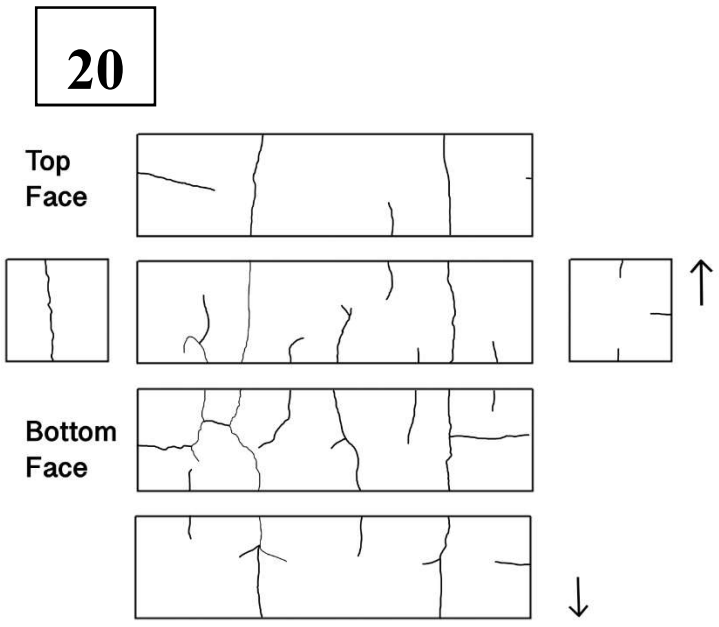
20
Top
Face
Bottom
Face

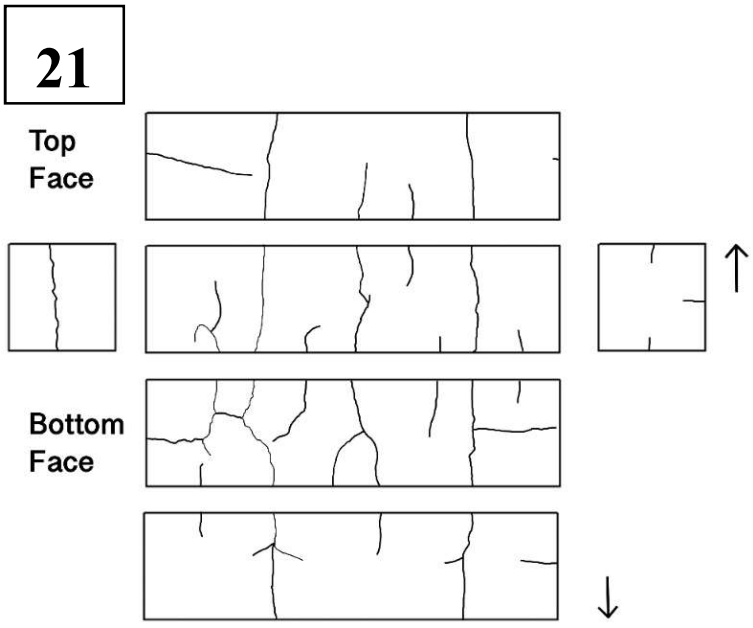
21
Top
Face
Bottom
Face

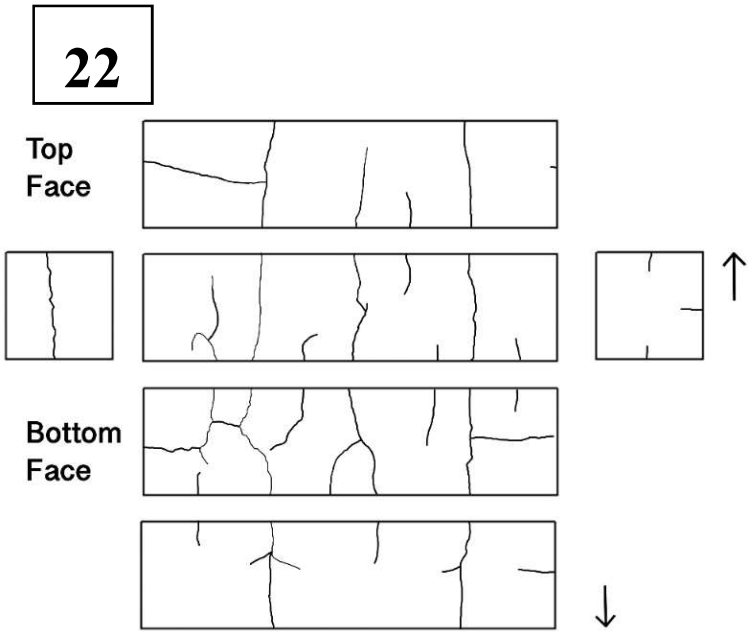
22
Top
Face
Bottom
Face

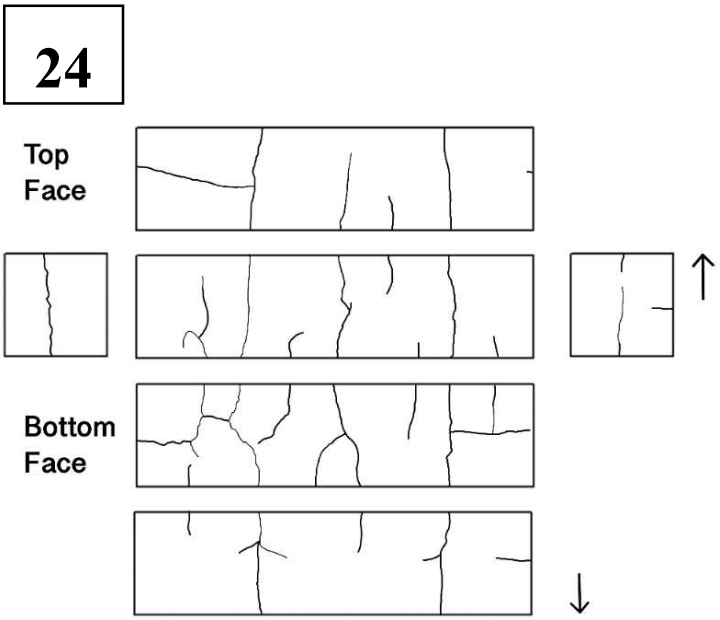
24
Top
Face
Bottom
Face

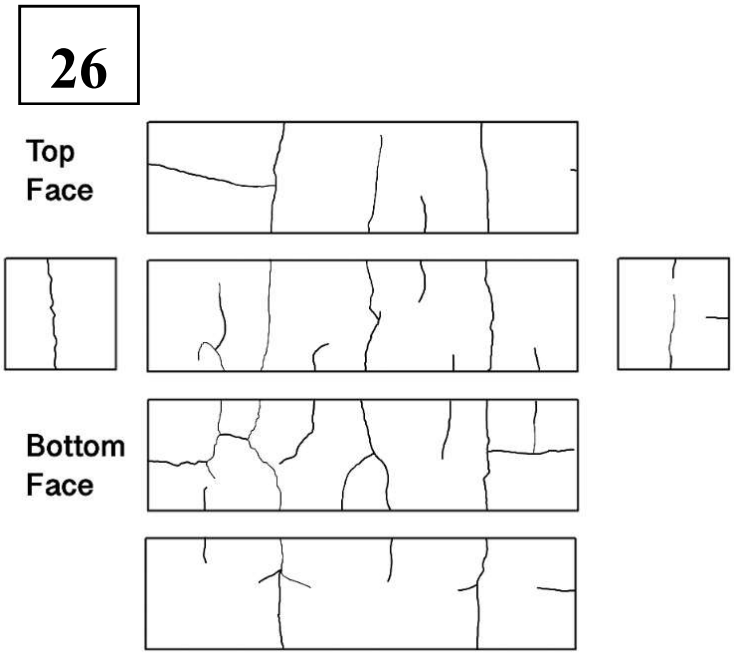
26
Top
Face
Bottom
Face

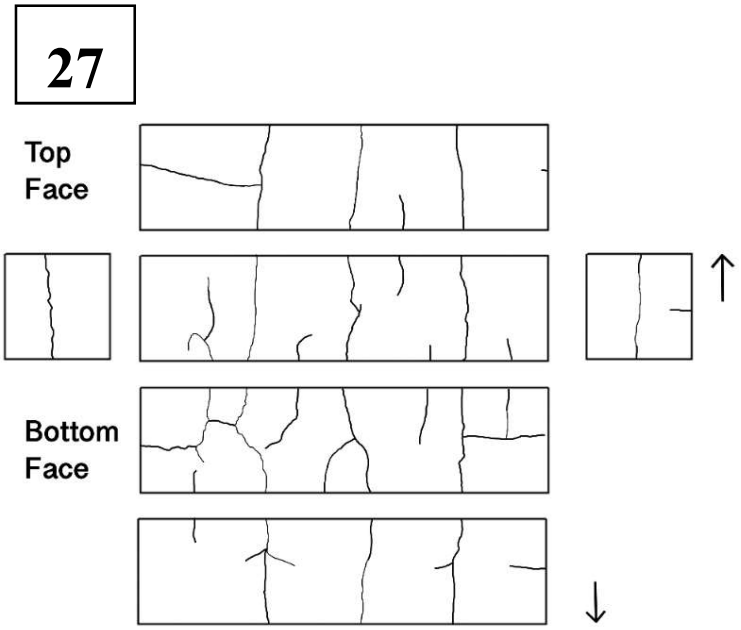
27
Top
Face
Bottom
Face

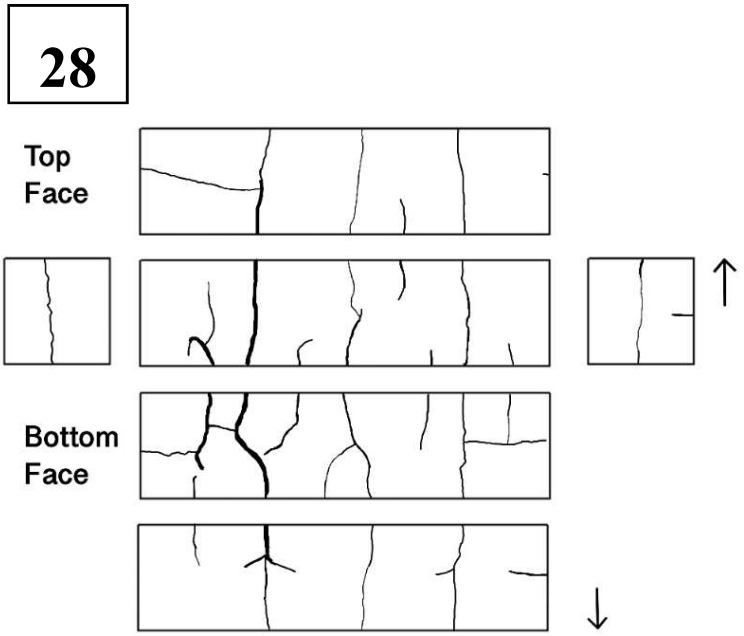
28
Top
Face
Bottom
Face

- M1

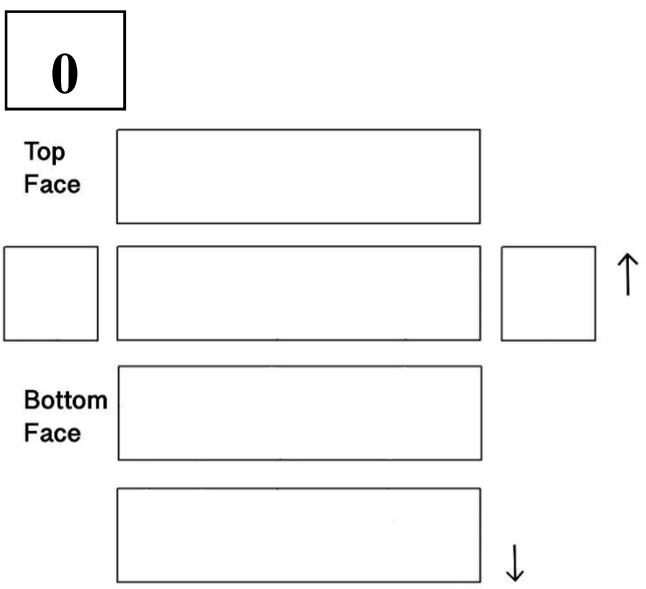
0
Top
Face
Bottom
Face

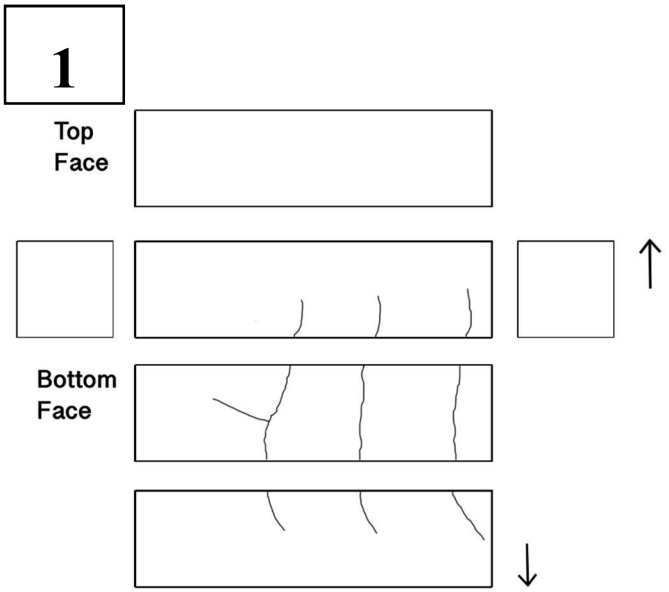
1
Top
Face
Bottom
Face

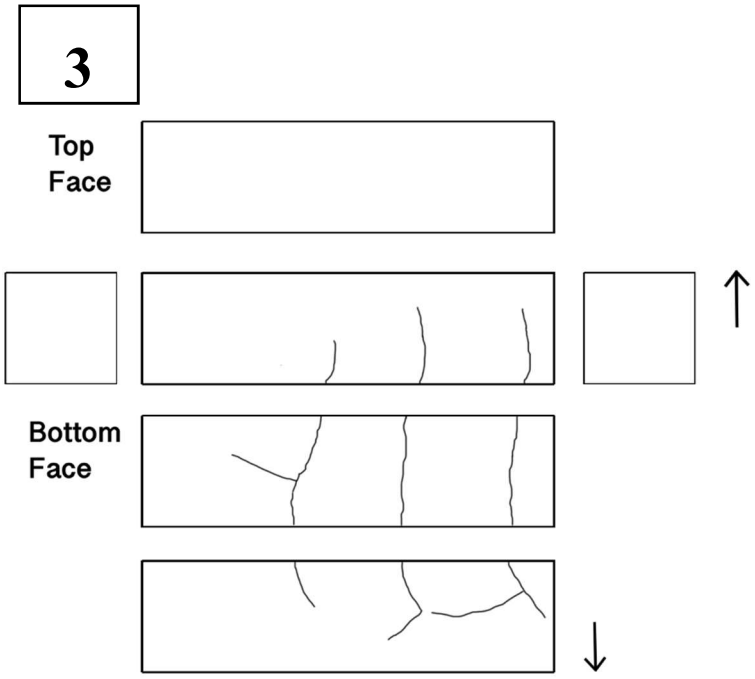
3
Top
Face
Bottom
Face

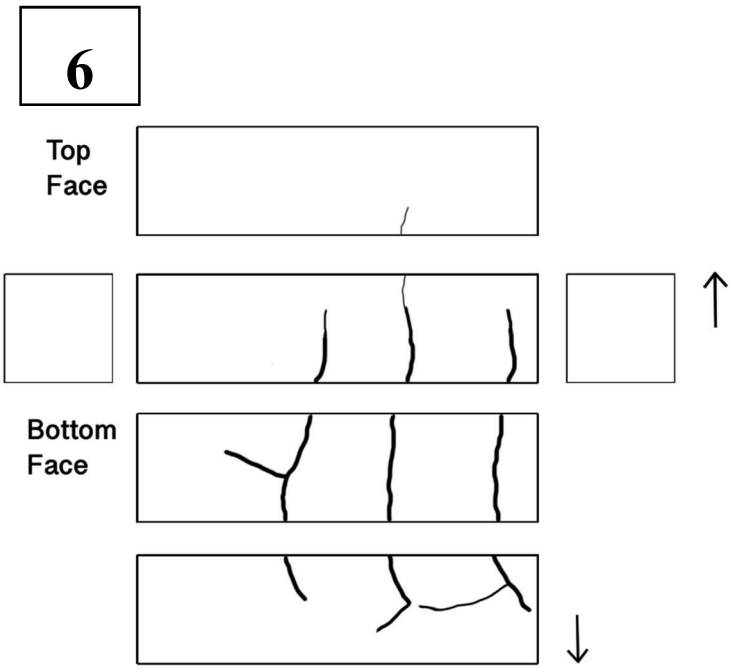
6
Top
Face
Bottom
Face

- M2